Abundance, variability and sources of Ice-Nucleating Particles in the Beijing area

Zur Erlangung des akademischen Grades eines
DOKTORS DER NATURWISSENSCHAFTEN (Dr.rer.nat.)
von der KIT-Fakultät für Physik des
Karlsruher Instituts für Technologie (KIT)

angenommene

DISSERTATION

von

M.Sc. Yaqiong Hu

Tag der mündlichen Prüfung:	01.08.2025
Referent:	Prof. Dr. Thomas Leisner
Korreferentin:	Prof. Dr. Corinna Hoose

Acknowledgements

> *“Die Monotonie und Einsamkeit eines ruhigen Lebens stimuliert den kreativen Geist.”*
> ——Albert Einstein
> *“The monotony and solitude of a quiet life stimulates the creative mind.”*

Looking back, it is still hard for me to believe that a Tibetan girl from a remote county in the Qinghai-Tibet Plateau could one day write her doctoral thesis in a distant land in Europe. In my journey of growth, “luck” and “perseverance” have always interwoven, guiding me through challenges. With this thesis, I would like to express my heartfelt gratitude to all the family members, teachers, friends, and companions who have shaped the person I am today.

I was born into an ordinary family in a small county in Qinghai. Thanks to a bit of talent and a lot of luck, I was always the top student in primary and junior high school, regarded as a “role model” by teachers and parents, and as a “study star” by classmates. High school studies and competition brought my first experience of struggle, and as my grades dropped, I often felt self-doubt and anxiety. I did not perform as well as I had hoped in the college entrance exam, and the disappointment of those around me made me question my own abilities. Torn between repeating another year or moving forward, I eventually followed my mother’s advice and chose a major that was not my first choice.

Fortunately, during my university years, I met someone who changed my life. After graduation, I worried about being ordinary, but I was not willing to give up easily. To be in the same city with him and to pursue my own growth, I chose to challenge myself by applying to one of the most prestigious graduate schools in our field in China. My results were not ideal, and I struggled for a long time between accepting a different offer or trying again. In the end, I chose to transfer and, by a twist of fate, became a visiting student at my dream institute. Looking back, those days were filled with uncertainty, but they also brought growth and courage.

In my second year of graduate studies, I finally moved to the city where he was pursuing his PhD. After graduation, I found a job, got married, had a child, and settled into a routine life. However, fierce workplace competition and doubts about the future kept pushing me to ask: Can I do more? Encouraged by outstanding colleagues, I began preparing to pursue a PhD abroad and applied for the CSC scholarship. Luck favored me once more, and I came to the Karlsruhe Institute of Technology in Germany, where I encountered a broader world and more rigorous academic challenges.

Fate does not show favoritism—every achievement often comes hand in hand with new challenges.At the end of 2023, my father was suddenly diagnosed with terminal cancer, with no opportunity for surgery. The devastating news shattered all my pride and strength. During most of my PhD, I could only accompany my father and family from afar, through phone calls and video chats while living in Germany. That winter,

he left us.My father lived a modest and quiet life, rarely expressing his feelings. But I always knew he was proud of me. Not being able to see him one last time or accompany him through the final stage of life is a regret I will carry for the rest of my life.Many people have asked me why I chose to pursue a PhD so far from home. The answer is simple: when I made the decision to study abroad, I believed my parents were still young and healthy. But life offers no “what ifs.” Now, all the sorrow and longing have become my motivation to move forward. I dedicate this dissertation to my father in heaven—may you continue to be proud of me in another world.

My deepest thanks go to my mother. No matter what choices or hardships I have faced, she has always offered unwavering support and gentle encouragement. I am grateful to my husband and parents-in-law for their understanding and care throughout my studies and research abroad, enabling me to pursue my dreams without distraction. Special thanks to my husband Yuxuan Bian for his constant understanding and companionship, sharing life’ s challenges with me, and often shouldering both parental roles alone. You and our son are my greatest comfort and anchor. To my lovely son Xuening Bian, your arrival has made my life complete and truly happy.

On my academic journey, I have never grown alone. I would like to sincerely thank my supervisor, Dr. Ottmar Möhler, for his academic guidance and life advice during my PhD. Under his rigorous yet open-minded approach, I gained growth, independence, and confidence. My gratitude also goes to Prof. Dr. Thomas Leisner and Prof. Dr. Corinna Hoose for serving as my thesis referees and providing invaluable academic feedback.

Thanks to every colleague in the AIDA laboratory and AAF team. Your teamwork and selfless support ensured the smooth progress of my experiments. I especially thank the technical team—Rainer Buschbacher, Tomasz Chudy, Olga Dombrowski, Jens Nadolny, Georg Scheurig, Steffen Vogt for your dedication and patience. My thanks also go to Olga Dombrowski and the INSEKT student assistants for their work on filter analysis, and to Dr. Nsikanabasi Silas Umo and Dr. Robert Wagner for their strong support in AIDA experiments and data analysis. Many thanks to Susanne Bolz for organizational help, to Frank Schwarz for IT support, and to Nicole Büttner and Dr. Romy Fösig for developing and optimizing data analysis tools for PINE and AIDA, which greatly facilitated my work.

I am grateful to my colleagues and friends in Karlsruhe for sharing each day with me. It was a pleasure to share an office with Dr. Pia Bogert, Alexander Böhmländer and Dr. Tobias Schorr, thank you for every fulfilling and joyful workday. Your companionship, encouragement, and help made a foreign land feel like home.

My sincere thanks go to the leaders and colleagues at the Beijing Weather Modification Center for their support and collaboration. Special thanks to Director Mengyu Huang for ongoing concern and help, to Ping Tian, Kai Bi, and all colleagues who assisted me in research. Thanks to the teams at the Haituo Mountain Observatory and the Pinggu Experimental Base, and to Prof. Yongchun Liu at Beijing University of Chemical Technology and his team for their collaboration and support.

I am grateful to my master’ s supervisor, Prof. Haiwen Liu, who accepted me at a time when I had no other options, and generously encouraged me to spend time as a visiting student in another group. Thanks to visiting supervisors, Dr. Yongfu Xu and Dr. Yangchun Li, the Senior Research Fellows at the Chinese Academy of Sciences, whose rigorous academic standards laid the foundation for my research journey.

Thanks to the China Scholarship Council for funding my studies abroad; without this scholarship, my research in Germany would not have been possible.

Thank you to all family and friends in Karlsruhe and around the world. Your

support, companionship, and kindness have been my strongest foundation. Whether facing challenges in research, life, or family, your encouragement and advice have always brought me comfort and strength.

Finally, thank you to everyone who has ever helped, encouraged, supported, or accompanied me on my journey through study, work, and life. I will always remember your warmth, kindness, and sincerity, and move forward with gratitude.

Above all, I also owe thanks to myself. Throughout the long, solitary, and sometimes anxious journey of study, it was perseverance and creativity that helped me endure every ordinary but challenging day. Thank you for not giving up, for growing and breaking through in the monotony and solitude.

Yaqiong Hu
June, 2025
Karlsruhe Institute of Technology, Germany

“Die Monotonie und Einsamkeit eines ruhigen Lebens stimuliert den kreativen Geist.”
——Albert Einstein
“宁静生活的单调与孤独激发了创造力。”
——阿尔伯特·爱因斯坦

每当回望来路，我都很难相信，那个从青海边远小县城走出的女孩，竟然能有一天在遥远的欧洲异国他乡，写下这篇博士论文。在我的成长字典里，“幸运”和“坚持”一直交错着前行。谨以此文，献给那些成就了今天的我的亲人、老师、朋友与同伴们。

我出生在青海小县城一个普通家庭。得益于天分和运气，小学初中时期我总能考出第一，是老师和家长眼中的“榜样”，同学们口中的“学霸”。高中的课程和竞争让我第一次感受到力不从心，成绩的下滑让我时常自卑和焦虑。高考时自认没有发挥好，周围亲友的失望让我一度怀疑自己的能力，也纠结要不要复读，但最终还是听从母亲的建议，选择了并不“心仪”的专业。

幸运的是，在大学里遇见了改变我一生的人。大学毕业后，我一边担心自己的平庸，一边又不愿轻易认输。为了能与他在同一座城市，同时实现自我成长，我毅然决定报考国内本领域最具声望的研究生院校之一。结果考得并不理想，在调剂和“再战一年”间徘徊许久，最终选择了调剂，又“曲线救国”地成为自己梦想学校的客座生。回头看，那段日子虽然忐忑，但也因此收获了成长和勇气。

研究生第二年，我如愿以偿来到他读博的城市，顺利毕业、工作、结婚、生子，开始了按部就班的生活。可单位的激烈竞争和对未来的迷茫，让我不断追问自己，是否能继续突破？于是，身边优秀同事的鼓励下，我开始准备出国读博，申报 CSC 国家奖学金。幸运再次眷顾我，让我来到德国卡尔斯鲁厄理工大学，真正见识到更广阔的世界和更严苛的学术挑战。

命运从不偏爱谁，每一次收获都伴随着新的考验。2023 年年底，我的父亲突然被确诊为癌症晚期，已无手术机会。晴天霹雳般的噩耗击溃了我所有的骄傲和坚强。博士阶段的大部分时间，我只能在德国与家乡之间用手机和视频陪伴父亲、家人。去年的冬天，父亲还是离开了我们。父亲一生朴实低调，不善言辞，但我知道，在他心里一直为我自豪。没能见到父亲最后一面、不能陪伴他走完生命的最后时光，是我一生的遗憾。很多人问我，为什么选择千里迢迢出国读博？答案其实很简单：当初决定出国，是因为觉得父母还年轻，身体还健康；但人生永远没有“如果”。如今，所有遗憾和思念，只能化作前行的动力，把我的这篇论文献给天堂里的爸爸——愿您在另一个世界，仍能为我感到骄傲。

我要感谢母亲。无论人生路上的任何选择与跌宕，她始终给予我最坚定的支持和最温柔的安慰。感恩丈夫和公婆，一路以来对我的包容和体贴，让我可以安心读书和科研，心无旁骛追逐梦想。特别感谢丈夫边宇轩的理解和陪伴，陪我共同面对生活的挑战，也独自承担起为人父母的责任。你和儿子，是我生命里最温暖的港湾。感谢可爱的儿子边雪宁，你的到来让我的人生变得完整幸福。

学业路上，我深知个人的成长从不是孤军奋战。衷心感谢我的导师 Dr. Ottmar Möhler，感谢您在博士期间给予我学术指导与生活帮助。在您严谨治学与开放包容的学术氛围中，我收获了成长、独立和自信。感谢 Prof. Dr. Thomas Leisner 和 Prof. Dr. Corinna Hoose 担任我的论文评阅人，并提出了宝贵建议。

感谢 AIDA 实验室与 AAF 团队的每一位同事。是你们的团队协作和无私支持，让实验工作顺利进行。特别感谢 Rainer Buschbacher, Tomasz Chudy, Olga Dombrowski, Jens Nadolny, Georg Scheurig, Steffen Vogt 等技术团队的辛勤付出和耐心帮助。感谢 Olga Dombrowski 和 INSEKT 项目学生助理对滤膜的分析工作。感谢 Dr. Nsikanabasi Silas Umo 和 Dr. Robert Wagner 在 AIDA 实验的开展和数据分析中的大力支持。感谢 Susanne Bolz 协助组织管理，感谢 Frank Schwarz 提供的信息技术支持，感谢 Nicole

Büttner, Dr. Romy Fösig 开发并优化了 PINE 和 AIDA 的数据分析工具，为我的数据处理带来了极大便利。

感谢和我一起在卡尔斯鲁厄度过每一天的同事与朋友们。感谢有幸能与 Dr. Pia Bogert，Alexander Böhmländer 和 Dr. Tobias Schorr 共享办公室度过每个充实而愉快的工作日。感谢你们在日常生活中的点滴陪伴、鼓励与帮助，让异国他乡也变得温暖而有归属感。

感谢北京市人工影响天气中心领导和同事们的帮助和合作。特别感谢黄梦宇主任一直以来的关心和支持，感谢田平、毕凯等同事在科研中的合作与帮助。感谢海坨山观测站团队、平谷实验基地的伙伴们，还有北京化工大学刘永春教授和他的团队在观测中的合作与支持。

感谢我的硕士导师刘海文教授，在我最无助的时候愿意接纳调剂的我，并以极大的宽容和鼓励让我去其他课题组客座完成硕士研究。感谢客座研究生导师徐永福研究员和李阳春研究员，你们严谨治学的精神，是我科研路上的启蒙。

感谢 CSC 国家留学基金管理委员会对我的资助，没有这份奖学金，就没有我在德国的科研之旅。

感谢所有卡尔斯鲁厄以及国内外的家人和朋友们。你们的支持、陪伴和善意，是我异国求学路上最坚实的依靠。无论是科研、生活、家庭还是人生选择上的迷茫和困惑，你们的鼓励和建议都让我收获了温暖与力量。

同时，也感谢所有在我求学、工作、生活道路上帮助、鼓励、支持和陪伴过我的人。我会铭记所有温暖、善良、真挚的情谊，怀着感恩的心，继续前行。

最后，我也想对自己说一声谢谢。在漫长、孤独甚至焦虑的求学时光里，正是坚持和创造力陪伴我走过每一个平凡又难熬的日子。谢谢自己没有放弃初心，在单调与孤独中不断成长、探索、突破自我。

虎雅琼
2025 年 6 月 23 日
德国卡尔斯鲁厄理工学院

Abstract

Ice-nucleating particles (INPs) are microscopic aerosol particles that serve as the seeds for the formation of ice crystals in clouds and by that also the initiation of precipitation processes. These processes exert fundamental influences on cloud properties and the climate system. Large uncertainties in the formulation of aerosol cloud interactions in current climate models underscore the urgent need for improved understanding of INPs. Beijing' s proximity to major Asian dust sources and the strong anthropogenic emissions in the surrounding area make it a unique natural laboratory to investigate INPs under complex atmospheric conditions.

Long-term and high-resolution INP observations in such anthropogenically influenced environments have been scarce, leaving a critical knowledge gap. This thesis used an innovative multi-method approach, combining controlled laboratory experiments using advanced facilities, long-term field observations at mountain, suburban, and urban sites in Beijing, and also an intensive campaign during the 2022 Winter Olympics emission control period with detailed aerosol and INP measurements. The use of multiple instruments with cross-validation significantly enhanced the robustness and reliability of the results.

The results reveal that Asian dust was the most efficient INP source that influences North China, and laboratory experiments further demonstrate that Asian dust has an ice-nucleating active site (INAS) density which decreases with temperature at a steeper rate than that represented by existing global dust parameterization, indicating unique ice-nucleating properties of Asian dust. According to the long-term INP offline observations, the INP concentrations exhibited pronounced seasonal and spatial variations, with values peaking in spring and dropping to a minimum in winter, and with the mountain site registering the highest and most variable concentrations versus lower, more stable levels at the urban and suburban sites.

Intensive online observations with CFDC and PINE revealed a clear correlation between INP concentrations and pollution levels, with INP numbers being approximately one order of magnitude higher during extremely polluted episodes compared to clean periods. However, discrepancies were observed between online and offline INP measurement techniques. Long-term offline observations using filter sampling showed that INP concentrations were lowest during winter when large-scale emissions are typically higher, suggesting that anthropogenic aerosols may not be efficient INPs. These findings highlight the need for further research to understand the discrepancies between different INP measurement techniques. Despite the differences, the nucleating efficiency (n_s) was consistently found to be low.Therefore, a new parameterization using surface area larger than 500 µm (SA_{500})was chosen to predict the INPs over the anthropogenically influenced area.

This thesis presents a pioneering dataset and a comprehensive experimental study that significantly advances the understanding of INP behavior in Beijing' s atmosphere; these findings carry broad implications for reducing aerosol cloud interaction uncertain-

ties in climate models, improving the accuracy of regional weather forecasts, and informing aerosol pollution management and public health strategies in megacities worldwide.

Preface

The PhD candidate confirms that the research presented in this thesis contains significant scientific contributions produced by herself. Chapter 5 in this thesis includes a limited portion of material from the following publication:

Hu, Y., Tian, P., Huang, M., Bi, K., Schneider, J., Umo, N. S., Ullmerich, N., Höhler, K., Jing, X., Xue, H., Ding, D., Liu, Y., Leisner, T., and Möhler, O. (2023). Characteristics of ice-nucleating particles in Beijing during spring: A comparison study of measurements between the suburban and a nearby mountain area. Atmospheric Environment, 293, 119451. https://doi.org/10.1016/j.atmosenv.2022.119451.

Grammarly, DeepL, and ChatGPT have been used for the improvement of postprocessing scripts, plotting scripts, and stylistic improvements in the thesis.

Contents

List of Figures

List of Tables

Chapter 1

Introduction

1.1 Aerosols and ice-nucleating particles (INPs)

Atmospheric science, as an interdisciplinary field that integrates physics, chemistry, and meteorology, provides the foundation for understanding Earth's climate and weather systems. Central to this complexity, atmospheric aerosol particles play a fundamental role in modulating both global and regional climate. Aerosols, defined as minute solid or liquid particles suspended in the atmosphere with diameters spanning from nanometers to tens of micrometers, affect Earth's radiative balance via two principal mechanisms: directly, by scattering and absorbing solar and terrestrial radiation, and indirectly, by acting as Cloud Condensation Nuclei (CCN) and ice-nucleating particles (INPs), fundamentally altering cloud ice formation and microphysical properties.

Reports from the Intergovernmental Panel on Climate Change (IPCC) have consistently emphasized that aerosol-cloud interactions constitute the largest source of uncertainty in current climate model projections (IPCC, 2021). This recognition underscores both the scientific urgency and practical relevance of research in this domain. Uncertainties in the representation of aerosol-cloud interactions directly undermine the reliability of climate change predictions and the formulation of effective mitigation strategies. Given that these interactions are a dominant factor underlying climate model uncertainty, advancing knowledge in this area is essential to enable more accurate climate projections and informed policy decisions.

Among all cloud types, those containing an ice phase—specifically mixed-phase clouds and cirrus—are particularly complex and climatically significant. Such clouds exert strong controls on Earth's radiative budget, the hydrological cycle, and climate sensitivity. Cloud formation is fundamentally initiated by aerosol particles serving as "seeds" for both cloud droplets and ice crystals (i.e., CCN and INPs). While CCN are typically abundant and responsible for the nucleation of liquid clouds, INPs constitute a rare but critically important subset of atmospheric aerosols that can induce ice formation at relatively high temperatures. Despite concentrations that are often several orders of magnitude lower than those of CCN, INPs play an irreplaceable role in ice-phase cloud microphysics, acting as a highly sensitive leverage point within the atmospheric system. Minor variations in INP concentration or activity can trigger substantial nonlinear changes in cloud phase, radiative properties, and precipitation efficiency (DeMott & Prenni, 2010).

Atmospheric ice formation proceeds primarily through two pathways: homogeneous and heterogeneous nucleation. In contrast to homogeneous nucleation, heterogeneous nucleation, catalyzed by INPs, enables ice formation at much warmer temperatures (0 °C to −38 °C) and is widely regarded as the dominant mechanism for primary ice production in the troposphere, particularly in mixed-phase clouds. INPs facilitate this process by providing solid surfaces with favorable crystallographic structures, reducing the nucleation energy barrier and allowing ice to form under lower supersaturation conditions than required for homogeneous freezing. This influence on cloud phase evolution, especially within climatically important mixed-phase cloud regimes, has direct implications for mid-latitude precipitation and radiative transfer.

Heterogeneous ice nucleation encompasses several distinct modes, each dependent on thermodynamic conditions and INP physicochemical properties; these modes are detailed in Chapter 2. In mid-latitude regions, INPs serve as the principal initiators of ice crystals in mixed-phase clouds containing both supercooled liquid water and ice. The presence and properties of INPs control cloud phase, radiative characteristics, and life cycle, thereby impacting Earth's energy balance. Thus, INPs regulate ice formation, indirectly influencing planetary albedo and the greenhouse effect. The distinction between INPs and CCN, along with the specific nucleation mechanisms they trigger, further illustrates the complexity of cloud processes.

1.2 Backgrounds and challenges of INP research

Research on INPs is essential for advancing cloud process representation in climate models, as accurate INP parameterization underpins robust understanding of cloud feedbacks and precipitation patterns, both central to the global water cycle and energy balance (Kanji et al., 2017). Nevertheless, substantial challenges persist. The scarcity of global, long-term, and high-resolution INP observational networks limits the ability to resolve seasonal and inter-annual variability. The low atmospheric concentrations of INPs, coupled with their diverse sources and physicochemical heterogeneity, make direct measurement exceptionally challenging, often leading to difficulties in instrument inter-comparison and standardization. Attributing observed INPs to specific natural or anthropogenic sources remains a major scientific hurdle, complicated by the strong temperature dependence and pronounced spatial and temporal variability of INP concentrations. Additionally, the ways in which atmospheric aging and chemical processing alter the ice-nucleating efficiency of different aerosol types remain incompletely understood. Despite decades of study—dating back to the pioneering work of Dufour in 1862 —substantial uncertainties persist regarding INP sources, concentrations, and seasonal cycles.

These enduring challenges, particularly regarding measurement comparability and source attribution, expose fundamental limitations in current atmospheric modeling. If consistent measurement of INPs across instruments is not achievable, or if their sources remain ambiguous, climate models cannot reliably simulate INP impacts, leading to systematic biases in global climate projections. This thesis addresses these global challenges through a multi-instrument, source-apportionment-focused approach, aiming to improve the robustness of atmospheric INP measurements and their interpretation.

Beijing presents a unique and challenging “natural laboratory” for INP research. Its proximity to major Asian dust sources—such as the Gobi and Taklamakan deserts—results in frequent dust events and elevated mineral dust loading. As a megacity, Beijing also experiences strong anthropogenic emissions in the surrounding area, contributing substantial fine-mode aerosols and marked seasonal variability. The confluence of these sources generates a complex aerosol mixture, often comprising aged and coated particles that combine natural dust with pollutants such as sulfate and nitrate. This atmospheric context enables investigation of the complex and often nonlinear interactions between natural and anthropogenic aerosols, and their integrated influence on INP activity. Insights gained from Beijing have broad relevance and transferability to other polluted urban centers globally, advancing understanding of INP behavior under strong anthropogenic influence.

Situated in the continental mid-latitudes of the North China Plain, Beijing frequently experiences mixed-phase cloud regimes, making detailed characterization of INPs critical for understanding regional precipitation and climate impacts. Accurate representation of INPs is vital for both weather forecasting and climate modeling, as global INP parameterizations may inadequately capture the unique aerosol dynamics of Beijing. The regional focus of this thesis, through the provision of customized datasets and parameterizations, aims to address this knowledge gap and support improved weather prediction, climate impact assessment, and environmental policy for this high-priority region.

1.3 Existing research and research gaps

Substantial progress has been achieved in global INP research, with comprehensive studies exploring mineral dust, biological particles, and combustion aerosols as key INP types. However, for severely impacted urban regions such as Beijing, comprehensive INP datasets remain scarce. In recent years, China has seen emerging studies of INPs, with measurements from cities such as Beijing, Nanjing, Tai'an, and Shenyang documenting INP concentrations influenced by both natural dust and anthropogenic aerosols. Notably, J. Chen et al. (2018) found that urban air pollution does not directly enhance INP concentrations, highlighting the dominance of natural mineral dust. Nevertheless, existing studies are typically restricted to short-term campaigns or specific conditions, lacking systematic, long-term datasets capable of fully capturing INP variability and sources in Beijing's polluted urban environment. The combined effects of natural dust and anthropogenic pollution on INP properties remain poorly constrained, especially in regions where these sources interact intensively.

This thesis targets the following persistent research gaps:

- **Lack of long-term continuous observations**: Current studies are mostly short-term, limiting comprehensive understanding of seasonal and inter-annual INP variability.

- **Unresolved properties of mixed pollution-dust INPs**: Interactions between natural dust and anthropogenic pollutants, particularly the impact of chemical aging on INP activity, are insufficiently characterized.

- **Unquantified impacts of major events and emission control policies**: The effects of major atmospheric events, such as the 2022 Winter Olympics emission control period or long-term haze episodes, on INP characteristics and sources remain largely unquantified.

- **Challenges in source apportionment**: Precisely attributing observed INP concentrations to their specific natural or anthropogenic sources in Beijing' s complex atmospheric environment continues to be a major challenge.

These knowledge gaps highlight not only a lack of data but a broader deficiency in the understanding of urban atmospheric systems, resulting in amplified uncertainties within regional atmospheric models. Addressing these gaps is thus essential for advancing fundamental knowledge of INPs in Beijing's unique atmospheric context.

1.4 Research objectives and innovations of this thesis

The overarching goal of this dissertation is to address the knowledge gaps outlined in Section 1.3, with a specific focus on the abundance, variability, and sources of INPs in the Beijing region. The broader significance of this research lies in its potential to improve global climate models, strengthen regional weather prediction, and inform air quality management and public health strategies in mega-cities. The specific objectives are as follows:

1. To quantify INP abundance and variability by establishing the first long-term, multi-site, four-season INP dataset for Beijing, resolving its concentration and spatiotemporal variability.
2. To identify the primary INP sources in Beijing, including contributions from Asian desert dust and anthropogenic pollution.
3. To evaluate the ice-nucleating efficiency of Asian desert dust through systematic laboratory experiments, quantifying activity across temperature and nucleation modes.
4. To assess the impact of major events, including large-scale emission controls during the 2022 Winter Olympics, on INP concentration and properties.

To comprehensively address these scientific questions, this thesis implements a systematic, multi-perspective research design, providing an unprecedented view of INP behavior in Beijing' s complex atmosphere. The approach combines three core methodologies: controlled laboratory experiments, extensive long-term field observations, and intensive field campaigns. This integrated strategy enables the investigation of intrinsic properties under controlled conditions (laboratory), long-term trends (field), and event-specific effects and source attribution (campaign). The multi-pronged approach substantially enhances the robustness and completeness of results, with key innovations as follows:

- **Integrated multi-method research**: This study combines laboratory experiments, long-term field observations, and targeted intensive field campaigns to deliver a comprehensive understanding of INP behavior, ensuring the reliability and completeness of findings.
- **Pioneering dataset**: The establishment of the first long-term, multi-site INP dataset for Beijing, providing unprecedented high-resolution data for the region.
- **Region-specific parameterization**: Development of a new INP parameterization scheme for Asian desert dust, which demonstrates marked differences from existing global benchmarks and is crucial for improved climate modeling.
- **In-depth insight into anthropogenic–natural interactions**: The thesis advances understanding of the often indirect and complex interactions between anthropogenic pollution and natural INPs, challenging conventional assumptions about the direct impact of pollution on ice nucleation.

- **Multi-instrument validation**: The continuous use and inter-comparison of multiple state-of-the-art INP measurement instruments (e.g., Aerosol Interaction and Dynamics in the Atmosphere (AIDA), Ice Nucleation Spectrometer of the Karlsruhe Institute of Technology (INSEKT), Portable Ice Nucleation Experiment (PINE), INKA, BeiJing-Continuous Flow Diffusion Chamber (BJ-CFDC), FINDA) significantly enhances the robustness and reliability of results, addressing a central challenge in INP research.

1.5 Thesis structure

The thesis is organized as follows:

- **Chapter 2:** Scientific Background provides the fundamental scientific background on atmospheric aerosols, ice formation in clouds, nucleation theory, previous INP studies, and the current state of INP research, highlighting the knowledge gaps specific to the Beijing region.
- **Chapter 3:** Experimental Methods details the comprehensive suite of advanced instrumentation and experimental methods employed in this work, including both laboratory facilities and field measurement systems.
- **Chapter 4:** Laboratory Ice Nucleation Experiments presents results from experiments characterizing the ice-nucleating properties of mineral dust from key Asian deserts, a primary natural source impacting Beijing.
- **Chapter 5:** Long-term Field Observations analyzes the first multi-year, continuous dataset of INP concentrations in the Beijing area, revealing their abundance and seasonal-to-interannual variability across different site types.
- **Chapter 6:** Intensive Field Campaign investigates the sources and characteristics of INPs during a unique intensive campaign, leveraging the emission controls of the 2022 Winter Olympics to disentangle anthropogenic and natural contributions.
- **Chapter 7:** Summary and Outlook synthesizes the key research findings of this thesis and proposes future research directions for INP studies.

This structure ensures a comprehensive exploration of INPs in Beijing, addressing critical scientific questions and contributing to improved climate and weather modeling.

Chapter 2

Scientific Background

This chapter provides the foundational scientific context and theoretical underpinnings for the research presented in this dissertation, focusing on INPs in the Beijing area. It begins by defining atmospheric aerosol particles and elucidating their multifaceted roles in the Earth’ s climate system, with a particular emphasis on their function as precursors for cloud formation. Subsequently, the chapter delves into the intricate mechanisms of ice formation within atmospheric clouds, highlighting the critical distinction between homogeneous and heterogeneous nucleation and providing a detailed exposition of the four primary heterogeneous ice-nucleation modes. A review of classical nucleation theory and the more advanced Ice Nucleation Active Site density (INAS density) approach follows, establishing the theoretical frameworks for quantifying INP activity. The chapter then synthesizes the current state of global and regional INP research, critically evaluating key findings, existing parameterization schemes, and the persistent knowledge gaps. Finally, it systematically articulates the unique importance and urgency of studying INP characteristics in the Beijing region, outlining the specific scientific questions that this dissertation aims to address and briefly introducing the advanced measurement techniques employed.

2.1 Atmospheric aerosol particles

Atmospheric aerosol particles are minute solid or liquid particulates suspended in the atmosphere, with diameters ranging from a few nm to tens of µm (Seinfeld & Pandis, 2006). These particles exhibit a vast size range and diverse physical and chemical properties—such as size, morphology, composition, and mixing state—that profoundly influence their atmospheric behavior, including transport, settling rates, and interactions with clouds and radiation. Aerosols originate from both natural and anthropogenic sources, contributing to their variability across space and time. Natural sources include wind-blown mineral dust from arid regions, sea spray from oceanic waves, volcanic emissions, and primary biological particles like pollen and bacteria (Hoose & Möhler, 2012). Anthropogenic sources, such as fossil-fuel combustion, industrial processes, and vehicular exhaust, emit primary particles or precursors for secondary aerosols formed via atmospheric reactions (An et al., 2019). This interplay of emission sources, transport, and transformation processes governs aerosols’ characteristics and determines their climatic and environmental impacts. Particle size affects atmospheric lifetime and travel distance, while chemical composition influences hygroscopicity and ice-nucleation ability; the mixing state further complicates their behavior by introducing non-linear effects (Riemer et al., 2019). Aerosols play critical roles in direct and indirect radiative effects, cloud and precipitation processes, and air quality, with high concentrations in urban areas like Beijing often linked to severe pollution and health risks (R.-J. Huang et al., 2014). Comprehensive characterization of these properties is essential for modeling aerosol–cloud interactions and climate feedbacks (S. C. Sullivan et al., 2017).

Aerosol size distributions in the atmosphere typically exhibit several modes, including the nucleation mode (particles with diameters less than 10 nm), the Aitken mode (10 nm to 100 nm), the accumulation mode (100 nm to 1000 nm or up to 2.5 µm), and the coarse mode (greater than 1 µm or 2.5 µm) (Seinfeld & Pandis, 2006; Whitby, 1978). These modes reflect different formation and growth mechanisms: nucleation-mode particles arise from new particle formation, Aitken and accumulation-mode particles are influenced by coagulation and condensation, and coarse-mode particles originate from mechanical processes such as wind-blown dust and sea spray (Kulmala et al., 2004). The size distribution of aerosol particles is a critical determinant of their climatic and cloud-forming impacts. Particles within the accumulation and coarse modes are particularly relevant for atmospheric optics and cloud formation processes (Kanji et al., 2017). Specifically, particles larger than approximately 50 nm to 100 nm can serve as CCN, with their activation efficiency governed by size and hygroscopicity as described by Köhler theory (Petters & Kreidenweis, 2007). For INPs, effectiveness is also size-dependent, with larger particles—typically 200 nm or greater—being more effective due to their greater surface area and higher probability of hosting ice-active sites (Hartmann et al., 2013). Coarse-mode particles, such as mineral dust, are notably effective INPs, and their concentration can serve as a first-order estimate of INP availability, especially during dust events (DeMott, Prenni, et al., 2010). Thus, size-resolved measurements of aerosol populations are essential for understanding their roles in cloud processes, activation spectra, and climate feedbacks.

The chemical composition of atmospheric aerosols is highly variable and diverse, encompassing inorganic salts such as sulfates, nitrates, and ammonium, as well as complex organic compounds, black carbon, mineral dust components like silicates, feldspars, and clays, sea salt, and a wide range of secondary organics (Seinfeld & Pandis, 2006). These constituents significantly influence the aerosols' physical and chemical properties, particularly their ability to act as INPs, with certain minerals—most notably feldspar—recognized for their high efficiency due to unique surface properties (Atkinson et al., 2013).

The Beijing area exemplifies a complex and dynamic aerosol environment, shaped by its proximity to major dust source regions such as the Gobi and Taklamakan deserts, and by intense urban activities, resulting in pronounced seasonal variability (Daellenbach et al., 2024). Spring is characterized by frequent dust storms from the Gobi and Taklamakan deserts, and Loess Plateaus, elevating mineral dust levels, while winter sees elevated carbonaceous aerosols—including black carbon and organic carbon—from coal combustion and vehicular emissions, predominantly contributing to the fine-mode particle population (R.-J. Huang et al., 2014). Summer conditions, with high temperature and humidity, favor secondary organic aerosol formation via photochemical reactions, increasing organic content; whereas autumn experiences a mix of industrial emissions and residual dust. This confluence of natural sources (e.g., desert dust, biogenic emissions) and anthropogenic sources (e.g., fossil fuel combustion, industrial processes) creates a complex mixture of aged, coated particles, often combining natural dust with pollutants such as sulfate and nitrate.

Recent shifts in Beijing's aerosol composition show nitrate dominating secondary inorganic aerosols due to reduced coal combustion emissions, unlike the historical sul-

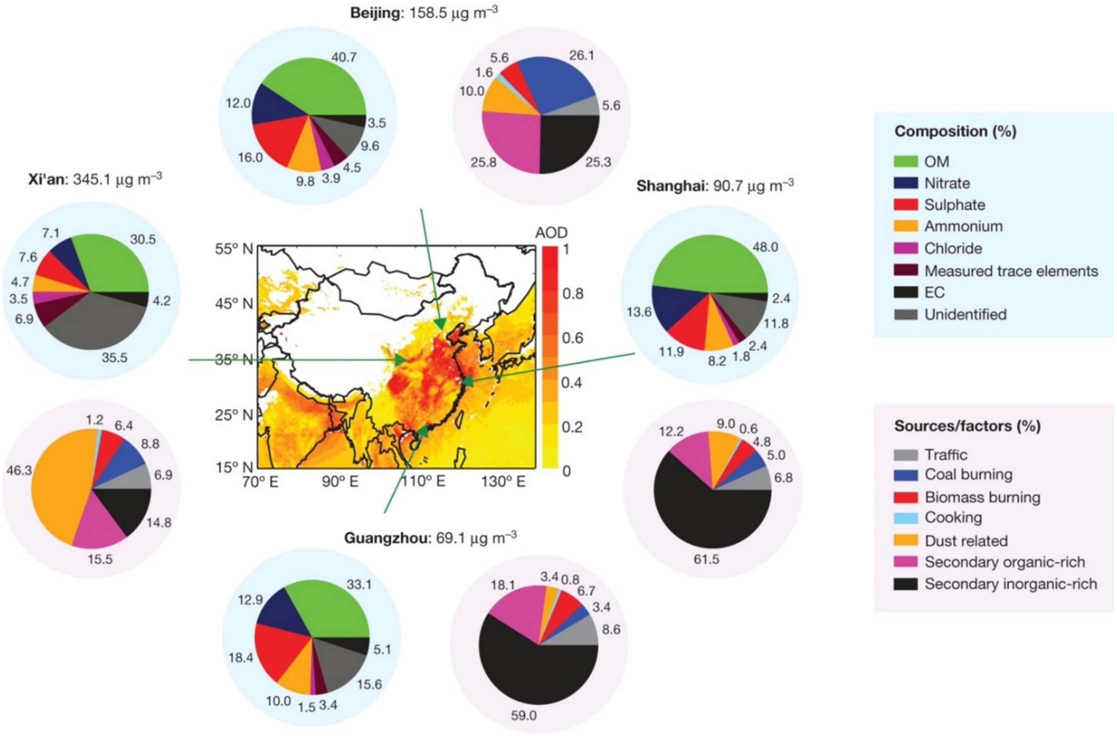

Figure 2.1: Chemical composition and source apportionment of $PM_{2.5}$ collected during the high pollution events of 5–25 January 2013 at the urban sites of Beijing, Shanghai, Guangzhou and Xi’ an (R.-J. Huang et al., 2014).

fate dominance in heavy-industry cities. The interaction between abundant natural dust and high anthropogenic pollution introduces uncertainty regarding the ice-nucleating activity of these mixed aerosols, raising questions about whether pollution enhances or suppresses the effectiveness of natural dust INPs (Bi et al., 2019). Atmospheric aging, involving pollutant coatings, can alter INP activity in complex, non-linear ways, necessitating deeper investigation beyond individual-source studies. The chemical makeup, particularly the presence of minerals like feldspars and clays or biological material such as bacteria and fungal spores, further enhances INP potential (Boose et al., 2016). Understanding this “aging effect” is critical for accurate INP parameterization in Beijing’ s regional atmospheric models, as dust concentration alone may not predict ice nucleation activity. Figure 2.1 illustrates the aerosol chemical components in Beijing, highlighting the interplay between dust, pollution, and secondary organics.

Aerosols significantly impact the Earth’ s climate system through direct and indirect effects, with semi-direct effects also influencing atmospheric stability. The direct effect involves the scattering and absorption of solar and terrestrial radiation, leading to atmospheric cooling or warming depending on aerosol optical properties—determined by its size, composition, and mixing state. The indirect effect is more complex, stemming from aerosols acting as CCN or INPs, thereby altering cloud properties such as albedo, lifetime, and precipitation efficiency (Lohmann & Feichter, 2005). In warm clouds ($T > 0\,°\mathrm{C}$), fine particulate matter ($PM_{2.5}$) can form numerous smaller droplets, increasing cloud optical depth and albedo—known as the Twomey effect—while potentially delaying precipitation. In mixed-phase and ice clouds, INPs are critical for initiating ice formation, thus influencing precipitation processes essential to regional weather patterns. The intricate nature of aerosol–cloud interactions, particularly the role of INPs, remains a major uncertainty in global climate models (Burrows et al., 2022; IPCC, 2021). Beyond their climatic role, aerosols adversely affect air quality and public health, especially in urban areas, by transporting toxic substances and serving as carriers for pathogens (Pöschl, 2005). Notably, in Beijing, while aerosols pose a significant pollution challenge, some may enhance precipitation—a vital resource in this water-scarce region—highlighting a complex trade-off in environmental policy decisions.

It is critical to note that not all atmospheric aerosol particles serve as “seeds” for cloud droplets or ice crystals; only a small fraction possess the necessary surface and chemical properties to initiate such processes. Among these, INPs constitute a rare yet vital subset, capable of triggering ice nucleation at relatively high temperatures (e.g., above $-38\,°\mathrm{C}$), unlike most particles that require much lower temperatures or cannot nucleate ice at all (DeMott, Prenni, et al., 2010). Despite their concentrations being orders of magnitude lower than those of CCN, INPs exert a disproportionate influence on cloud microphysics, macroscopic properties, life cycles, precipitation formation, and radiative forcing. This leverage within the atmospheric system implies that even minor changes in INP concentration or activity can significantly alter cloud phase, radiative properties, and precipitation efficiency, positioning INPs as a sensitive yet pivotal element in climate feedback mechanisms.

Primary INP sources include mineral dust from arid regions such as the Gobi and Taklamakan deserts—rich in efficient ice-nucleating minerals such as feldspar and clay minerals—which dominate in Beijing, particularly during dust storm events (Hoose & Möhler, 2012). Biological aerosols, including bacteria, fungal spores, and pollen, are also highly effective INPs, initiating ice formation at warmer temperatures, while anthropogenic particles like soot, industrial emissions, and fly ash exhibit variable ice nucleation activity, remaining under active scientific investigation (Govindarajan & Lindow, 1988).

2.2 Ice formation in atmospheric clouds

The formation of ice crystals within atmospheric clouds is a fundamental process that profoundly governs cloud microphysics, dictates the development and intensity of precipitation, and critically influences the Earth’s radiative balance. The presence of ice particles significantly alters cloud properties, including their albedo (reflectivity), lifetime, phase, and efficiency in producing precipitation. In mixed-phase clouds —where supercooled liquid water and ice crystals coexist—the Wegener–Bergeron–Findeisen (WBF) process serves as a core mechanism driving precipitation (Bergeron, 1935; Wegener, 1912). This process exploits the principle that, at the same sub-zero temperature, the saturation vapor pressure over ice is lower than that over supercooled liquid water, establishing a vapor pressure gradient that causes supercooled droplets to evaporate while ice crystals grow rapidly through vapor deposition. This accelerated growth enables ice crystals to attain sizes sufficient to sediment out of the cloud, initiating precipitation more efficiently than in purely liquid-phase clouds reliant on collision–coalescence.

Predominant in mid-latitude regions, the WBF process amplifies the role of INPs; even a small number of initial ice crystals, nucleated by rare INPs, can trigger a cascade of growth that substantially enhances precipitation (H. Pruppacher & Klett, 2010). This amplification underscores the critical need for accurate INP characterization in weather modification efforts, such as cloud seeding, and for improving regional precipitation forecasting, particularly in areas like Beijing facing water scarcity and extreme weather events.

Beyond precipitation, cloud phase exerts significant radiative consequences: ice clouds typically exhibit lower optical depth than liquid clouds of equivalent water content, affecting albedo and longwave radiation emission, which may result in warming or cooling effects depending on cloud altitude and thickness. The contrast in radiative properties between pure ice clouds (e.g. cirrus) and mixed-phase or liquid clouds highlights the climate significance of phase transitions, particularly as anthropogenic activities and climate change alter atmospheric aerosol loadings.

Clouds in the atmosphere are broadly categorized into three types based on their dominant phase: warm clouds, consisting purely of liquid water droplets at temperatures above 0 °C; mixed-phase clouds, containing both supercooled liquid water and ice crystals at temperatures between 0 °C and approximately −38 °C; and ice clouds, composed primarily of ice at temperatures below −38 °C. Mixed-phase clouds, prevalent in mid- to high latitudes, play a critical role in precipitation formation and Earth' s radiative balance due to the dynamic coexistence of supercooled liquid water and ice crystals. Supercooled liquid water, a metastable state where liquid persists below its normal freezing point, is common in the atmosphere because homogeneous nucleation—the spontaneous formation of ice crystals—requires temperatures below −38 °C (Koop et al., 2000). In mixed-phase clouds, which typically occur above this threshold, ice formation depends entirely on heterogeneous freezing initiated by INPs. The persistence of supercooled water, as highlighted by Korolev et al. (2017), significantly influences cloud phase, lifetime, and precipitation efficiency. Furthermore, these clouds are highly sensitive to temperature and INP availability; even minor variations can shift the liquid–ice phase partitioning, altering radiative properties and precipitation potential. This sensitivity positions mixed-phase clouds as a key component of climate feedback mechanisms, where changes in INP concentrations—driven by natural variability or anthropogenic activities—could exert substantial, non-linear effects on regional climate, particularly in a warming world where their regimes may shift.

Ice formation in the atmosphere occurs primarily through two pathways: homogeneous and heterogeneous nucleation. Homogeneous ice nucleation involves the spontaneous crystallization of pure supercooled water droplets in the absence of foreign particles or impurities, requiring exceptionally cold temperatures below −38 °C (approximately 235 K). This process is relevant mainly for high-altitude cirrus clouds in the upper troposphere, where low temperatures and sparse aerosol concentrations prevail. In contrast, heterogeneous nucleation, triggered by INPs, enables ice formation at warmer temperatures (−38 °C to 0 °C) and is the dominant mode of primary ice production in the troposphere, particularly in mixed-phase clouds, which constitute the most climatically significant regime. INPs catalyze this process by providing a solid surface with a favorable crystallographic structure, significantly lowering the energy barrier for nucleation and allowing ice to form at lower supersaturations than homogeneous freezing permits (H. Pruppacher & Klett, 2010). The distinction between these pathways underscores the critical role of INPs in controlling ice formation; without them, mixed-phase clouds would remain liquid down to very low temperatures, profoundly affecting their properties and precipitation potential.

Heterogeneous ice nucleation can proceed via several distinct pathways or modes, each contingent on the thermodynamic conditions (temperature and relative humidity) and the specific properties of the INP. These modes are generally categorized into four primary types: deposition nucleation, condensation freezing, immersion freezing, and contact freezing—each with specific physicochemical requirements and characteris-

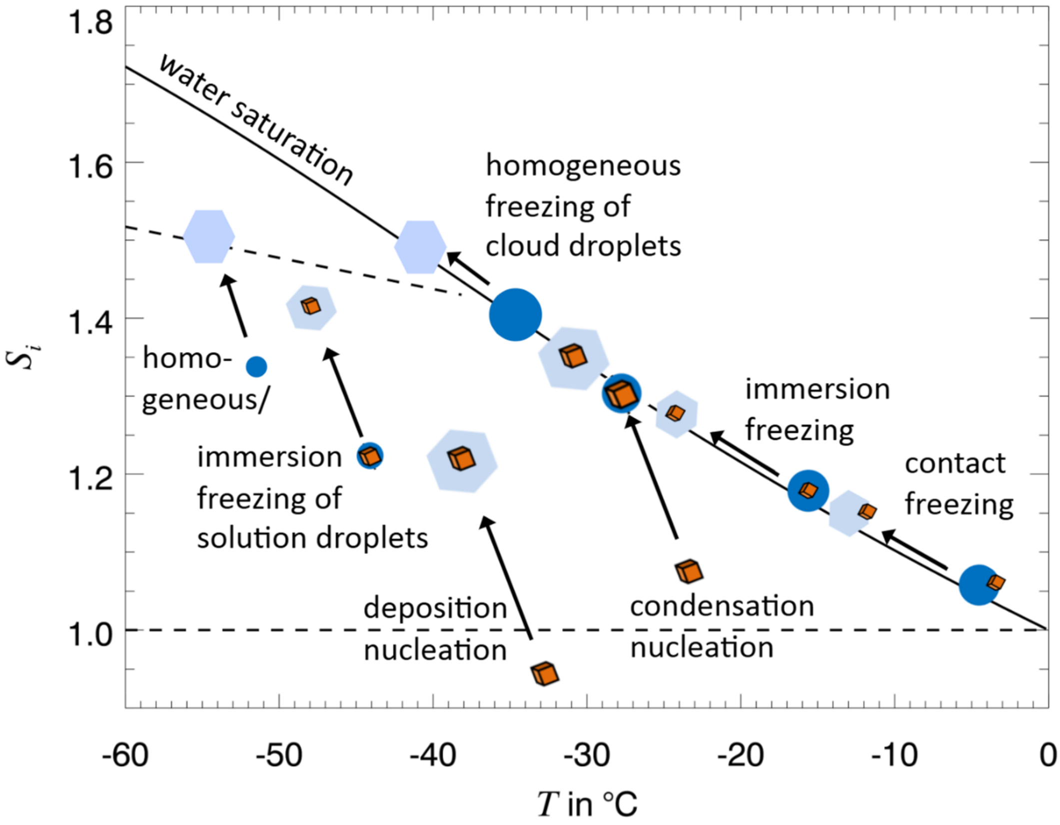

Figure 2.2: Schematic representation of the different nucleation modes (Hoose & Möhler, 2012).

tic temperature and supersaturation ranges, as illustrated in Fig. 2.2.

Deposition nucleation. Occurs when water vapor directly deposits onto the surface of an INP to form ice, bypassing an intermediate liquid phase. This mode requires conditions to be supersaturated with respect to ice ($\mathrm{RH_i} > 100\%$) but can occur below saturation with respect to liquid water ($\mathrm{RH}_w < 100\%$). It is particularly significant in the formation of cirrus clouds.

Condensation freezing. Involves the condensation of liquid water onto a particle, followed immediately by its freezing. This pathway typically occurs at or above water saturation, though its precise mechanism is debated and considered less common in the atmosphere.

Immersion freezing. Is widely regarded as the dominant mechanism for ice formation in mixed-phase clouds (Murray et al., 2012). It takes place when an INP, already immersed within a supercooled liquid droplet, triggers the droplet's freezing from within. This mode is relevant across a broad temperature range, typically from 0 °C to −35 °C.

Contact freezing. Is initiated when an INP collides with the outer surface of a supercooled droplet and triggers its freezing upon contact. While generally considered less frequent than immersion freezing, it can be locally significant.

The relative importance of these four modes varies considerably with cloud type and prevailing meteorological conditions. For instance, deposition and condensation freezing are thought to play a more significant role in the formation of cirrus clouds, whereas immersion freezing is the key process governing the glaciation of mixed-phase stratiform clouds, which profoundly impact the Earth’ s radiative budget. The clear delineation of these modes, each with distinct physical processes and typical conditions, implies that an INP’ s “activity” is not a single, fixed value but is highly dependent on the specific mode and environmental conditions. This means an INP effective in immersion freezing might not be equally effective in deposition nucleation. This complexity necessitates that INP measurements and subsequent parameterizations explicitly specify the nucleation mode and the conditions under which activity is observed.

Ice formation in clouds significantly influences their development, radiative properties, and precipitation potential. Once ice crystals form in a mixed-phase cloud, they grow rapidly through the WBF process, in which the lower saturation vapor pressure over ice compared to supercooled liquid water drives a vapor flux from evaporating droplets to growing ice crystals. This efficient growth enables ice crystals to reach sizes sufficient for sedimentation, initiating precipitation more effectively than in purely liquid-phase clouds. The transition to an ice-dominated cloud, or cloud glaciation, alters radiative properties, rendering the cloud optically thinner and less reflective to solar radiation, with distinct infrared emissive characteristics (Mülmenstädt et al., 2015).

INPs are pivotal in this process, controlling ice formation and the liquid-to-ice partitioning, thus impacting cloud lifetime, albedo, and Earth’ s energy balance. The efficiency of heterogeneous ice nucleation—the primary pathway for ice formation in mixed-phase clouds—depends on ambient temperature, supersaturation, and the physicochemical properties of INPs. Modes such as immersion freezing, typically occurring between $-15\,^{\circ}\mathrm{C}$ and $-30\,^{\circ}\mathrm{C}$, and deposition nucleation, favored at lower temperatures and ice supersaturation, exhibit varying effectiveness (Vali et al., 2015). The WBF process amplifies the influence of sparse INPs by depleting supercooled water, further affecting precipitation onset and radiative outcomes (Cziczo et al., 2009).

The concentration and characteristics of INPs play a critical role in regulating ice crystal number concentrations within clouds, significantly influencing cloud lifetime, precipitation efficiency, and radiative forcing. For instance, higher INP concentrations can lead to more numerous but smaller ice crystals, altering precipitation processes compared to scenarios with fewer, larger crystals. This effect propagates to broader climate feedbacks, since changes in INP abundance shift the balance between liquid and ice phases, thereby modulating cloud reflectivity, longevity, and precipitation efficiency (Cziczo et al., 2013).

In the Beijing region, persistently high aerosol loads that stem from a complex mix of natural dust and anthropogenic pollutants shape regional cloud properties and precipitation patterns. The area’ s mid-latitude continental climate frequently experiences mixed-phase clouds, making INP characteristics particularly relevant for understanding local precipitation, fog and ice formation, and broader climate–system impacts. Beijing’ s unique aerosol environment, characterized by dynamic interactions between natural and anthropogenic particles, presents both a challenge and an opportunity for INP research. Global INP parameterizations, often derived from less complex environments, may not fully capture Beijing’ s complex atmosphere conditions, underscoring the need for region-specific observational and modeling studies.

2.3 Classical nucleation theory

Classical Nucleation Theory (CNT), originating from the foundational works of Gibbs, Volmer, and Weber, provides a cornerstone framework for understanding phase transitions, notably the critical process of ice nucleation from supercooled water or water vapor in atmospheric contexts (Fletcher, 2011; H. Pruppacher & Klett, 2010). CNT characterizes nucleation as a stochastic process requiring the surmounting of a thermodynamic energy barrier to form a stable new phase. This barrier arises from the Gibbs free energy change ΔG, which balances a negative bulk free-energy term—favoring the transition to the ice phase as the thermodynamic driving force—and a positive surface free-energy term, reflecting the energetic cost of forming a new interface between the ice embryo and its surroundings. A critical radius r^* emerges, below which embryos are unstable and dissipate, and above which they become stable critical nuclei capable of spontaneous growth. The energy barrier' s height ΔG^* governs the nucleation rate J, quantifying critical nuclei formation per unit volume and time. In atmospheric science, CNT elucidates ice formation within supercooled water droplets or on particle surfaces, where r^* and ΔG^* vary with temperature and supersaturation—lower temperatures or higher supersaturations reducing the barrier and enhancing nucleation. Because phase transitions depend on overcoming an energy barrier, CNT serves as a foundational tenet of physical chemistry, offering a robust, adaptable basis for modeling atmospheric ice nucleation despite its complexities.

In CNT, the Gibbs free-energy change ΔG for forming a spherical ice embryo of radius r is expressed as

$$\Delta G = \frac{4}{3}\,\pi\, r^3\, \Delta G_v + 4\,\pi\, r^2\, \sigma$$

where ΔG_v is the volume free-energy difference favoring ice formation, and σ is the interfacial tension between the ice embryo and supercooled water. The critical radius r^*, at which ΔG is maximized, is

$$r^* \;=\; -\,\frac{2\,\sigma}{\Delta G_v}\,,$$

with the corresponding energy barrier

$$\Delta G^* = \frac{16\,\pi\,\sigma^3}{3\,(\Delta G_v)^2}\,.$$

The nucleation rate J, representing the number of critical nuclei formed per unit volume per unit time, follows

$$J = J_0\,\exp\!\Big(-\frac{\Delta G^*}{k\,T}\Big)$$

where J_0 is a pre-exponential factor, k is Boltzmann' s constant, and T is temperature (Kashchiev, 2000). The surface-energy term $4\,\pi\, r^2\,\sigma$ incurs an energetic cost for creating a new ice–water interface, establishing the energy barrier that allows supercooled water to persist. A larger σ increases ΔG, requiring lower temperatures for nucleation. For homogeneous nucleation in pure water, absent impurities or foreign surfaces, significant supercooling is necessary, with spontaneous freezing typically occurring below approximately −38 °C (Koop et al., 2000). Conversely, heterogeneous nucleation on insoluble substrates, such as mineral particles, reduces this energetic threshold, enabling ice formation at warmer temperatures.

In the context of heterogeneous nucleation, CNT is extended by introducing the contact angle θ, which characterizes the interaction between the ice embryo and the INP surface (Hoose & Möhler, 2012). The presence of an INP significantly reduces the energy barrier for ice nucleation compared to homogeneous nucleation, thereby promoting ice

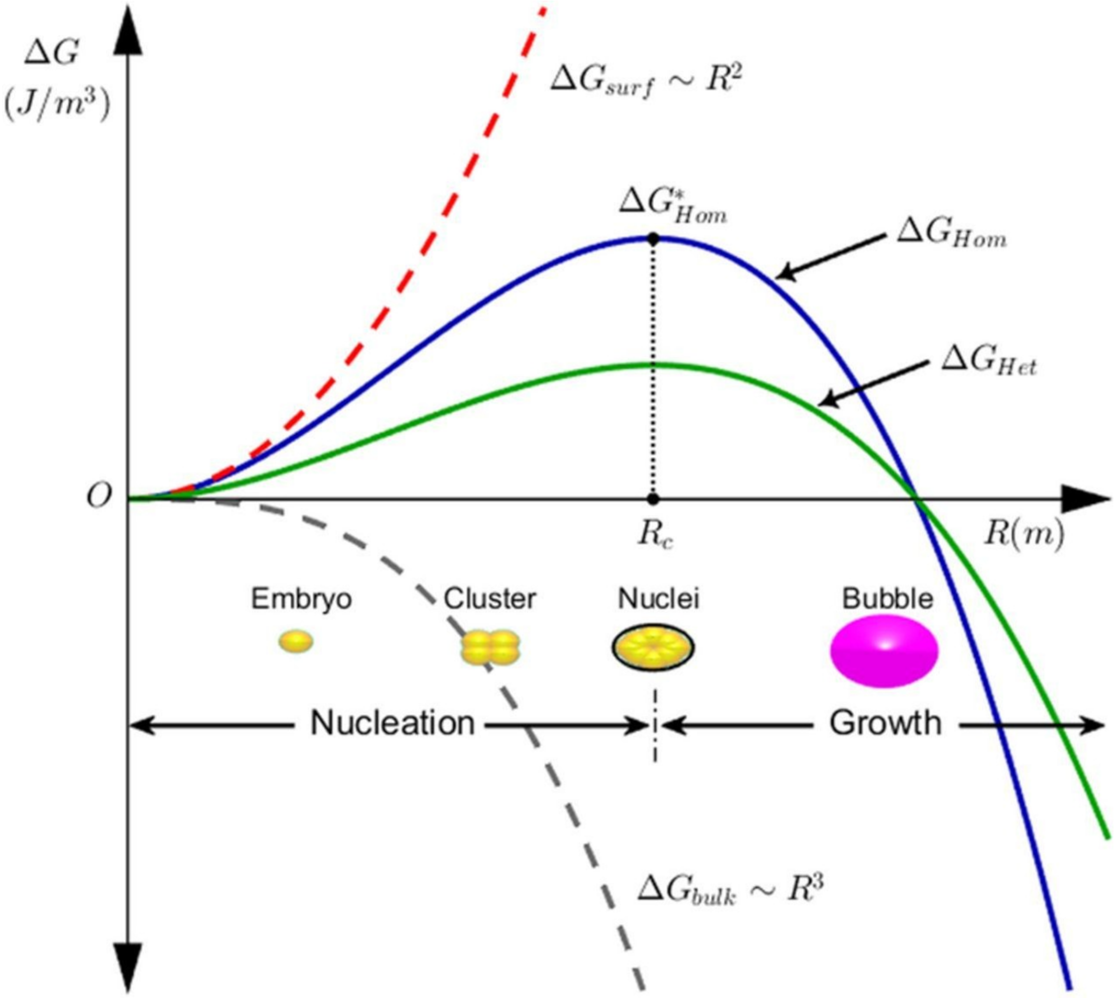

Figure 2.3: Gibbs free energy change during nucleation. The surface free energy ΔGsurf (dashed red line), bulk free energy ΔGbulk (dashed black line), homogeneous nucleation free energy ΔGHom (blue line), and the heterogeneous nucleation free energy ΔGHet (green line) are presented as a function of the radius R. The nucleation stages are also sketched for reference. The embryo and cluster states are reversible and the nuclei state is irreversible. (Taqieddin et al., 2018).

crystal formation at warmer temperatures (see Fig. 2.3). This reduction is quantified by a correction factor $f(\theta)$, such that the energy barrier for heterogeneous nucleation is

$$\Delta G_{\text{het}} = \Delta G_{\text{hom}} \times f(\theta), \quad f(\theta) = \frac{\left(2 + \cos\theta\right)\left(1 - \cos\theta\right)^2}{4}.$$

A smaller contact angle indicates a more favorable interaction, reflecting enhanced wettability or a template effect of the INP surface, which lowers the energy barrier and increases nucleation efficiency. In Beijing’s atmosphere, mineral dust particles from Asian deserts, particularly those rich in feldspar, serve as key INPs. Their specific surface properties, such as roughness and chemical composition, influence the contact angle and thus their ice-nucleation efficiency (Cziczo et al., 2013). This theoretical framework enables the parameterization of nucleation activity based on the physical and chemical properties of INPs, providing a mechanistic link between laboratory studies and atmospheric observations.

Despite its foundational role in understanding ice nucleation, CNT faces significant limitations when applied to the complexities of atmospheric processes. These limitations stem from its idealized assumptions, such as treating ice embryos as perfectly spherical and the surrounding medium as continuous, which fail to accurately represent the behavior of microscopic clusters or the irregular, chemically heterogeneous surfaces of real atmospheric INPs (Hiranuma, Möhler, et al., 2015). Key parameters like interfacial tension σ and contact angle θ are often uncertain and vary with temperature and INP type, complicating precise predictions. CNT also neglects atmospheric dynamics, such as aerosol transport and mixing, which influence INP distribution, and struggles to account for the complexity of aged or coated aerosols—such as mineral dust coated with organic material—whose nucleation properties are altered by atmospheric processing. A significant advancement is the "active-site" theory, which posits that nucleation occurs preferentially at specific nanoscale features on a particle's surface, explaining why larger particles are more effective INPs (Marcolli et al., 2007). Despite these challenges, CNT remains a critical tool for developing process-based ice nucleation models and site-density spectra, serving as the basis for many atmospheric model parameterizations. However, its application requires empirical calibration to laboratory and field data to address real-world complexities, highlighting the need for observational constraints to refine and validate INP parameterizations (Khvorostyanov & Curry, 2005; Niemand et al., 2012).

2.4 INAS density approach

Traditionally, INP measurements have been reported as the number concentration of particles activated at or below a given temperature per unit volume of air (e.g., L^{-1} or m^{-3}) (Vali, 1971). While this metric provides a practical measure of the overall freezing potential in a given environment, it is an "extensive quantity," meaning it depends on both the intrinsic ice-nucleating ability of the aerosol and its total concentration or surface area in the air, influenced by factors such as aerosol loading and atmospheric dilution. This dependence significantly limits direct comparisons of ice-nucleation efficiency across different aerosol types, locations, or environmental settings (DeMott, Prenni, et al., 2010).

For instance, in the complex atmospheric environment of Beijing, where abundant mineral dust from Asian deserts coexists with a high burden of urban pollutants, a high INP concentration may reflect elevated aerosol abundance rather than the presence of highly efficient INPs, obscuring the relative contributions of various sources and their true intrinsic efficiencies. The traditional INP concentration metric conflates the quantity of aerosols with their ice-nucleating ability, making it challenging to isolate the efficiency of different INP types, especially in environments with highly variable aerosol concentrations, such as urban areas during dust storms versus background periods (Kanji et al., 2017). This limitation highlights the need for a more refined metric, particularly in complex settings where distinguishing between the effects of high aerosol loads and highly active INPs is essential for accurate source apportionment and targeted interventions.

To overcome the limitations of traditional INP quantification, which relies on number concentration and is influenced by aerosol abundance, the INAS density approach was developed as a more precise and physically meaningful measure of nucleation efficiency (Connolly et al., 2009). INAS density, denoted as $n_s(T)$, quantifies the number of ice-nucleating active sites per unit surface area of aerosol particles at a given temperature T, serving as an intensive quantity that isolates the inherent ice-nucleating efficiency of the particles (Vali et al., 2015). This metric is particularly valuable for comparing the ice nucleation capabilities of diverse aerosols, such as mineral dust and biological particles, and for direct integration into climate models, as it reflects the underlying physicochemical properties and surface reactivity of the particles (Hoose et al., 2010). By normalizing to surface area, this conceptual shift from an extensive to an intensive quantity enables a more universal parameterization of heterogeneous ice nucleation and facilitates intercomparison between laboratory and field measurements, unaffected by variations in aerosol loading or sampling volume (Hoose & Möhler, 2012).

INAS density is experimentally measured using both offline and online techniques, each offering distinct advantages. The classic offline method involves droplet freezing assays: aerosol particles are collected from ambient air onto filters or substrates, resuspended in pure water, and partitioned into small droplets (e.g., in 96-well plates). These droplets are placed on a temperature-controlled cold stage and cooled at a controlled rate, while the fraction of droplets frozen at each temperature, $f(T)$, is recorded. The INAS density is then calculated as

$$n_s(T) \;=\; -\frac{\ln\bigl[1 - f(T)\bigr]}{A}$$

where A is the total particle surface area in the droplets (Murray et al., 2012). Offline methods primarily measure immersion freezing, a dominant mode in mixed-phase cloud regime, but can be subject to sampling biases (e.g., favoring larger particles).

Online methods, such as Continuous Flow Diffusion Chambers (CFDCs), expose ambient aerosols directly to controlled temperature and humidity conditions, measuring ice crystal formation in real time. The INAS density $n_s(T)$ is derived by dividing the measured INP concentration by the total aerosol surface-area concentration (DeMott et al., 2018). While CFDCs offer high temporal resolution, they may have reduced sensitivity for very small particles. Both approaches are essential for understanding INP behavior in dynamic environments, where a multi-instrument approach leverages their complementary strengths—offline methods for broad temperature range and direct immersion freezing measurement, and online methods for real-time variability capture—supporting comprehensive INP characterization. The temperature dependence of n_s reflects the activation energy of freezing and the distribution of active sites, varying significantly among aerosol types and with particle processing history.

The INAS density approach is widely employed in atmospheric modeling to provide a physically based parameterization for ice nucleation processes (Phillips et al., 2008). By integrating measured or parameterized $n_s(T)$ values with aerosol surface-area distributions, this framework enables the prediction of ice crystal number concentrations, allowing models to more accurately simulate INP concentrations across diverse atmospheric conditions and thereby enhance simulations of cloud microphysics and precipitation. Parameterizations commonly express the logarithm of $n_s(T)$ as a linear function of temperature, facilitating empirical fits that can be readily incorporated into global and regional climate models (Fig. 2.4). This approach also permits the distinction and separate treatment of various INP sources, such as mineral, biological, and anthropogenic aerosols. Although some studies normalize INP activity to mass or particle number, normalization by surface area is preferred due to the fundamentally surface-mediated nature of ice nucleation. Furthermore, the INAS density framework underpins empirical and process-based parameterizations for dust and biological INPs in contemporary models (Hoose & Möhler, 2012). By providing a robust, intrinsic measure of INP activity, INAS

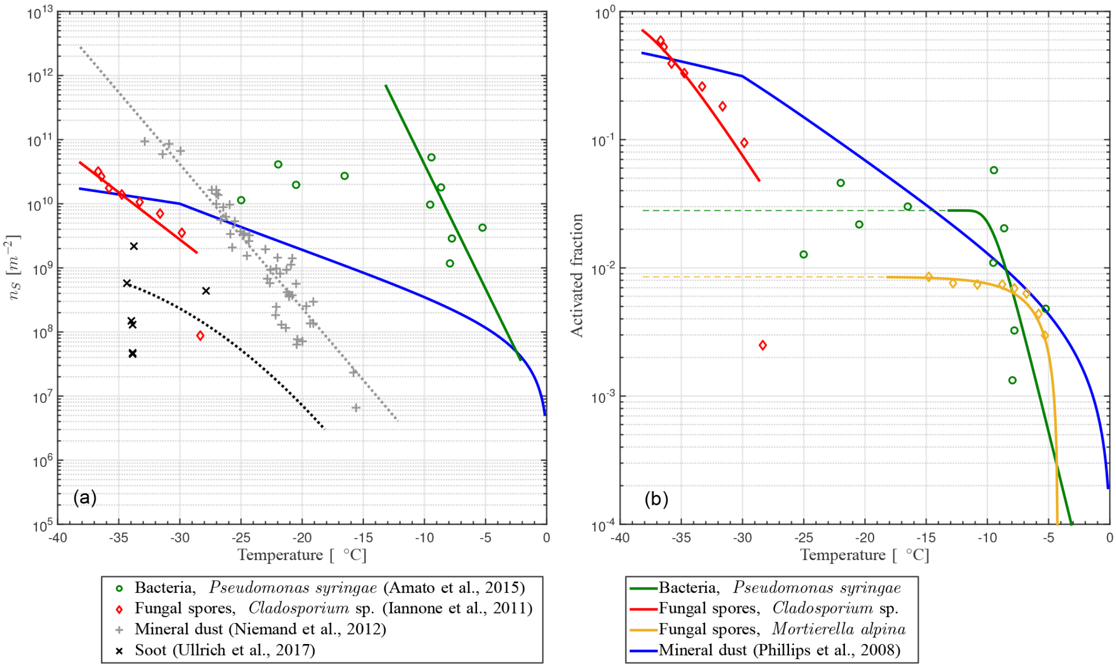

Figure 2.4: (a) INAS density n_s and (b) ice-active fraction f_IN versus temperature T for PB-INPs as well as mineral dust and soot (Hummel et al., 2018).

density bridges the gap between microscopic ice nucleation events and macroscopic cloud behavior, such as precipitation and radiative properties, thereby contributing to the refinement of cloud microphysical parameterizations and the improvement of weather and climate models.

INAS density measurements from field and laboratory studies have revealed significant variations in ice-nucleation efficiency across different aerosol types, with mineral dust, biological particles, and anthropogenic particles exhibiting distinct behaviors (Atkinson et al., 2013). Mineral dust, particularly prevalent in Beijing due to its proximity to the Gobi Desert, consistently shows high $n_s(T)$ values, comparable to Saharan dust and often attributed to its abundance of ice-active minerals like K-feldspar (Ullrich et al., 2017). Asian dust from the Taklamakan and Gobi deserts has especially high INAS densities, with studies noting that larger particles during East Asian dust events exhibit higher nucleation efficiency and that chemical aging does not suppress their ice-nucleating ability (Boose et al., 2016; J. Chen et al., 2021).

In contrast, biological particles such as bacteria and fungal spores display higher $n_s(T)$ values at warmer temperatures (e.g. $-2\,°\mathrm{C}$ to $-15\,°\mathrm{C}$), due to their unique proteinaceous ice-nucleating macromolecules, making them particularly relevant in less-dusty conditions or specific ecosystems (O'Sullivan et al., 2015). Anthropogenic particles, including coal soot and industrial emissions, generally activate as INPs only at much colder temperatures, typically below $-30\,°\mathrm{C}$ to $-25\,°\mathrm{C}$ (Knopf et al., 2010). These differences imply a temperature-dependent dominance of INP sources in the atmosphere, with biological INPs being crucial at warmer temperatures and mineral dust dominating at colder temperatures, a pattern that varies seasonally and with cloud altitude in regions like Beijing. Figure 2.4 illustrates representative $n_s(T)$ spectra for key aerosol types, highlighting the diversity of their ice-nucleation activities across atmospheric temperature ranges.

2.5 Previous studies on INPs

Historical development of INP research Research into INPs began in the mid-20th century, establishing foundational knowledge for atmospheric science through pioneering studies such as those by Ludlam (1948) and Mossop (1970), which explored ice-crystal formation mechanisms in clouds. These efforts identified mineral dust and biological particles as effective INPs (Vali, 1971), distinguishing homogeneous nucleation—occurring in pure water droplets below −38 °C—from heterogeneous nucleation, facilitated by aerosols at warmer temperatures. The development of CNT provided a thermodynamic framework, with Fletcher (1958) introducing a stochastic approach to heterogeneous nucleation.

By the early 2000s, researchers had defined key heterogeneous nucleation modes —immersion, condensation, contact, and deposition freezing—and established empirical parameterizations linking INP concentrations to temperature and aerosol properties (DeMott et al., 2003). Field campaigns and laboratory studies, including those examining Saharan dust and plant-derived materials (Connolly et al., 2009), advanced measurement techniques and INP source understanding. Integration of CNT-based parameterizations into global climate models marked a significant milestone (Hoose et al., 2010), while Murray et al. Murray et al. (2011) underscored immersion freezing' s dominance in mixed-phase clouds. Today, INP research is mature yet evolving, driven by the need to refine models with new observations and address uncertainties, particularly regarding atmospheric ice formation' s impact on precipitation efficiency and cloud radiative properties.

Laboratory studies on INP activity Laboratory research has significantly deepened our understanding of the INP activity of various aerosol types, with rapid advancements in recent years driven by state-of-the-art instruments and methods, providing critical data for accurate cloud process modeling.

Mineral dusts, especially alkali feldspar minerals like K-feldspar, consistently exhibit high ice-nucleation efficiency, initiating freezing at temperatures as warm as −5 °C in the immersion mode under certain conditions, while other clay minerals such as kaolinite and illite are active at colder temperatures, modulated by their surface properties (Atkinson et al., 2013; Murray et al., 2011).

Atmospheric aging, for example coatings of sulfuric acid or organic compounds on mineral dust, can suppress or enhance nucleation ability depending on the coating' s chemical nature and environmental conditions (Cziczo et al., 2009; R. C. Sullivan et al., 2010). Biological particles, including bacteria (e.g., *Pseudomonas syringae*), fungal spores, and pollen grains, are exceptionally efficient INPs, triggering ice formation at temperatures as high as −2 °C due to protein-based macromolecules on their surfaces (Maki et al., 1974; Pummer et al., 2012). Marine biogenic aerosols from sea spray and microbial activity are significant INP sources in marine environments, typically active between −20 °C to −10 °C (T. W. Wilson et al., 2015).

Combustion aerosols, such as soot and ash from biomass burning, display variable efficiency, often active below −20 °C, influenced by fuel type and aging processes (Grawe et al., 2016; Umo et al., 2015). Advanced techniques, including CFDCs, droplet-freezing assays, and cloud chambers, have enabled precise INP activity measurements under atmospherically relevant conditions, yielding data essential for atmospheric models (Boose et al., 2016; O'Sullivan et al., 2015). INP activity is highly nuanced, depending on mineral type, particle size, surface properties, and aging, transcending broad classifications like “mineral dust” and necessitating detailed characterization.

Advances and challenges in INP parameterization schemes Over the past decades, parameterization schemes for representing INPs in atmospheric models have undergone significant advancements, moving beyond early simplistic relationships based solely on temperature and supersaturation (Meyers et al., 1992). Contemporary schemes now incorporate aerosol-specific properties, such as the INAS density approach, which quantifies nucleation sites per unit surface area, directly linking INP activity to fundamental aerosol characteristics (Connolly et al., 2009; Niemand et al., 2012). These parameterizations typically relate INP concentrations to the surface area of mineral dust, the abundance of biological particles, or empirically derived relationships based on laboratory spectra (DeMott, Prenni, et al., 2010; Ullrich et al., 2017). These advancements have been integrated into numerical weather prediction and climate models, substantially enhancing simulations of mixed-phase cloud properties and precipitation patterns.

However, persistent discrepancies between model predictions and field measurements remain, particularly in regions with complex aerosol compositions such as Beijing and East Asia (Kanji et al., 2017). These discrepancies stem from challenges in accurately capturing aerosol variability, the dynamic effects of atmospheric aging—such as coatings on dust particles that alter nucleation efficiency (Cziczo et al., 2009), and the low concentrations of highly efficient biological INPs. Recent efforts, including the standardization of measurement techniques and the development of comprehensive INP databases (DeMott et al., 2018), aim to address these gaps. The iterative process of refining models through new observational data is crucial for reducing uncertainties and advancing our understanding of INP sources, activation mechanisms, and environmental controls.

Global field measurement campaigns Global field campaigns have provided critical insights into the abundance, variability, and sources of INPs across diverse environments, revealing significant spatial and temporal variability in INP concentrations (Table 2.1). Studies such as the Southern Ocean Cloud Radiation Aerosol Transport Experimental Study (SOCRATES), utilizing CFDCs, and campaigns across North America and the Atlantic have identified seasonal shifts, with biological INPs dominating at warmer temperatures (−15 °C to −10 °C) during summer and mineral dust prevailing at colder temperatures (−30 °C to −20 °C) in winter (T. W. Wilson et al., 2015).

Mineral dust from major arid regions, including the Sahara, Taklamakan, and Gobi deserts, is a primary INP source below −15 °C, with Saharan dust outbreaks demonstrating high nucleation efficiency and influencing precipitation over vast downwind regions (Boose et al., 2016). Marine biological aerosols, linked to oceanic productivity, contribute significantly to INP populations in oceanic areas between −20 °C and −10 °C (McCluskey et al., 2017), while terrestrial biological aerosols, such as pollen and fungal spores, prevail in continental forests, particularly in spring and summer, contributing INPs at warmer temperatures (Després et al., 2012; S. Huang et al., 2021; Huffman et al., 2013; Möhler et al., 2007).

Combustion sources, including biomass burning, also enhance INP concentrations, especially in polluted regions (Umo et al., 2015). Despite these advances, significant knowledge gaps persist in mid-latitude urban areas and megacities, where the interplay of local emissions, secondary particle formation, and long-range transport complicates INP characterization (J. Chen et al., 2021). International intercomparison studies, such as the Fifth International Workshop on Ice Nucleation (FIN-02), have exposed variability among instruments, highlighting the need for standardized measurement protocols to ensure data consistency (DeMott et al., 2018). Direct field measurements remain essential to constrain INP parameterizations and reduce model uncertainty, particularly in complex, mixed-pollution environments where current data are underrepresented.

INP research in Asia and Eastern Asia Research has firmly established Asian dust from the Gobi and Taklamakan deserts as a dominant INP source with transregional impacts on cloud formation and precipitation (Uno et al., 2009). Studies have consistently shown that dust events are the primary driver of high INP concentrations in northern China, particularly during spring (Su et al., 2023). For example, Chen et al. developed specific parameterizations for temperatures ranging from −35 °C to −6 °C based on size-resolved INP measurements during spring dust events in Beijing (2018–2019) (J. Chen et al., 2021), highlighting the high ice-nucleating efficiency of these dusts, which contain abundant feldspar and clay minerals. Vertical INP profiles over the North China Plain further confirm dust’ s pervasive influence at various altitudes.

Beyond mineral dust, marine biogenic INPs linked to biological activity off the Indian coast have been documented (T. W. Wilson et al., 2015), while urban studies in Tokyo reveal seasonal variations in INP spectra (Tobo et al., 2020). Despite these advances, comprehensive INP studies in Chinese cities like Beijing remain scarce, with limited long-term, high-resolution observations on how urban pollution interacts with natural dust to affect ice nucleation efficiency.

This knowledge gap hinders the accurate representation of INPs in regional weather and climate models, a critical issue given Asia’ s rapid urbanization and the transboundary nature of INP transport, underscoring the need for international collaboration in atmospheric research. The transboundary nature of Asian dust underscores the need for international collaboration to understand regional INP sources within broader atmospheric circulation systems (Fig. 2.5).

Table 2.1: Key global iIce-nucleating particle field observation projects

Campaign/Study	**Location**	**Environment**	**Key Findings**	**Instruments**
SOCRATES (J. C. Wilson & Liu, 1980)	Southern Ocean	Oceanic	Biological INPs dominate at $-15\,°\mathrm{C}$ to $-10\,°\mathrm{C}$ in summer; dust at $-30\,°\mathrm{C}$ to $-20\,°\mathrm{C}$ in winter	CFDC
FIN-02 (DeMott et al., 2018)	North America, Europe	Mixed	Highlighted instrument variability; need for standardized protocols	CFDC, DFA
Saharan Air Layer (Boose et al., 2019)	Canary Islands	Desert	High INP efficiency of Saharan dust at $-15\,°\mathrm{C}$	CFDC, AIDA
Beijing Dust Events (J. Chen et al., 2018)	Beijing, China	Urban/Desert	Dust dominates INP populations during spring storms	DFA, CFDC
Indian Monsoon (T. W. Wilson et al., 2015)	Indian Coast	Oceanic	Marine biogenic INPs linked to biological activity	CFDC
Tianshan Mountains (Y. Li & Du, 2003)	Tianshan Mountains, China	Mountain	INP average $11\,\mathrm{L}^{-1}$ on non-dust days, hundreds during dust intrusions	Not specified (likely DFA/CFDC)
Huangshan Mountain (Jiang et al., 2015)	Huangshan Mountain, China	Mountain	INP ranged from $0.27\,\mathrm{L}^{-1}$ to $18.74\,\mathrm{L}^{-1}$	Not specified (likely DFA/CFDC)
Urban Beijing (J. Chen et al., 2018)	Urban Beijing, China	Urban	No significant correlation with urban pollution; natural sources dominate	INDA, LINA
Eastern Beijing (Bi et al., 2019)	Eastern Beijing, China	Urban/Suburban	INP variations linked to air-mass origins, higher with dust	CFDC
Suburban/Mountain Beijing (Y. Hu et al., 2023)	Suburban/Mountain Beijing, China	Suburban/Mountain	Distinct INP concentrations due to different air masses	DFA

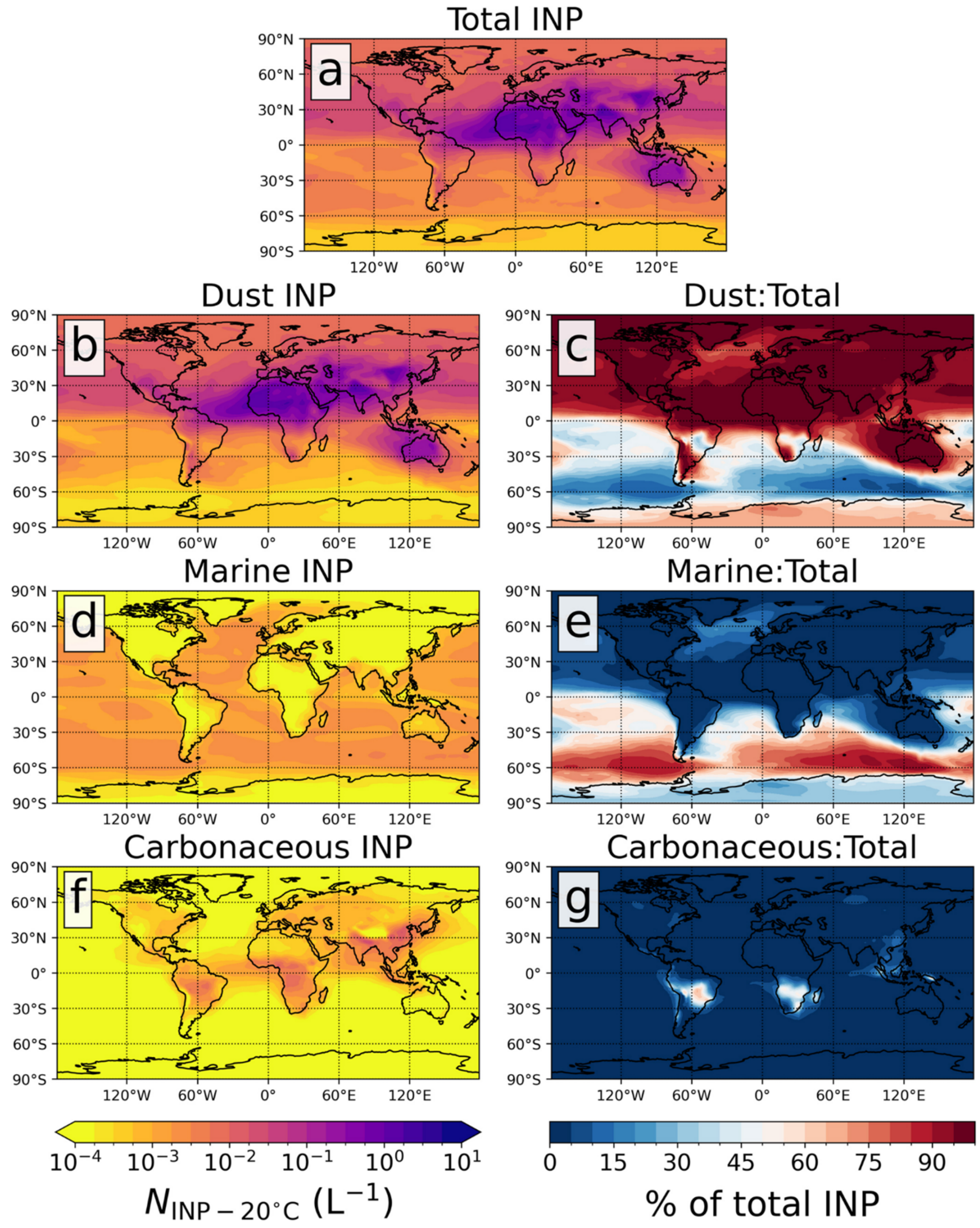

Figure 2.5: Annual mean $N_{\mathrm{INP}}(T)$ concentrations in the boundary layer at 500 m and a temperature of $-20\,^{\circ}\mathrm{C}$ for (a) total, (b) dust, (d) marine-sourced, and (f) BC $N_{\mathrm{INP}}(-20\,^{\circ}\mathrm{C})$. The marine-sourced INPs are parameterized using SSA. Panels (c), (e), and (g) show the ratio (expressed as a percentage) of $N_{\mathrm{INP}}(-20\,^{\circ}\mathrm{C})$ to total $N_{\mathrm{INP}}(-20\,^{\circ}\mathrm{C})$ for dust, marine-sourced, and BC INPs, respectively, highlighting regions dominated by each source of INPs (Herbert et al., 2025).

INP research in China INP research in China has expanded beyond traditional desert regions to encompass diverse environments, including remote mountain ranges, the Tibetan Plateau, vast deserts, agricultural fields, forests, and densely populated urban centers such as Beijing, Nanjing, Tai' an, and Shenyang. Observational studies have revealed significant variability in INP concentrations, influenced by both natural dust and anthropogenic aerosols. For instance, Jiang et al. (2016) reported INP concentrations of $11\,\mathrm{L}^{-1}$ on non-dust days in the Tianshan Mountains, surging to hundreds per liter during dust events, while (Shi et al., 2006) documented $23.3\,\mathrm{L}^{-1}$ to $85.4\,\mathrm{L}^{-1}$ at the Qinghai Plateau. In urban and suburban settings, concentrations vary widely—from $0.001\,\mathrm{L}^{-1}$ to $604\,\mathrm{L}^{-1}$ in Beijing (J. Chen et al., 2018; You et al., 2002)) to $1.57\,\mathrm{L}^{-1}$ to $37.5\,\mathrm{L}^{-1}$ in Tai' an (Jiang et al., 2020). The high ice-nucleating efficiency of Chinese mineral dusts from the Taklamakan and Gobi deserts, rich in feldspar and clay minerals, has been confirmed (Boose et al., 2016; J. Chen et al., 2021; Ullrich et al., 2017), with dust storms—particularly in spring—elevating INP levels across northern China and affecting cloud formation and precipitation through long-range transport (Su et al., 2023; Uno et al., 2009). However, systematic long-term, high-resolution INP measurements remain scarce, especially in urban areas like Beijing, where seasonal and episodic variability is driven by dust outbreaks, secondary aerosols, and local emissions (Bi et al., 2019; Y. Hu et al., 2023). The lack of vertical INP profiles, source-resolved data, and studies on mixed pollution–dust episodes further limits understanding of INP distribution and dynamics (J. Chen et al., 2021; Y. Hu et al., 2023). These gaps, particularly pronounced in northern China and Beijing—a region marked by complex aerosol loads—hinder the development of accurate, region-specific parameterizations for atmospheric models, impeding advances in weather forecasting, climate modeling, and air quality management. Comprehensive studies integrating laboratory, field, and aircraft measurements are thus essential to address these deficiencies and enhance regional climate and environmental strategies.

2.6 The importance and state of the study on INP characteristics in Beijing/China

Beijing' s exceptional aerosol environment, shaped by a dynamic interplay of natural and anthropogenic sources, positions it as a critical location for studying INPs. The city' s proximity to major dust sources, such as the Gobi and Taklamakan deserts, coupled with severe urban pollution from industrial activities, traffic, and coal combustion, creates a complex aerosol profile (Fig. 2.6). This complexity is further intensified by regional dust transport, agricultural activities, and biomass burning in surrounding areas (Bi et al., 2019; Che et al., 2019). Situated on the North China Plain in a mid-latitude continental climate, Beijing frequently experiences mixed-phase clouds, making INP characteristics vital for understanding regional precipitation, fog, and ice formation, and broader climate impacts. Accurate INP characterization is essential for enhancing weather forecasting and climate modeling, as global parameterizations may fail to capture Beijing' s unique aerosol dynamics (Hoose et al., 2010; Phillips et al., 2008). The confluence of these diverse sources results in highly non-linear aerosol–cloud interactions, establishing Beijing as a global “hotspot” for INP research. Insights gained here are not only locally significant but also relevant to other polluted megacities, advancing our understanding of INP behavior in anthropogenically perturbed atmospheres.

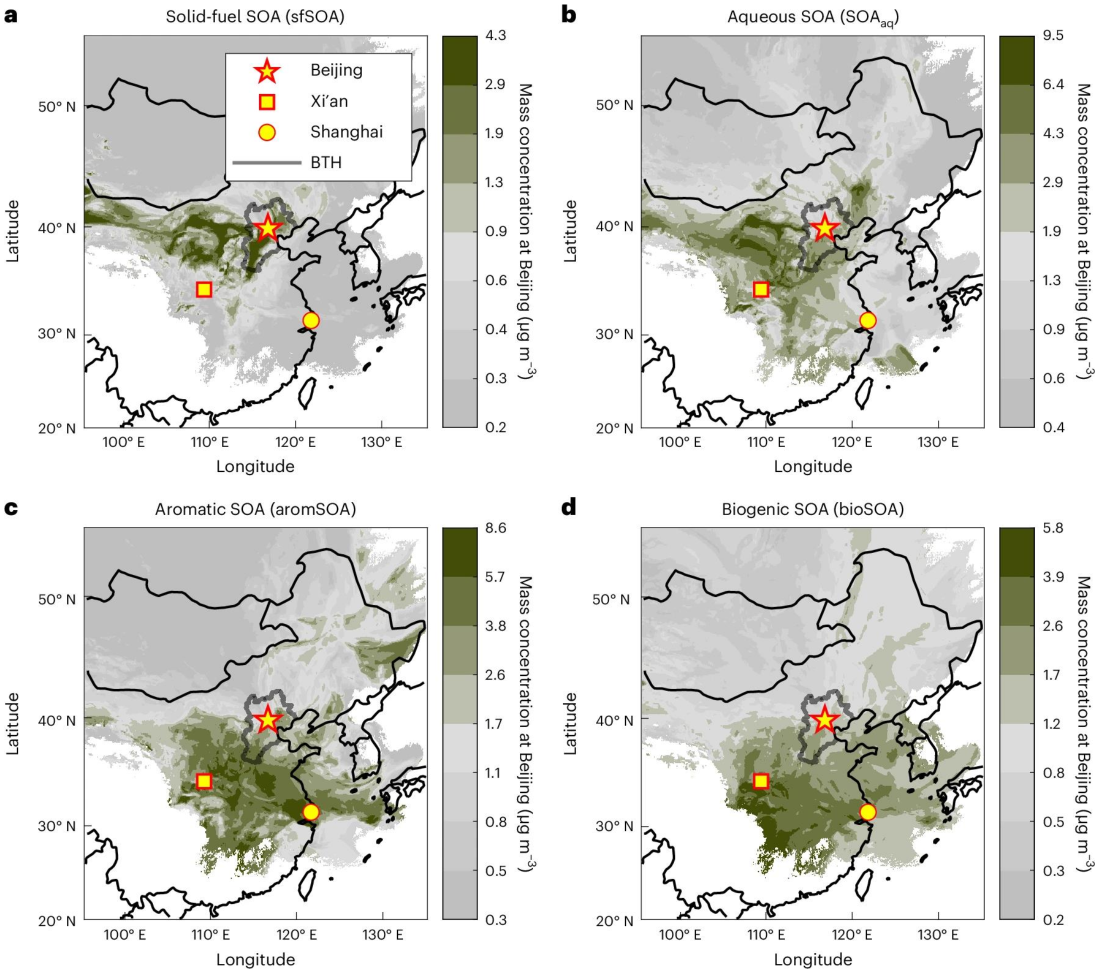

Figure 2.6: Geographical origins of SOA categories in Beijing and other regions. (Daellenbach et al., 2024).

INP research in Chinese cities, though relatively scarce compared to North America and Europe, is an emerging field gaining momentum. Studies across urban and suburban sites in China, including Beijing (J. Chen et al., 2018), Nanjing (L. Yang et al., 2013), Tai’ an (Jiang et al., 2020), and Shenyang (Zhou et al., 2016), have reported INP concentrations ranging from $0.001\,\mathrm{L}^{-1}$ to $10\,\mathrm{L}^{-1}$, indicating the presence and activity of INPs even in heavily polluted urban environments. These investigations highlight the influence of both natural dust and anthropogenic aerosols on INP populations, with concentrations peaking during springtime dust storms and remaining low during severe winter haze events dominated by anthropogenic pollution (J. Chen et al., 2023). Despite high pollution levels, primary anthropogenic aerosols, such as soot, often show a minor direct contribution to INPs, particularly in the immersion freezing mode, compared to mineral dust ((J. Chen et al., 2018)). This conclusion suggests that the critical role of anthropogenic pollution may be indirect, through chemical aging and coating processes that modify the ice nucleation activity of natural INPs. However, the available dataset remains limited, and systematic multi-year, multi-site INP monitoring across Chinese urban regions is lacking, underscoring a key uncertainty in understanding aerosol–cloud interactions in these complex environments.

Recent field campaigns in Beijing have significantly advanced our understanding of

INP characteristics, sources, and variability. J. Chen et al. (2018) found no significant correlation between INP concentrations and urban pollutants such as $PM_{2.5}$, black carbon, or total particle concentrations in urban Beijing, suggesting that natural sources, particularly mineral dust, dominate the INP population. This was corroborated by Bi et al. (2019), who observed clear variations in INP concentrations linked to air-mass origins, with higher concentrations associated with northerly and westerly air masses carrying desert dust from the Gobi and Taklamakan deserts. A comparison between suburban and mountain sites by Y. Hu et al. (2023) revealed distinct INP characteristics influenced by local sources and regional transport. These studies utilized advanced techniques, including continuous-flow diffusion chambers and droplet-freezing assays, to quantify INPs across temperatures from $-5\,°\mathrm{C}$ to $-30\,°\mathrm{C}$. Historical data from the 1990s indicate long-term variations in INP concentrations, potentially due to changes in dust transport and urban emissions (You et al., 2002). Mineral dust is consistently identified as the dominant INP source, particularly during spring dust storms, when INP concentrations increase by one to two orders of magnitude, with temperature-dependent spectra closely tied to mineral dust content (Bi et al., 2019; Y. Hu et al., 2023). Despite severe anthropogenic pollution, mineral dust remains the primary driver of INP concentrations, challenging the assumption that pollution directly enhances INP activity in mixed-phase clouds.

Despite significant progress in global INP research and initial studies in China, critical knowledge gaps persist in understanding INPs specific to Beijing. These gaps include:

(a) **Lack of Long-Term Continuous Observation Data**: Existing studies are primarily short-term campaigns, limiting a comprehensive understanding of seasonal and interannual INP variability and baseline conditions. This restricts the ability to capture diverse meteorological regimes and source patterns over extended periods.

(b) **Unclear Characteristics of Pollution-Dust Mixed INPs**: The interactions between natural dust and anthropogenic pollutants, particularly the effects of chemical aging on INP activity, remain unresolved, with contradictory literature on whether pollution coatings suppress or enhance ice nucleation efficiency.

(c) **Unknown Vertical Distribution**: Most observations are ground-based, leaving the vertical distribution of INPs in the atmosphere largely unknown. Aircraft measurements are essential for characterizing INPs in the free troposphere, where they directly interact with cloud systems, and for understanding long-range transport pathways.

(d) **Unquantified Impact of Major Events**: The impact of significant atmospheric events, such as the 2022 Winter Olympic Games or prolonged haze events, on INP characteristics and sources remains largely unquantified.

(e) **Source Apportionment Challenges**: Robust source apportionment studies are needed to quantitatively determine the relative contributions of mineral dust, biological particles, and anthropogenic aerosols to Beijing’s INP population.

Beijing’s unique atmospheric environment, characterized by the interplay of dust outbreaks, severe pollution, and intense urbanization, serves as a natural laboratory for studying ice-nucleating particles (INPs) and their role in aerosol–cloud–precipitation interactions under extreme and variable conditions. This doctoral dissertation addresses critical scientific questions to fill knowledge gaps regarding INP abundance, variability, and sources in this region, vital for global climate and regional air quality. Specifically, it investigates: These questions, strategically aligned with identified knowledge gaps, guide the research structure and ensure its relevance to improving regional atmospheric models, weather forecasting, climate impact assessment, and air quality policies in megacities.

To comprehensively answer the aforementioned scientific questions, this dissertation employs a systematic and multi-faceted research approach. This integrated strategy combines various methodologies to provide a holistic and unprecedented view of INPs in the complex Beijing environment.

- Laboratory studies (Chapter 4) will be conducted to investigate the intrinsic ice nucleation properties of key INP sources relevant to Beijing, specifically focusing on mineral dust originating from Asian deserts. These experiments aim to understand their inherent ice-nucleating abilities.

- Long-term field observations (Chapter 5) will be carried out to establish the baseline INP concentration patterns and seasonal variability in the Beijing area, directly addressing the critical lack of continuous, high-resolution data for this region.

- Intensive field campaigns (Chapter 6), particularly during significant events such as the Winter Olympic Games, will focus on detailed source apportionment studies and the specific impact of pollution on INP characteristics.

This comprehensive experimental design captures the full spectrum of INP sources, properties, and atmospheric variability in Beijing. By addressing the multifaceted nature of the INP problem—encompassing intrinsic properties, long-term variability, event-specific impacts, and vertical distribution—this approach enhances the robustness and completeness of the findings. The results will provide new insights for parameterizing INP impacts in regional and global climate models, ultimately improving weather forecasting, climate impact assessment, and air quality policies in megacities.

2.7 State of the art of instruments to measure ice-nucleating particles

Accurate measurement of INPs is crucial for understanding their fundamental role in cloud microphysics and enhancing the predictive capabilities of weather and climate models, particularly in regions like Beijing with complex and dynamic aerosol environments. Measuring atmospheric INPs poses significant challenges due to their extremely low concentrations, typically ranging from less than $0.01\,\mathrm{L}^{-1}$ to $100\,\mathrm{L}^{-1}$ of air—often fewer than one per liter even at moderate supercooling. This concentration is orders of magnitude lower than that of total aerosol particles or CCN, requiring highly sensitive instruments to detect rare freezing events amidst a vast background of non-ice-active aerosols.

Over the decades, a variety of techniques have been developed, broadly classified into: (a) online direct-sampling methods, which continuously expose ambient air to controlled cooling to induce ice formation, and (b) offline analyses, involving the collection of aerosol samples onto substrates for subsequent laboratory freezing tests.

In recent years, single-particle detection techniques have emerged as an important additional category. The choice of instrumentation is pivotal, determining the ability to address specific scientific questions, such as capturing rapid fluctuations in INP concentrations or identifying the chemical nature of ice-forming particles. The inherent difficulty of measuring INPs, driven by their low abundance, results in diverse and complex instrumentation that often demands resource-intensive efforts, careful calibration, and validation. Achieving both high temporal resolution and broad temperature coverage remains challenging, often necessitating a multi-instrument approach for comprehensive studies.

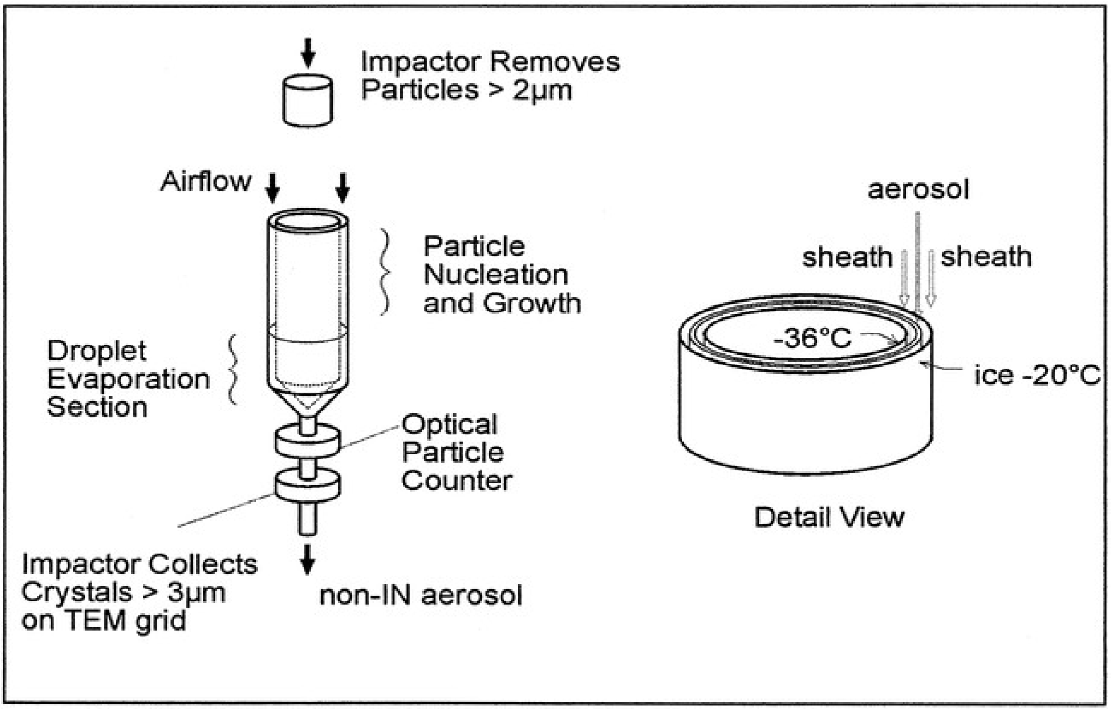

Figure 2.7: Simplified illustration of CFD chamber components and operating principles. (Rogers et al., 2001).

Online direct-sampling methods, particularly CFDCs, are widely recognized as essential tools for real-time monitoring of ice-nucleating particles (INPs) due to their high temporal resolution, which is crucial for capturing dynamic changes in INP concentrations (Fig. 2.7). In a typical CFDC, an aerosol sample stream is precisely guided between two concentric, ice-coated walls maintained at different temperatures, creating a well-defined temperature and supersaturation profile within the laminar flow (DeMott et al., 2003; Garimella et al., 2016). This controlled environment exposes airborne particles to specific conditions relevant for cloud glaciation, allowing particles that act as INPs to form ice crystals, which are then detected by an optical particle counter (Rogers, 1988). Prominent examples of CFDCs include the CFDC-1 and CFDC-2 from Colorado State University, the Horizontal Ice Nucleation Chamber (HINC-Auto), and the Spectrometer for Ice Nuclei (SPIN), the latter combining focused flow and single-particle detection to resolve particle-resolved ice nucleation properties (Brunner & Kanji, 2021; Garimella et al., 2016; Kanji & Abbatt, 2006; Rogers et al., 2001). In Beijing, Bi et al. (2019) successfully utilized an automated CFDC to measure INP concentrations during spring, effectively capturing variations linked to episodic dust events. However, CFDCs are typically limited to operating at temperatures below approximately −15 °C and require significant operational resources.

Other online systems, such as expansion chambers like AIDA, Cosmics Leaving OUtdoor Droplets (CLOUD), PINE, and Leipzig Aerosol Cloud Interaction Simulator (LACIS), simulate cloud formation through rapid adiabatic cooling, offering precise control over thermodynamic conditions and closely mimicking cloud-parcel conditions (Bogert, 2024; Kirkby et al., 2011; Möhler et al., 2003). Despite their advantages, these instruments often face a trade-off: those optimized for high temporal resolution may sacrifice environmental control or temperature range, and vice versa. Consequently, a comprehensive study, especially in dynamic environments like Beijing, typically requires a strategic combination of instruments to cover different aspects of INP variability.

Offline methods provide a crucial complementary approach to online techniques for measuring ice-nucleating particles (INPs), primarily through droplet freezing assays. In these methods, aerosol particles are collected from ambient air onto a substrate, such as a filter, or into a liquid medium, then washed off or resuspended in pure, deionized water. The resulting suspension is partitioned into numerous small droplets (typically 50–100 droplets, each 1 µL–100 µL in volume) and placed on a hydrophobic, temperature-controlled cold stage. As the stage is cooled at a controlled rate, the number of droplets that freeze is recorded, often with camera assistance, enabling the statistical determination of INP concentration as a function of temperature (Vali et al., 2015). This observed freezing spectrum allows calculation of the cumulative concentration of INPs active in the immersion mode (Hader et al., 2014; Tobo et al., 2013). Common examples of offline systems include the Colorado State University Ice Spectrometer (CSU-IS), the Leipzig Ice Nucleation Array (LINA), the Micro-Orifice Uniform Deposit Impactor–Droplet Freezing Technique (MOULDI-DFT), and the Nucleation by Immersed Particles Instrument (µL-NIPI) (Whale et al., 2015). These methods offer several advantages: they probe a wide temperature range down to the homogeneous freezing point of water, provide direct and unambiguous measurement of immersion freezing—a dominant mechanism in mixed-phase clouds—and permit subsequent chemical or biological analyses of collected samples, which is invaluable for detailed source apportionment and identification of specific INP sources. However, their primary limitation is poor time resolution, typically ranging from hours to days per sample, averaging over short-term atmospheric variability and complicating efforts to link INP concentrations to specific, transient events.

Beyond the principal methods of CFDCs and droplet-freezing assays, a suite of advanced techniques offers unique capabilities for INP research. Balloon-borne instruments, such as FRIDGE and DeSMI, enable *in situ* measurements of INP concentrations in the upper troposphere and lower stratosphere, regions that are challenging to access with conventional platforms (Bundke et al., 2008). Emerging technologies further expand measurement capabilities: advancements in microscopy and spectroscopy, such as Raman spectroscopy or digital holography combined with cold stages, offer the potential to probe molecular interactions at the ice–water–particle interface or detect freezing events in real time; infrared spectrometers like laser-ablation mass spectrometry (LAMS) can track freezing-induced changes in individual particles; and digital holography and photothermal detection methods allow for high-temporal-resolution monitoring of freezing events in micro-droplets or airborne particles. Additionally, single-particle freezing counters, such as the SPIN instrument at KIT, link particle-level physical or chemical properties to their ice-nucleation ability in real time (Garimella et al., 2016). Ongoing advancements in microfluidics, lidar, and integrated online–offline approaches are expected to further refine INP measurements (Mamouri & Ansmann, 2016; Tarn et al., 2018). However, each of these techniques is constrained by its detection principle, sensitivity, and operational complexity, and no single instrument can measure all INP types and nucleation modes across all relevant atmospheric conditions. Therefore, a multi-instrument approach is essential for the comprehensive characterization of the atmospheric INP population.

The diversity of measurement techniques for INPs poses significant challenges in comparing datasets obtained from different instruments and campaigns. Each instrument operates on its own specific principles, possesses unique sensitivities, and may introduce potential artifacts, leading to systematic differences in measured INP concentrations even when sampling the same air mass. To address this, the atmospheric science community has organized international intercomparison workshops, such as the Fifth International Ice Nucleation Workshop (FIN-03), to quantify uncertainties and establish best practices for INP measurements (Burrows et al., 2022; DeMott et al., 2025; Hiranuma, Augustin-Bauditz, et al., 2015). Field and laboratory intercomparison studies further reveal substantial variability among instruments, depending on their detection principles, operational conditions, and the type of INP measured (DeMott et al., 2015). A key consensus from these efforts is that researchers must report detailed instrument parameters and operating conditions (including temperature, humidity, and supersaturation) along with all INP data to ensure transparency, which is critical for the meaningful interpretation and synthesis of global INP datasets. Recognizing potential systematic uncertainties is also essential when comparing across datasets. To enhance spatial and temporal coverage, ongoing efforts focus on developing robust, autonomous, and cost-effective instruments, such as automated CFDCs, for long-term monitoring across a broader network of sites (Brunner & Kanji, 2021).

In this thesis, both offline (droplet freezing assay) and online (AIDA chamber, PINE expansion chamber, CFDCs) techniques are employed to achieve complementary insights into INP concentrations, variability, and sources in the Beijing area. The combination of methods allows both source-specific sensitivity and time-resolved monitoring, which is crucial for advancing the understanding of INP impacts on clouds and climate in complex urban environments.

2.8 Summary

This dissertation provides a comprehensive characterization of the abundance, variability, and sources of ice-nucleating particles (INPs) in the Beijing region. INPs play a central role in atmospheric processes, regulating cloud formation, precipitation efficiency, and Earth's radiative balance. As highlighted in the literature, INPs exert a strong influence on climate and are critical to the global water cycle. Clouds modulate precipitation and hydrological cycling and, through their radiative effects, influence planetary temperature. The Beijing area, shaped by the interaction of natural mineral dust from major deserts and intense anthropogenic pollution, represents a global hotspot for INP studies. The confluence of diverse sources results in highly nonlinear aerosol–cloud interactions, positioning Beijing as both an ideal and inherently complex natural laboratory for advancing mechanistic understanding of INP behavior.

Chapter 3

Experimental Methods

This chapter provides a comprehensive overview of the experimental setups and instruments used to investigate INPs in this work. Section 3.1 introduces the AIDA cloud expansion chamber (Aerosol Interaction and Dynamics in the Atmosphere), describing its design, aerosol generation and characterization methods, and typical expansion experiments under mixed-phase and cirrus cloud conditions. Section 3.2 details the droplet-freezing assay INSEKT (Ice Nucleation Spectrometer of the Karlsruhe Insitute of Technology), an offline immersion freezing technique employed both in the laboratory and during field campaigns to measure INP concentrations as a function of temperature. The continuous-flow diffusion chamber developed at KIT, INKA (Ice Nucleation instrument of the Karlsruhe Institute of Technology) is presented in Section 3.3, highlighting its working principles, controlled supersaturation conditions, and integration with AIDA for online ice nucleation measurements. Section 3.4 introduces PINE (Portable Ice Nucleation Experiment), a mobile cloud expansion chamber that simulates the rapid cooling of an ascending air parcel to activate supercooled droplets and ice crystals for *in situ* INP detection. Finally, Section 3.5 outlines additional instrumentation used to complement and validate the core experiments, including a novel fully-automated CFDC for field deployment in China (BJ-CFDC), a cold-stage droplet freezing analyzer FINDA, and an aerosol particle monitoring system (GRIMM 180 Environmental Dust Monitor). This suite of instruments and methods collectively provides a robust approach to assess the ice-nucleating ability of different aerosol samples under a wide range of experimental conditions.

3.1 The cloud expansion chamber AIDA

3.1.1 General instrumentation

The AIDA cloud expansion chamber at the Karlsruhe Institute of Technology was built between 1995 and 1997 as an atmospheric simulation chamber for aerosol studies. Only later was its operation extended for investigations on aerosol-cloud interactions and for studies on the ice-nucleation ability of different aerosol types.

A detailed description of the AIDA chamber is provided in, for example, Möhler et al. (2003), Möhler et al. (2006) or Wagner et al. (2006). AIDA (see Figures 3.1 and 3.2) is a cylindrical aluminum vessel with dished ends, approximately 7 m in height and 4 m in diameter, resulting in a total volume of roughly 84 m^3. The chamber is placed inside a thermal insulation structure, where the temperature of ventilated air can be regulated in a wide range from 60 °C to -90 °C, by using a large refrigeration system or liquid nitrogen evaporation. Multiple thermocouples are mounted at various levels along

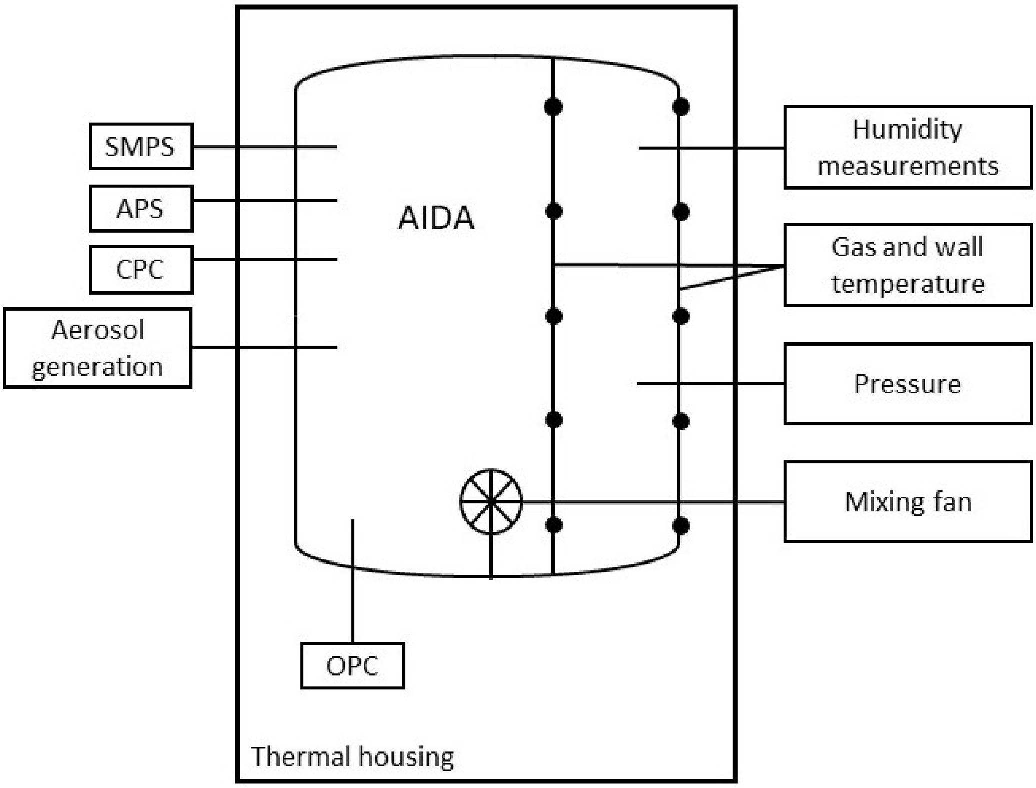

Figure 3.1: Setup of the AIDA cloud expansion chamber, including the main instrumentation needed for the ice nucleation measurements in this work.

the chamber wall to monitor the temperature, while a separate chain of thermocouples records the gas-phase temperature inside the chamber. The pressure inside AIDA can be controlled between 1000 mbar and below 1 mbar. An expansion system comprising two adjustable mechanical pumps enables rapid evacuation, allowing the chamber to simulate the rise of an air parcel with minimum pressures as low as 0.01 mbar.

A mixing fan is placed approximately 1 meter above the floor to ensure homogeneous mixing of the entire air volume. This guarantees a uniform distribution of temperature, water vapor, and aerosols throughout the chamber. In addition, the AIDA chamber is equipped with a comprehensive suite of measurement instruments that monitor thermodynamic conditions and track the formation of simulated clouds during experimental campaigns.

Before each experiment, the chamber is thoroughly cleaned by several flushing cycles with clean, dry synthetic air at pressures between 1 and 10 mbar. To establish the desired water vapor concentration, ultra-pure water is then evaporated into the evacuated chamber before it is refilled with synthetic air. This procedure not only sets the initial humidity, but also forms a thin ice layer on the chamber walls, helping to maintain ice-saturated conditions and providing sufficient water vapor during expansion cooling experiments.

The entire experimental process is automated and monitored via a LabVIEW-based control system. A comprehensive suite of instruments continuously monitors the thermodynamic state of the chamber and tracks cloud formation throughout the experiment.

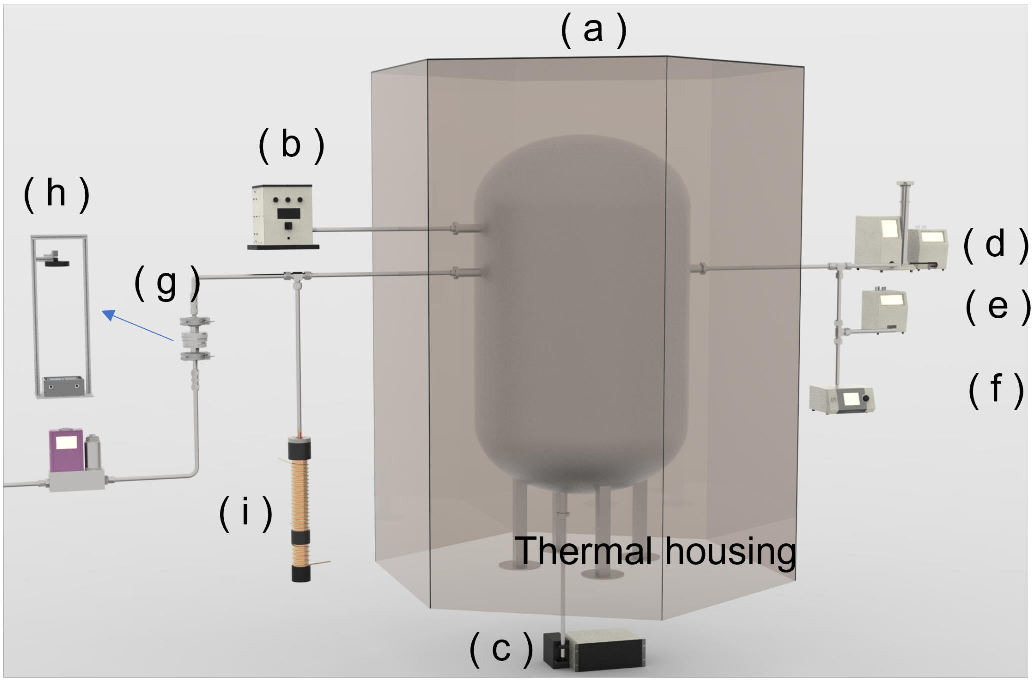

Figure 3.2: Setup of the AIDA cloud expansion chamber and associated instrumentation for the ice nucleation measurements in this study. Shown are: (a) the chamber housed in a thermal insulation structure, (b) the RBG, (c) the OPC, (d) the SMPS, (e) the CPC, (f) the APS, (g) the filter holder for sample collection, (h) the INSEKT instrument for offline filter analysis (see Section 3.2), and (i) the INKA instrument for online INP measurements (see Section 3.3).

3.1.2 Aerosol generation

Aerosol particles such as mineral dust, salts, or aqueous solution droplets are introduced into the AIDA chamber using different injection systems depending on their physical phase state.

Figure 3.2 shows the cutaway diagram of the structure of AIDA together with the aerosol injection and characterization instruments. Solid dust particles are generated from a bulk sample containing particles in both the sub-micron and super-micron size ranges. To reduce the abundance of larger particles in the sample, the material is first sieved to select particles with diameters between 0 µm to 75 µm. Dispersion is achieved using a rotating brush generator (RBG 1000, Palas GmbH; see Figure 3.2(b)). In this device, the sieved material is placed in a piston which is slowly pushed upward. A rotating brush lifts the particles and entrains them into an air stream. This aerosol-laden air typically passes through a cyclone impactor and a dispersion nozzle to remove particles with diameters larger than approximately 5 µm, as such coarse particles are generally not relevant for cloud formation under atmospheric conditions. The size-selected aerosol is then introduced into the AIDA chamber.

Although not used in the present study, other types of aerosol particles can also be introduced into the AIDA chamber. Salt particles such as ammonium sulfate are typically generated by atomizing dilute aqueous solutions (0.1–1 wt%) using an ultrasonic nebulizer, followed by drying in a desiccation column to produce solid residuals, which are then injected into the chamber. Aqueous sulfuric acid droplets are produced using a custom-built generator in which concentrated sulfuric acid is heated above 100 °C to form vapor. This vapor is transported by a flow of synthetic air through a cooling line, where it undergoes homogeneous nucleation, forming droplets that are subsequently introduced into the chamber.

3.1.3 Measurement techniques for aerosol and hydrometeor characterization

This section provides an overview of the measurement techniques employed at the AIDA facility for determining the number concentration and size distribution of aerosol particles, cloud droplets, and ice crystals. These techniques include electrical mobility and aerodynamic sizing for aerosols, as well as optical detection methods capable of distinguishing between spherical droplets and aspherical ice particles.

Electrical mobility and aerodynamic measurement of aerosols

The aerosol introduced into AIDA is characterized with respect to its number concentration and size distribution. While the number concentration is determined using a single instrument, the size distribution is derived from the combined measurements of two instruments that exploit different aerosol properties. The following section describes the three instruments employed and their respective measurement principles.

Condensation particle counter The number concentration of aerosol particles in AIDA, including those with diameters of 10 nm and larger, is measured using a Condensation Particle Counter (CPC[1], model 3010, TSI Inc.; see Figure 3.2(e)). Since most aerosol particles are too small to be detected optically, their optical size must be increased to enable detection. In the CPC, the aerosol first passes through a saturator filled with butanol vapor. The aerosol-laden flow is then directed into a cooler region, the condenser, where butanol condenses onto the particles, thus increasing their optical size. Subsequently, these enlarged particles pass through a laser beam, and the resulting scattered light is detected and used to count the particles (P. Kulkarni et al., 2011; Welker, 2012). The CPC operated at AIDA provides number concentration measurements with a temporal resolution of 1 s and can detect particle concentrations up to 10 000 cm^{-3} (TSI, 2002).

Scanning mobility particle sizer The Scanning Mobility Particle Sizer (SMPS[2]; consisting of a DMA 3071 and a CPC 3772, both from TSI Inc.; see Figure 3.2(d)) measures the aerosol size distribution in the range of 10 nm to 800 nm, based on the electrical mobility of the particles(Singh & Kuang, 2024). Upon entering the system, the particles are brought to a known equilibrium charge distribution. They then pass through a Differential Mobility Analyzer (DMA), which classifies them according to their electrical mobility. The classified particles are subsequently counted by the CPC (Flagan, 1999). By continuously varying the electric field strength, the instrument selects particles of different sizes, producing a complete size distribution within the specified range (P. Kulkarni et al., 2011; Welker, 2012).

---

[1] https://tsi.com/discontinued-products/condensation-particle-counter-3010/, last accessed April 24, 2025

[2] https://tsi.com/products/particle-sizers/scanning-mobility-particle-sizer-spectrometers/general-scanning-mobility-particle-sizer-(smps)-3938/, last accessed April 24, 2025

The SMPS provides the *mobility diameter* (d_{me}), which assumes spherical particles. To account for aspherical shapes, this value is converted into the *volume equivalent diameter* (d_{ve}), which represents the diameter of a sphere with the same volume. Aspherical particles experience greater aerodynamic drag, which is characterized by the dynamic shape factor χ. The conversion is given by:

$$d_{\mathrm{ve}} = \frac{d_{\mathrm{me}}}{\chi} \quad . \tag{3.1}$$

Aerodynamic particle sizer The Aerodynamic Particle Sizer (APS 3021[3], TSI Inc.; see Figure 3.2(f)) characterizes the aerosol size distribution within the diameter range of 0.5 µm to 20 µm, based on the aerodynamic diameter(TSI, 2013). Upon entering the APS, particles are accelerated through a nozzle, resulting in different velocities due to their varying inertias. The particles then cross two laser beams, and their transit time between the beams is used to determine their velocity, which is then converted into a size bin corresponding to the aerodynamic diameter(J. C. Wilson & Liu, 1980). The aerodynamic diameter refers to the diameter of a spherical particle with the same settling velocity as the measured aspherical particle. It is converted to the volume equivalent diameter using the following relationship:

$$d_{\mathrm{ve}} = \sqrt{\frac{\chi}{\rho}} \cdot d_{\mathrm{ae}} \quad , \tag{3.2}$$

where ρ is the average density of the aerosol particles.

After converting the SMPS and APS data to volume equivalent diameters using Equations 3.1 and 3.2, the two datasets are merged to obtain the complete aerosol size distribution in AIDA. Due to the finite measurement times of each instrument, the SMPS is operated with a scanning duration of 6 min, while the APS requires 4 min.

From the measured size distribution of the particle number concentration $c_{n,\mathrm{aero}}(\log d_{\mathrm{ve}})$, the aerosol surface area concentration size distribution $c_{s,\mathrm{aero}}(\log d_{\mathrm{ve}})$ can be calculated assuming spherical particles as:

$$c_{s,\mathrm{aero}}(\log d_{\mathrm{ve}}) = \pi d_{\mathrm{ve}}^2 \, c_{n,\mathrm{aero}}(\log d_{\mathrm{ve}}) \tag{3.3}$$

Here, d_{ve} denotes the volume equivalent aerosol particle diameter used throughout the aerosol characterization in AIDA.

The total aerosol surface area concentration $c_{s,\mathrm{aero}}$ is of particular relevance in the investigation of heterogeneous ice nucleation. It can be derived in two ways: either by summing the size-resolved surface area concentrations across all size bins (as described in Eq. 3.3), based on SMPS and APS data, or by calculating it from the parameters of a lognormal fit to the measured size distribution.

For a lognormal size distribution, $c_{s,\mathrm{aero}}$ is given by:

$$c_{s,\mathrm{aero}} = \pi c_{n,\mathrm{aero}} \exp\left(2 \ln d_{p,\mathrm{m}} + 2 \ln^2 \sigma_{\mathrm{g}}\right) \tag{3.4}$$

where $c_{n,\mathrm{aero}}$ is the total particle number concentration, $d_{p,\mathrm{m}}$ is the median particle diameter, and σ_{g} is the geometric standard deviation of the lognormal distribution.

---

[3] https://tsi.com/products/particle-sizers/supermicron-capable-particle-sizer-spectrometers/aerodynamic-particle-sizer-aps-3321/, last accessed April 24, 2025

Optical detection of aerosols, cloud droplets, and ice crystals

The number concentration and size distribution of large aerosol particles, cloud droplets, and ice crystals in AIDA are measured using two optical particle counters (OPCs, model *welas*, Palas GmbH) installed at the bottom of the AIDA chamber. These OPCs cover two complementary size ranges: 0.7 µm to 46 µm and 5 µm to 240 µm (Wagner & Möhler, 2013). Each system consists of a detector unit (welas 2300 and welas 2500), which is enclosed in a thermally controlled housing to prevent evaporation of cloud droplets and sublimation of ice crystals, and a separate control unit (welas 2000).

The welas sensor utilizes a white light source and detects light scattered by individual particles at scattering angles centered around 90° (sideward scattering). As particles traverse the detection volume, they scatter light in a manner that depends on both their size and shape. Aspherical particles, such as ice crystals, typically scatter light with higher intensity compared to spherical particles of the same volume. This difference in optical response enables the discrimination between ice crystals and liquid cloud droplets based on the fact that ice crystals exhibit a larger apparent optical size compared to liquid cloud droplets. (Järvinen et al., 2014).

The investigated air sample from the AIDA chamber passes through a cuvette inside the welas sensor; however, only 10.5 % of the total air volume is sampled within the optical detection volume. This sampling efficiency must be taken into account when calculating the droplet and ice particle number concentrations in AIDA experiments.

3.1.4 Water measurement

The total water concentration inside the AIDA chamber is measured using a dew point mirror (373LX, MBW Calibration), while gas-phase water vapor concentrations, both under cloud-free and in-cloud conditions, are measured with the tunable diode laser (TDL) absorption spectrometer (APicT, AIDA PCI in-cloud Tunable diode laser), which has an accuracy of approximately 5% (Fahey et al., 2014).

For the humidity measurements, a laser beam is directed through the AIDA chamber. Its intensity is attenuated by water vapor absorption, and the transmitted signal is detected. This signal is directly related to the partial pressure of water vapor, $e(T)$, which is used together with the saturation vapor pressure to calculate the relative humidity with respect to water (RH_w) and the saturation ratio with respect to ice (S_{ice}), as follows:

$$\mathrm{RH}_w = \frac{e(T)}{e_{s,\mathrm{wat}}(T)} \cdot 100 \qquad ; \qquad S_{\mathrm{ice}} = \frac{e(T)}{e_{s,\mathrm{ice}}(T)} \tag{3.5}$$

Here, T is the gas temperature inside the chamber (in K), which must be in the valid range.

$$123 < T < 332 \text{ K} \tag{3.6}$$

for the parametrization described below. The saturation vapor pressures over liquid water and ice are calculated using the expressions from Murphy and Koop (2005) :

$$\begin{aligned} e_{s,\mathrm{wat}}(T) \approx \exp\Bigg\{ & 54.842763 - \frac{6763.22}{T} - 4.21 \cdot \log(T) + 0.000367 \cdot T + \tanh\left(0.0415 \cdot (T - 218.8)\right) \\ & \cdot \left[53.878 - \frac{1331.21}{T} - 9.44523 \cdot \log(T) + 0.014025 \cdot T \right] \Bigg\} \end{aligned} \tag{3.7}$$

$$e_{s,\mathrm{ice}}(T) = \exp\left\{9.550426 - \frac{5723.265}{T} + 3.53068 \cdot \log(T) - 0.00728332 \cdot T\right\} \tag{3.8}$$

Two configurations of the TDL system are employed. In the single-pass setup (SpAPicT, Single Path APicT), the laser beam crosses the chamber once. In the multi-pass configuration (APicT), the beam traverses the chamber multiple times, which enhances measurement sensitivity. This configuration is particularly suitable for low-temperature experiments in the cirrus cloud regime, where water vapor concentrations are typically low.

3.1.5 Offline and online ice nucleating particle measurements

For offline INP measurements using INSEKT (see Section 3.2), aerosol-laden air from the AIDA chamber is pumped through stainless steel filter holders (Sartorius Membranfilter GmbH, SM16254) with modified connections, mounted via vertical inlets at the side of AIDA. These holders are equipped with 47 mm Nuclepore track-etched polycarbonate membrane filters with 0.2 µm pore diameters (Whatman).

To minimize the background INP signal originating from the filter material itself, the filters are pre-cleaned by soaking in a 10% hydrogen peroxide (H_2O_2) solution for 10 minutes, following the procedure described in Hiranuma, Augustin-Bauditz, et al. (2015). Residual H_2O_2 is removed by rinsing the filters three times with 0.1 µm pore-diameter-filtered deionized water (18 MΩ). The cleaned filters are then dried in a particle-free, laminar flow clean box and individually stored in sterile aluminum envelopes until use for aerosol sampling.

Aerosol collection is conducted at a flow rate of 10 stdL/min over a duration of approximately 2 hours. After sampling, the loaded filters are individually sealed and stored in a freezer until further analysis. Before INP analysis, the aerosol particles collected on the filters are resuspended in clean water (see Section 3.2 for procedural details) and probed for their ice nucleation ability.

In addition to offline methods, the online INP measurement technique INKA (see Section 3.3) is utilized to investigate the total aerosol population in the AIDA chamber. The instrument is connected via a horizontal sampling line and samples aerosol-laden air from the chamber at flow rates ranging from 0.631 L/min to 1.251 L/min over a period of approximately 4 hours. Once the sampling and particle collection have been completed, the AIDA cloud expansion experiment (see Section 3.1.6) is started.

With this setup, the aerosol particles used in INP studies are well characterized by various instruments, all sampling from the same aerosol population. This coordinated approach is particularly valuable for the inter-comparison of different INP measurement techniques and helps to eliminate discrepancies that may otherwise arise due to variations in aerosol generation or sampling conditions.

3.1.6 Typical procedure for AIDA expansion and ice nucleation experiment

Prior to each expansion experiment, the AIDA chamber undergoes a thorough cleaning procedure. This process lasts approximately 4 hours and involves evacuating the chamber to a pressure below 2 hPa, followed by ten flush cycles, in which the chamber is refilled with dry, clean synthetic air to 10 hPa and then evacuated again below 2 hPa.

After this, the chamber is further evacuated for 1 hour to below 0.1 hPa. During this period, the chamber is also cooled or heated to the desired starting temperature.

After the cleaning cycle, ultrapure water vapor is introduced and allowed to condense onto the chamber walls, forming a thin ice layer that serves as a humidity reservoir throughout the experiment. The chamber is then refilled with dry, particle-free synthetic air to ambient pressure.

Once the target conditions are established, aerosol particles are injected into the AIDA chamber (see Section 3.1.2). For this study, the aerosol number concentrations at the time of injection typically ranged from $100\,\mathrm{cm}^{-3}$ to $200\,\mathrm{cm}^{-3}$, depending on the aerosol type and temperature regime. At higher temperatures, larger total aerosol surface areas are required to obtain measurable ice number concentrations.

Following aerosol injection, the number concentration and size distribution of the particles are initially characterized using CPC, SMPS, and APS instruments (see Section 3.1.3). For INP experiments, the particles are further analyzed prior to the AIDA expansion using both offline (INSEKT) and online (INKA) measurement techniques. These INP-specific characterizations are performed concurrently with aerosol sampling and continue until just before the onset of the AIDA cloud expansion, which itself serves as an additional online INP measurement.

Once INP measurements are complete, the AIDA cloud expansion is initiated to further assess the ice nucleation activity of the aerosol population. The expansion begins by connecting the chamber to the vacuum system (Figure 3.3, $t = 0\,\mathrm{s}$), initiating a controlled pressure reduction. This leads to a nearly adiabatic expansion of the chamber air, resulting in a drop in gas temperature T_{gas} and a corresponding increase in relative humidity (Figure 3.3, panels 1 and 2). The cooling rate, determined by the pumping speed, is generally around $3\,\mathrm{K\,min}^{-1}$, which corresponds to an effective vertical updraft velocity of approximately $5\,\mathrm{m\,s}^{-1}$.

In immersion freezing experiments (Figure 3.3 a), the relative humidity increases until water saturation is reached. Aerosol particles are activated as CCN, forming a supercooled liquid cloud. The droplets grow by condensation of water vapor and begin to freeze at lower temperatures. Ice crystals, which are distinguished by their larger size and asphericity, are identified by applying a size threshold to the OPC signal (Figure 3.3, panel 4). Particles exceeding this threshold are counted as ice crystals. While Welas 1 detects all particle sizes, Welas 2, which is optimized for larger particles, is used to obtain accurate ice number concentration measurements (Figure 3.3 a, panel 3).

Data analysis begins once the ice number concentration exceeds a threshold of $0.1\,\mathrm{cm}^{-3}$ (indicated by the red line at $t = 70\,\mathrm{s}$) (Ullrich et al., 2017). This evaluation period continues until approximately 295 s after the start of the expansion, when the ice concentration reaches its maximum. The saturation ratios with respect to water and ice (S_{water} and S_{ice}) reach the peak and remain constant thereafter. In this experiment, the AIDA expansion was terminated at a pressure of 750 mbar by stopping the pumping of air out from the chamber.

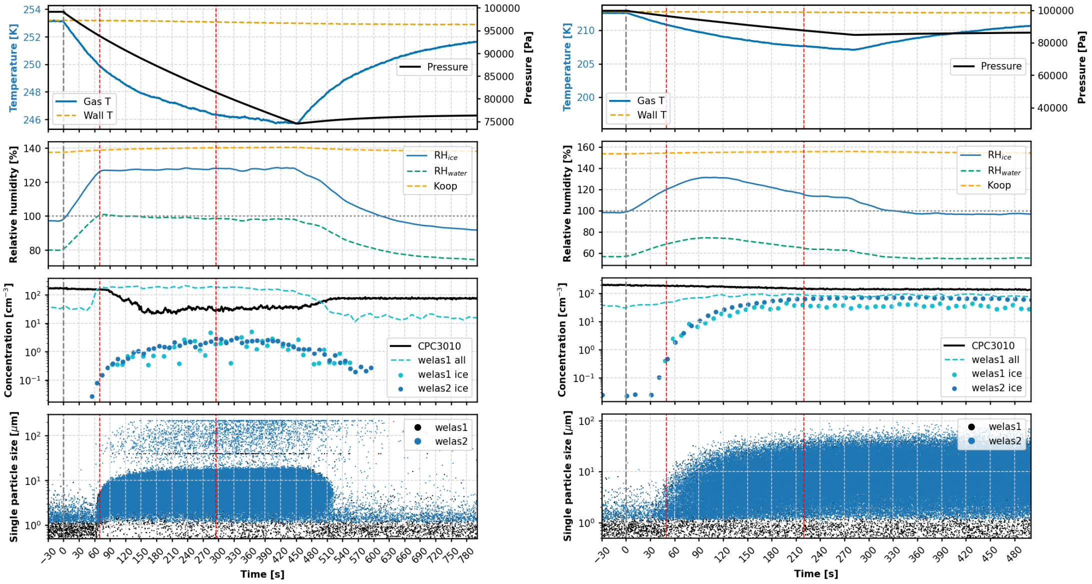

Figure 3.3: Time series of representative AIDA heterogeneous freezing experiments. Left: (a) Immersion freezing experiment. Right: (b) Deposition nucleation experiment.Each sub-panel shows, from top to bottom: Panel 1 –chamber gas temperature (T_{gas}, blue), wall temperature (T_{wall}, orange), and pressure (p, black, right axis); Panel 2 –relative humidity with respect to liquid water (RH_{water}, green) and ice (RH_{ice}, blue), together with the Koop line (orange dashed); Panel 3 –aerosol concentration measured with the CPC (c_n^{CPC}, black), total concentration from welas 1 (c_n^{total}, blue dashed), which includes aerosol particles, cloud droplets and ice crystals, and the ice concentration measured with the welas 1 (light-blue markers) and the welas 2 (blue markers) ; Panel 4 –single particle data from welas 1 (black dots) and welas 2500 (blue dots). Particles with diameters below 4 µm are considered aerosols, those between 4 µm and 25 µm are cloud droplets, and particles larger than 25 µm are classified as ice crystals. In all panels, the vertical grey dashed line marks the expansion start, and the two vertical red dashed lines delimit the time window used for further analysis.

In deposition nucleation experiments (Figure 3.3 b), ice crystals form at relative humidities only slightly above ice saturation, without an intermediate liquid phase (first vertical red line at $t = 50\,\text{s}$). The crystal growth rates are slower, and the resulting particles are generally smaller. Due to its higher sensitivity in the small particle range, Welas 1 is preferred for detecting deposition-mode ice crystals. Data analysis begins when the ice number concentration exceeds the background threshold of $0.1\,\text{cm}^{-3}$. Measurements are interpreted as deposition nucleation data as long as the ice number concentration continues to rise up to the point where relative humidity reaches its maximum (second vertical red line at $t = 220\,\text{s}$). The ice particle number concentration at this humidity peak is defined as the representative deposition nucleation point for the experiment. The corresponding temperature is determined as the average temperature between the onset of data analysis and the time of peak humidity.

At the end of the expansion, the chamber pressure stabilizes, and the gas temperature (T_{g}) gradually increases due to heat transfer from the chamber walls, while the wall temperature (T_{w}) remains nearly constant. As the gas warms, the saturation ratios with respect to ice and water decrease, eventually falling below unity. This shift to sub-saturated conditions leads to the evaporation of remaining cloud droplets and

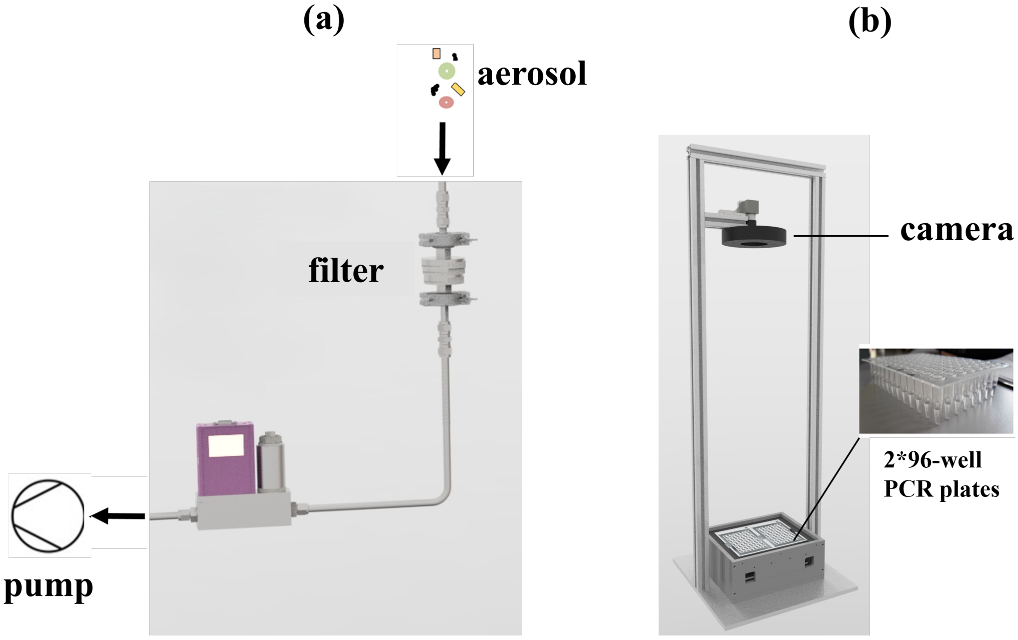

Figure 3.4: Schematic illustration of the setup for aerosol filter sampling (a) and the configuration of the droplet freezing assay INSEKT (b).

the sublimation or sedimentation of ice crystals formed during the expansion. Once the cloud has fully dissipated, the experiment is concluded and the chamber is set to an automated cleaning and preconditioning program in preparation for the next expansion experiment.

3.2 The droplet freezing assay INSEKT

Droplet freezing assays are commonly employed for batch analysis of INPs. In this method, droplets containing an aqueous suspension of INPs are arranged in PCR trays and cooled at a specified rate until all droplets freeze (Harrison et al., 2018; Miller et al., 2021; Schneider, Höhler, Heikkilä, et al., 2021).This technique is particularly advantageous for immersion mode analysis, where a wide range of INPs can be tested under controlled conditions (Miller et al., 2021; Tobo, 2016). The Ice Nucleation Spectrometer of the Karlsruhe Institute of Technology (INSEKT) is an droplet freezing assay designed to investigate the ice nucleation activity of aerosol particles collected either from laboratory experiments at AIDA or from field campaigns (Schneider, Höhler, Heikkilä, et al., 2021). INSEKT is based on an ice spectrometer originally developed at Colorado State University (Hill et al., 2016), and operates over a wide temperature range from approximately −5 °C to −26 °C, corresponding to 268 K to 247 K. It measures INP concentrations as a function of activation temperature in immersion freezing mode.

3.2.1 Aerosol sampling and preparation

As shown in Figure 3.4 a, Aerosol particles are collected using a filter holder fitted with a nuclepore track-etched polycarbonate membrane (Whatman), with a diameter of 47 mm and the typical pore sizes of 0.2 µm. A mass flow controller regulates a constant sampling flow. Depending on aerosol concentrations, sampling durations vary from

30 min to 2 h in laboratory settings and up to several days in field deployments. Collected filters are pre-cleaned with 10% H_2O_2 and rinsed with deionized water before use.

Post-sampling, filters are stored frozen and transported under clean conditions. For analysis, they are immersed in 8 mL of nanopure water (filtered through a 0.1 µm syringe filter) and rotated for 20 min to extract particles. The resulting suspension is diluted with clean water in ratios such as 1:15 and 1:225, or even 1:3375. Aliquots of 50 µL are pipetted into two 96-well PCR plates, organized into groups for undiluted, diluted, and blank (nanopure water) samples. All handling is conducted in a clean flow cabinet using pre-cleaned tweezers.

3.2.2 Experimental setup and freezing detection

The Figure 3.4 b showed the configuration of the droplet freezing assay INSEKT. The PCR plates are inserted into two aluminum cooling blocks connected to a chiller (LAUDA Proline RP 890), which circulates ethanol at a constant cooling rate of $0.33\,\mathrm{K\,min^{-1}}$. The blocks are housed in a PVC box insulated with 2 cm of Armaflex material and covered with an anti-reflection coated glass pane. A continuous flow of particle-free synthetic air ($80\,\mathrm{L\,h^{-1}}$) flushes the interior to prevent condensation.

Eight temperature sensors (Pt100) are embedded near the wells and measure temperature at a resolution of 2 Hz. A camera mounted above the PCR plates (focal distance 60 cm) detects brightness changes in wells as freezing occurs. Temperature, cooling rate, and optical changes are monitored and recorded by LabVIEW software.

3.2.3 Freezing experiment and INP quantification

After initial cooling to 273.15 K, the PCR plates are cooled at a controlled cooling rate of $0.33\,\mathrm{K\,min^{-1}}$(i.e., temperature decrease) in the immersion freezing phase. Freezing events are identified by brightness changes in the wells, and the frozen fraction is computed as a function of temperature. INP concentrations per standard liter of sampled air are calculated in 0.5 K temperature bins using the method of Vali (1971), corrected by nanopure water blanks.

The cumulative number of INPs per volume of aerosol suspension, $c_{n,\mathrm{INP,liq}}$, is given by:

$$c_{n,\mathrm{INP,liq}}(T) = -\frac{\eta}{V_{\mathrm{drop}}} \ln\left(\frac{N_u(T)}{N_{\mathrm{all}}}\right) \tag{3.9}$$

where η is the dilution factor, V_{drop} is the droplet volume, $N_u(T)$ is the number of unfrozen samples at temperature T, and N_{all} is the total number of samples.

Handling blank filters (i.e., filters exposed without air sampling) help account for contamination from filter surfaces and are checked for cleanliness. Background freezing is evaluated by including blanks (nanopure water), then the corrected INP concentration per standard liter of sampled air is calculated as:

$$\begin{aligned} c_{n,\mathrm{INP,corr}}(T) &= -\frac{\eta}{V_{\mathrm{drop}}} \cdot \frac{V_{\mathrm{wash}}}{V_{\mathrm{air}}} \left[\ln\left(\frac{N_u(T)}{N_{\mathrm{all}}}\right) - \ln\left(\frac{N_{u,\mathrm{bgr}}(T)}{N_{\mathrm{all,bgr}}}\right)\right] \\ &= -\frac{\eta}{V_{\mathrm{drop}}} \cdot \frac{V_{\mathrm{wash}}}{V_{\mathrm{air}}} \ln\left(\frac{N_u(T)}{N_{\mathrm{all}} - \left(N_{f,\mathrm{bgr}} \cdot \frac{N_{\mathrm{all}}}{N_{\mathrm{bgr}}}\right)}\right) \end{aligned} \tag{3.10}$$

Here, V_{wash} is the volume of water used to suspend the aerosol particles, and V_{air} is the volume of sampled air, $N_{f,\mathrm{bgr}}$ and $N_{u,\mathrm{bgr}}$ are the numbers of frozen and unfrozen samples in the background measurement, respectively, and $N_{\text{all,bgr}}$ is the total number of background samples.

To quantify the contribution of heat-sensitive INPs, primarily those of biological origin such as proteinaceous particles, aerosol suspensions were subjected to an additional heat treatment following established protocols (Hill et al., 2016; O'Sullivan et al., 2018; T. W. Wilson et al., 2015). Specifically, suspensions of collected aerosols were heated to approximately 100 °C for 20 minutes to denature protein-based ice-nucleating components. After cooling to room temperature, the heat-treated suspensions were analyzed using the same INSEKT protocol as for the untreated samples.

3.2.4 Application in AIDA: INAS density

INSEKT-derived INP concentrations are combined with aerosol surface area data from CPC, SMPS, and APS measurements (Section 3.1.3) to calculate the INAS density (Ullrich et al., 2017):

$$n_s = \frac{N_{\text{INP}}}{A_{\text{aerosol}}} \tag{3.11}$$

Assuming a one-to-one correspondence between INPs and ice crystals, N_{INP} is equal to the measured INP concentration. Surface area concentrations are derived from particle size distributions.

3.3 The continuous flow diffusion chamber INKA

CFDCs are widely used to investigate the ice nucleation activity of atmospheric and laboratory-generated aerosol particles under controlled temperature and relative humidity conditions. These instruments simulate conditions relevant to cloud formation by generating well-defined gradients of temperature and water vapor saturation within a confined flow channel. As aerosol particles pass through this environment, those capable of acting as INPs initiate ice formation, which is subsequently detected, often via optical particle counters.

Over the past several decades, various CFDC designs have been developed, each tailored to specific experimental needs. These include CFDCs with concentric cylinder configurations, such as the vertical alignment used by Rogers (1988) and Rogers et al. (2001), parallel-plate geometries, including both horizontal and vertical orientations as described by Kanji and Abbatt (2009), Stetzer et al. (2008), and Garimella et al. (2016). Despite differences in geometry, cooling methods, and automation, all CFDCs operate on the same fundamental principle: aerosol particles are exposed to controlled supersaturation conditions with respect to ice or liquid water, allowing for the activation and growth of ice crystals.

At Karlsruhe Institute of Technology (KIT), two CFDC instruments have been developed and deployed: the laboratory-based INKA and its mobile counterpart mINKA. Both instruments are based on the classical concentric-cylinder CFDC design, providing high precision and flexibility for a wide range of experimental conditions. INKA is optimized for long-duration laboratory experiments, including those coupled with the AIDA cloud chamber, while mINKA is designed for field campaigns and remote measurements. These instruments offer automated Relative humidity (RH) scans, high-resolution temperature control, and detailed ice particle detection. In the following sections, the working principle, experimental procedures, and instrumentation of the INKA system are

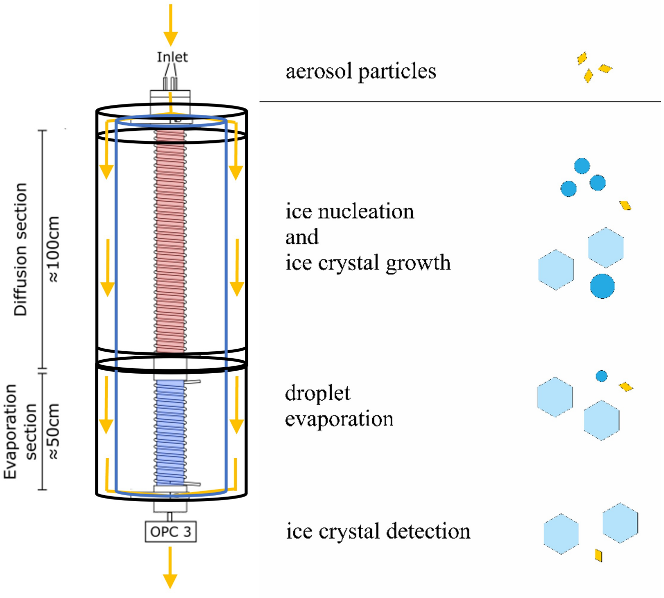

Figure 3.5: Schematic of the different cylindrical CFDC sections, which are passed by sampled aerosol: Ice nucleation and ice crystal growth section, droplet evaporation section, and particle detection.

described in detail, with reference experiments illustrating its capabilities. INKA enables precise measurements of ice nucleation under controlled conditions using RH scans and a robust thermal management system. Its integrated OPC and automated data acquisition allow for reliable identification and quantification of ice particles, supporting a broad range of cloud microphysics research applications.

3.3.1 Working principle

INKA is based on a cylindrical CFDC design consisting of two vertically-oriented concentric copper cylinders that form an annular gap of approximately 1.14 cm in width and 150 cm in length. The aerosol sample enters the annular gap from the top through a nozzle and is confined near the center by dry, particle-free sheath air(see Figures 3.5).

The chamber walls are coated with a thin, uniform ice layer formed through an icing procedure. Temperature gradients across the ice-coated walls create a steady-state temperature and water vapor pressure profile within the annular gap. These gradients result in supersaturated conditions conducive to ice nucleation. The upper two-thirds of the chamber serve as the activation section, where aerosol activation and ice nucleation occur. The lower third, with walls at equal temperature, acts as the evaporation section, facilitating the growth of ice particles while evaporating droplets.

The flow velocity profile inside the chamber is calculated considering both laminar flow and buoyant effects due to the temperature gradient. Under ideal conditions, the aerosol lamina is confined to a narrow region, experiencing nearly constant thermodynamic conditions. Relative humidity scans are achieved by adjusting wall temperatures via automated control.

3.3.2 Instrumentation and operation modes

INKA's flow system comprises three pumps, two mass flow controllers, eight valves, and three pressure sensors. Cleaning and icing cycles precede each measurement. Cleaning involves evacuating the chamber to reduce background frost. During icing, the chamber is cooled and flooded with deionized water to form a uniform ice layer on the walls.

Aerosol measurements are conducted with a total flow of $10\,\mathrm{L\,min^{-1}}$ to $12.5\,\mathrm{L\,min^{-1}}$, with the aerosol flow making up 5–10% of the total. The aerosol enters through the top and is enclosed by sheath air. Sampling can be conducted in direct flow mode. Filtered sample flows are used to determine background counts. After several hours of operation, the icing layer must be renewed.

3.3.3 Cooling and temperature control

Temperature regulation is achieved using two cryostats circulating ethanol through copper coils attached to the cylinder surfaces. The upper and lower sections of the chamber can be cooled independently, enabling operation in different modes (ice nucleation or ice growth). Temperature sensors (T-type thermocouples) monitor wall temperatures at multiple heights. A Pt100 sensor serves as a reference.

Wall temperature uncertainties arise from differences in heat transfer efficiency and ice layer thickness variation. The conservative estimate for overall uncertainty in wall temperature is 0.5 K. The aerosol lamina temperature, defined by the center of the annular gap, is determined using mean values from selected thermocouples.

3.3.4 Optical particle counter and data acquisition

An Optical Particle Counter (OPC) mounted downstream of the evaporation section distinguishes between small aerosol particles and larger ice crystals by applying a size threshold. INKA uses a Climet CI-3100 OPC, integrated with a LabVIEW-controlled data acquisition system. Each particle's signal height and duration are recorded at 1 Hz resolution. The OPC's detection range spans from approximately 0.5 µm upwards.

3.3.5 Typical experiment and data analysis

A typical INKA saturation scan, performed at the nominal temperature of −28 °C with desert dust particles sampled from the AIDA chamber, is shown in Figure 3.6. The experiment begins with a background measurement using HEPA-filtered air. Background counts are subtracted from measurement data to isolate ice nucleation signals. The aerosol inlet is then opened, and wall temperatures are adjusted to increase the relative humidity in the activation section.

Ice particle formation is monitored as saturation ratios rise. Ice crystals are identified via size thresholding in OPC data. Data analysis is terminated at the onset of droplet breakthrough, where incomplete droplet evaporation interferes with size-based classification. The INP number concentration is derived from the count of particles exceeding the threshold within a known sample volume and time interval.

For immersion freezing analysis, the selected point is typically at 5 % lower relative humidity than the droplet breakthrough onset. The selected relative humidity and temperature values reflect maximum ice nucleation without droplet interference.

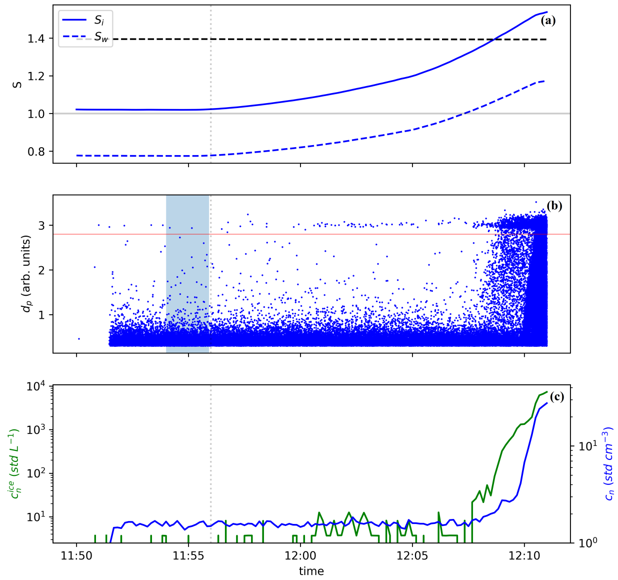

Figure 3.6: Time series of INKA measurements during an ice saturation ratio scan conducted at a nominal aerosol temperature of −28 °C with desert dust particles. (a) Saturation ratio with respect to ice (solid blue line) and liquid water (dashed blue line). (b) Normalized single particle signals from OPC3; each blue dot represents an individual aerosol particle or ice crystal. The red horizontal line indicates the ice threshold. The shaded area marks the period used for background ice concentration evaluation. (c) Ice crystal number concentration (green line, left axis) and total particle number concentration (blue line, right axis).

3.3.6 Uncertainty in temperature and INAS density

The temperature dependence of ice nucleation requires a careful assessment of the uncertainty. Variability in wall temperature sensors and ice layer thickness introduces uncertainties in lamina temperature. A conservative uncertainty of 0.5 K is used for all INKA data.

For INAS density calculations, aerosol surface areas are derived from AIDA's aerosol characterization, with a measurement uncertainty of 34 %. Combined with INP counting errors, this contributes to the total INAS density uncertainty.

3.4 The mobile cloud expansion chamber PINE

The PINE is an *in situ* instrument developed for the real-time quantification of INP concentrations in both ambient and laboratory-generated aerosols. Based on the operational concept of the large-volume AIDA cloud chamber, PINE induces the formation of supercooled droplets and ice crystals by imposing a rapid reduction in pressure and temperature, thus replicating the thermodynamic conditions characteristic of ascending air parcels in the atmosphere, was first described in detail by Möhler et al. (2021). Between 2016 and 2019, PINE was developed and built at the Karlsruhe Institute of Technology in collaboration with the University of Leeds and was commercialized by Bilfinger Nuclear & Energy Transition GmbH (Würzburg, Germany; see Figure 3.7a). The current commercial model, with a chamber volume of 10 L, provides a temporal resolution of approximately 6 min and supports fully automated remote operation for extended field and laboratory campaigns. Since all the measurements presented in this work were performed with the version ”PINE-05-0X”, the term PINE in the following always refers to this PINE version.

3.4.1 Instrument setup

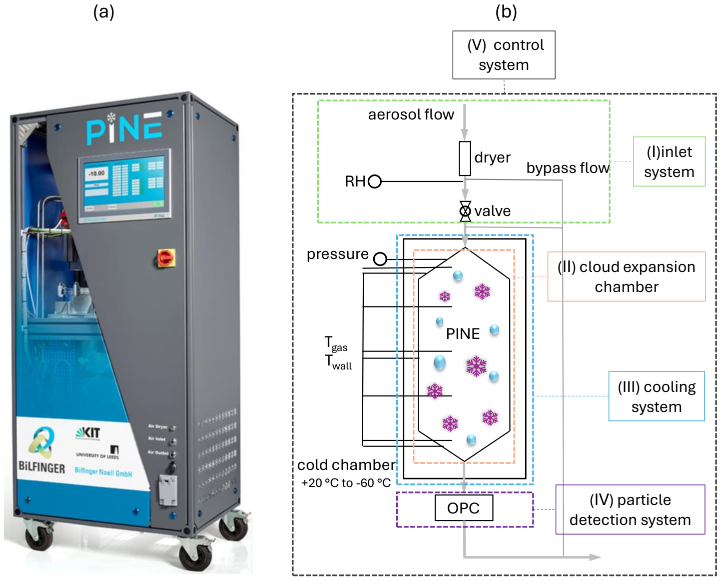

Figure 3.7: Setup of the PINE chamber. Picture (a) shows the commercial version of the PINE chamber. (b) shows the five main parts of the PINE instrument (with minor changes from Möhler et al. (2021)), and more detailed overview of the single components of the several parts.

PINE comprises five parts (Figure 3.7b): (I) an inlet system, (II) a cloud expansion chamber, (III) a cooling system, (IV) a particle detection system, and (V) a control system. All parts are briefly explained below.

The inlet system incorporates a dual membrane dryer (Perma Pure, MD-700-24S) to remove moisture and prevent frost formation on chamber walls. A dew point sensor (Vaisala DMT143) downstream of the dryer continuously monitors aerosol humidity.

The cloud expansion chamber is a 10 L stainless-steel vessel in which aerosols are activated to liquid droplets or ice crystals via controlled depressurization. Gas temperature is measured at five vertical positions, and wall temperature is recorded at three levels. Chamber pressure is monitored by a transducer (Thyracont VSC43MV; ±0.3 % uncertainty).

The cooling system uses a Stirling cooler (Thales LPT9310) to maintain chamber temperatures between 0 °C and −65 °C. The chamber is housed within a vacuum-insulated vessel, achieving cooling rates up to 0.6 $^{\circ}\mathrm{C\,min^{-1}}$.

The particle detection system is a full-flow optical particle counter (OPC; Palas GmbH fidas-pine) located downstream, which detects side-scattered light to distinguish ice crystals from droplets. Full-flow sampling maximizes sensitivity at low particle concentrations.

The control system employs a LabVIEW program to set and regulate temperature, pressure, dew point, and flow-rate setpoints, and to record continuous time-series data from all sensors and particle measurements.

3.4.2 Operating principle

PINE operates in cycles of flush, expansion, and refill. After stabilizing at the target temperature, flush mode (4 min to 5 min, $1\,\mathrm{L\,min^{-1}}$ to $2\,\mathrm{L\,min^{-1}}$) replaces chamber air with conditioned aerosol under constant temperature and pressure.

In expansion mode, the inlet valve closes while outflow ($2\,\mathrm{L\,min^{-1}}$ to $5\,\mathrm{L\,min^{-1}}$) is maintained, reducing chamber pressure to approximately 85 % of its initial value. The resulting temperature drop raises supersaturation with respect to water or ice; once the corresponding saturation threshold is reached, aerosol particles are activated to form supercooled ice crystals and/or water droplets, depending on temperature and aerosol properties. The total number of Ice crystals (ΔN_{ice}) are obtained from the OPC and converted to INP concentration:

$$n_{\mathrm{INP}} = \frac{\Delta N_{\mathrm{ice}}}{\Delta V_{\mathrm{exp}}} = \frac{\Delta N_{\mathrm{ice}}}{\Delta f_{\mathrm{exp}} \cdot \Delta t_{\mathrm{exp}}}, \tag{3.12}$$

where ΔV_{exp} is the sample volume determined by the expansion flow rate (Δf_{exp}) and duration (Δt_{exp}). The uncertainty in the measured INP concentration is estimated to be ±20 %, and the uncertainty in nucleation temperature is ±1 °C due to temperature gradients within the chamber (Möhler et al., 2021).

Refill mode reopens the inlet valve, restoring chamber pressure with filtered air and preparing for the next cycle. Each cycle lasts 4 min to 6 min, allowing 10–15 cycles per hour.

Daily background sequences with HEPA filter (Whatman, WHA2609T) filtered air verify the absence of frost artifacts: no ice crystals are detected over two to three consecutive cycles. PINE accommodates both constant-temperature experiments for high temporal resolution and programmed temperature ramps for detailed temperature-dependent nucleation studies.

3.5 Other instruments

3.5.1 BJ-CFDC: A novel continuous flow diffusion chamber

The BJ-CFDC (Figure 3.8), a commercial Continuous Flow Diffusion Chamber with Ice-Activated Surfaces jointly developed by Handix Corporation (USA) and the team of Prof. Paul DeMott at Colorado State University, was employed for continuous measurements of INP concentrations at −20 °C, −25 °C and −30 °C. The instrument adopts the same chamber geometry and operating principles as previous well-established CFDC designs (Petters & Kreidenweis, 2007; Rogers et al., 2001), ensuring full compatibility with existing datasets.

The chamber consists of a vertical cylindrical flow path bounded by two ice-coated walls maintained at controlled temperatures to generate a supersaturated environment with respect to water. Aerosol particles pass through this region, and those containing ice-nucleating particles activate into ice crystals, which are optically detected after any accompanying droplets have evaporated. To avoid interference from larger particles, a 2.5 µm cut-off impactor is positioned upstream of the chamber.

A motorized three-way valve (Hanbay Inc., Canada) alternated between ambient aerosol and filtered air to allow for periodic background measurements, accounting for frost-induced signals from the chamber surfaces. The control software was programmed to switch sampling modes every five minutes, providing INP data with 10 min temporal resolution. An additional three-way valve facilitated switching between nitrogen supply

Figure 3.8: Exterior view of the novel online Continuous Flow Diffusion Chamber (BJ-CFDC).

and a vacuum line for chamber conditioning. Vacuum was applied using an Agilent IDP-3 scroll pump, which was operated via a software-controlled relay, while nitrogen flow was regulated through a mass flow controller. All system components, including valve states and pump operation, were integrated into a LabVIEW-based control interface.

At the base of the chamber, a sliding metal plate enabled switching between aerosol and ice crystal sampling modes, water filling, and sealing for vacuum application. This plate also hosted the optical particle counter (OPC), the water inlet, and a blanking port. Plate movement was automated using stepper motors driven by an Arduino microcontroller running Grbl firmware, commonly applied in CNC devices. Vertical and horizontal motion were independently controlled, and limit switches ensured accurate repositioning.

Formation of the ice-coated walls was automated by pumping a predefined water volume into the chamber and allowing it to drain. A water level sensor monitored the tank volume, and the pump was shut off automatically via LabVIEW once the target level was reached. This procedure replaced the earlier manual approach and ensured reproducibility between cycles.

Temperature control of the chamber was achieved using two recirculating ethanol bath chillers (Julabo FP50HL, Germany), connected to copper coils lining the inner and outer chamber walls, following the design described in Rogers et al. (Rogers et al., 2001). Chiller communication was handled via RS-232 interface. Initial temperature setpoints were derived algorithmically based on desired operating conditions and were dynamically adjusted through PID feedback loops. Further fine-tuning was implemented in LabVIEW to maintain thermal stability, with wall temperature gradients held below 0.5 °C. The system also enabled rapid heating for de-icing during chamber reconditioning.

The automation system supported continuous operation. Measurement sequences—such as evacuation, leak checks, chamber cooling, ice generation, and sample flow initiation—were preprogrammed. Background correction was performed using filtered air measurements. At the end of each cycle, the ice walls were melted and the chamber evacuated before beginning a new sequence.

3.5.2 Freezing ice nucleation detection analyzer FINDA

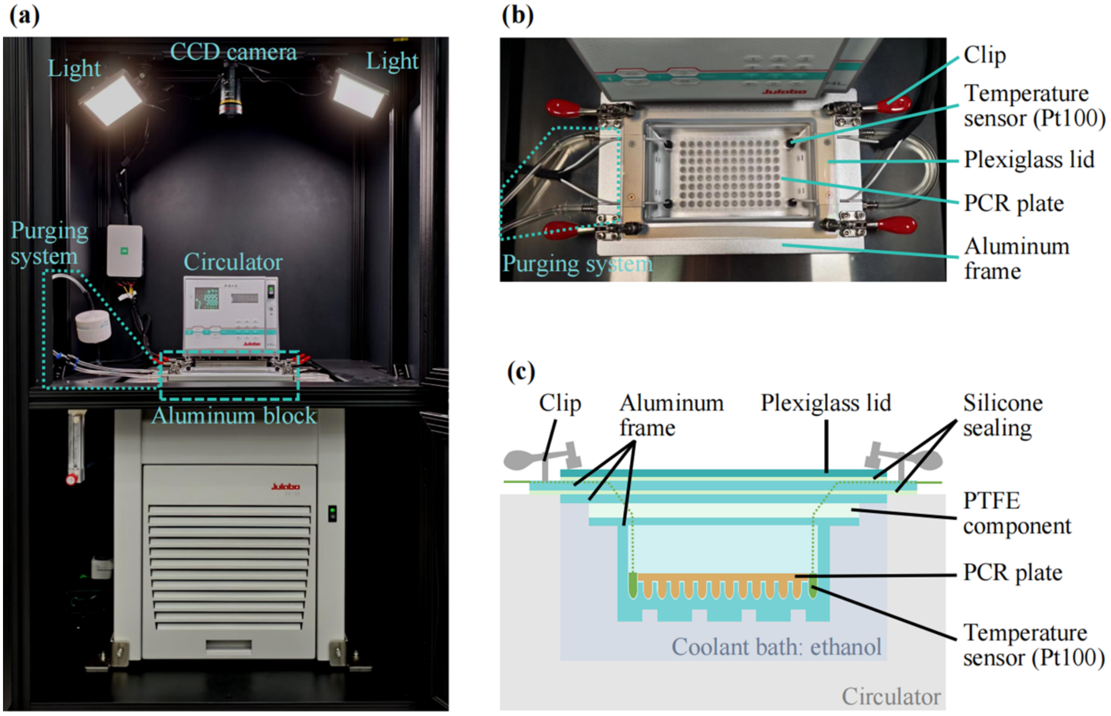

Figure 3.9: (a) The overview of the setup of FINDA. (b) The top view of the aluminum block with a PCR plate inside. (c) Schematic of the aluminum block from the front view.

The FINDA follows the basic design approach proposed by Hill et al. (2014), Schneider, Höhler, Wagner, et al. (2021), and Y. Ren et al. (2024), with its origins traceable to the cold stage concept of Vali (1971). As illustrated in Figure 3.9a, the setup includes a custom aluminum block serving as a cold stage for a standard 96-well PCR plate. Temperature control is achieved using a refrigerated/heating circulator (FP50-HL, JULABO, Germany), and temperature is monitored with four Pt100 resistance sensors (NI 9217 and NI 9171, National Instruments, USA). The system also incorporates a CCD camera (GOX-5102-USB, JAI, Denmark), two LED light panels (Luxpad23, Naguan, China), and a nitrogen purging unit. These components are installed within a custom-built matte-black enclosure that provides controlled lighting and limits contamination from room air. A computer connects to the camera, sensors, and circulator, running a LabVIEW program for system control and data acquisition.

Freezing of droplets in the PCR plate is recorded using the CCD camera, which captures changes in LED light reflection over time. The camera is mounted above the PCR region using an adjustable zoom lens (12 mm to 120 mm, Qiyun Photoelectric, China), allowing visual tracking of freezing events at the individual well level.

The aluminum block is partially immersed in the bath of the temperature circulator and sealed with a silicone gasket to prevent contact between the coolant and the plate. An acrylic cover is placed above the block to insulate the chamber and limit mixing with ambient air. To reduce frost buildup on the lid, a PTFE spacer is inserted between the acrylic and the metal block to minimize upward heat conduction from the coolant (Figure 3.9c).

A machined cavity inside the block holds a 96-well 0.2 mL PCR plate (Boibio, China) and the four Pt100 sensors. These sensors (model 5157701, YAGEO Nexensos, Germany) are embedded into thermally conductive epoxy (Omegabond 200, Omega Engineering, USA) inside tubes cut from PCR plates, providing thermal contact between the sensors and the droplet layer. The Pt100 sensors are Class A, with an accuracy of $\pm 0.15\,°\mathrm{C}$ at $0\,°\mathrm{C}$. Final droplet temperatures are calculated from the average of the four sensor readings after individual calibration. For routine experiments, a cooling rate of $-1.0\,°\mathrm{C}\,\mathrm{min}^{-1}$ is used. Typically, the system is held at $2\,°\mathrm{C}$ for 10 min before the cooling experiment begins.

Before the start of each run, clean dry nitrogen is passed over the PCR plate at $6\,\mathrm{L}\,\mathrm{min}^{-1}$ to reduce moisture and particles in the chamber (Figure 3.9a,b). The gas is filtered through a 0.2 µm HEPA filter (HEPA-CAP, Whatman™, UK). During cooling, the nitrogen flow is paused to avoid introducing heat near the droplet surface.

A custom LabVIEW program was developed to operate the system through a user interface, allowing control of the coolant bath circulator and real-time monitoring of droplet freezing in the PCR plate using the CCD camera. Both temperature data and pixel intensities for each well are recorded at a frequency of 1 Hz and stored for subsequent analysis. Taking into account the vertical thermal conductivity and lateral temperature variation across the cold stage, the overall temperature uncertainty of FINDA is estimated to be approximately $\pm 0.6\,°\mathrm{C}$.

In each assay, an ensemble of 50 µL droplets is cooled at rate β. At temperature T, the frozen fraction

$$\mathrm{FF}(T) = \frac{N(T)}{N_0}$$

is determined by thresholding the droplet grayscale intensity, where N_0 is the total droplet count and $N(T)$ is the number frozen by T. The cumulative INP concentration per droplet volume V_{drop} is then

$$C_{\mathrm{INP}}(T) = -\frac{\ln\left[1 - \mathrm{FF}(T)\right]}{V_{\mathrm{drop}}}.$$

For mass-normalized samples, dividing $C_{\mathrm{INP}}(T)$ by the sample mass concentration C_m yields INPs per unit mass (Hill et al., 2014).

FINDA has been tested using Milli-Q ultrapure water as well as reference substances such as Arizona Test Dust and Snomax®. The freezing behavior observed under these conditions aligns well with results reported in earlier studies. FINDA’ s performance was validated against the INSEKT droplet-freezing assay using both the Snowmax biological standard and ambient aerosol suspensions. As shown in Figure 3.10, FINDA and INSEKT produce equivalent INP spectra, confirming FINDA’ s suitability for coordinated INP field observations. Additionally, FINDA has been applied to measure ice-nucleating particles (INPs) in precipitation samples collected from various locations in China (Y. Ren et al., 2024).

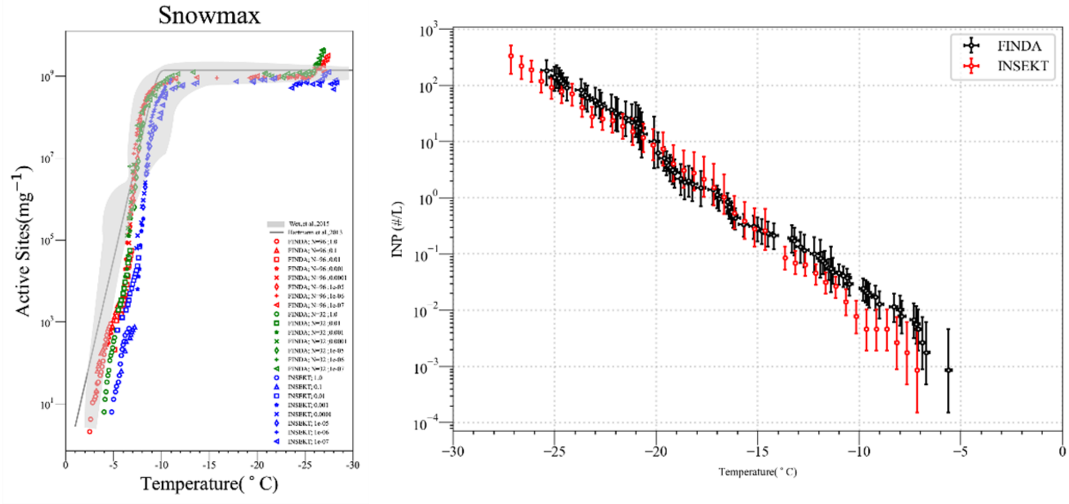

Figure 3.10: Comparison of FINDA and INSEKT performance in immersion-freezing assays using the SnowMax biological ice-nucleating standard (left panel) and ambient aerosol samples (right panel).

3.5.3 GRIMM 180 environmental dust monitor

The GRIMM 180 Environmental Dust Monitor (GRIMM Aerosol Technik GmbH & Co. KG, (https://www.durag.com/de/produktfilter-837.htm?productID=EDM%20180, last seen April 24, 2025), Figure 3.11) is a high-precision, continuous, real-time aerosol analyzer that reports mass concentrations (µg m^{-3}) of PM$_1$, PM$_{2.5}$ and PM$_{10}$ alongside size-resolved particle counts in 31 channels.

Figure 3.11: Photograph of the GRIMM 180 Environmental Dust Monitor.

Table 3.1 lists the particle size channels. Ambient air is drawn at 1.2 L min^{-1} through a measurement cell where a 660 nm semiconductor laser induces 90° light scattering; a photodiode classifies each scattering pulse by amplitude. Onboard data-logging intervals are user-configurable from six seconds to sixty minutes, and an RS-232 interface (with multiple protocol options) provides seamless integration with external DAQ systems. Visual and audible alarms alert the operator when concentrations exceed preset thresholds, and the rugged design ensures reliable operation from −20° C to 50° C and up to 95 % relative humidity.

Table 3.1: GRIMM 180 Particle Size Channels (µm)

Channel	1	2	3	4	5	6	7	8	9	10	11
Diameter	0.25	0.28	0.30	0.35	0.40	0.45	0.50	0.58	0.65	0.70	0.80

Channel	12	13	14	15	16	17	18	19	20	21	22
Diameter	1.00	1.30	1.60	2.00	2.50	3.00	3.50	4.00	5.00	6.50	7.50

Channel	23	24	25	26	27	28	29	30	31
Diameter	8.00	10.00	12.50	15.00	17.50	20.00	25.00	30.00	32.00

Table 3.2: Key Specifications of the GRIMM 180

Parameter	Specification
Light source	Semiconductor laser (660 nm)
Detection angle	90°
Sampling flow rate	$1.2\,\mathrm{L\,min^{-1}}$ (constant)
Particle size range	0.25 µm–32 µm
Mass concentration range	$0.1\,\mathrm{\mu g\,m^{-3}}$–$6000\,\mathrm{\mu g\,m^{-3}}$
Data interval	6 s –60 min (configurable)

Chapter 4

Laboratory Ice Nucleation Experiments with Mineral Dust from Asian Deserts

4.1 Introduction

In order to extend the temperature range and evaluate differences between measurement techniques as well as regional variations in Asian desert-dust ice-nucleating properties, 16 immersion-freezing experiments were conducted during two dedicated AIDA campaigns called INAD01 (Ice Nucleation characteristic of Asian desert Dust particles 01) and INAD02. Seven different dust samples from Asian deserts and the Saharan desert were used for these experiments. Although SD4 (Sahara Dust sample 4) has been employed in numerous prior studies, the other natural Asian desert dust samples (AD03–AD08) were investigated here for the first time. Mineral dust presents multiple active sites that trigger ice formation in a wide temperature interval, resulting in a gradual increase in ice concentration. All results in this section are expressed as n_s plotted against temperature.

Eight different dust samples from Asian deserts and the Saharan desert were used for these experiments.

Two dedicated AIDA campaigns INAD01 and INAD02 were conducted to study the ice nucleating characteristics of desert dust particles, with a special focus on different source regions in Asia to investigate regional variations in Asian desert-dust ice-nucleation properties. The campaigns comprised 16 immersion-freezing experiments at mixed-phase cloud conditions and 19 deposition nucleation experiments at cirrus cloud conditions. Three different measurement techniques were used to measure the ice nucleation ability of the dust particles, as summarized in Table 4.1: 1) direct expansion experiments in the cloud simulation chamber AIDA, 2) on-line ice nucleation measurements with the Continuous Flow Diffusion Chamber INKA that sampled the dust particles from the AIDA chamber, and 3) off-line freezing runs with filter-collected particles from the AIDA chamber using the Droplet Freezing Array INSEKT. The two campaigns INAD01 and INAD02 took place at the AIDA cloud chamber facility from April to May 2022 and from March to April 2023, respectively.

Section 4.2 provides details of the investigated dust samples, describes the aerosol generation process, and outlines the experimental procedure. Section 4.3 summarizes the key steps in standard data processing. Section 4.4 describes a particular data correction for the size distribution measurements during the INAD01 campaign. Section 4.5

then presents and discusses the ice nucleation results collected using the three measurement techniques, separated into either mixed-phase cloud (Section 4.5.1) or cirrus (Section 4.5.2) conditions. Section 4.6 provides a summary and an outlook."

Table 4.1: Overview of instruments used in laboratory ice nucleation experiments conducted during the INAD01 and INAD02 campaigns, including instrument names and types, operational temperature ranges, detectable freezing modes, limits of detection (LOD), and—for the Droplet Freezing Array—the analyzed liquid volume.

Instrument	Instrument type	Temp. Range (°C)	Freezing Mode	LOD (L^{-1})	Liquid volume (µL)
AIDA	Expansion chamber	0 to -90	Immersion, Deposition	0.5	
INKA	CFDC	-10 to -60	Immersion, Deposition	~1	
INSEKT	Droplet Freezing Array	-5 to -25.5	Immersion	~1e-2	50

4.2 Dust samples and experimental procedure

For this study, seven natural desert dust samples (AD03, AD04, AD05, AD06, AD07, AD08, SD4) were collected from different source regions as summarized in Table 4.2. Six Asian Desert dust samples (AD03–AD08) were collected on the surface of the deserts from various locations in Xinjiang and Inner Mongolia, China, as shown in Figure 4.1 (a). AD03 was obtained on 14 January 2022 at Lop County, Hotan Prefecture (37.5177° N, 80.4413° E). AD04 was collected the same day at Tashairieik Township, Xinhe County, Aksu Prefecture (41.5941° N, 82.5941° E). Also on 14 January 2022, AD05 was sampled at the Tazhong Atmospheric Environment Observation Station in the central Taklamakan Desert (39.0000° N, 83.6667° E). The date of sampling for AD06 was 29 July 2017 at Xini Tao Haigacha near Bayanhaote Town, Alxa Left Banner, Inner Mongolia (38.7892° N, 105.3746° E). AD07 was collected on 13 January 2022 at Aizila Village, Dongbaza Hui Township, Shanshan County (42.8559° N, 90.2237° E). Finally, AD08 was obtained on 11 January 2022 in the Tarim Populus of Xinjiang (37.0200° N, 80.1100° E). The source region of AD06 is the Gobi Desert, while the other five samples originate from the Taklamakan Desert. The Saharan desert dust sample SD4 was collected from surface 50 km north of Cairo, Egypt (Kanji et al., 2011; Megahed, 2007; Niemand et al., 2012; Ullrich et al., 2017).

As shown in Figure 4.1 (b), each raw sample was initially dry-sieved using a vibratory sieve shaker to remove particles larger than 75 µm. The sieved fraction with particle diameters less than 75 µm was then used for particle dispersion and injection into the AIDA chamber. For AD03, AD04, and AD05, additional immersion-freezing measurements with INSEKT were performed with the bulk samples. For that purpose, a portion of the < 75 micron size fraction was again sieved in a second step to obtain a size fraction with particle diameters smaller than 20 µm, which was then used for the offline freezing runs. For the samples AD06 and AD07 only a very limited amount

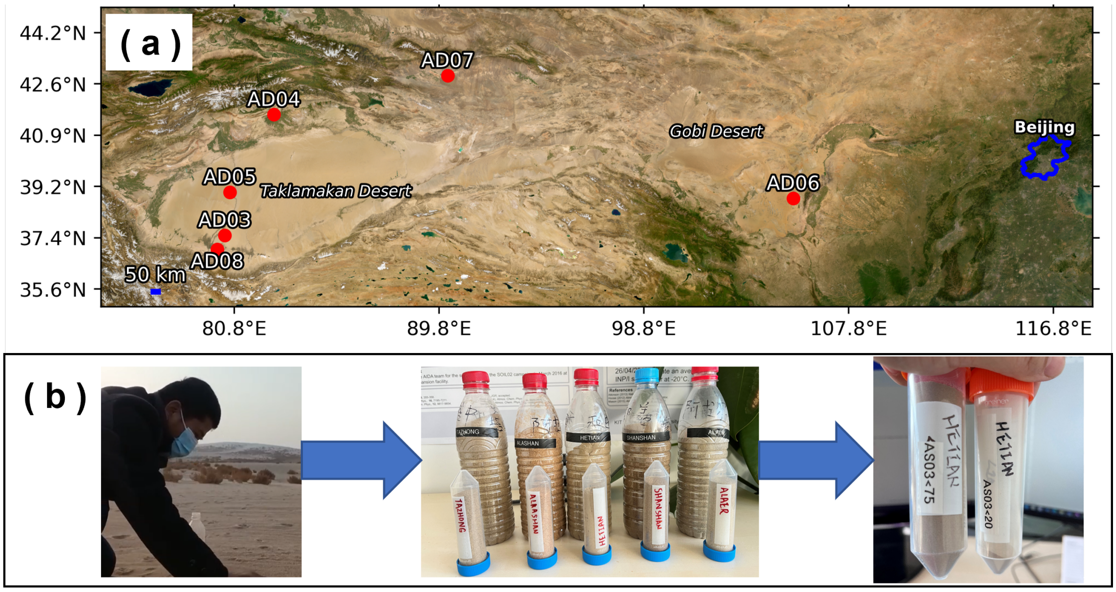

Figure 4.1: (a) Area map showing the source regions of the Asian Desert dust samples AD03–AD08 used in the AIDA campaigns (red dots). (b) Workflow diagram illustrating the processing steps from initial sample collection of the raw material (left), through the first sieving stage (centre), to the fine-sieved (< 20 micron) dust fractions applied in the supplementary bulk INSEKT experiments (right).

Table 4.2: Abbreviation and origin of the desert dust samples

AIDA label	Sampling date	Location	Desert
AD03	14.01.2022	37.5177°N, 80.4413°E	Asian (Taklamakan) Desert
AD04	14.01.2022	41.5941°N, 82.5941°E	Asian (Taklamakan) Desert
AD05	14.01.2022	39.0000°N, 80.6667°E	Asian (Taklamakan) Desert
AD06	29.07.2017	38.7892°N,105.3746°E	Asian (Gobi) Desert
AD07	13.01.2022	42.8559°N, 90.2237°E	Asian (Taklamakan) Desert
AD08	11.01.2020	37.0200°N, 80.1100°E	Asian (Taklamakan) Desert
SD4	18.02.2003	50 km N of Cairo	Saharan Desert

of the <75 micron size fraction was obtained from the sieving process. Each of these two samples was used in a single AIDA expansion experiment. However, due to the low concentrations of aerosols generated by the RBG disperser (approximately 15 and 19 $\mathrm{cm^{-3}}$, respectively), the resulting data quality was not sufficient for robust analysis. Consequently, the experiments based on AD06 and AD07 are not further discussed in this study.

As described in Section 3.1.2, the dust samples were aerosolized using a rotating-brush generator. Before injection into the AIDA vessel, the aerosol stream was passed through a cyclone impactor with a nominal 50% cut-off diameter of about 1 µm to 5 µm to remove coarse particles. The Scanning Mobility Particle Sizer (SMPS) and aerodynamic particle sizer (APS) yield the mobility diameter d_{me} and aerodynamic diameter d_{ae}, respectively. In order to merge the data from both instruments into one size distribution, the equivalent diameters from both instruments were converted into the volume-equivalent diameter d_{ve}, for which the particle density ρ and dynamic shape factor χ are needed. For desert dust, a bulk density of $\rho = 2.6\,\mathrm{g\,cm^{-3}}$ and a shape factor of $\chi = 1.2$ were adopted. These values are consistent with those reported by Kaaden et al. (2009). Due to a malfunction of the APS during the INAD01 campaign, a detailed cross-calibration procedure had to be developed for data correction. This procedure is described in detail in Section 4.4.

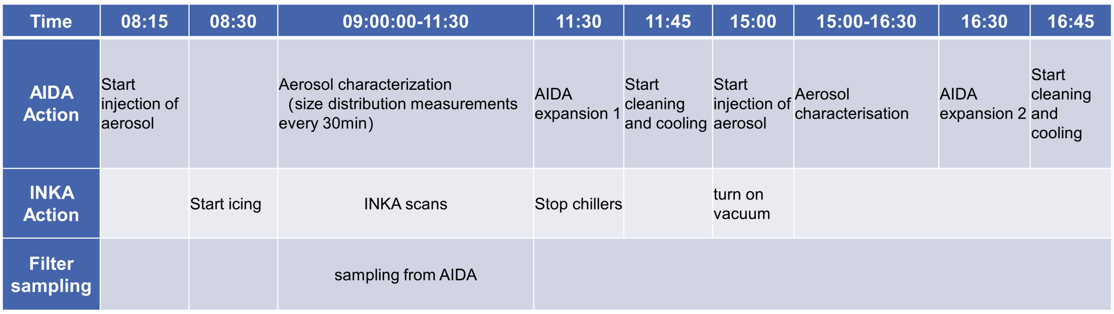

Time	08:15	08:30	09:00:00-11:30	11:30	11:45	15:00	15:00-16:30	16:30	16:45
AIDA Action	Start injection of aerosol		Aerosol characterization (size distribution measurements every 30min)	AIDA expansion 1	Start cleaning and cooling	Start injection of aerosol	Aerosol characterisation	AIDA expansion 2	Start cleaning and cooling
INKA Action		Start icing	INKA scans	Stop chillers		turn on vacuum			
Filter sampling			sampling from AIDA						

Figure 4.2: A typical timeline of the experimental procedure of an AIDA experiment day including aerosol injection and characterization, filter sampling and INKA measurements, as well as the AIDA expansion experiments.

All experiments in both campaigns followed a similar daily schedule (see Figure 4.2 with all times in local time LT). This procedure made it possible to carry out two AIDA expansion experiments per day at different temperatures and/or with different aerosol particles. INKA scans and filter sampling for the INSEKT analysis were only carried out once a day in the morning hours. At approximately 08:15 LT the dust aerosol was injected into the AIDA vessel (Section 3.1.2) and INKA simultaneously initiated its icing process. Size distributions were measured every 30 min by the SMPS and the APS. From 09:00 LT to 11:30 LT, INKA performed continuous INP measurements and particles were sampled on filters for offline analysis with INSEKT. The first experiment was then concluded by an AIDA expansion experiment at 11:30 LT. Vessel cleaning and adjustment of the AIDA temperature for the second experiment started at 11:45 LT. A second injection and characterization sequence began at approximately 15:00 LT and was concluded with an AIDA expansion at 16:30 LT.

4.3 Data processing

4.3.1 Ice particle number concentration

Ice crystals were detected by two optical particle counters, welas1 and welas2 (Palas GmbH), based on 90° light scattering (Benz et al., 2005). A white light beam defines a three-dimensional 'T'-shaped detection volume, and particles traversing this region scatter light, with the scattering intensity depending on their size, shape, and orientation. Each event of scattering by an individual particle is recorded by a Photomultiplier tube (PMT).

The total concentration of detected particles, n_p, is

$$n_p = \frac{N_p}{\bar{v}_p \, \Delta t \, S_{\mathrm{odv}}}, \tag{4.1}$$

Here, N_p is the number of pulses recorded by the PMT during interval Δt, S_{odv} is the cross-sectional area of the optical detection volume (welas1: $(280\,\mu\mathrm{m})^2$, welas2: $(493\,\mu\mathrm{m})^2$), and $\bar{v}_p$ is the mean particle velocity given by

$$\bar{v}_p = \frac{L_{\mathrm{odv}}}{\bar{\tau}}, \tag{4.2}$$

with L_{odv} being the length of the optical detection volume (welas1: 280 µm, welas2: 313 µm) and $\bar{\tau}$ the average pulse duration.

To distinguish ice crystals from smaller-sized seed aerosol particles and cloud droplets, a size threshold d_i^* is applied. The corresponding ice number concentration is calculated as

$$n_i = \frac{N_p(d_p \geq d_i^*)}{\bar{v}_p \, \Delta t \, S_{\mathrm{odv}}} \,. \tag{4.3}$$

4.3.2 Nucleation time interval and binning

The nucleation time interval Δt is defined as the period beginning when n_i exceeds a background value of about (0.1 cm^{-3}) and ending when it approaches its maximum value. This interval is divided into time bins of at least 10 s duration with a minimum of five ice counts per time bin. For each time bin k, $n_{i,k}$ is computed using Eq. (4.3), with an estimated relative uncertainty of 20% (Wagner & Möhler, 2013). The time bin-averaged temperature T and saturation ratio S_i are used with propagated uncertainties.

For immersion freezing experiments, welas2 is used because of its larger detection volume and therefore higher sensitivity for low ice crystal number concentrations. In deposition mode at lower temperatures, welas1 is used due to its higher detection sensitivity for smaller crystals.

4.3.3 Aerosol surface area concentration

Simultaneous aerosol number-size distributions are obtained from SMPS and APS measurements as function of the volume equivalent diameter of aerosol particles. Assuming spherical particle shape, the surface area distribution is computed as

$$f_S(\ln d_p) = \pi \, d_p^2 \, f_N(\ln d_p), \tag{4.4}$$

where f_N denotes the particle number size distribution. Each distribution is fitted with a lognormal function to derive the median diameter d_m and the geometric standard deviation σ_g. Figure 4.3 shows representative examples of the lognormal fits to the number concentration (top) and the surface area concentration (bottom) distributions for four different aerosol particle types. The black curves show the best-fit lognormal models, yielding total number concentration (n_{ae}), surface area (s_{ae}), median diameter (d_m), and geometric standard deviation (σ_g). The combined APS and SMPS data provide a robust basis for subsequent ice-nucleation analysis as function of the aerosol surface area concentrations. Figure 2 in the appendix presents the normalized particle number size distributions (PNSD) of the AD03 sample, as measured by the APS in four independent experiments during the INAD02 campaign. The results demonstrate that, for this sample, the characteristic features of the size distribution are consistent across all individual experiments, indicating a reproducible aerosolization and measurement process. This repeatability underscores that the experimental protocol is robust and provides a reliable basis for a comparative analysis of ice-nucleating properties from different experiuments with different aerosol samples. As mentioned above, Section 4.4 details the necessity of correcting the APS data during the INAD01 campaign.

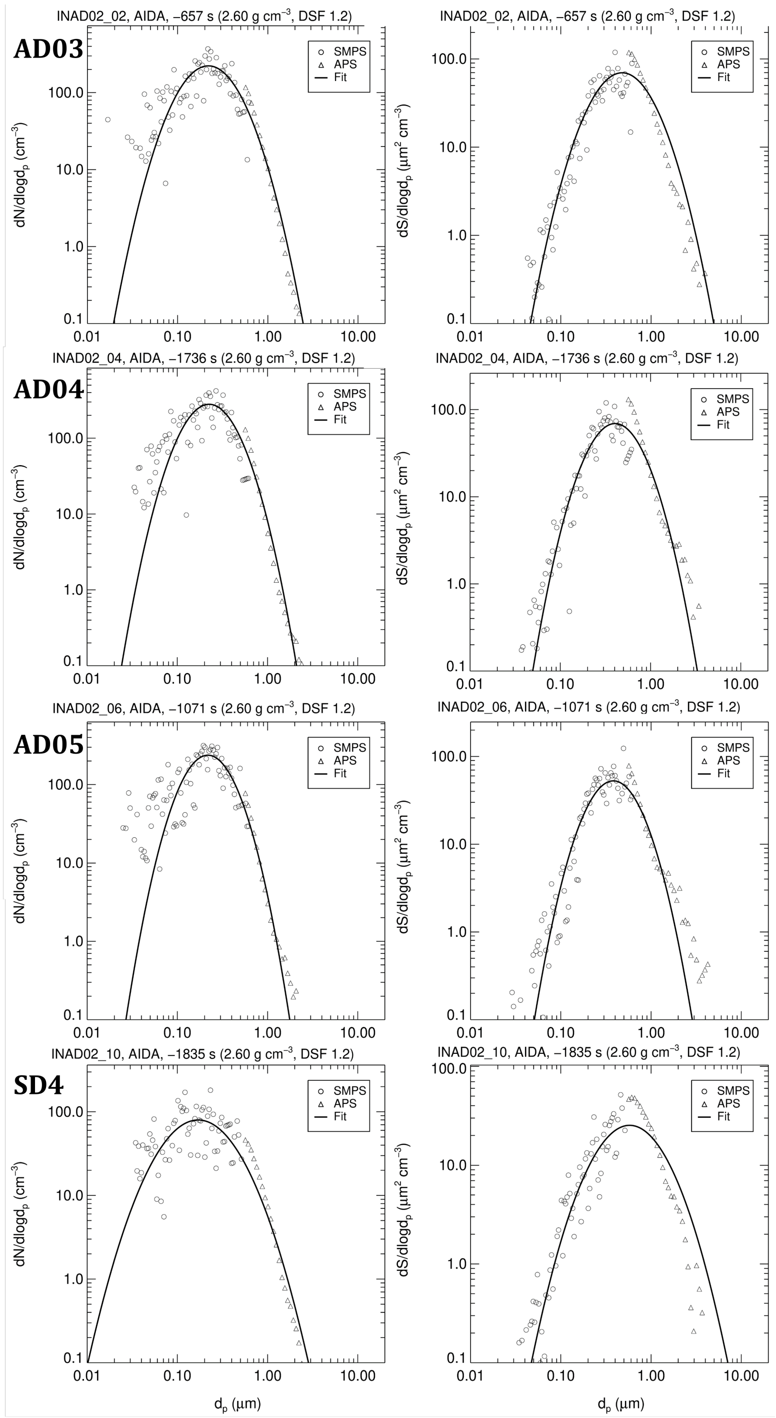

(a) **(b)**

Figure 4.3: Example lognormal fits to number concentration (a) and surface area concentration (b) distributions for representative dust samples. Each panel, from left to right, shows results for AD03, AD04, AD05, and SD4. The black curves indicate the best-fit lognormal models, from which the total number concentration (n_{ae}), surface area concentration (s_{ae}), median diameter (d_m), and geometric standard deviation (σ_g) are derived. Combined APS and SMPS measurements provide a robust characterization of the aerosol size properties relevant for ice-nucleation experiments.

4.3.4 Aerosol size distribution integration

The total aerosol surface area concentration $s_{\mathrm{ae},0}$ is obtained by integrating the surface area concentration size distribution f_S. In each time bin k, only particles with $d_p \geq d_{p,\mathrm{act},k-1}$ contribute, where $d_{p,\mathrm{act},k-1}$ is the aerosol activation diameter from the previous time bin. Correcting for pressure dilution (p_k/p_0) and the fraction of surface area above this threshold (aerosol activation diameter) using the Cumulative Distribution Function (CDF) Φ, the corrected surface area is

$$s_{\mathrm{ae},k} = s_{\mathrm{ae},0}\,\frac{p_k}{p_0}\,\Phi\!\left(\frac{\ln d_{p,\mathrm{act},k-1} - \ln d_m}{\ln \sigma_g}\right), \tag{4.5}$$

where Φ is the standard normal CDF.

4.3.5 Binned ice-active site densities

The ice-nucleating active site density, n_S, is defined as the ratio of the ice number concentration, n_i, to the aerosol surface area concentration, s_{ae}:

$$n_S(T, S_i) = \frac{n_i(T, S_i)}{s_{\mathrm{ae}}}\,, \tag{4.6}$$

where T is the temperature and S_i the saturation ratio with respect to ice. To derive n_S, the ice number concentration and aerosol surface area concentration are computed for each time bin defined within the nucleation interval.

For each time bin k, the binned active site density is calculated as:

$$n_{S,k}(T, S_i) = \frac{n_{i,k}(T, S_i)}{s_{\mathrm{ae},k}}\,, \tag{4.7}$$

where $n_{i,k}$ and $s_{\mathrm{ae},k}$ represent the time bin-wise values of ice number concentration and aerosol surface area concentration, respectively. The estimated combined uncertainty using error propagation is approximately 40%, based on a 20% relative error in $n_{i,k}$ (Wagner & Möhler, 2013) and 34% in $s_{\mathrm{ae},k}$(Ullrich et al., 2017).

4.4 Calibration and performance assessment of the aerodynamic particle sizer (APS-4) during the INAD01 campaign

The Aerodynamic Particle Sizer (APS-4, model 3321, TSI Inc.) was used next to a SMPS to measure aerosol size distributions over a broad size range during the INAD01 campaign. Combined measurements of the aerosol number size distributions with these instruments allow for computing the aerosol surface area distributions, which are needed to derive total surface area concentrations and, subsequently, calculate the ice-active site densities for ice nucleation analysis.

Instrument Diagnostics and Initial Performance A post-campaign evaluation revealed that APS size and concentration measurements were inconsistent with co-located instruments. A service inspection at TSI Inc. confirmed that detector misalignment had caused systematic sizing and concentration biases. Following realignment, APS measurements returned to expected ranges, but a robust recalibration was required to ensure traceability to an independent reference.

Cross-calibration with a condensation particle counter Simultaneous CPC (model 3010, TSI Inc.) measurements of the total number concentration $c_{n,\mathrm{cpc}}$ provided an accurate reference for the number concentration of particles larger than 10 nm. We defined three candidate calibration factors to scale the APS concentration output:

$$\text{cf2}, \quad \text{cf5}, \quad \text{cf10}$$

and compared total aerosol number concentrations n_{ae} derived from SMPS+APS data against CPC values under each cf setting.

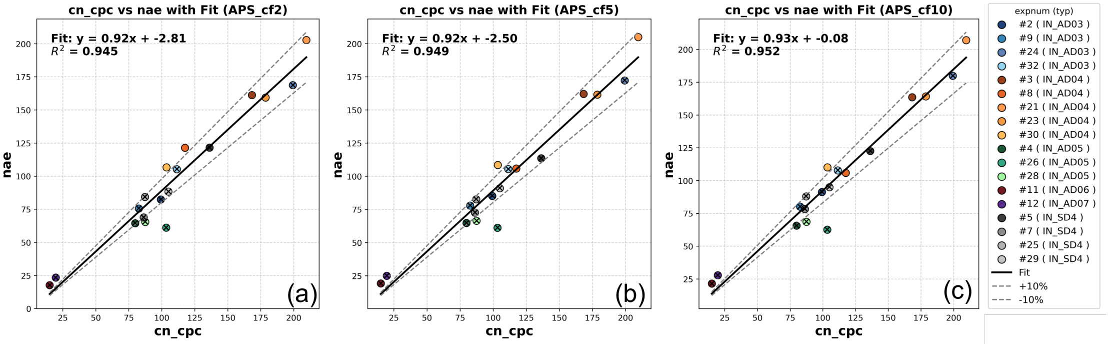

Figure 4.4: Comparison of CPC-derived number concentration $c_{n,\mathrm{cpc}}$ and SMPS/APS-derived total concentration n_{ae} during INAD01 campaign under three APS calibration factors (cf2 (a), cf5 (b), cf10 (c)). The marker color indicates the aerosol sample and the shading the experiment number. Solid lines are linear regressions; dashed lines show ±10% about the 1:1 line. Crossed symbols are excluded via Analysis of Variance (ANOVA) testing.

As shown in Figure 4.4, all three factors yield high correlation ($R^2 > 0.95$) between n_{ae} and $c_{n,\mathrm{cpc}}$.cf2 and cf10 systematically shift the calculated n_{ae} values slightly lower and higher, respectively, relative to cf5, which produces the smallest systematic bias. However, the variation remains largely within ±10 %, suggesting that the applied calibration range effectively constrains the systematic uncertainty in APS number concentration estimates. These results, while not sufficient to uniquely identify a single "optimal" calibration factor, support the use of cf5 as a central value as the baseline, with cf2 and cf10 defining lower and upper uncertainty bounds, respectively.

Uncertainty quantification of surface area

Table 4.3: Aerosol number n_{ae} and surface area s_{ae} concentrations under APS calibration factors cf2, cf5, cf10, and resulting uncertainty bounds.

Exp	Type	$c_{n,\mathrm{cpc}}$ (cm^{-3})	$n_{ae,\mathrm{cf2}}$ (cm^{-3})	$n_{ae,\mathrm{cf5}}$ (cm^{-3})	$n_{ae,\mathrm{cf10}}$ (cm^{-3})	$s_{ae,\mathrm{cf2}}$ ($\mathrm{\mu m}^2\,\mathrm{cm}^{-3}$)	$s_{ae,\mathrm{cf5}}$ ($\mathrm{\mu m}^2\,\mathrm{cm}^{-3}$)	$s_{ae,\mathrm{cf10}}$ ($\mathrm{\mu m}^2\,\mathrm{cm}^{-3}$)	Δs_- ($\mathrm{\mu m}^2\,\mathrm{cm}^{-3}$)	Δs_+ ($\mathrm{\mu m}^2\,\mathrm{cm}^{-3}$)	Unc. − (%)	Unc. + (%)	Δs_{avg} ($\mathrm{\mu m}^2\,\mathrm{cm}^{-3}$)	$s_{ae} \pm \Delta s$ ($\mathrm{\mu m}^2\,\mathrm{cm}^{-3}$)
2	AD03	99.23	82.40	85.17	91.27	25.78	36.40	51.80	10.62	15.40	-29.18	42.30	13.00	36.40 ± 13.0
9	AD03	82.55	75.63	77.89	80.14	19.19	26.37	36.69	7.18	10.32	-27.22	39.12	8.70	26.37 ± 8.7
24	AD03	199.28	168.72	172.25	179.86	42.97	54.12	72.85	11.14	18.73	-20.59	34.62	14.90	54.12 ± 14.9
32	AD03	111.38	105.29	105.40	107.77	21.93	26.95	34.34	5.01	7.39	-18.61	27.44	6.20	26.95 ± 6.2
3	AD04	168.25	161.30	162.12	163.52	40.37	43.41	46.22	3.03	2.81	-6.99	6.48	2.90	43.41 ± 2.9
21	AD04	209.48	202.80	204.95	207.03	48.52	54.46	62.93	5.94	8.46	-10.90	15.54	7.20	54.46 ± 7.2
23	AD04	178.63	159.37	161.56	164.22	43.24	50.23	61.05	6.99	10.82	-13.92	21.53	8.90	50.23 ± 8.9
30	AD04	103.48	106.68	108.52	110.14	27.81	32.87	39.69	5.06	6.82	-15.39	20.74	5.90	32.87 ± 5.9
4	AD05	79.79	64.47	64.79	65.69	15.41	16.87	18.72	1.47	1.85	-8.69	10.94	1.70	16.87 ± 1.7
26	AD05	103.26	61.08	61.21	62.60	17.28	21.11	26.42	3.83	5.31	-18.12	25.17	4.60	21.11 ± 4.6
28	AD05	87.40	65.46	66.42	68.63	17.39	23.38	31.78	5.99	8.41	-25.61	35.96	7.20	23.38 ± 7.2
5	SD4	136.19	121.54	113.52	122.55	28.38	45.36	68.65	16.98	23.30	-37.44	51.36	20.10	45.36 ± 20.1
7	SD4	86.18	68.82	72.65	78.33	19.51	29.02	44.24	9.51	15.22	-32.78	52.45	12.40	29.02 ± 12.4
25	SD4	87.15	84.24	82.63	87.98	28.04	38.06	54.40	10.02	16.34	-26.32	42.93	13.20	38.06 ± 13.2
29	SD4	104.98	88.34	91.03	94.98	19.31	27.86	38.36	8.55	10.50	-30.70	37.67	9.50	27.86 ± 9.5

Table 4.3 presents a comprehensive comparison of aerosol number and surface area concentrations obtained from CPC and SMPS/APS under three calibration scenarios (cf2, cf5, cf10) for the INAD01 experiments. For each experiment, the CPC-derived total number concentration $c_{n,\mathrm{cpc}}$ is listed alongside the SMPS/APS-derived values n_{ae} and corresponding aerosol surface area concentrations s_{ae} under each calibration factor. The differences in surface area between cf5 and cf2/cf10 are used to quantify asymmetric uncertainty bounds (Δs_- and Δs_+), which are expressed in both absolute units and relative percentages. For example, in experiment INAD01_2 the surface area from cf5 is $36.4\,\mu\mathrm{m}^2\,\mathrm{cm}^{-3}$, with cf2 and cf10 yielding $25.78\,\mu\mathrm{m}^2\,\mathrm{cm}^{-3}$ and $51.8\,\mu\mathrm{m}^2\,\mathrm{cm}^{-3}$, corresponding to −29.2 % and +42.3 % deviations from the cf5 baseline. We thus report

$$36.4\,^{+42.3\%}_{-29.2\%}\,\mu\mathrm{m}^2\,\mathrm{cm}^{-3},$$

and propagate these asymmetric uncertainties through all surface-area-based quantities by standard methods. cf5 was adopted as the baseline calibration factor for further data analysis. This value reflects an optimal balance between under- and overestimation. To account for calibration-induced variability, the results using cf2 and cf10 are included as bounds for uncertainty. This approach offers a transparent and consistent method for incorporating calibration-related variability into the surface area estimation and ensures that active site densities reflect instrument-specific uncertainty constraints.

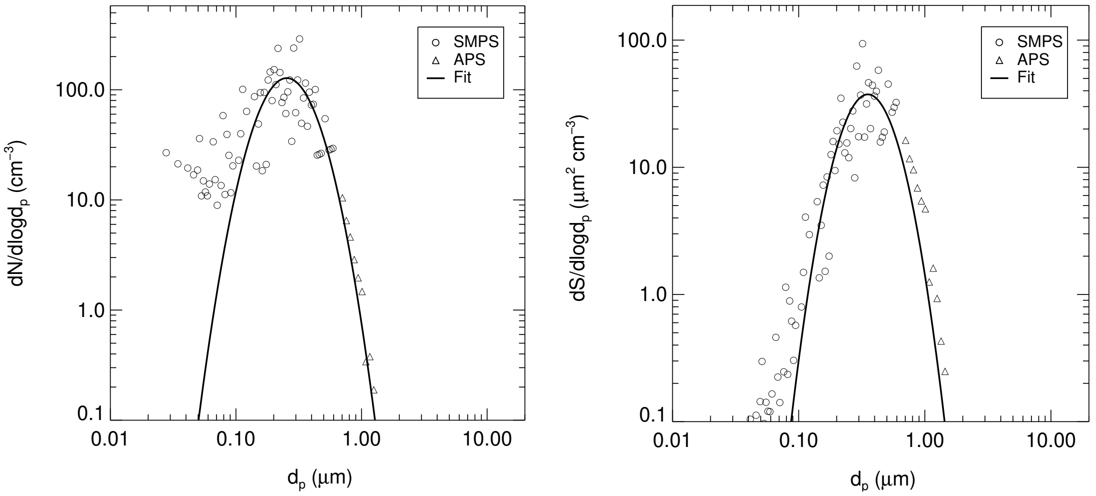

(a) Number distribution $f_N(\ln d_p)$. **(b)** Surface area distribution $f_S(\ln d_p)$.

Figure 4.5: Example lognormal fits to number concentration (left) and surface area concentration (right) distributions under calibration factor cf5. The black curve is the best-fit lognormal model, yielding total number n_{ae}, surface area s_{ae}, median diameter d_m, and geometric standard deviation σ_g.

Example lognormal fits Figure 4.5 presents an example of aerosol size distribution measured in the AIDA cloud chamber and the lognormal fitting of the number and surface area distributions under cf5. The left panel presents the number-concentration distribution $f_N(\ln d_p)$, while the right panel shows the surface-area-concentration distribution $f_S(\ln d_p)$. The solid black curve represents the best-fit lognormal distribution. From this fit, we extract the total aerosol number concentration n_{ae}, the total surface area concentration s_{ae}, the median diameter d_m, and the geometric standard deviation σ_g.

4.5 Results and discussion

4.5.1 Experiments in the mixed-phase cloud regime

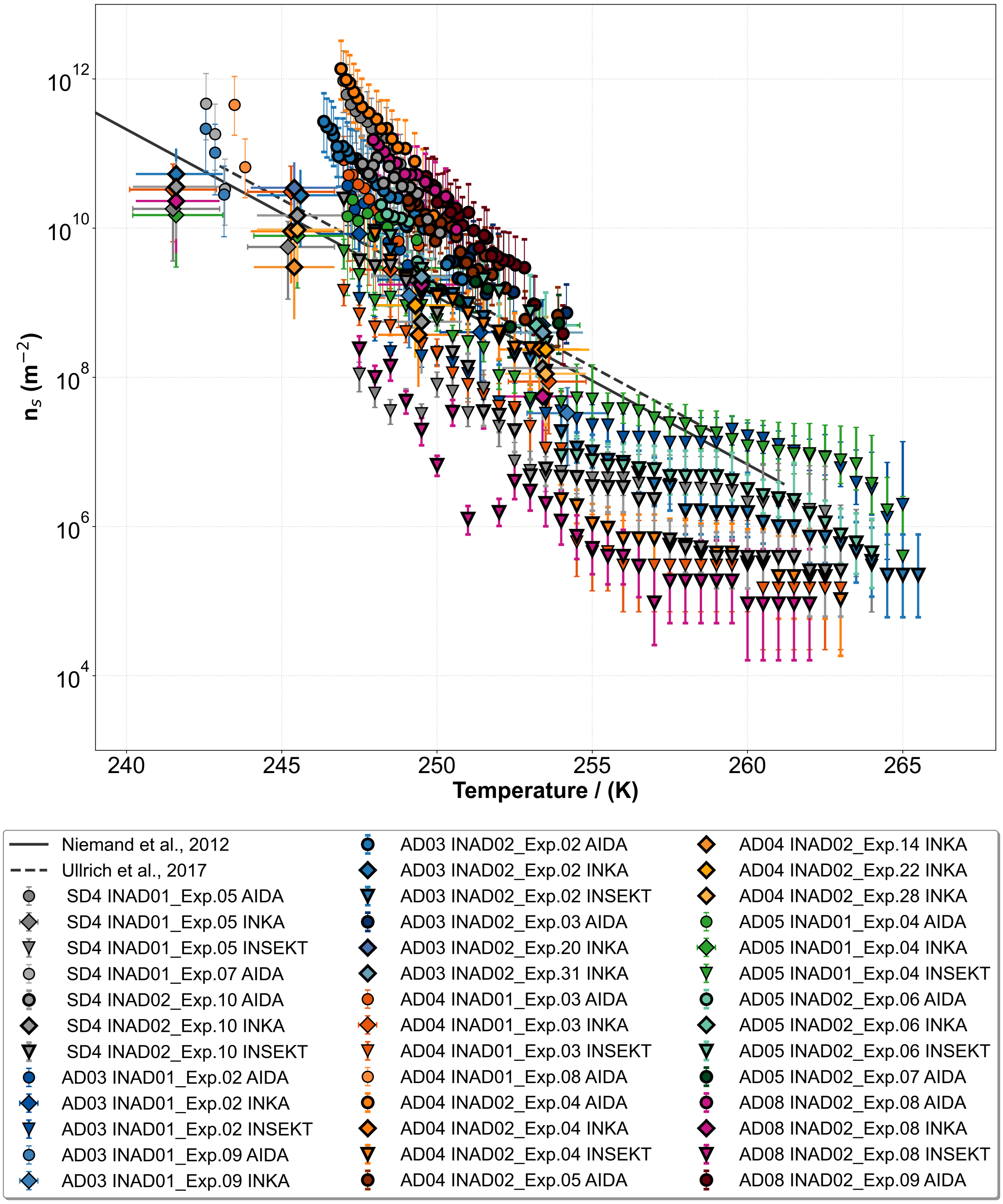

Figure 4.6: INAS densities as a function of temperature for all immersion freezing experiments on desert dust listed in 4.4 from AIDA, INKA and INSEKT results.

Table 4.4: Conditions for immersion freezing experiments with desert dust conducted during the INAD01 and INAD02 campaigns, including the aerosol sample used, the pre-expansion temperature inside AIDA (T_{start}), and the aerosol number concentration inside AIDA measured by the CPC ($n_{ae,0}$) alongside the corresponding aerosol surface-area concentration ($S_{ae,0}$) at the onset of ice nucleation used to calculate n_s under immersion-freezing conditions. Additionally, the experiment numbers for INKA ramps conducted at various temperatures, as well as the time periods for filter sampling for offline INSEKT analyses, are provided. All times are local time.

Campaign	Exp. no.	Date	Sess.	Aerosol	$n_{ae,0}$ (cm^{-3})	$S_{ae,0}$ ($\mu\text{m}^2\,\text{cm}^{-3}$)	T_{start} (K)	INKA ramps (°C)						Filter sampling		
								−20	−22	−24	−26	−28	−32	start	stop	Duration (min)
INAD02	3	2023 Mar 06	pm	AD03	198.42	54.08	256.91							–	–	–
INAD01	2	2022 Apr 20		AD03	98.07	36.40	252.58	8	10	9	11	12	13	11:55	12:55	60
INAD02	2	2023 Mar 06	am	AD03	169.37	46.63	253.13	1		2		3	4	09:47	11:17	90
INAD01	9	2022 Apr 27		AD03	81.96	26.37	246.58	46		47				–	–	–
INAD02	5	2023 Mar 07	pm	AD04	212.54	49.62	256.89							–	–	–
INAD01	3	2022 Apr 21		AD04	166.44	43.41	252.54	15		16		17	18	09:42	10:45	63
INAD02	4	2023 Mar 07	am	AD04	185.04	47.27	253.00	5		6		7		09:06	10:36	90
INAD01	8	2022 Apr 26	pm	AD04	115.62	23.95	247.17							–	–	–
INAD02	7	2023 Mar 08	pm	AD05	166.26	31.06	257.01							–	–	–
INAD01	4	2022 Apr 22		AD05	78.75	16.87	252.53	25	26	27	28	29	30	–	–	–
INAD02	6	2023 Mar 08	am	AD05	179.44	34.95	253.17	8	9	10	11			10:25	11:55	90
INAD02	9	2023 Mar 09	pm	AD08	207.97	55.64	257.20							–	–	–
INAD02	8	2023 Mar 09	am	AD08	180.59	49.43	253.20	12		13		14	15	09:12	10:50	98
INAD01	5	2022 Apr 25		SD4	130.24	45.36	252.51	35		36		37	38	10:07	11:07	60
INAD02	10	2023 Mar 10	am	SD4	77.52	20.18	253.00	16	17	18		19	20	10:09	13:09	120
INAD01	7	2022 Apr 26	am	SD4	83.37	29.02	246.56							–	–	–

Table 4.4 lists all AIDA experiments with the desert dust particles in the mixed-phase cloud regime performed during the INAD01 and INAD02 campaigns with their corresponding initial aerosol number and surface area concentration, temperature, and INAS density for the first analyzed time bin. Also indicated are the individual experiment numbers of the INKA ice nucleation measurements conducted at different temperatures, as well as the sampling periods for the filters that were analyzed off-line with INSEKT. Altogether, 16 immersion-freezing experiments were conducted during the two campaigns: four using AD03, four using AD04, three using AD05, two using AD08, and three using SD4.

As a first general overview of the measurement data, Figure 4.6 presents the temperature-dependent INAS densities derived from all immersion-freezing experiments with desert dust listed in Table 4.4.The supplementary INSEKT measurements with the $<$ 20-micron sieved AD03, AD04 and AD05 bulk samples are shown and briefly discussed in the appendix .1.1. In Figure 4.6, the marker color denotes the dust sample, and the shading intensity denotes different experiments conducted with the same dust sample. Circles represent AIDA results, where each experiment produces multiple data points corresponding to successive time bins. Diamonds represent INKA data (one point per temperature ramp), and inverted triangles represent INSEKT filter analyses (a continuous series of points over an extended temperature range for each sample). The measurement ranges differ by instrument: INSEKT measurements extend from 247 K to 265.5 K, AIDA expansions were typically started at approximately 257 K, 253 K, and 247 K, while INKA data cover the range from 253 K to 241 K in 2 K steps. Bold black outlines highlight data from the INAD02 campaign. As a general feature, there is a steady increase in the INAS densities from approximately $1.0 \times 10^5\,\mathrm{m}^{-2}$ at 265 K to $4.0 \times 10^{12}\,\mathrm{m}^{-2}$ at 242 K. At a given temperature, the sample-to-sample variability in INAS densities spans up to two orders of magnitude. The solid and dashed lines are reference parameterizations obtained from AIDA immersion-freezing measurements with other desert dust samples by Niemand et al. (2012) and Ullrich et al. (2017), respectively, providing benchmarks to which the present results are directly comparable. Before addressing this topic, it should be noted that, apart from inter-dust variability, the data also show an offset of up to two orders of magnitude between the measurements of the different INP instruments and techniques for the same dust type over the whole captured temperature range. Hereby, it tends that the freezing experiment INSEKT and the online method INKA show a better agreement among each other. These two instruments measured consistently lower n_s values than AIDA, which defined the upper end of the detected n_s range. An offset between different INP instruments and techniques may be related to their sensitivity for different freezing modes. INSEKT is limited to immersion freezing only, because the INP concentration is obtained from the freezing of liquid suspension volumes. Ice crystals that form at water subsaturated conditions are small in size at the beginning of their formation process and grow in size over time by deposition of water vapor on their surface. During an AIDA expansion, such ice crystals can be detected, because the way of the ice crystal to the detector can be a few minutes, which is enough time for them to grow to sizes that can be detected in the OPC. Also the cooling rate during an expansion of about $3\,\mathrm{K\,min}^{-1}$, at which AIDA is typically operated for expansions in the mixed-phase cloud regime, is slow enough that the ice crystals formed from the vapor phase have enough time to grow in size. Vogel (2022) further demonstrated that, in mixed-phase cloud studies, AIDA sometimes records a strong ice signal from deposition–nucleation occurring early in the experiment at ice-supersaturated, but water sub-saturated conditions. Consequently, even relatively weak signals from vapor-formed ice crystals can be detected in AIDA, which may result in a higher total ice concentration compared to other INP instruments. CFDCs are sensitive for detecting ice that formed below water saturation. However, depending on the size of the aerosol particles it can be challenging to distinguish ice crystals from larger aerosol particles or not yet fully evaporated liquid droplets. For the analysis of CFDC data, a fixed water supersaturation value is used, at which the ice concentration is then calculated.

From the overview plot in Figure 4.6, it seems that the new measurement data for the Asian dust particles follow a different slope compared to the Niemand et al. (2012) and Ullrich et al. (2017) parameterizations, with frequently lower INAS densities above 253 K and, at least for the AIDA data, higher values below 253 K. This will be quantified below by providing a new parameterization for the ice nucleation ability of the investigated Asian dust samples. For the further discussion, it is now first useful to separate the measurement data from Figure 4.6 into subplots for the individual dust samples. For that purpose, Figure 4.7 presents the temperature-dependent INAS densities obtained from immersion-freezing experiments for each desert dust sample: (a) AD03, (b) AD04, (c) AD05, (d) AD08, and (e) SD4, as listed in Table 4.4. In addition, panel (e) includes results from a previous AIDA measurement campaign, as summarized in Table 4.5, which are shown as light-blue circles for comparison. The symbol colors and types in Figure 4.7 are identical to those in Figure 4.6.

Table 4.5: Previous immersion freezing experiments with SD4 desert dust. $n_{\mathrm{ae},0}$ is the initial aerosol number concentration measured by the CPC, $s_{\mathrm{ae},0}$ is the initial aerosol surface area concentration, and T_{start} at the onset of ice nucleation. Published by (Niemand et al., 2012).

Campaign	**Exp No.**	**Date** (yyyy mmm dd)	**Aerosol**	$n_{\mathrm{ae},0}$ (cm^{-3})	$s_{\mathrm{ae},0}$ ($\mu\mathrm{m}^2\ \mathrm{cm}^{-3}$)		T_{start} (K)
ACI04	7	2010 Sept 30	SD4	173.88	212.46	—	253.9
ACI04	10	2010 Sept 30	SD4	121.79	140.54	—	249.7
ACI04	34	2010 Oct 06	SD4	138.21	142.70	181.34	252.0
ACI04	37	2010 Oct 07	SD4	114.84	86.19	237.97	258.7

From Figure 4.7, different trends for the temperature-dependent INAS densities can be retrieved for the various Asian dust samples. Only the AD03 and AD05 ice nucleation data exhibit a slope that is in good agreement with the two previous parameterizations by Niemand et al. (2012) and Ullrich et al. (2017). These two samples (and to some extent also SD4) exhibit a pronounced ”bulge”, i.e., comparatively high INAS densities in the 257 K to 265.5 K region, which might be due to biological material adsorb to the dust (Boose et al., 2016; Conen et al., 2011; O'Sullivan et al., 2016; Schnell, 1977). In contrast, AD04 and AD08 do not show the characteristic ”bulge”, thus having a much lower ice nucleation ability in that temperature range. The SD4 results in this study are comparable to those from previous investigations at similar temperatures, though the literature data tend to exhibit less scatter, which may be attributable to systematic or instrumental differences between studies.

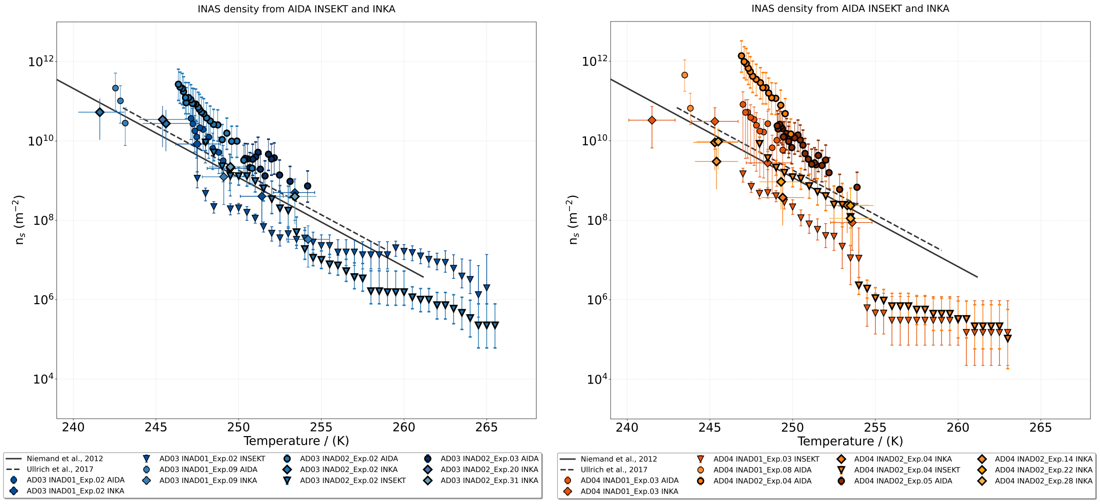

(a) AD03 **(b)** AD04

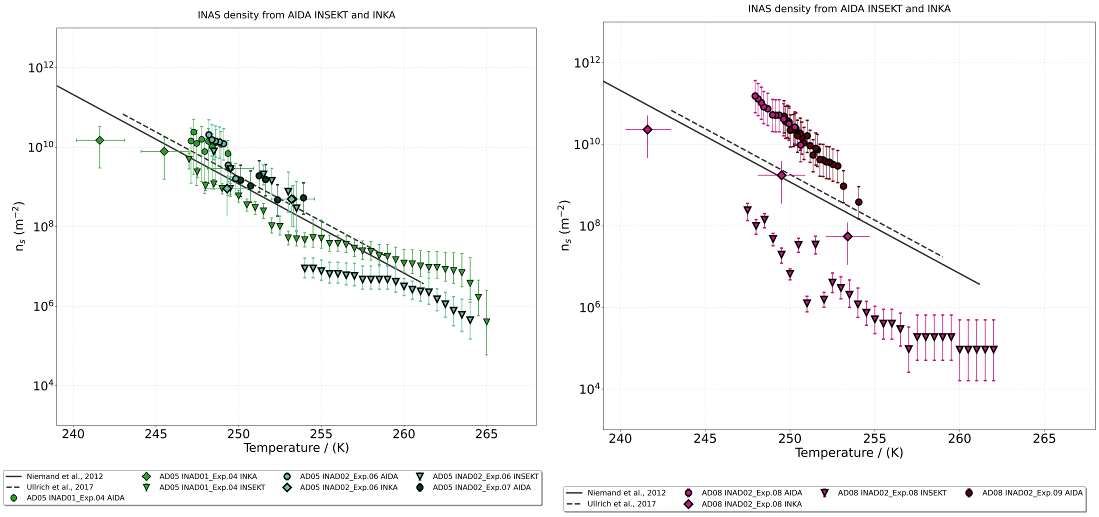

(c) AD05 **(d)** AD08

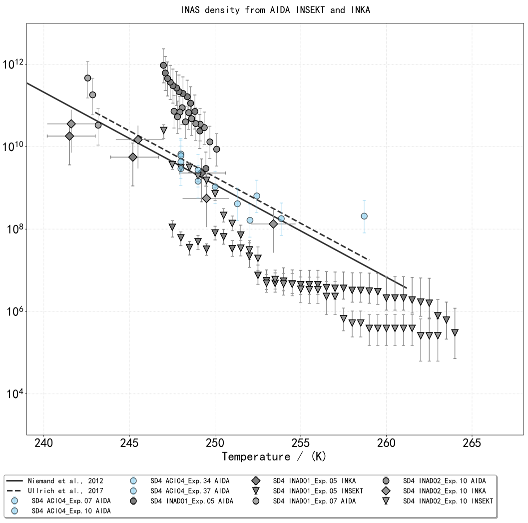

(e) SD4

Figure 4.7: INAS densities as a function of temperature for all immersion freezing experiments on each desert dust sample ((a) AD03, (b) AD04, (c) AD05, (d) AD08, (e) SD4), listed in Table 4.4 from AIDA, INKA and INSEKT results.

A new parameterization for the temperature-dependent ice nucleation ability of the Asian dust samples in the mixed-phase cloud regime

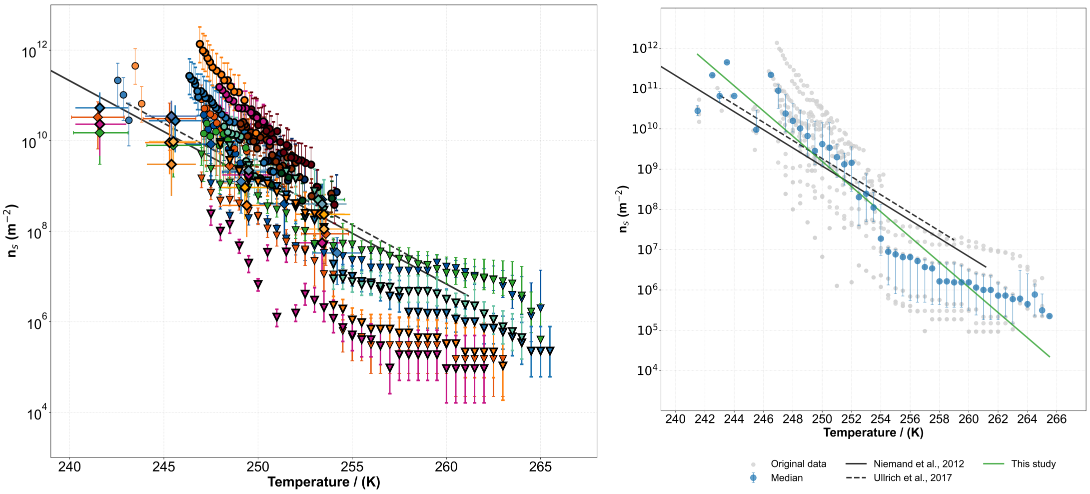

(a) INAS densities

(b) Parameterization

Figure 4.8: **(a)** INAS densities as a function of temperature for all immersion-freezing experiments with All the Asian desert dust samples in the campaigns INAD01 and INAD02, combining AIDA, INKA and INSEKT results(same data and legend as in Figure 4.6, with SD4 results omitted). **(b)** Parameterization derived from the same dataset shown in panel (a). Gray points represent the individual color-coded measurements from panel (a); blue circles denote the median values of n_s at each temperature, with vertical caps indicating the 25 % and 75 % percentiles. The two previous reference parameterizations are shown for comparison: the solid black line corresponds to Niemand et al. (2012), and the dashed black line corresponds to Ullrich et al. (2017).

Panel (a) of Figure 4.8 shows the same data as Figure 4.6, but with the ice nucleation data of SD4 omitted, i.e. only the Asian dust data. In panel (b), these individual AIDA, INKA, and INSEKT results for the various dust samples are all represented by gray circles, and the median values of ns at each temperature were computed and displayed as blue circles.

Following the methodology adopted for AIDA cloud chamber experiments in (Niemand et al., 2012) and (Ullrich et al., 2017), an Arrhenius-type model was fitted to the averaged Asian dust data across the entire temperature range (see Figure 4.8, green line). For direct comparison, all three parameterizations can be reformulated in the standard exponential form:

$$n_s(T) = \exp(\alpha - \beta T), \mathrm{m}^{-2} \tag{4.8}$$

where $n_s(T)$ denotes the ice-nucleating active site (INAS) in m^{-2}, T is the absolute temperature in K, and α and β are empirical fitting parameters. The values of α and β for the new Asian desert dust and the two previous parameterizations are compiled in Table 4.6. The temperature range column indicates the interval over which each parameterization was originally derived and validated.

The parameterization from Niemand et al. (2012) was derived from AIDA chamber experiments with Saharan and Asian dusts and serves as a widely used benchmark in atmospheric modeling studies. The Ullrich et al. (2017) employed a similar functional

Table 4.6: Summary of representative INAS parameterizations for desert dust immersion freezing. All follow the standard form $n_s(T) = \exp(\alpha - \beta T)$.

Parameterization	α	β	Temperature Range (K)
Niemand et al. (2012)	150.153	0.517	237.15 – 261.15
Ullrich et al. (2017)	150.577	0.517	243 – 259
This study (Asian desert dust)	233.1	0.845	241.5 – 265.5

form and slope, but extended the range of tested dust types and conditions, resulting in only minor changes to the parameter values and comparably conservative estimates of $n_s(T)$ across the relevant temperature range.

In contrast, the new parameterization in this study integrates immersion-freezing data obtained from three complementary instruments AIDA, INKA, and INSEKT, thereby expanding the temperature range towards higher temperatures, and focuses on different dust source regions is characterized by substantially higher values of α and β compared to Niemand et al. (2012) and Ullrich et al. (2017), reflecting a steeper negative dependence of $n_s(T)$ as function of the temperature. This is e.g. due to the fact that some of the included dust samples such as AD04 and AD08 (see Figure 4.7) proved to be rather ice-inactive at higher temperatures. Consequently, the averaged dataset yielded a different temperature dependence to that observed for the dust samples included in the two previous studies, pointing to differences in particle composition or surface properties. This steeper slope suggests a much stronger sensitivity to temperature, which has also been observed in other regional studies focused on Asian dust (Reicher et al., 2019). The differences in parameter values highlight the variability in ice nucleation efficiency among dust types, underlining the importance of using region-specific parameterizations for improved accuracy in climate models, particularly in dust-affected regions of East Asia.

4.5.2 Experiments in the cirrus regime

Table 4.7: Parameters for deposition-nucleation AIDA experiments with desert dust conducted during the INAD01 and INAD02 campaigns, including the aerosol sample used, the pre-expansion temperature inside AIDA (T_{start}), and the aerosol number concentration inside AIDA measured by the CPC ($n_{ae,0}$) alongside the corresponding aerosol surface-area concentration ($S_{ae,0}$) at the onset of ice nucleation used to calculate n_s under cirrus conditions. All times are local time (LT).

Campaign	Exp. no.	Date		Aerosol	$n_{ae,0}$ (cm^{-3})	T_{start} (K)	$S_{ae,0}$ ($\mathrm{\mu m^2\,cm^{-3}}$)
INAD01	20	2022 May 09	am	AD03	213.34	227.71	54.18 ± 19.02
INAD02	12	2023 Mar 20	am	AD03	173.09	227.59	58.35
INAD02	26	2023 Mar 28	am	AD03	206.12	222.64	49.42
INAD01	24	2022 May 10	pm	AD03	194.21	218.14	54.12 ± 14.9
INAD02	17	2023 Mar 22	am	AD03	199.49	212.57	50.30
INAD01	32	2022 May 13	pm	AD03	112.23	208.17	26.95 ± 6.2
INAD02	31	2023 Mar 30	am	AD03	93.46	208.10	29.53
INAD02	20	2023 Mar 23	am	AD03	93.50	197.55	23.29
INAD01	21	2022 May 09	pm	AD04	208.20	228.11	54.46 ± 7.2
INAD02	13	2023 Mar 20	pm	AD04	208.93	228.17	58.79
INAD02	27	2023 Mar 28	pm	AD04	209.97	223.07	41.75
INAD01	23	2022 May 10	am	AD04	178.30	217.28	50.23 ± 8.9
INAD02	14	2023 Mar 21	am	AD04	203.70	212.58	58.97
INAD01	30	2022 May 13	am	AD04	102.37	207.28	32.87 ± 5.9
INAD02	28	2023 Mar 29	am	AD04	104.30	207.92	27.66
INAD02	22	2023 Mar 24	am	AD04	85.29	197.55	25.57
INAD01	26	2022 May 11	pm	AD05	101.48	218.13	21.11 ± 4.6
INAD01	28	2022 May 12	am	AD05	84.77	207.53	23.38 ± 7.2
INAD01	25	2022 May 11	am	SD4	85.02	217.49	38.06 ± 13.2

Table 4.8: Parameters for deposition-nucleation INKA ramp experiments conducted during the INAD01 and INAD02 campaigns, including the aerosol sample used, the experiment numbers for INKA ramps conducted at various temperatures. All times are local time.

Campaign	Date	Aerosol	INKA ramps (K)						
			237	233	229	225	221	217	213
INAD02	2023 Mar 23	AD03	29	30			31		
INAD01	2022 May 10	AD04				90	91	92	
INAD02	2023 Mar 28	AD04							93
INAD02	2023 Mar 21	AD04	23						
INAD02	2023 Mar 29	AD04		42		43			
INAD02	2023 Mar 24	AD04		34			35		
INAD01	2022 May 11	AD05							100
INAD01	2022 May 12	AD05			98	99			97
INAD01	2022 May 11	SD4	95			96			

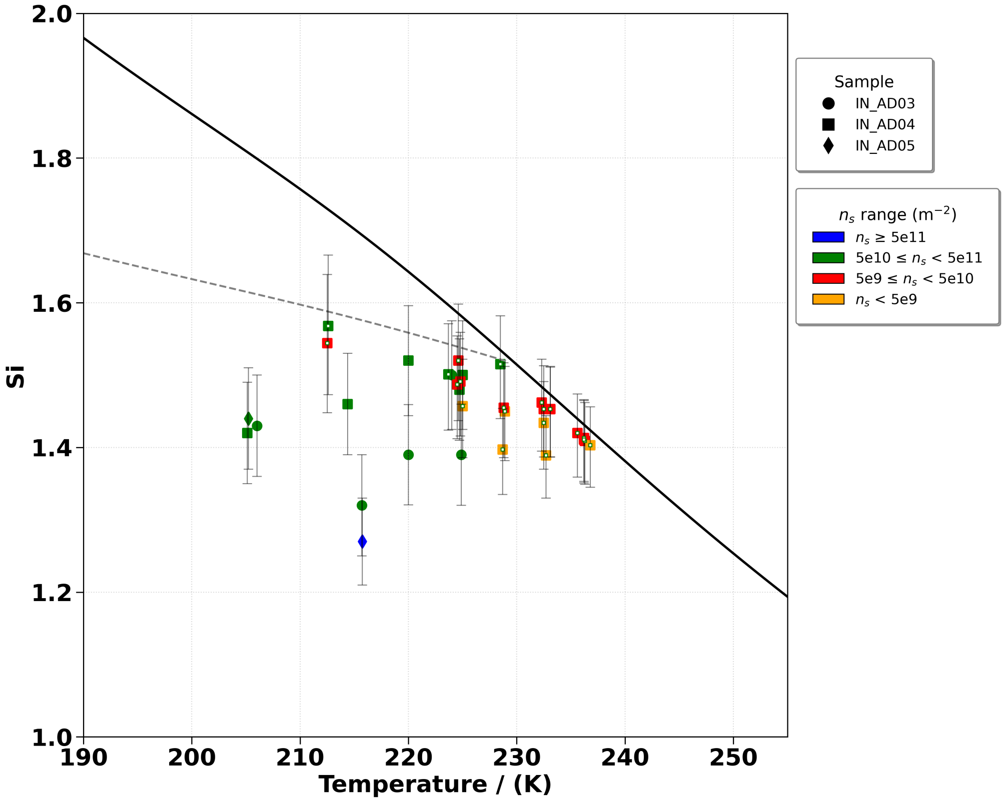

Figure 4.9: Color-coded INAS densities as a function of temperature and ice saturation ratio for all deposition nucleation experiments with the three Asian dust samples listed in Table 4.7 and Table 4.8. The black solid line indicates the ice saturation ratio S_i at water saturation and the gray dotted line represents the homogeneous freezing threshold for solution droplets ($\Delta a_w = 0.34$, (Koop et al., 2000)). The different symbols indicate the different dust types and the different colors the order of magnitude of the INAS density as follows: orange: $5 \cdot 10^8 \leq n_s < 5 \cdot 10^9\,\mathrm{m}^{-2}$, red: $5 \cdot 10^9 \leq n_s < 5 \cdot 10^{10}\,\mathrm{m}^{-2}$, green: $5 \cdot 10^{10} \leq n_s < 5 \cdot 10^{11}\,\mathrm{m}^{-2}$ and blue: $5 \cdot 10^{11} \leq n_s < 5 \cdot 10^{12}\,\mathrm{m}^{-2}$.

Figure 4.9 presents the color-coded INAS densities plotted in the ice saturation ratio–temperature space for all new deposition-mode ice nucleation experiments with the Asian desert dust samples (Table 4.7 and Table 4.8). Error bars reflect the uncertainty in the ice saturation ratio.

The new deposition nucleation measurements were performed down to temperatures of about 204 K, yielding INAS densities ranging from $5.21 \times 10^8\,\mathrm{m}^{-2}$ up to $1.75 \times 10^{12}\,\mathrm{m}^{-2}$. In this new dataset, all three Asian desert dust samples AD03, AD04, and AD05 exhibit highly consistent trends across the investigated temperature and ice saturation ratio ranges. The data points for these samples nearly overlap throughout the entire measurement window, indicating no significant differences in their ice nucleation activity. This close clustering suggests that the ice-nucleating efficiencies of these dust samples are very similar.

A new parameterization for the temperature- and humidity-dependent ice nucleation abilitiy of the Asian dust samples in the cirrus regime

The deposition-mode INAS density for the investigated aerosol particles was parameterized as a function of temperature and ice saturation ratio, following the approach of Ullrich et al. (2017) used for AIDA cloud-chamber dust-sample experiments. The empirical expression is

$$n_\mathrm{S}(T, S_i) = \exp\left\{\alpha\,(S_i - 1)^{1/4}\,\cos\left[\beta\,(T-\gamma)\right]^2\,\frac{\operatorname{arccot}[\kappa\,(T-\lambda)]}{\pi}\right\}, \qquad (4.9)$$

where

$$\operatorname{arccot}(x) = \frac{\pi}{2} - \arctan(x).$$

The five coefficients, α, β, γ, κ, and λ, define the position and curvature of the n_S isolines in the S_i–T plane. The best-fit parameters for both this study and previous work are listed in Table 4.9. Fitting was performed within the physical region $1.0 \leq S_i \leq S_\mathrm{homo}$ and over the valid temperature ranges indicated.

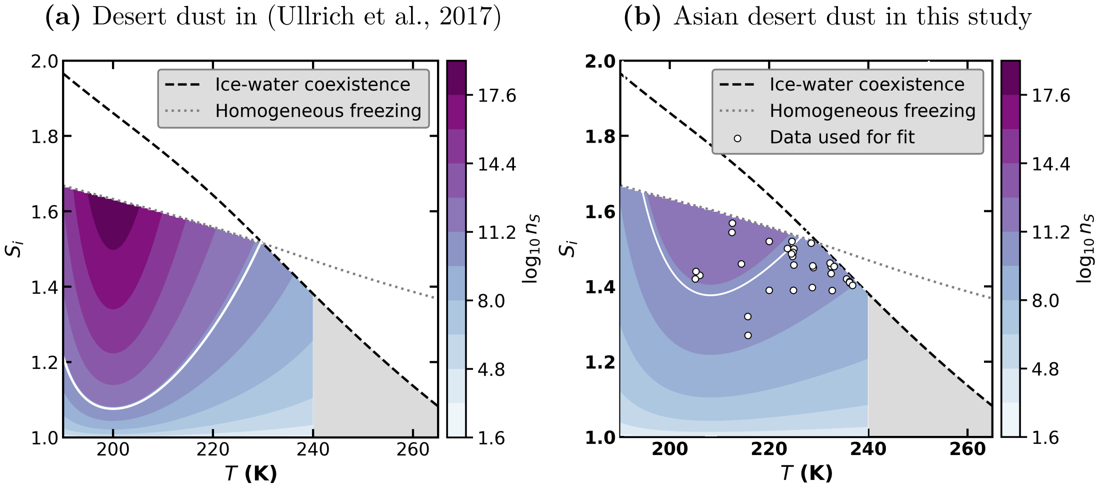
(a) Desert dust in (Ullrich et al., 2017)

(b) Asian desert dust in this study

Figure 4.10: Comparison of parameterizations for the temperature- and humidity-dependent ice nucleation active site (INAS) density, n_s, based on Eq. (4.9) and the fit parameters in Table 4.9. Panel (a) displays the scheme by Ullrich et al. (2017), which integrates dust samples from diverse regions worldwide, including the Sahara and Asia. Panel (b) shows the best-fit result developed in this study for Asian desert dust samples (AD03, AD04, and AD05). The root mean square error (RMSE) for $\log_{10} n_\mathrm{S}$ is 1.87 for desert dust (a) and 0.788 for Asian desert dust (b). The black dashed line indicates the ice saturation ratio at water saturation, the gray dotted line shows the homogeneous freezing threshold for solution droplets ($\Delta a_w = 0.34$; (Koop et al., 2000)), the white solid line marks the $n_\mathrm{S} = 10^{11}\,\mathrm{m}^{-2}$ isoline, and white points indicate the experimental data used for fitting.

As shown in Figure 4.10, compared to the Ullrich et al. (2017) parameterization, which integrates dust samples from multiple regions worldwide, including the Sahara and Asia, the scheme developed in this study is based specifically on samples collected from several locations in Asia. The resulting fit predicts systematically lower n_s values at a given temperature and ice saturation ratio, and exhibits a steeper temperature dependence, particularly near the homogeneous freezing threshold. These differences

Table 4.9: Best-fit parameters for Eq. (4.9) applied to desert dust; valid temperature ranges are indicated in brackets.

Aerosol	α	β	γ	κ	λ	Valid T (K)	Reference
Desert dust	285.692	0.017	256.692	0.080	200.745	[206, 240]	Ullrich et al., 2017
Asian desert dust	239.6	0.011	300	0.043	202.4	[204, 238]	This study

reflect the distinct ice nucleation characteristics of Asian dust relative to the global dataset and underscore the importance of region- and source-specific parameterizations.

Quantitatively, the new parameterization reduces the overall RMSE for $\log_{10} n_s$ to 0.788, demonstrating improved agreement with the Asian dust dataset compared to the Ullrich et al. (2017) fit (RMSE = 1.87). However, the empirical function fails to capture the single highest observed n_s value (blue point), likely due to the under-representation of such extreme cases in the dataset and the dominance of the least-squares optimization by the bulk of the data. This highlights both the strength and limitation of the current scheme: while it effectively reproduces the majority of observations, isolated outliers are not well represented. Such discrepancies are inherent in empirical fitting and further emphasize the need for parameterizations tailored to specific dust sources and regions.

4.6 Summary and discussion

Chapter 4 presents the laboratory investigation of ice nucleation by mineral dust from Asian deserts with a Saharan reference sample (SD4), quantifying efficiencies under immersion-freezing and deposition-nucleation modes over a temperature range of −8°C to −70°C. Using the AIDA cloud expansion chamber, the INKA continuous-flow diffusion chamber, and the INSEKT droplet-freezing array on samples AD03–AD08, this study extends immersion-freezing parameterizations for desert dust to higher temperatures compared to previous studies.

For the immersion freezing temperature range of mixes-phase clouds, some Asian dust samples showed a markedly steeper negative slope in INAS density, $n_s(T)$, with decreasing temperature compared to the previously published slope for several dust types from different desert areas (Table 4.6). At cirrus cloud temperatures, the Asian dust samples investigated in this thesis, showed lower n_s values in the deposition nucleation mode at a given temperature and ice saturation ratio (Figure 4.9). Both findings indicate unique mineralogical or surface-chemical properties for the dust samples from the different Asian desert regions that influendce their ice-nucleating activity. These differences imply that cloud microphysics models may need to use more regional desert dust sources and INAS parameterizations to correctly formulate and predict primary ice formation rates in mixed-phase and cirrus clouds.

The proposed parameterization reduces the root mean square error from 1.87 in previous formulations to 0.788, demonstrating substantially improved agreement with measured $n_s(T)$. Joint analysis of AIDA, INKA, and INSEKT data yields higher fitting parameters α and β and enhanced temperature sensitivity, thereby better capturing the aerosol free-energy barriers characteristic of Asian mineral dust.

Instrument intercomparisons across the immersion-freezing regime reveal systematic biases up to two orders of magnitude, arising from differential sensitivities to nucleation modes: INSEKT’ s immersion-freezing specificity versus AIDA’ s mixed-phase cloud regime deposition detection, and varied detection thresholds. Challenges in APS flow calibration and uncertainty quantification further complicate cross-instrument consistency. These findings underscore the imperative for coordinated inter-instrument campaigns, standardized measurement protocols, and transparent reporting of instrument-specific operational parameters.

By characterizing the distinct activation behavior and thermal stability of Asian desert dust, this work provides new physical insights and establishes a robust framework for interpreting ambient INP observations in Beijing and similar continental regions. Future research should integrate detailed chemical and morphological characterization to link nucleation pathways to specific dust components and implement region-specific parameterizations within atmospheric models to refine predictions of cloud microphysics and climate feedbacks in Asia.

Chapter 5

Long-term Field Observation of INPs

5.1 Introduction

Long-term observations of ice-nucleating particles face several significant challenges that hinder the comprehensive understanding of their role in the atmosphere. A critical flaw is the lack of global coverage and continuous longer-term data, with many regions of the Earth, including entire continents and oceans, underrepresented or completely absent from INP measurements(Burrows et al., 2022).Most existing data primarily covers short periods of days or weeks, and few studies have managed to make long-term observations that span multiple seasons or years, which are essential to evaluate year-to-year variations(Burrows et al., 2022). Furthermore, many instruments traditionally used for measuring INPs are not designed for continuous long-term monitoring due to their complex and labor-intensive operating principles(Burrows et al., 2022). This limitation poses a barrier to the systematic collection of data needed to understand the vertical distribution of INPs, particularly at altitudes where they are transported over long distances and where cloud formation occurs(Burrows et al., 2022; Hill et al., 2023). As a result, much of the current knowledge on INPs remains incomplete, with substantial gaps in understanding their climatology and life cycles(Burrows et al., 2022). Recent studies suggest that while some urban pollution aerosols may not efficiently act as INPs, the overall anthropogenic impact on the INP concentrations is still unclear(Burrows et al., 2022; Hill et al., 2023). The challenge is compounded by the fact that ideal monitoring techniques with short but densely spaced sampling have not been available in the past, and were limited by both technological and human resources (Burrows et al., 2022). Despite these hurdles, initiating long-term measurement campaigns with intensive short-term sampling can help establish baseline data on the INP concentration and variability(Burrows et al., 2022). The significance of obtaining continuous long-term observations cannot be overstated, as they are essential for gaining insights into ice nucleation activities at specific sites, contributing to develop more accurate climate models, and and to better predict the future climate scenarios(Hill et al., 2023; Möhler et al., 2021).

This section mainly focuses on a one-year comprehensive analysis of all three sites and an extended long-term observation at the suburban site to elucidate the seasonal cycle and compare various field measurement methods. Notably, the study covers the spring season, which is significantly influenced by long-range dust transport from Asian desert regions. The continuous measurements provided a new and unique data set on the diurnal and seasonal variation of the temperature-dependent INP concentration.

5.2 Overview of campaign

The following sections provide an overview of the INP measurements performed at the 3 sites (mountain, suburban, and city) in Beijing, China. Section 5.2 firstly describes the stations and their location (Section 5.2.1). The next section 5.2.2 provides an overview of the conducted campaigns to investigate the INP concentration in Beijing aera. Section 5.3 discusses the results.

5.2.1 Field locations

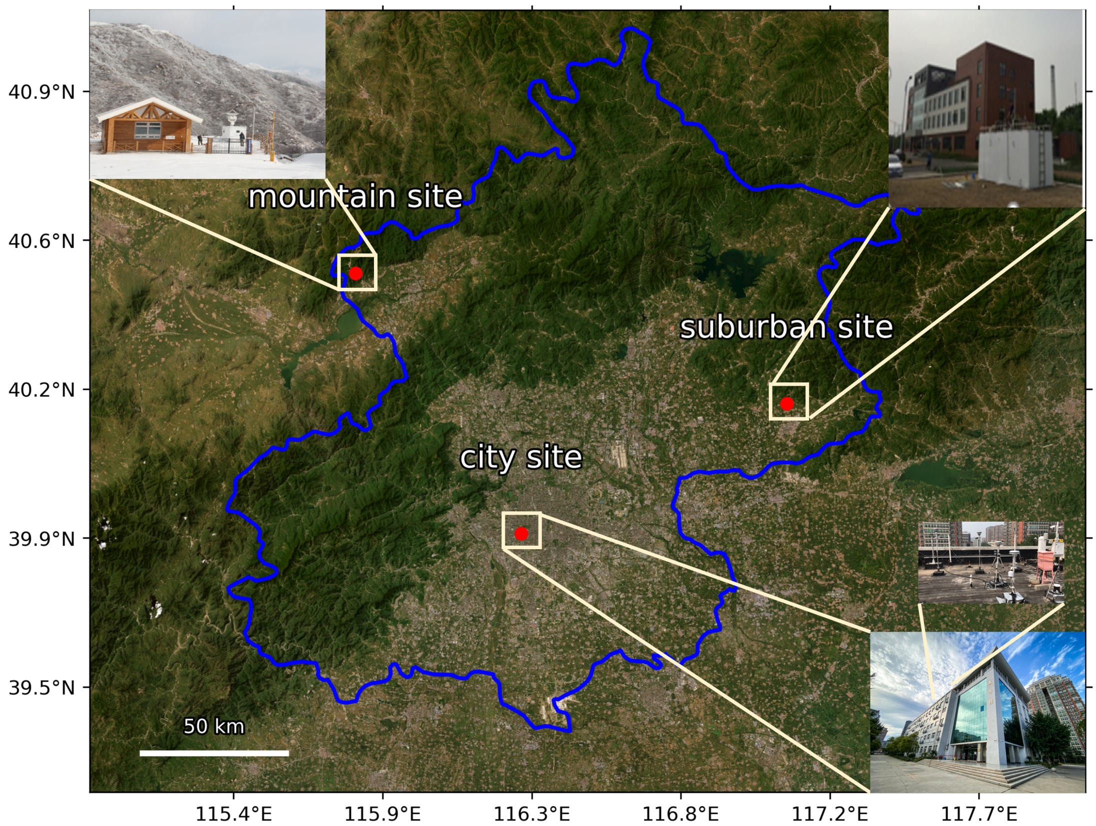

Figure 5.1: Area map showing the 3 field sites for filter sampling and INP measurement activities. The mountain site, suburban site and city site in Beijing area.

Measurements of INPs were conducted at three representative sites in Beijing (the capital of China), North China Plain, China (figure 5.1).

Yan Station (115.78°E, 40.52°N), the mountain site, is located in Yanqing District, Beijing, China, at an altitude of 1,344 m above sea level (Ding et al., 2019). Approximately 110 km northwest of central Beijing, it lies on the northern side of the Taihang Ridge. Operated by the Beijing Weather Modification Center, this Alpine Specialized Observation Station is equipped with instruments for measuring aerosols, clouds, and meteorological parameters. The site is located on the windward side of the urban area and is surrounded by forests and meadows, providing a clean background environment

(D. Liu et al., 2020). Moreover, the surrounding forest may emit biological aerosols during the spring, potentially serving as a significant source of INP (W. Hu et al., 2020).

The Beijing Cloud Laboratory and Observational Utilities Deployment Base (CLOUD Base, CB) (117.116667°E, 40.166667°N) site is located in Pinggu District, Beijing, China. This site is located on a plain remote from the urban center, surrounded by farmland and low-rise buildings, and can be affected by local sources and pollutants transported from the south during pollution episodes (Bi et al., 2019).Here it is named suburban site.

The city site is located in a typical urban area of Beijing at the west campus of Beijing University of Chemical Technology (BUCT) (116.310342°E, 39.948228°N) in Haidian District, Beijing, China. The observation site is adjacent to multiple busy roads, including a crossroad approximately 500 meters away at the intersection of Beijing's 3rd Ring Road and another trunk road to the northeast. This site is representative of an urban environment heavily influenced by human activities, particularly direct vehicular emissions. Measurement instruments were deployed on the fifth floor of the main teaching building (approximately 15 meters above ground level)(Lian et al., 2022; Y. Liu et al., 2020; J. Zhang et al., 2022).

5.2.2 Overview of INP measurement activities

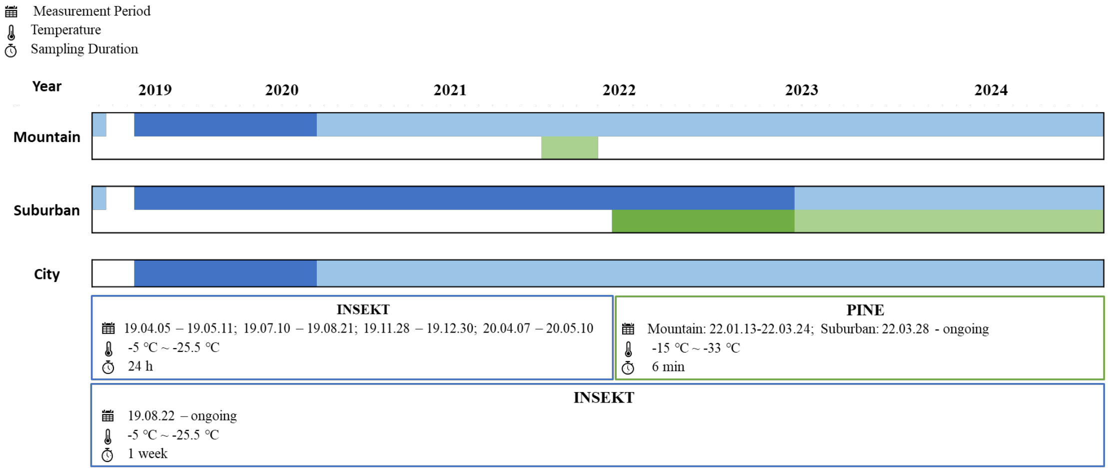

Figure 5.2: Overview of all measurement periods conducted at the three sites in the Beijing area to measure the INP concentration using the instruments INSEKT (blue frame) and PINE-05-03 (green frame)

In collaboration with the Beijing Weather Modification Center (BWMC), the KIT has established continuous INP observations at three sites in Beijing since April 2019, producing a five-year record of INP spectra acquired with INSEKT and since January 2022 also in parallel with PINE. The ice-nucleating particle (INP) measurements presented in this section represent the first application of the INSEKT freezing experiment to analyze aerosol filter samples from the Beijing region and constitute the first continuous record of INP concentrations spanning more than one year in China. Figure 5.2 provides an overview of the periods covered by the long-term measurement series and the intensive field campaigns. The INP measurement instruments included the freezing experiment INSEKT (indicated by blue frames; see Section 3.2) and the continuous-online chamber PINE (model 05-03, Bilfinger Nuclear & Energy Transition GmbH; indicated by green frames; see Section 3.4). A comparison of INSEKT measurements conducted at the mountain site and the suburban site during a spring campaign in 2019 has been published by Y. Hu et al. (2023), and these data are referenced in this chapter exclusively for the heat-treatment comparison during spring.

This section focuses on the INSEKT-based analysis of filter samples collected over one year (July 2019 to July 2020) at three sites in the Beijing region, as well as the long-term time series obtained at the suburban site, with the aim of investigating differences in INP concentrations across varying environmental backgrounds within a few hundred kilometers and comparing INSEKT results with those from PINE. Filter samples collected during spring in 2019 and 2020 were additionally analyzed in the laboratory following heat treatment to quantify the contribution of heat-labile INPs; these results are described in Section 3.2.

The INSEKT and PINE measurements presented in this chapter focus on the MPC (mixed-phase cloud) temperature regime. The observational campaign commenced in April 2019, with initial daily filter sampling at both the mountain and suburban sites during an intensive observation period in spring. Beginning in July 2019, the city site was included, and long-term time series measurements commenced, with filters collected daily during intensive periods for around one month each season and weekly during other periods; these observations continue at present (status: Summer 2025). PINE observations began in January 2022, initially at the mountain site during a two-month intensive campaign (analyzed in detail in Chapter 6), followed by the commencement of long-term measurements at the suburban site.

Within this thesis, INSEKT filter analysis is reported for samples collected through August 2020 at the mountain and city sites and through December 2022 at the suburban site.The PINE data analyzed in this chapter cover March 2022 to March 2023 at the suburban site, with additional mountain site data from January to March 2022 presented in Chapter 6. Collectively, these measurements provide a comprehensive long-term record of INP concentrations in the Beijing region spanning more than three years.

5.3 Results and discussion

The variation in the measured INP concentration is discussed as well as potential influencing factors. The comprehensive long-term data sets of both PINE and INSEKT measurements were used to validate existing parameterizations for the INP concentration and n_s. As an outcome from these measurements, a new INP parameterization for North Beijing Plain aerosol was developed.

5.3.1 INP temperature spectra

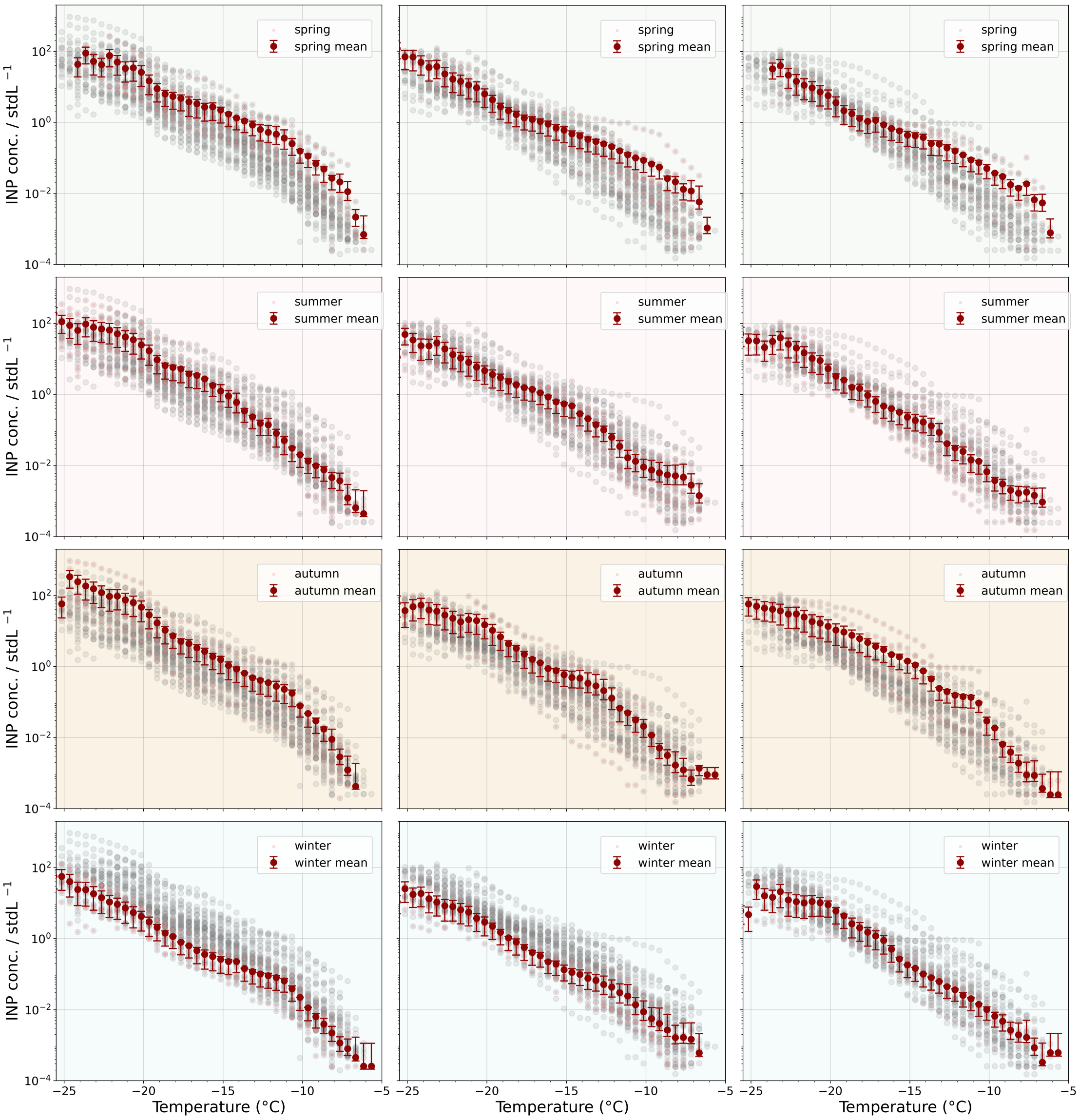

(a) mountain site **(b)** suburban site **(c)** city site

Figure 5.3: INP temperature spectra measured with INSEKT during the different seasons from July 2019 to July 2020 at the mountain site (left), the suburban site (upper middle), and the city site (right). Background colors denote seasons (spring: light green, summer: light pink, autumn: light yellow, winter: light blue). Gray points represent the single INP data from all seasons, light red points show the respective seasonal data, and dark red points with error bars indicate seasonal means with standard deviation.

Figure 5.3 presents the temperature spectra of the INP concentrations measured with INSEKT at the mountain, suburban, and city sites for each season from July 2019 to July 2020. To ensure comparability despite variable observation intervals (daily and weekly), most results in this chapter have been aggregated as weekly averages; only specific case studies and heat treatment analyses retain daily resolution (for daily/weekly comparison, see Appendix .2.1).

In each subplot, the background color denotes the season (spring: light green, summer: light pink, autumn: light yellow, winter: light blue). Gray points show the INP data from all seasons at each site, light red points highlight the seasonal data, and dark red points with error bars indicate the seasonal mean and its standard deviation.

Across all three sites, the INP concentrations systematically increase with decreasing temperature. The highest concentrations are consistently observed in spring, followed by autumn, with the lowest values in winter. In all sites, the spring spectra display a characteristic arch-shaped enhancement in the temperature range from about 255 to 268, K, while the autumn enhancement is weaker and less distinct.

While the general shape of the INP spectra is similar at all three sites, notable differences exist in absolute concentrations and the degree of seasonal variability. The mountain site exhibits the greatest variability within seasons, especially in spring and autumn, as evidenced by the broader spread of data points. In contrast, the winter spectra are more compact and uniform across all sites, while the suburban and city sites generally show less dispersion throughout the year.

Absolute INP concentrations and the amplitude of seasonal differences also vary between sites. These results demonstrate pronounced temporal and spatial variability in atmospheric INP concentrations across the Beijing region, underscoring the strong influence of seasonal cycles and the need to consider both local conditions and broader atmospheric processes for interpreting the observed INP patterns. Further analysis of the factors driving these variations will be presented in subsequent sections.

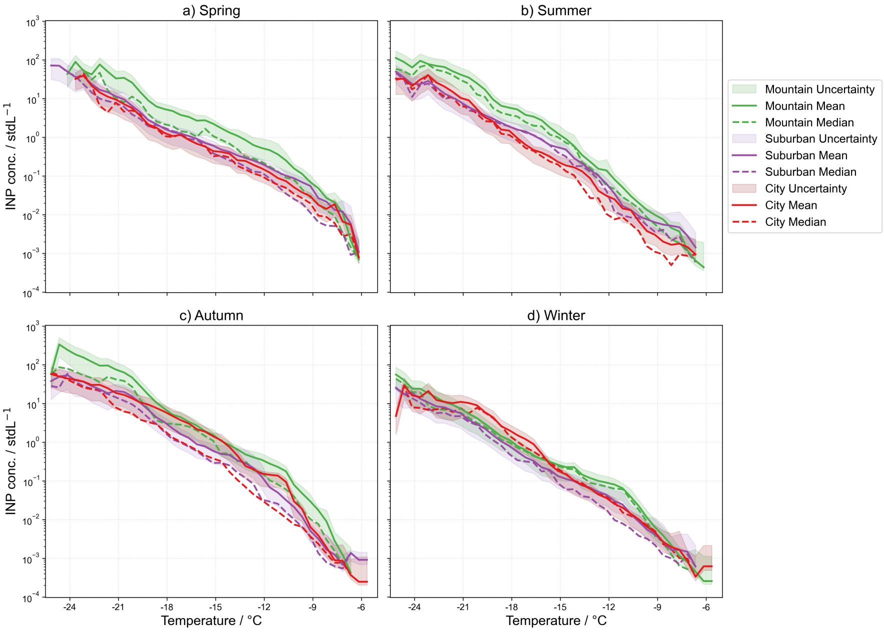

Figure 5.4: INP temperature spectra measured at the Beijing mountain site (green), suburban site (violet), and urban site (scarlet) across different seasons: (a) spring, (b) summer, (c) autumn, and (d) winter. The light-colored areas represent the range of all data, the dark-colored lines indicate the mean (solid) and median (dashed) values.

Figure 5.4 presents a direct comparison of INP temperature spectra for the mountain, suburban, and city sites in Beijing, shown separately for each season. In each subplot, shaded areas represent the spread (uncertainty) of INP concentrations, with solid and dashed lines indicating the mean and median, respectively, for each site (mountain: green, suburban: violet, city: red).

Across all seasons, the mountain site consistently shows the highest INP concentrations throughout the temperature spectrum, with differences particularly evident at lower temperatures. The suburban site generally shows lower concentrations in autumn compared to the other two sites, but exhibits relatively high INP levels at the upper end of the temperature range in summer. At the city site, a distinct peak in winter is observed at lower temperatures, in contrast to the flatter spectra at the mountain and suburban sites.

For all sites and seasons, INP concentrations increase systematically as temperature decreases. The mean values tend to exceed the medians, most notably at the mountain site and at lower temperatures, indicating the influence of episodic high-INP events. The suburban and city sites generally show smaller differences between mean and median, suggesting a more consistent INP background with fewer extreme enhancements.

The comparison between mean and median INP concentrations by site (see Appendix .2.2) demonstrates that, particularly at the mountain site, the mean values are systematically higher than the medians in most seasons, especially at lower temperatures. This reflects the influence of episodically high INP events that shift the mean to higher values, resulting in a positively skewed distribution. In contrast, the suburban and city sites exhibit smaller differences between mean and median, indicating a more constant background with fewer extreme events. These findings are consistent with the broader seasonal and spatial patterns presented in Figures 5.3, and further support the conclusion that the mountain site experiences greater variability and more frequent episodes with high INP concentrations.

These results highlight pronounced spatial and seasonal differences in the INP abundance in the Beijing region, as well as the importance of episodic events and site-specific factors influencing the INP variability.

5.3.2 Seasonal variation of the INP concentration

Figure 5.5 presents weekly time series of the INP concentrations measured at the mountain, suburban, and city sites in Beijing from July 2019 to July 2020 at three representative activation temperatures: $-20\,°C$, $-15\,°C$, and $-10\,°C$. The background colors indicate the different seasons, allowing for a direct comparison of temporal patterns observed at the different sites.

Across all three temperatures, a clear seasonal cycle is evident at each site, with the highest INP concentrations observed in spring and autumn, and the lowest in winter. This pattern is most pronounced at $-20\,°C$, where the amplitude of seasonal differences is greatest. Peaks in INP concentration during spring and autumn are apparent, while winter consistently exhibits the lowest values across all sites and temperatures. Summer concentrations are generally intermediate, but still lower than in spring and autumn.

Spatial differences between sites remain consistent: The mountain site exhibits the highest and most variable INP concentrations at all temperatures, particularly in spring and autumn, with frequent sharp peaks. The suburban and city sites display lower and more stable INP concentrations, with fewer pronounced peaks, and their seasonal cycles are less pronounced than at the mountain site. At $-10\,°C$, which represents the upper boundary for immersion freezing, overall concentrations are lower, and the magnitude of seasonal and spatial differences is less for all sites.

These results highlight robust seasonal and spatial variability in atmospheric INP

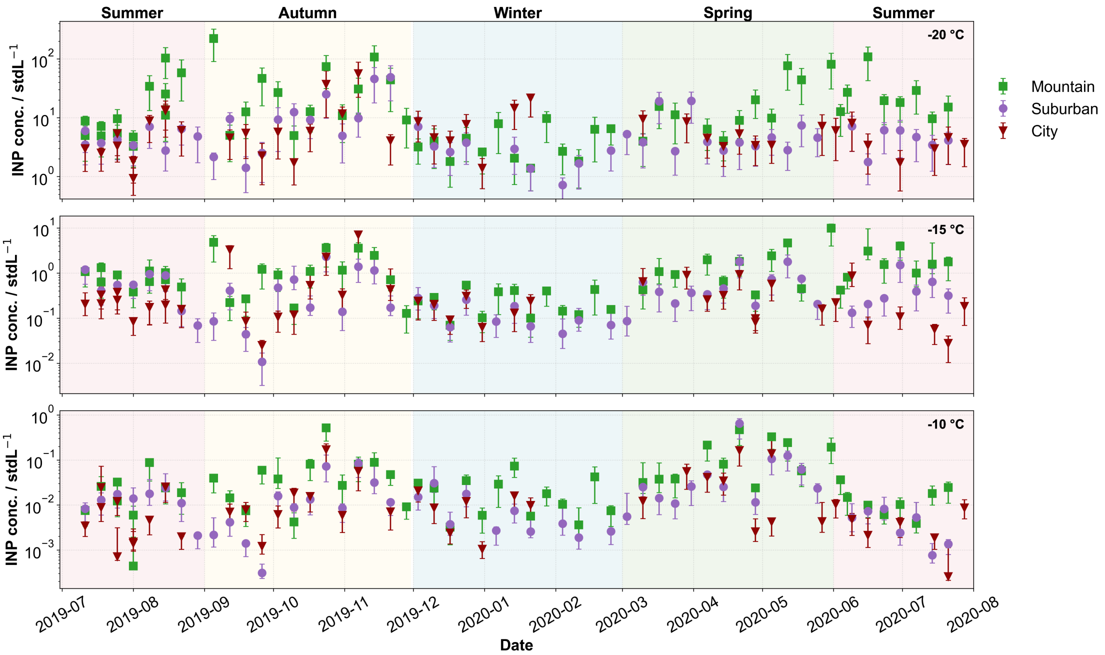

Figure 5.5: Time series of the INP concentration measured at the Beijing mountain site (green square), the suburban site (violet circles), and the city site(scarlet triangles) at the temperatures $-20\,°\mathrm{C}$, $-15\,°\mathrm{C}$, and $-10\,°\mathrm{C}$ from July 2019 to July 2020. The temporal resolution of the original data is primarily 1-day during the intensified observation periods and 7-day for regular intervals. In this figure, the time resolution has been standardized to a 7-day interval. The colored background indicates the seasons with spring in green, summer in pink, autumn in yellow, and winter in blue.

abundance in the greater Beijing region. The mountain site not only records the highest concentrations, but also the greatest temporal variability, underscoring its sensitivity to episodic source events or meteorological shifts. In contrast, the suburban and city sites are characterized by more homogeneous and stable INP backgrounds.

These multi-site, long-term observations underscore the importance of spatially and temporally resolved INP records for improving our understanding of primary ice nucleation in the region and for informing parameterizations in regional climate and weather models.

Figure 5.6 displays the time series of INP concentrations across the full temperature range (from $-25.5°$C to $-5°$C) at the mountain, suburban, and city sites in Beijing from July 2019 to July 2020, as measured with INSEKT. Each panel represents one site, with the color scale indicating the activation temperature and the vertical axis depicting the logarithmic INP concentration.

The seasonal cycles and site-to-site differences observed in previous figures are further illustrated here across the complete immersion freezing spectrum. All three sites exhibit distinct temporal patterns, characterized by recurring periods of enhanced INP concentrations, particularly during spring and autumn. The elevated concentrations typically correspond to lower temperatures (blue shades), especially at the mountain site, which consistently displays the highest INP concentrations throughout the year. These high concentration episodes are most prominent during spring, with the mountain site frequently reaching values above $1,\mathrm{L}^{-1}$ at temperatures below $-20°$C.

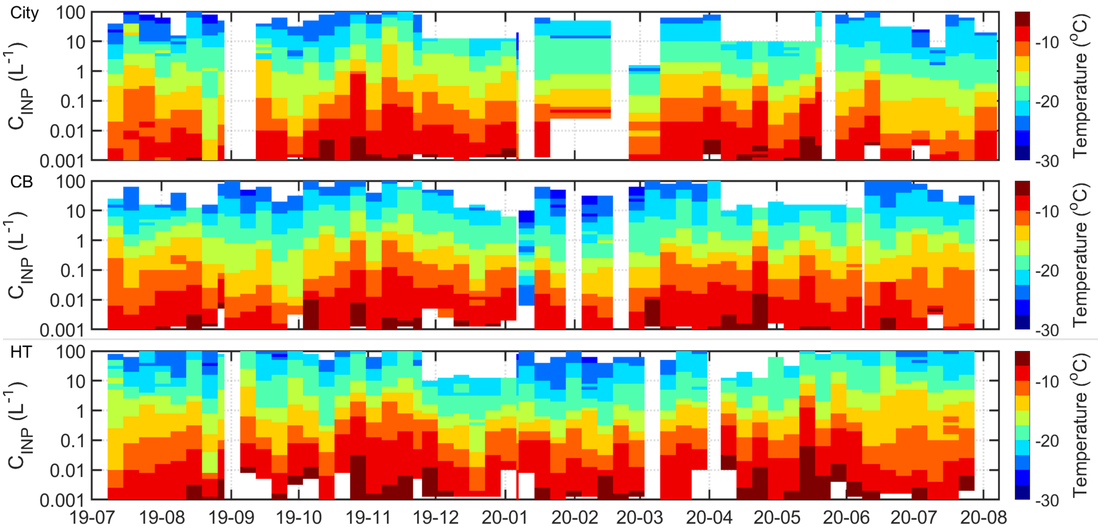

Figure 5.6: Time series of the INP concentration across the full activation temperature range at the mountain site (upper), suburban site (middle), and city site (bottom) from July 2019 to July 2020.The data were processed in the same way as for Figure 5.5.

The suburban site generally exhibits intermediate INP concentrations, with pronounced seasonal modulation and fewer extreme events compared to the mountain site. The city site is characterized by lower INP concentrations across the whole temperature spectrum, particularly at the lowest temperatures. Periods of reduced INP concentrations are most apparent in winter, where all sites record minimal concentrations, even at temperatures that are more favorable for ice nucleation during other seasons.

Short-term fluctuations and episodic increases in INP concentrations are evident at all sites, particularly at the mountain location, which is consistent with its greater exposure to regional and long-range dust transport events. In contrast, the suburban and city sites display more gradual transitions and smaller temporal variability. Across all sites, the warmest activation temperatures (red-yellow shades, > -15°C) are associated with the lowest INP concentrations, highlighting the temperature sensitivity of the INP population.

Overall, this figure provides a comprehensive overview of both the seasonal and temperature-dependent variability in INP concentrations at the three sites. The observed spatiotemporal patterns emphasize the dominant role of the mountain site in regional INP abundance, as well as the importance of cold-season and episodic events in shaping the INP climatology of the greater Beijing area. A more detailed analysis of the controlling factors and potential source attributions will be presented in subsequent sections.

Figure 5.7 presents the time series of INP concentration ratios between the mountain, suburban, and city sites at three representative activation temperatures (-20 °C, -15 °C, and -10 °C). Each panel allows for a direct comparison of spatial differences and their evolution across seasons.

A pronounced seasonal trend is apparent, particularly at -20 °C, where the INP concentration ratios between the mountain site and the other two sites (mountain/suburban, mountain/city) are frequently elevated, especially during spring and autumn. These periods are characterized by higher variability and more frequent high values, indicating intervals when the INP concentrations at the mountain site substantially exceed those

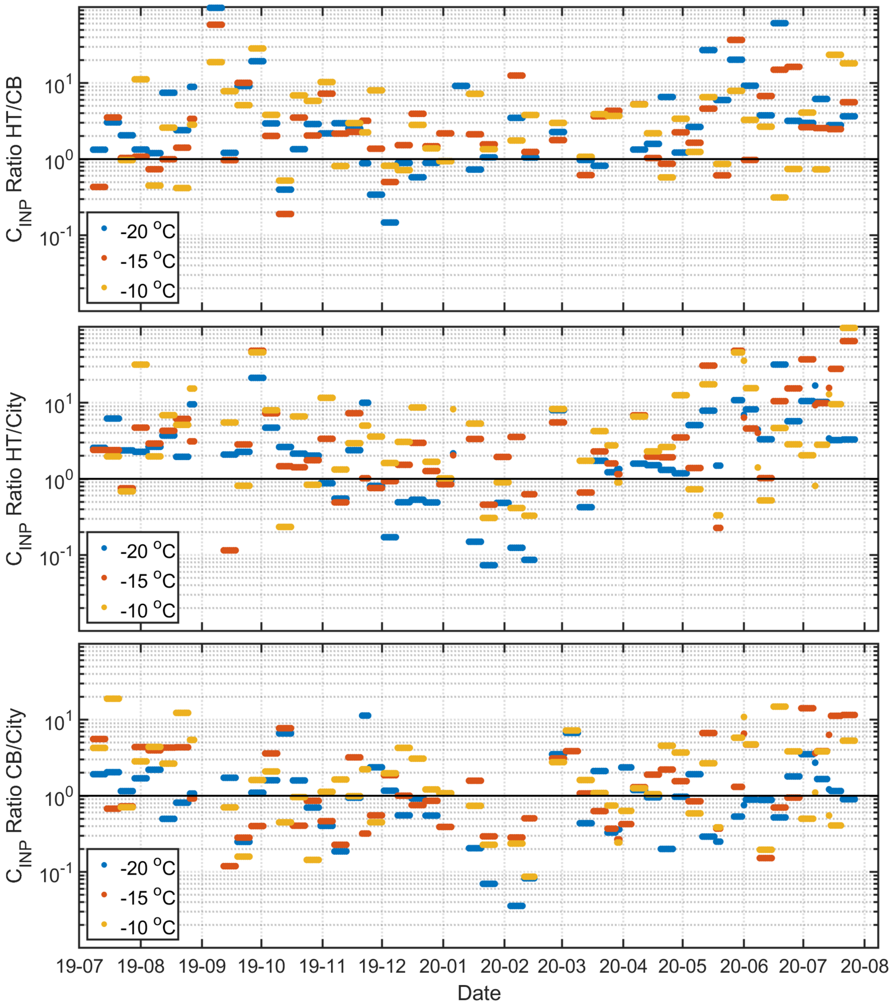

Figure 5.7: Time series of the weekly INP concentration ratio for mountain/suburban (upper), mountain/city (middle), and suburban/city (bottom) at the temperatures −20 °C, −15 °C, and −10 °C from July 2019 to July 2020.

at the suburban and city locations. This enhanced variability at low temperatures likely reflects the influence of episodic processes that are seasonally modulated.

In contrast, at −10 °C, the site-to-site ratios are generally lower and less variable, remaining closer to unity throughout the year. This pattern suggests a more homogeneous spatial distribution of INPs active at warmer temperatures, with reduced seasonal contrast. The ratios at −15 °C display intermediate characteristics, both in terms of amplitude and temporal variability.

Overall, the site-to-site differences are most pronounced at colder activation temperatures, where the mountain site often exhibits the highest INP concentrations relative to the suburban and city sites, particularly during spring and autumn. In the warmer regime, spatial contrasts diminish and the ratios become more stable, indicating a more uniform distribution of INP sources or a shift in dominant INP types. The observed trends are consistent across all three site pairs (mountain/suburban, mountain/city, suburban/city).

5.3.3 Relation to meteorology and aerosol properties

Figure 5.8 presents the time series of the INP concentrations across the full temperature spectrum, alongside the aerosol number concentrations for diameters exceeding 500 nm and 2000 nm, at the mountain, suburban, and city sites. Here, N_{500} denotes the number concentration of aerosol aerosols with aerodynamic diameters larger than 500 nm, while N_{2000} refers to aerosols with diameters exceeding 2000 nm (i.e., 2 μm); these parameters serve as proxies for the abundance of coarse and super-coarse aerosol fractions, respectively, which are considered potential carriers of INPs in the atmosphere.

Consistent with the patterns observed in earlier figures, INP concentrations (color shading) at all three sites display marked temporal variability and pronounced seasonal cycles. Higher INP concentrations generally occur in spring and autumn, while the lowest values are found in winter.

The relationship between INP concentrations at different temperature intervals and the abundance of large aerosol particles (N_{500} and N_{2000}) varies among the sites. At the mountain site, clear co-variations between peaks in INP concentrations and increases in large aerosol number concentrations are evident, especially during spring and autumn. This synchronization is most pronounced at lower temperatures, suggesting that coarse particles are more effective as INPs under colder conditions. In contrast, at the suburban and city sites, the correspondence between INP and coarse particle concentrations is less pronounced and more sporadic. These differences may reflect variations in aerosol source types, atmospheric processing, and meteorological influences among the sites. Across all sites, the association between INP and coarse particles is strongest at the lowest temperature interval (−20 °C), but becomes weaker at higher temperatures (−10 °C), indicating a shift in the dominant INP-active particle type with temperature.

This suggests that very large particles (>2 µm) may contribute to the INP populations during strong dust or biological events, but their overall influence is less consistent compared to the N_{500} size fraction.

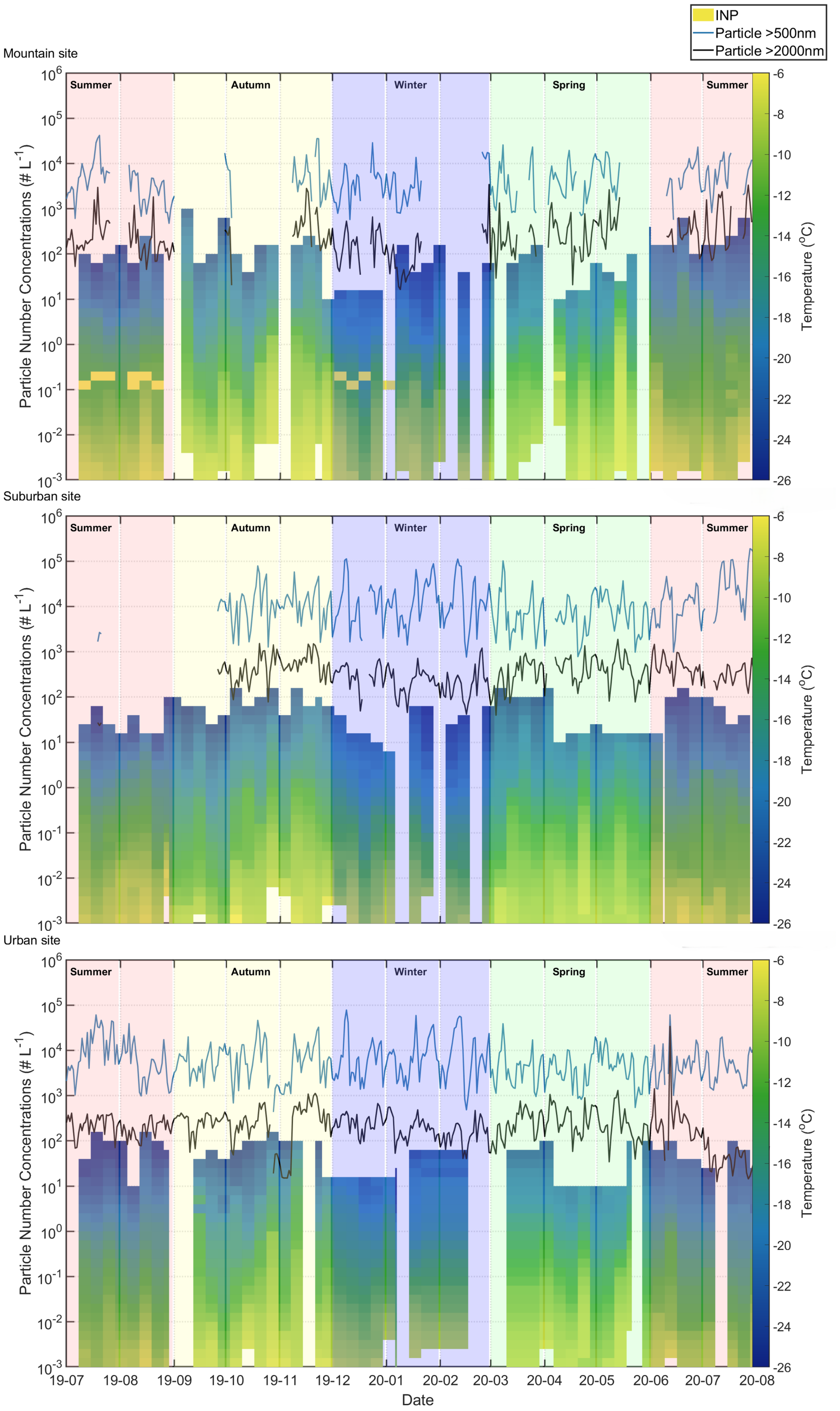

Figure 5.8: Time series of the INP concentration (color-coded by temperature), and the aerosol number concentrations for diameters >500 nm and >2000 nm (lines) at the mountain site (top), suburban site (middle), and city site (bottom) from July 2019 to July 2020.

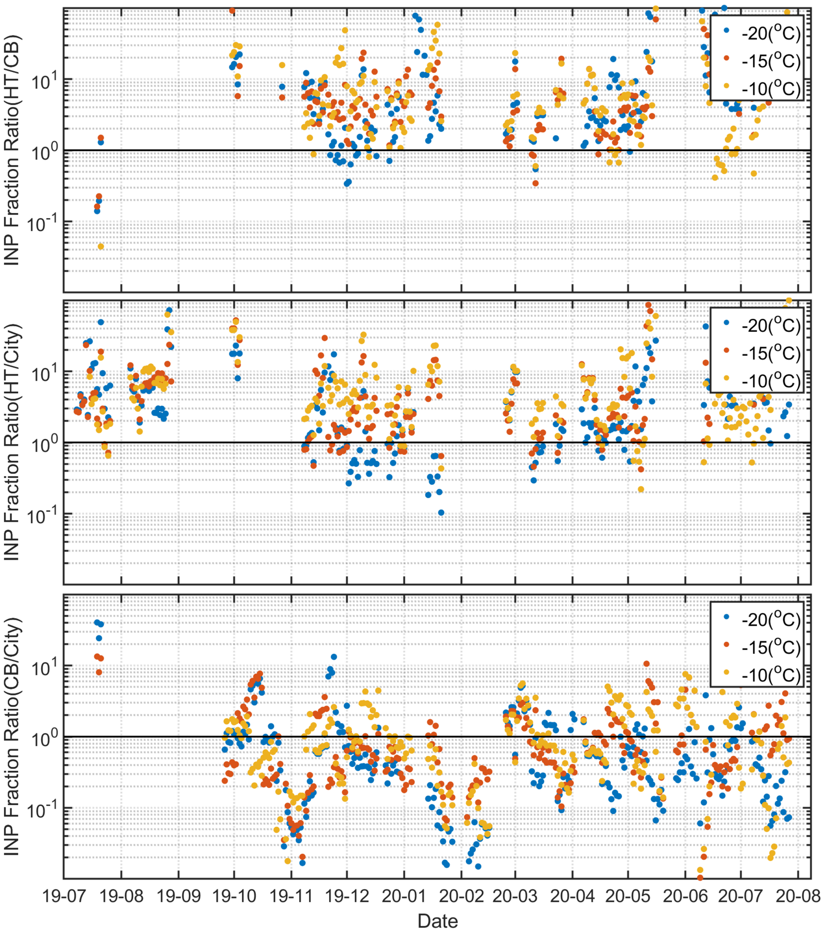

Figure 5.9: Time series of the INP activated fraction ratio mountain/suburban (upper), mountain/city (middle), and suburban/city (bottom) at the temperatures −10 °C, −15 °C and −20 °C from July 2019 to July 2020.

Figure 5.9 shows the time series of the INP activated fraction ratio, defined as the ratio of INP concentration to the number concentration of coarse aerosol particles (N_{500}), for all three site pairs (mountain/suburban, mountain/city, and suburban/city) at three representative temperatures (−10 °C, −15 °C and −20 °C). This metric serves as a proxy for the ice nucleation efficiency per coarse particle at each site.

Across all site pairs and temperatures, the active fraction ratio displays substantial temporal variability, frequently spanning more than an order of magnitude. The ratios for mountain/suburban and mountain/city are generally greater than unity, indicating that coarse particles at the mountain site are, on average, more ice-active than those at the suburban and city sites. This distinction is especially pronounced at lower temperatures (−20 °C) and during spring and autumn, when enhanced dust and primary aerosol input is typical at the mountain site.

For the suburban/city comparison, the active fraction ratio fluctuates around unity for most of the period, indicating broadly similar ice nucleation efficiencies per coarse particle at the two sites. However, there is a slight tendency for higher values at the city site, especially in winter, when the ratio consistently exceeds one. This suggests that during colder periods, coarse aerosol particles in the city may be somewhat more ice-active, possibly due to shifts in source composition or atmospheric processing that enhance INP activity in urban environments.

A pronounced seasonal dependence is evident: active fraction ratios are higher and more variable in spring and autumn, but lower and more stable in winter and summer. This pattern mirrors the seasonal cycles in absolute INP concentrations and supports the view that both source composition and atmospheric conditions modulate the ice-nucleating activity of the coarse aerosol fraction.

Overall, these results highlight the strong influence of site characteristics, source strength, and temperature on the ice-nucleating efficiency of coarse particles. The higher and more variable active fractions at the mountain site likely reflect episodic inputs from mineral dust and other efficient INP sources, while the lower and less variable fractions at the suburban and city sites point to more stable but less ice-active particle populations.

Figure 5.10 presents a multi-parameter time series for the mountain, suburban, and city sites. For each site, the four panels display, from top to bottom: (1) air temperature (°C), (2) relative humidity (%), (3) wind speed (point position) and direction (point color), and (4) INP concentrations across the measured temperature range. At all sites, the air temperature and relative humidity show clear seasonal cycles, with temperature maxima in summer and minima in winter. The relative humidity shows both seasonal and synoptic-scale variability, reflecting shifts in air mass characteristics and weather patterns.

A detailed comparison reveals that INP concentrations exhibit strong temporal co-variation with meteorological parameters, particularly at the mountain site. Here, episodes of high INP concentrations predominantly occur during colder periods and coincide with increased wind speeds, especially when winds originate from the northwest and west. These patterns are most pronounced in spring and autumn, seasons typically associated with regional dust transport and enhanced primary aerosol input. Notably, the strongest INP enhancements at the mountain site are observed in the lower activation temperature range (e.g., $-20\,°C$ to $-15\,°C$), supporting the conclusion that coarse mineral dust particles, advected under specific synoptic conditions, are a dominant source of INPs during these periods.

In contrast, the suburban and city sites exhibit lower INP concentrations and less distinct wind-driven variability. At these locations, seasonal cycles in INP abundance are present but less tightly linked to episodic wind events, suggesting a greater influence of local or regional background sources. The correspondence between INP peaks and meteorological conditions weakens at higher activation temperatures (e.g., $-10\,°C$), consistent with an increasing contribution from biogenic or secondary particles whose emission and activation are governed by different processes.

Across all sites, winter is characterized by persistently low INP concentrations, regardless of wind speed or direction, indicating a reduced contribution from both dust and biological sources during this season.

Overall, these results demonstrate that the temporal variability of INP concentrations is closely tied to the interplay of meteorological conditions, aerosol source strength, and activation temperature. The mountain site, in particular, highlights the importance of wind-driven dust events for episodic increases in INP abundance, while the suburban and city sites underscore the role of local emissions and background aerosol populations.

5.3.4 Biological contribution from heat treatment experiments

The mountain site offers a unique opportunity to investigate the seasonal and short-term variability of heat-sensitive INPs using the heat treatment protocol described in

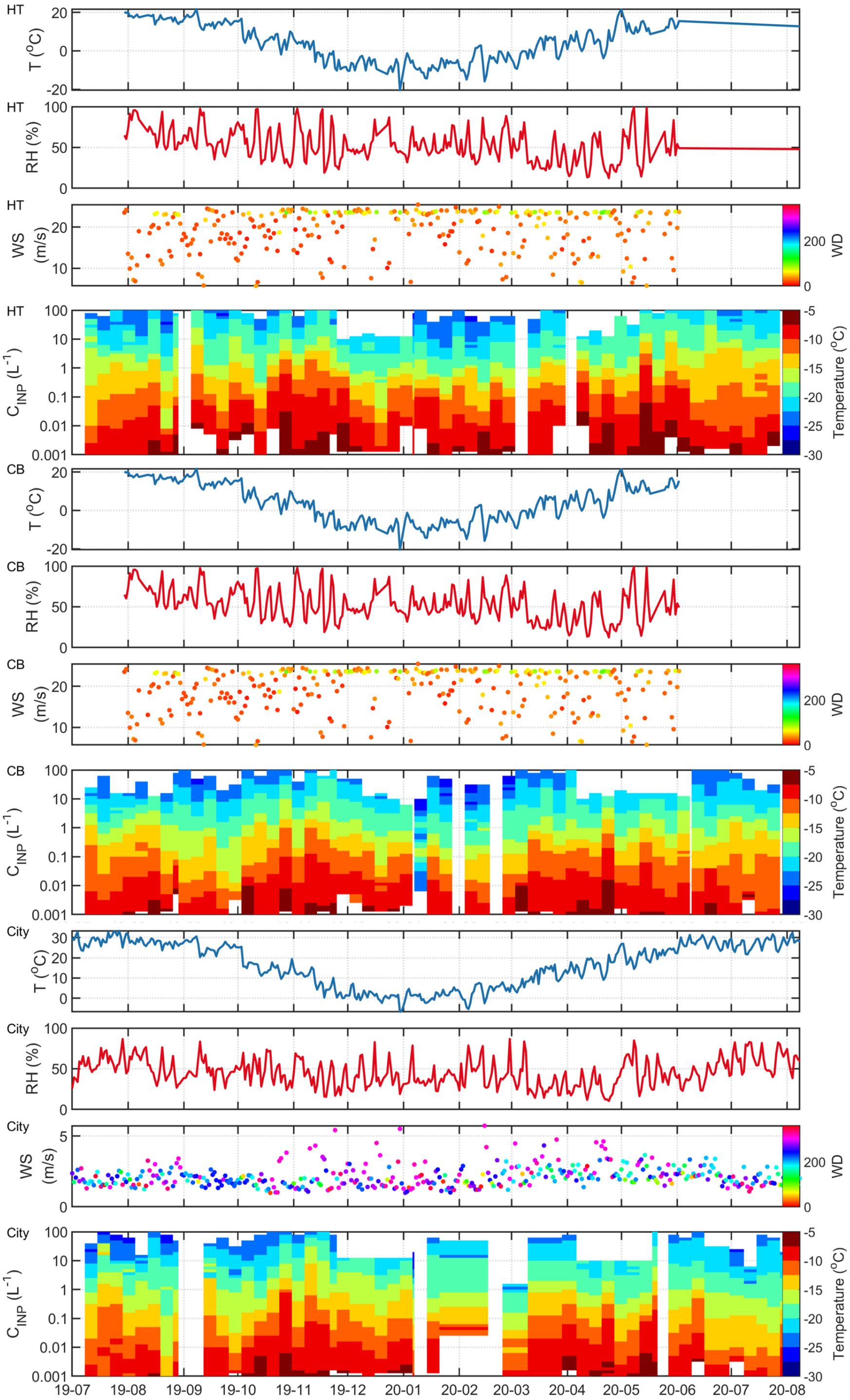

Figure 5.10: Time series of key meteorological parameters (air temperature, relative humidity, wind speed and direction) and the INP concentrations across the full temperature spectrum at the mountain (upper), suburban (middle), and city (bottom) sites from July 2019 to July 2020

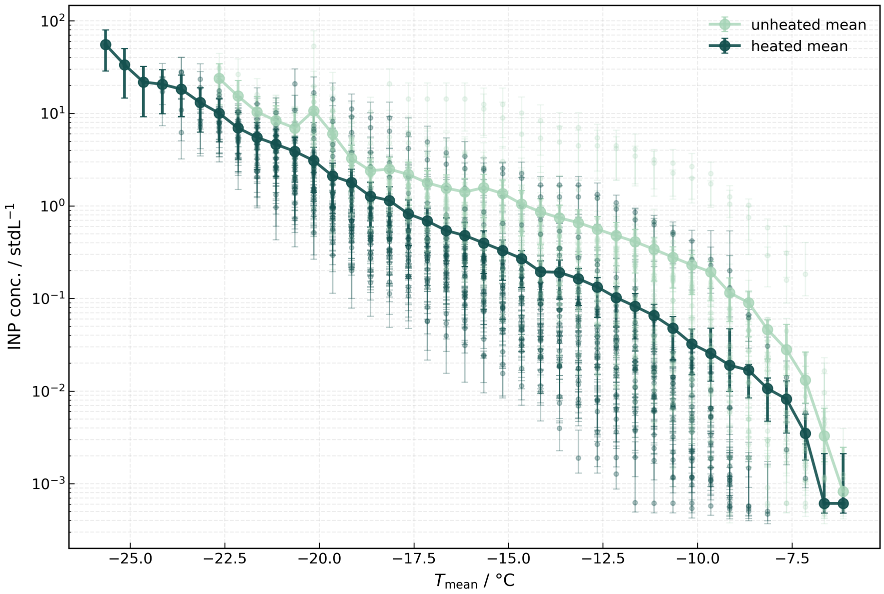

Figure 5.11: Comparison of INP temperature spectra with and without heating in spring 2020

Section 3.2. Figure5.11 summarizes the INP temperature spectra for both untreated and heated samples during the spring of 2020 with daily resolution respectively. The plot shows all daily filter results as well as their mean values. Across the full temperature spectrum, INP concentrations increase as temperature decreases, with the untreated samples (light green) exhibiting systematically higher values than the heat-treated samples (dark green). The difference between untreated and heated samples is most pronounced at higher activation temperatures, notably between −14 °C and −7 °C, while at lower temperatures (−20 °C), the gap becomes smaller. This pattern is consistent with the presence of heat-sensitive INPs that are active at higher temperatures and are likely of biological origin (Hill et al., 2016; O'Sullivan et al., 2018; T. W. Wilson et al., 2015).

Figure5.12 illustrate the time series of INP concentrations at three representative temperatures (−14 °C, −17 °C, and −20 °C) for both untreated and heated samples.The time series for individual activation temperatures further support this interpretation. For each day during the 2020 spring intensive filter sampling period, the INP concentration at −14 °C and −17 °C is strongly reduced after heat treatment, both in absolute value and in temporal variability, while at −20 °C the reduction is less pronounced. This indicates that a substantial fraction of INPs active at higher temperatures are denatured by heating, supporting their attribution to proteinaceous biological particles, whereas INPs active at lower temperatures are more heat-resistant and likely of mineral or non-proteinaceous origin.

Figure 5.13(c) shows the INP temperature spectra obtained from heated dust samples. It is evident that heating caused a pronounced reduction in INP concentrations at temperatures above −10,° C, decreasing concentrations by approximately one order of magnitude. In contrast, the impact of heating was negligible at temperatures below −15,° C. This temperature-dependent response is consistent with previous findings indicating that biological INPs typically exhibit reduced activity upon heating, whereas mineral dust particles largely retain their ice nucleation ability after heat treatment (Hill et al., 2016; Peckhaus et al., 2016). Therefore, the observed higher INP concentrations

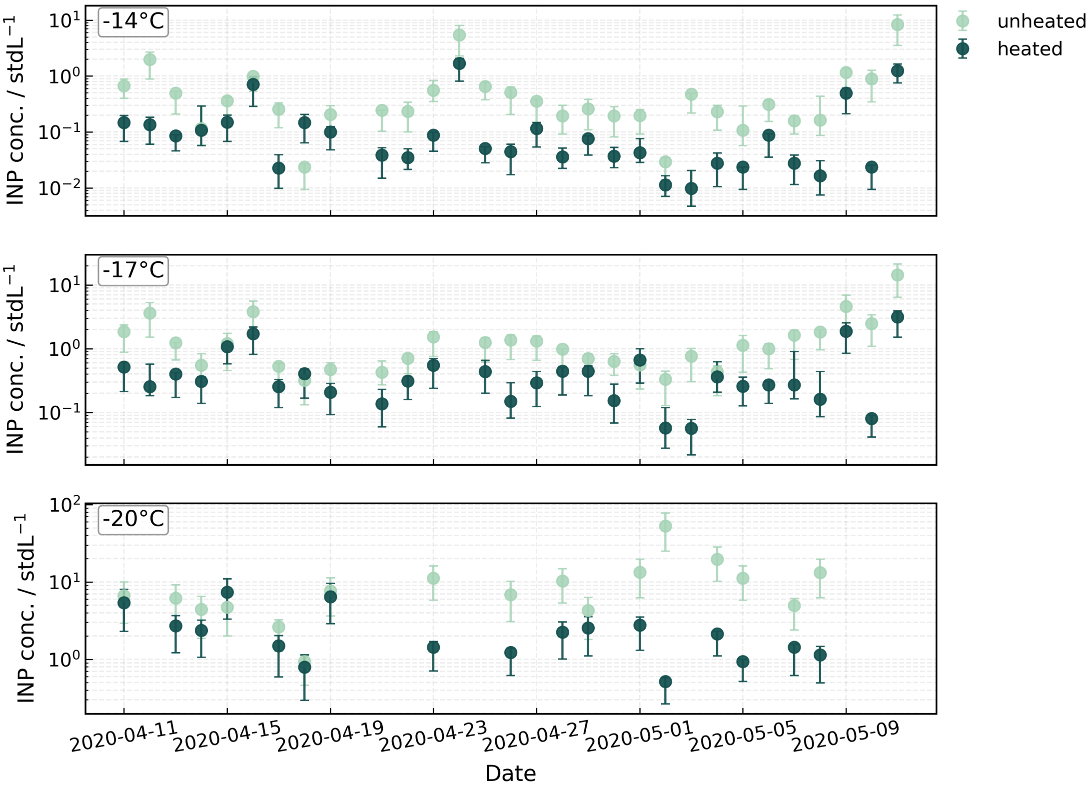

Figure 5.12: Comparison of INP concentration timeseries in spring 2020 at representative activation temperatures (−14 °C, −17 °C, and −20 °C) for untreated versus heat-treated samples

at warmer temperatures could be attributed to proteinaceous biological aerosol particles (PBAP) mixed with mineral dust during long-range atmospheric transport. This inference aligns with earlier studies (J. Chen et al., 2021; Tobo et al., 2020) highlighting the significant contribution of biological components to the ice-nucleation activity of transported Asian dust.

Figure 5.13(b) illustrates similar INP concentrations measured simultaneously at the mountain and suburban sites during the two dust events, underscoring the spatial homogeneity of INP concentrations during dust transport episodes. Nonetheless, notable differences in both INP temperature spectra and absolute concentrations were observed between the two dust events. Backward trajectory analysis (Fig. 5.13(a)) revealed distinct source regions for the dust events: the first dust plume originated from arid regions in northern Mongolia, while the second originated from the Gobi Desert situated between China and Mongolia. Correspondingly, the average INP concentration at $-20,^{\circ}$ C was significantly higher (approximately 450.9,L^{-1}) during the Gobi Desert dust event, nearly an order of magnitude greater than the INP concentrations observed during the earlier dust event at the same site.

Together, these results highlight the episodic occurrence and substantial variability of heat-sensitive (likely biological) INPs during spring at the mountain site, as well as the importance of considering both temperature and thermal stability when interpreting INP measurements. The application of heat treatment thus provides a robust tool to distinguish between different INP types and their seasonal behavior in ambient aerosol

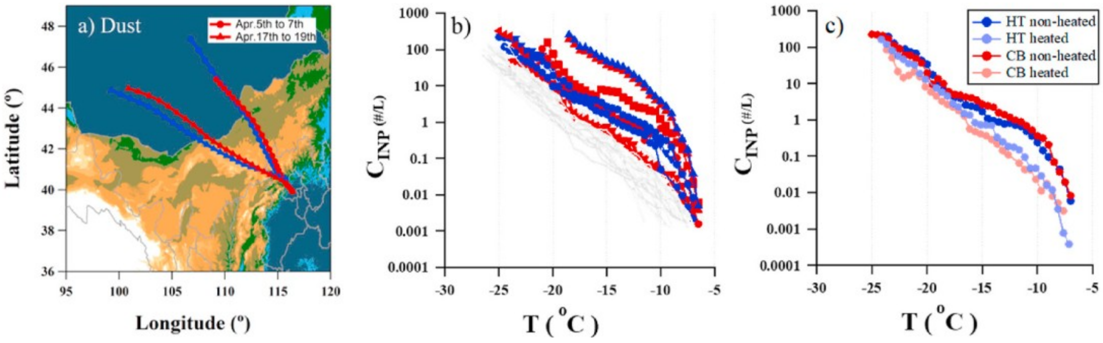

Figure 5.13: a) Backward trajectories for two dust events. b) INP temperature spectra during the dust events. Blue lines correspond to the HT mountain site, red lines to the CB suburb site, and Grey lines to non-dust days. c) The comparison of INP temperature spectra between heated (light colors) and non-heated (dark colors) dust samples. (This figure is adapted from (Y. Hu et al., 2023)

populations.

5.3.5 Long-term INP climatology and instrument intercomparison

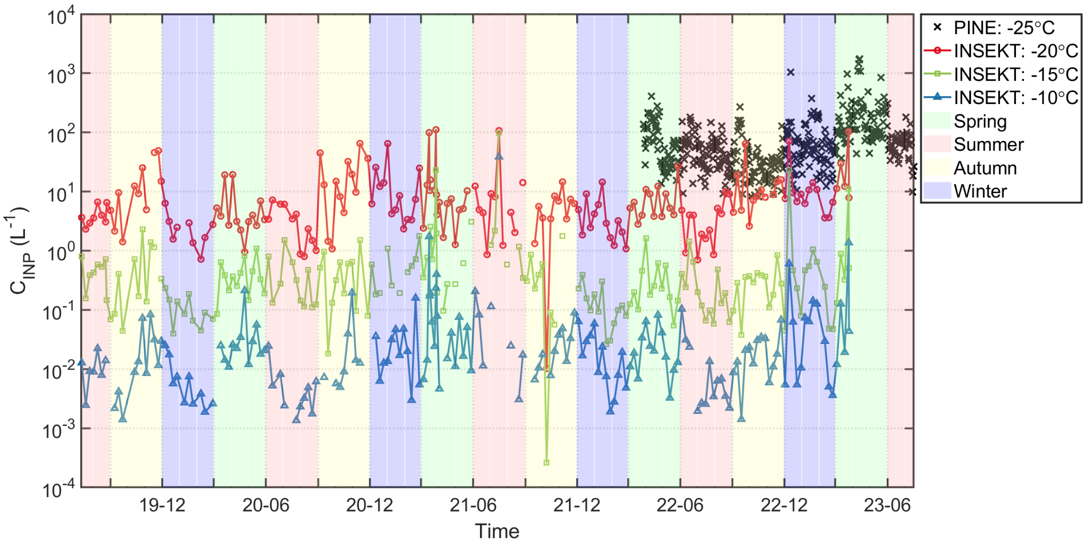

Figure 5.14: Time series comparison of INP concentrations measured with INSEKT at three representative activation temperatures (−20 °C, −15 °C, and −10 °C) at the suburban site from July 2019 to March 2023, shown together with hourly averaged PINE measurements at −25 °C from March 2022 to July 2023.

To comprehensively characterize the temporal evolution and the seasonal variability of INP concentrations, as well as to assess consistency between measurement techniques, this section presents and compares long-term INSEKT and PINE observations at the suburban site from July 2019 to March 2023.

Figure 5.14 presents the weekly averaged time series of INP concentrations at the suburban site, as measured by INSEKT at three activation temperatures (−20 °C,

−15 °C, and −10 °C), together with hourly PINE measurements at −25 °C from March 2022 to March 2023. Seasonal periods are indicated by the colored background.

The data reveal robust and recurring seasonal patterns at the suburban site. INP concentrations are typically highest during spring and autumn, reach their lowest values in winter, and remain intermediate or more variable in summer. This seasonal cycle is evident across all activation temperatures, though its magnitude and variability depend on the temperature interval considered. At colder activation temperatures (e.g., PINE at −25 °C and INSEKT at −20 °C), INP concentrations are generally higher and display greater temporal fluctuations, consistent with an enhanced contribution from mineral dust and other efficient INP sources. At warmer activation temperatures (e.g., −10 °C), concentrations are lower overall and seasonal contrasts are reduced, reflecting the limited presence of highly active INPs at these temperatures.

Periods of anomalously high or low INP concentrations occasionally occur, but do not disrupt the overall seasonal pattern. In addition, a comparison of the PINE and INSEKT time series for overlapping periods and comparable temperature ranges (−25 °C and −20 °C) indicates similar seasonal behavior and overall trends.

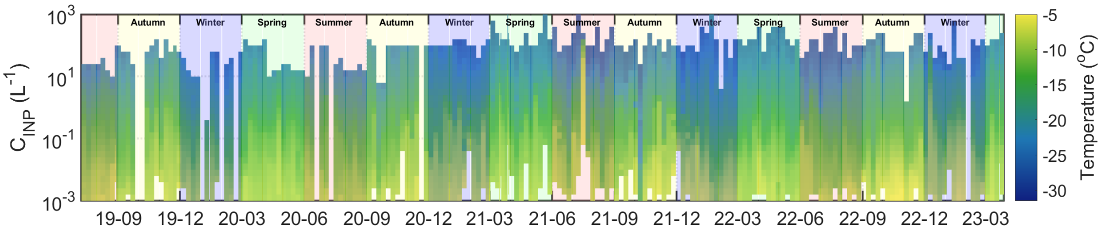

Figure 5.15: Time series of INP concentrations at the suburban site covering the full activation temperature from July 2019 to March 2023. Color shading indicates the activation temperature. This figure provides a comprehensive view of temporal variations and seasonality across the entire observed temperature spectrum.

Figure 5.15 presents the complete INP concentration spectrum measured by INSEKT at the suburban site from July 2019 to March 2023. Each column corresponds to a specific observation week, while the color shading indicates the activation temperature. The figure vividly illustrates the strong seasonal modulation of INP abundance across the temperature range. Spring and autumn are characterized by enhanced concentrations across nearly all temperature intervals, reflecting episodic events such as dust outbreaks or biological emissions. Winter is marked by persistently low INP levels, whereas summer exhibits more variable behavior. The continuous coverage across the full temperature range allows detailed assessment of both seasonal cycles and the evolution of temperature-dependent INP populations.

Figure 5.16 compares the weekly mean INP temperature spectra for four seasons, as measured by both INSEKT and PINE. Both instruments reveal similar seasonal patterns: highest INP concentrations in spring and autumn, lowest in winter, and strong dependence of concentration on decreasing temperature. In general, both instruments show a good agreement of the measured INP concentration, only for the summer period, PINE measures somewhat higher INP concentrations than INSEKT at higher temperatures. At lower temperatures, the INP concentrations measured by PINE and INSEKT fall along a consistent trend line. The differences at higher temperatures may be attributed to methodological factors such as differences in aerosol sampling, detection limits, or calibration procedures, and will be discussed in more detail in a subsequent section.

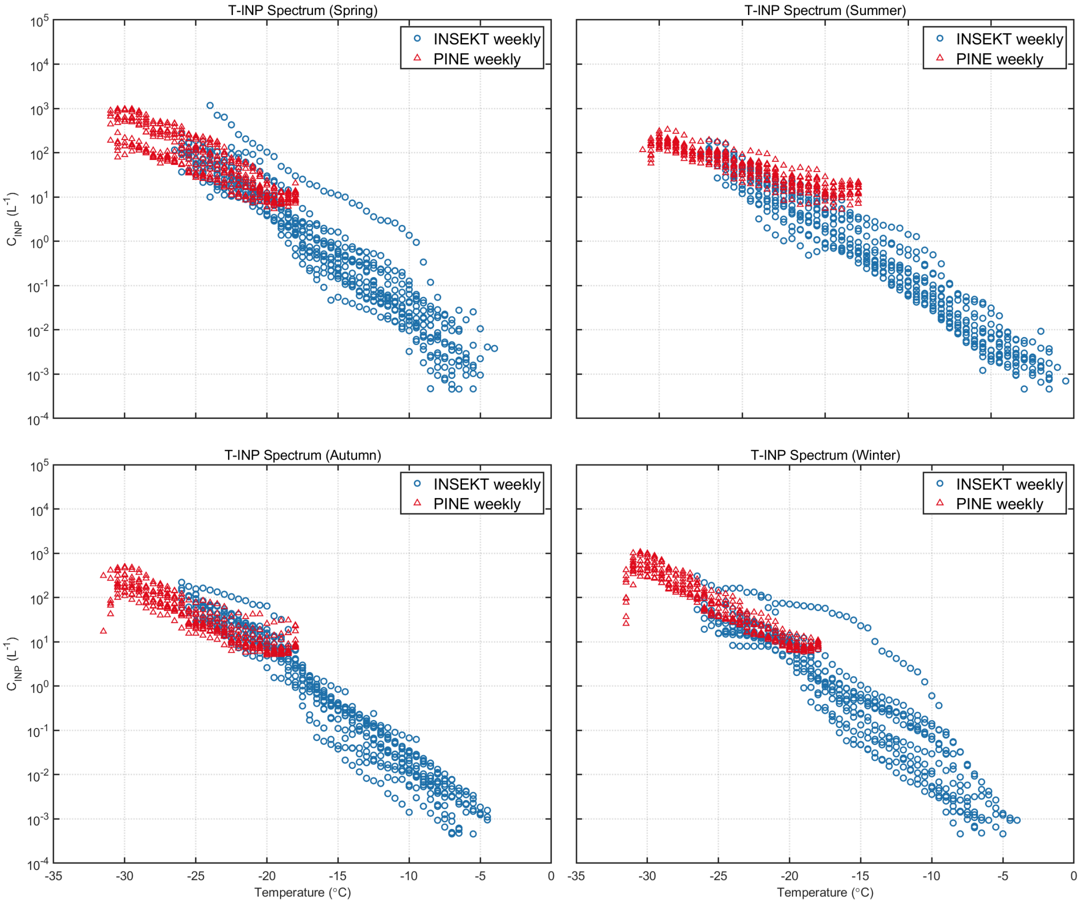

Figure 5.16: Seasonal INP temperature spectra measured with the INSEKT and PINE instruments at the suburban site from March 2022 to March 2023. Blue open circles denote weekly mean INSEKT data, and red open triangles denote weekly mean PINE data.

Figure 5.17 provides a focused comparison of PINE and INSEKT weekly INP concentrations at nearly identical activation temperatures range (−8–−26 °C), over the period March 2022 to March 2023. The time series for both instruments are in good overall agreement regarding the occurrence of seasonal maxima and minima as well as the timing of episodic events. PINE data tend to yield higher absolute concentrations than INSEKT, particularly during certain spring and autumn peaks. This difference may reflect instrument-specific biases, differences in time resolution (e.g., PINE's higher frequency of measurement), or subtleties in sample handling and analysis.

All together, the following key points result from the combined INSEKT and PINE measurements:(i) Both INSEKT and PINE reveal strong and recurrent seasonal cycles of INP abundance at the suburban site, with pronounced maxima in spring and autumn and minima in winter;(ii) the INP concentrations systematically increase with decreasing temperature, with the largest seasonal amplitude and event-driven variability occurring at the coldest activation temperatures.(iii) direct comparisons between INSEKT and PINE demonstrate good agreement in seasonal variability and event timing;and (iv) the consistency of seasonal patterns across both instruments and over multiple years provides confidence in the reliability of the observed long-term INP climatology at the suburban

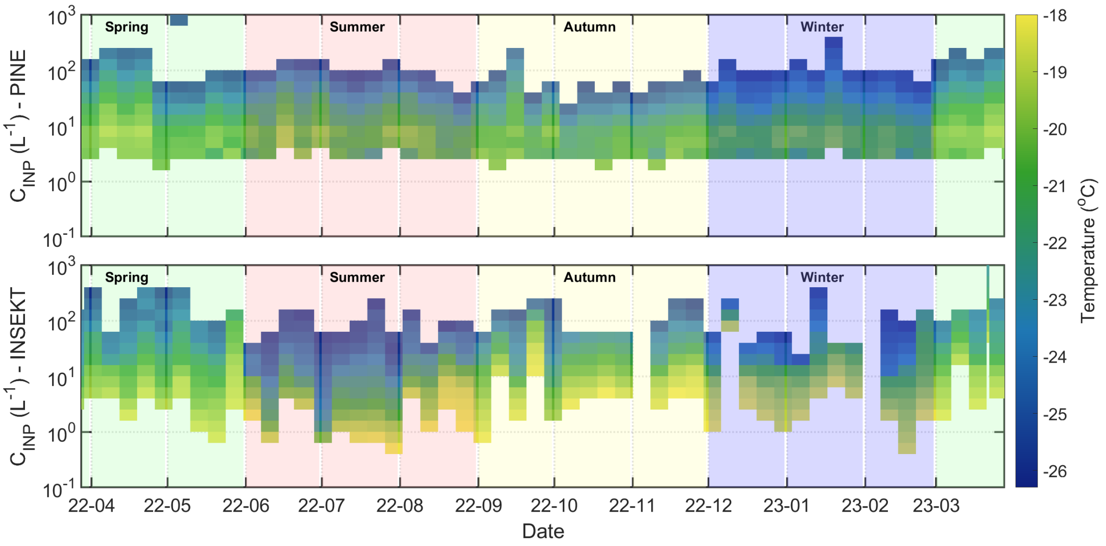

Figure 5.17: Direct comparison for the INP concentrations time series from the INSEKT and PINE instruments at the suburban site, using the overlapping activation temperature intervals.

site.

5.3.6 The parameterization of INP concentration

Single-parameter parameterization of INP concentration

INP number concentrations in the atmosphere are commonly parameterized as an exponential function of temperature, an approach widely adopted in atmospheric models to facilitate implementation and comparison (DeMott, Prenni, et al., 2010; Meyers et al., 1992). The generic form of this parameterization is expressed as:

$$N_{\mathrm{INP}}(T) = A\exp(BT) \tag{5.1}$$

where $N_{\mathrm{INP}}(T)$ represents the INP number concentration (in L^{-1}) active at temperature T (in °C), and A and B are empirically determined fitting coefficients.

The values of A and B are obtained by fitting the measured INP concentrations as a function of temperature using non-linear regression. For the present dataset, the best-fit coefficients are $A = 9.18 \times 10^{-5}\,\mathrm{L}^{-1}$ and $B = 0.25190\ ^{\circ}\mathrm{C}^{-1}$, as derived from campaign observations at the three sites for one year.

Figure 5.18 illustrates the measured INP number concentrations as a function of activation temperature, overlaid with the exponential fit according to Equation 5.1. Also shown for comparison are parameterizations developed in previous studies, including those by DeMott, Prenni, et al. (2010), Fletcher (1962), and Meyers et al. (1992).

The fitted exponential function captures the fundamental dependence of INP concentration on temperature, with number concentrations increasing rapidly as temperature decreases. Despite the general agreement, significant scatter is evident among different parameterizations, attributable to regional differences in aerosol sources, composition, meteorology, and measurement methodology. In particular, the present study reveals higher INP concentrations at moderate supercooling compared to some earlier schemes, likely reflecting the influence of local mineral dust and anthropogenic emissions.

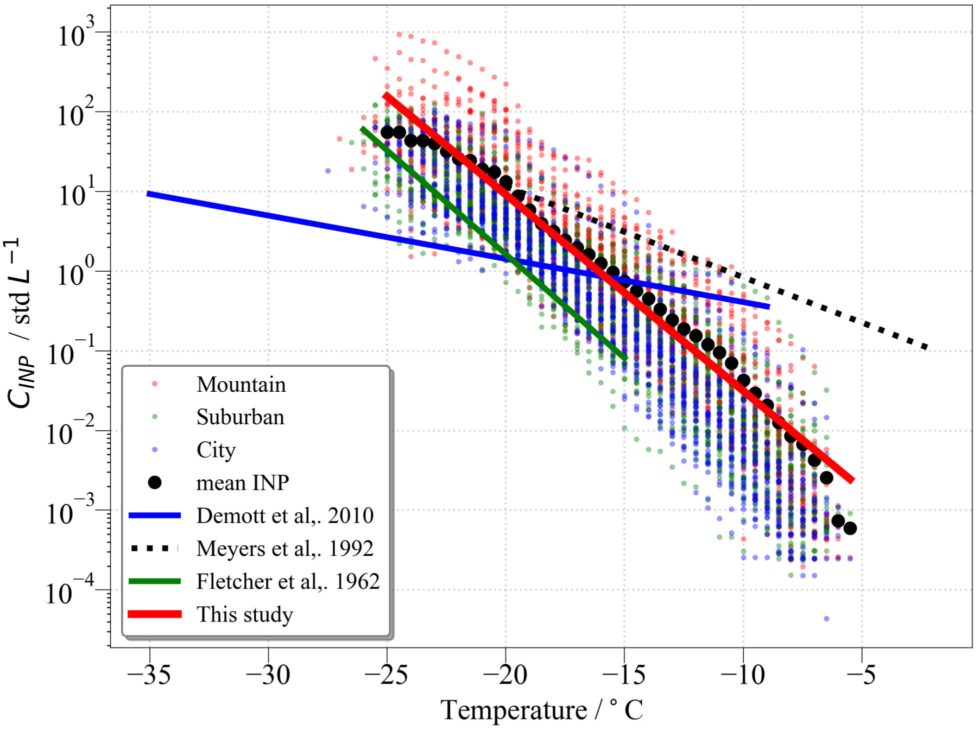

Figure 5.18: Atmospheric INP number concentrations as a function of activation temperature, including an exponential fit derived in this study and established parameterizations from the literature. Red, green, and blue symbols represent individual observations at the mountain, suburban, and city sites, respectively. The solid red line denotes the fit from this study. The solid blue lines indicate the parameterizations of DeMott, Prenni, et al. (2010), the black dotted line shows the scheme of Meyers et al. (1992), and the solid green line corresponds to Fletcher (1962).

Due to the wide variability in INP concentrations observed at a given temperature—often spanning several orders of magnitude—a single-parameter, temperature-only approach is insufficient for representing the spatial and temporal heterogeneity characteristic of atmospheric INPs in this region. These results highlight the need for extended multi-parameter schemes that incorporate additional physical and chemical predictors, such as aerosol surface area, composition, and air mass history, to improve representation in weather and climate models.

Multi-parameter parameterization of INP concentration

Atmospheric INP concentrations in Beijing are strongly influenced by aerosol properties. DeMott, Prenni, et al. (2010) demonstrated that INP concentrations exhibit a robust correlation with activation temperature and aerosol abundance, proposing a globally averaged parameterization for INPs. More recent findings indicate that immersion-freezing mode INP concentrations are better correlated with the number concentration of aerosols in the 1.0–2.5μm diameter range than with those in the 0.5–2.5 μm range (Y. Z. Ren et al., 2023). While these parameterizations successfully reproduce observed data, they are typically based on online CFDC observations and thus limited to a narrow temperature range (−20°C to −30°C).

To obtain a broader temperature spectrum, the present study establishes a new parameterization for INP concentrations by integrating long-term observational data collected across diverse environments in Beijing, including mountainous, suburban, and urban sites. The results reveal a pronounced influence of aerosol variability on ambient INPs; synoptic and meteorological conditions modulate INP concentrations by altering aerosol loading. The newly developed empirical relationship incorporates both aerosol number concentration and activation temperature, and is expressed as:

$$C_{\mathrm{INP}} = 10^{-a} \cdot (-T)^{b} \cdot N_{500}^{-cT+d} \tag{5.2}$$

where C_{INP} denotes the INP number concentration, N_{500} is the aerosol number concentration with diameters greater than 0.5 μm, and T is the activation temperature. The empirical coefficients are $a = 8.81$, $b = 7.45$, $c = 0.0365$, and $d = -0.916$.

Equation 5.2 accounts for both temperature and aerosol abundance, capturing the non-linear relationship between these variables and INP concentrations over a wide temperature range. This multi-parameter framework is compared against previously published schemes, including the global-average parameterization by DeMott, Prenni, et al. (2010), a Beijing mountain site parameterization (Bi et al., 2020), and the parameterization from Y. Z. Ren et al. (2023).

Figure 5.19 presents the comparison between measured INP concentrations and values predicted by different parameterization schemes. Panels (a)–(d) correspond to the DeMott, Prenni, et al. (2010) global average, Bi et al. (2020) for Beijing mountain, Y. Z. Ren et al. (2023), and the new parameterization proposed in this study, respectively.

Figure 5.19 demonstrates that the new parameterization developed in this work yields the best agreement with observed values, especially for low INP concentrations. Alternative schemes tend to overestimate INP concentrations by 2–3 orders of magnitude at low concentrations, despite performing reasonably at higher concentrations. The discrepancy is primarily attributed to the restricted temperature ranges used in the development of prior parameterizations, as they are largely derived from CFDC measurements conducted between −20°C and −30°C, limiting their predictive capability at warmer temperatures. The newly established parameterization therefore more accurately represents INP concentrations across the full observed temperature spectrum, especially above −15 °C.

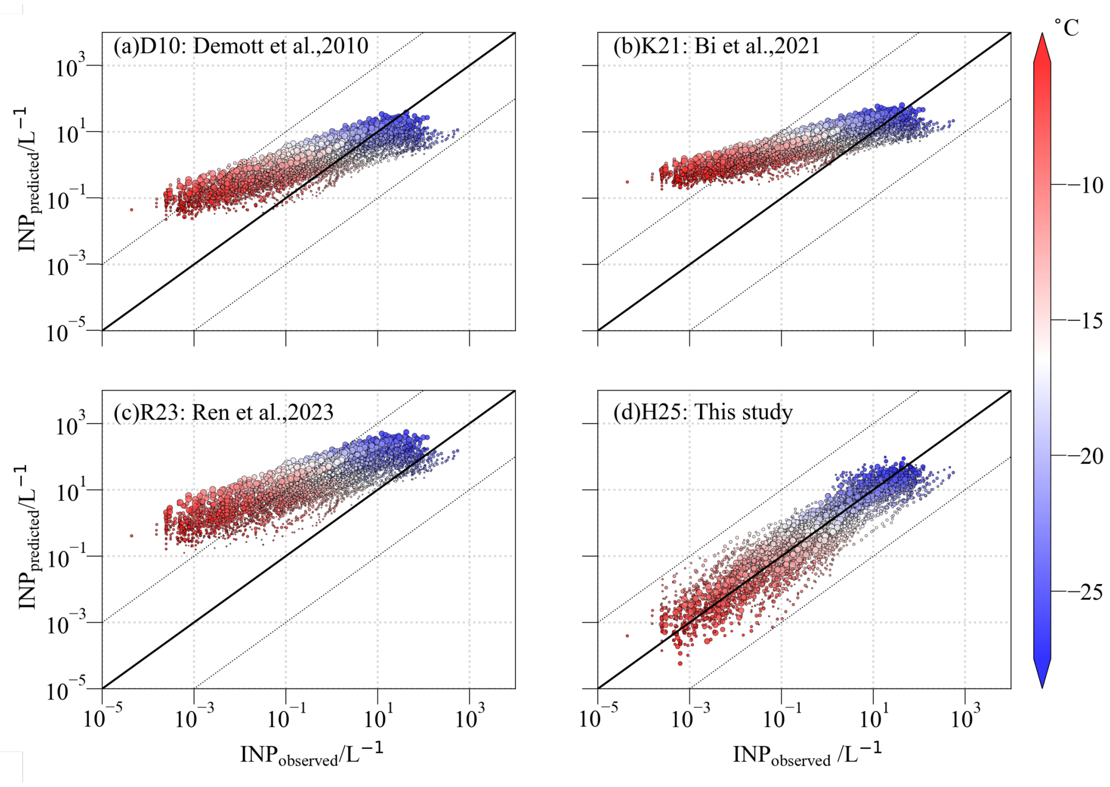

Figure 5.19: Comparison of INSEKT-observed INP concentrations with predictions from different parameterization schemes: (a) global-average scheme of DeMott, Prenni, et al. (2010); (b) parameterization for the Beijing mountain site by Bi et al. (2020); (c) scheme of Y. Z. Ren et al. (2023); (d) revised multi-parameter scheme proposed in this study. Schemes (a)–(c) share the functional form of DeMott, Prenni, et al. (2010) but use different empirical coefficients, whereas (d) employs the modified formulation introduced here (see Equation 5.2). In each panel, the x-axis shows observed INP concentrations, and the y-axisthe corresponding model predictions. The solid line is the 1:1 reference. Marker size encodes aerosol concentration and color denotes activation temperature.

5.4 Summary

This chapter presents a comprehensive, multi-site and long-term field observation of the abundance and variability of INPs in the Beijing region. Three representative sites (urban, suburban, and mountain) were selected to reflect distinct aerosol source environments. Observations, conducted continuously since April 2019, used the freezing experiment INSEKT and the continuously measuring online instrument PINE, complemented by in situ measurements of meteorological and aerosol parameters. This chapter focuses on more than one year of filter-based sampling at all three sites (July 2019 to July 2020) and an extended time series at the suburban site (July 2019 to March 2023), with the aim of elucidating spatial differences in INP concentrations across diverse environmental backgrounds and comparing INSEKT and PINE results. The resulting multi-year, multi-site dataset represents the first high-resolution, continuous record of INPs in the Beijing area, filling a critical observational gap.

The INP concentrations exhibit a marked seasonal cycle, with highest values in spring, followed by autumn, and the lowest values in winter, a pattern consistently observed at all sites and most pronounced at lower activation temperatures. Spatial variability is also evident: the mountain site consistently records the highest and most variable INP concentrations, with frequent spikes and broader data distributions indicative of sensitivity to episodic events and regional transport. In contrast, the suburban and urban sites are characterized by lower and more stable INP backgrounds, suggesting more homogeneous local influences.

There is a clear association between INP concentrations and the abundance of coarse-mode aerosols (N_{500} and N_{2000}), which are representative of mineral dust and other primary INP carriers. At the mountain site, INP concentration peaks frequently coincide with increases in coarse particle concentrations, especially during spring and autumn and at lower temperatures, reflecting strong dust influences during these periods and conditions. In the suburban and urban environments, the correspondence between INPs and coarse particles is less pronounced and more episodic, suggesting differences in dominant sources or atmospheric processing. The INP-to-N_{500} active fraction further reveals that, on average, coarse particles at the mountain site are more ice-active than those at urban locations, underscoring the central role of natural dust sources.

Even in polluted environments, natural dust and episodic events remain the primary determinants of INP climatology in Beijing. Persistently elevated INP concentrations in spring (the season characterized by frequent dust events) and at the mountain site (frequently influenced by regional dust transport) underscore the dominant influence of natural mineral dust on the INP variability, especially in the immersion freezing regime. The strong correlation between INPs and coarse particles (N_{500}, N_{2000}) at the mountain site directly supports this conclusion. Despite severe wintertime anthropogenic pollution, the INP concentrations remain lowest at all sites and temperatures, indicating that, unlike mineral dust, anthropogenic aerosols are less efficient INPs in mixed-phase cloud regime (J. Chen et al., 2018). This finding demonstrating that although pollution poses a major air quality concern, its direct contribution to ice nucleation, particularly in mixed-phase cloud regime, is likely secondary to that of natural dust. This may have important implications for regional weather modification strategies and climate modeling, where accurate source attribution is essential.

The observation of slightly elevated active fractions at the urban site during winter suggests such complex interactions, likely driven by changes in the aerosol composition or atmospheric processing that enhance the ice activity of background INPs. These results indicate that the relationship between pollution and INP activity is neither simple nor linear. Chapter 6 further explores the impact of emission control strategies on INP abundance. Future research should focus on the specific chemical and physical changes induced by atmospheric aging processes in polluted environments and their implications for INP ice nucleation efficiency.

Parallel measurements using two independent instruments (the offline filter-based INSEKT sampler and the online PINE chamber) exhibited very good agreement during their overlapping period. Both instruments captured the same timing of seasonal maxima and short-term INP spikes, indicating that the observed climatological patterns are robust and not an artifact of a single technique. Minor systematic differences were noted (with PINE occasionally reporting slightly higher INP abundances, particularly at warmer activation temperatures in summer), but these did not affect the overall seasonal trend. The strong correspondence between INSEKT and PINE measurements thus provides confidence in the reliability of the long-term INP dataset and confirms a consistent seasonal INP climatology for the region.

The comprehensive dataset enabled the development of improved empirical parameterizations for predicting INP concentrations from more accessible variables. A temperature-only exponential fit of the form $N_{\mathrm{INP}}(T) = A\exp(BT)$ was derived to represent the baseline relationship between INP abundance and temperature. However, substantial scatter in the observations highlights that temperature alone cannot explain the full variability in INP concentrations, echoing the need for additional predictors. Building on prior studies that link INPs to aerosol loading (DeMott, Prenni, et al., 2010; Y. Z. Ren et al., 2023), a new multi-parameter scheme was developed by incorporating the number concentration of coarse aerosol particles (N_{500}, representing particles larger than 0.5 µm) alongside temperature. This two-factor parameterization (Equation 5.2) captures the non-linear dependence of INPs on both variables and is valid over a broad temperature spectrum of $-25\,°\mathrm{C}$ to $-5\,°\mathrm{C}$. This result is a key outcome of the study, providing a more reliable empirical basis for modeling ice-nucleating particles in atmospheric simulations of the Beijing area and beyond.

Chapter 6

Intensive Field Campaigns on the Abundance and Sources of INPs During the Winter Olympic Games

This section analyses immersion-mode ice-nucleating particles measured at a mountaintop site during the 2022 Beijing Winter Olympics, when stringent emission controls—industrial shutdowns, traffic restrictions, and clean-heating initiatives—substantially lowered regional primary emission sources (e.g., SO_2, NO_x, black carbon, and $PM_{2.5}$). We (i) investigate the evolution of INP concentrations from −5 °C to −30 °C with the PINE, CFDC, INSEKT, and FINDA instruments; (ii) quantify the relative contributions of mineral dust, secondary inorganic aerosols, organic matter, and biological particles to INP variability; and (iii) derive empirical parameterizations linking INP number concentration to particle properties, yielding region-specific constraints for weather and climate models.

6.1 Introduction

INPs govern the first appearance of ice in mixed-phase clouds, thereby controlling cloud lifetime, precipitation efficiency, and short-wave and long-wave radiative forcing. Because heterogeneous freezing can initiate more than 20 K warmer than homogeneous freezing, ambient INP concentrations of only 10^{-1}–10^{0} L^{-1} may determine whether a cloud glaciates or remains liquid (Cantrell & Heymsfield, 2005). Yet the global INP budget is still poorly constrained: (i) the ice-nucleating active site density (n_s) of different particle classes spans 6–8 orders of magnitude, and (ii) the relative source strengths of mineral dust, marine organics, biomass smoke, biological material and anthropogenic pollution vary strongly with region and season. Quantifying the anthropogenic contribution is particularly challenging in rapidly urbanizing areas, where primary emissions, atmospheric aging rates, and synoptic transport all fluctuate on diurnal to synoptic time-scales.

Previous limited urban field studies have produced apparently contradictory results. Microscopy and INP measurements in Mexico City (Knopf et al., 2010) and Toronto (Corbin et al., 2012) identified elemental-carbon-rich and organic combustion particles that activated immersion freezing above −30 °C. In contrast, observations in central Beijing found that winter haze episodes dominated by secondary inorganic and carbonaceous pollution did not elevate INP concentrations between −20 °C and −30 °C (Che et al., 2019; J. Chen et al., 2018). Reconciling these discrepancies requires "perturbation experiments" in which anthropogenic sources are systematically altered while meteorology, mineral dust, and biomass burning remain comparatively steady.

The 2022 Olympic and Paralympic Winter Games (4 Feb – 13 Mar 2022) provided a great opportunity to investigate whether the anthropogenic pollution could contribute to the INPs. A coordinated air-quality plan across the North China plain suspended more than 2000 industrial facilities and restricted heavy-duty diesel traffic. These actions reduced wintertime SO_2, NO_x, black carbon, and $PM_{2.5}$ mass by 30–60% relative to climatological means and shifted the aerosol population toward more oxidized, less internally mixed particles (Du et al., 2023; W. Li et al., 2024; Y. Liu et al., 2022). Bayesian counter-factual analyses indicate that without interventions Beijing’ s $PM_{2.5}$ would have been approximately 34% higher during the Olympic fortnight (Y. Liu et al., 2022). Such a large, well-documented perturbation enables us to isolate human-source impacts on the regional INP reservoir.

Most prior INP studies in Beijing have relied on urban or suburban ground stations, where strong local plumes obscure the regional background. We therefore established a continuous INP observatory at Haituo mountain in Beijing. During daytime convective mixing, pollutants emitted across the plain reach Haituo’ s summit, representing the well-mixed top-of-boundary-layer aerosol; at night, the site often locates in the residual layer or free troposphere, reducing fresh local influences. Crucially, the mountain environment lacks wintertime biomass-burning plumes common in lowland villages, and also the sparsely populated terrain eliminates fresh vehicular and cooking emissions that may influence urban ground-level INP variability.

INPs were measured with a continuous-flow diffusion chamber ice activation spectrometer (CFDC-IAS, Handix Scientific, USA) and a PINE chamber (Möhler et al., 2021). The CFDC was operated at fixed temperatures (−20 °C, −25 °C, −30 °C) under water-supersaturated conditions (principle identical to the CSU-CFDC (DeMott et al., 2018; Rogers et al., 2001)) to provide high time resolution INP concentrations, while the PINE yielded high-temporal-resolution (5 min to 12 min) immersion-freezing spectra between −17 °C and −30 °C, both with low instrumental background. For offline INP analysis, aerosol particles were collected on filters and later examined via immersion-freezing assays using INSEKT and FINDA (Y. Ren et al., 2024), covering a temperature range from −5 °C to −25 °C. Complementary measurements included: (a) High-Resolution Time-of-Flight Aerosol Mass Spectrometry (HR-ToF-AMS) for non-refractory aerosol composition, (b) an APS and a SMPS for size-resolved particle number and surface-area distributions, and (c) a Wideband Integrated Bioaerosol Sensor (WIBS) for single-particle fluorescence as a proxy for biological material.

By coupling a stringent emission-control experiment with high-resolution mountain measurements, our study delivers the most comprehensive assessment of how anthropogenic activity intersects with regional ice-nucleating particle populations in North China.

This chapter is structured as follows. Section 6.2 describes the observation site, including its geographic setting and relevance for capturing regional background conditions during the Winter Olympic Games. Section 6.3 provides an overview of the deployed instrumentation and sampling protocols, detailing both online and offline measurements of INPs and aerosol physicochemical properties. Section 6.4 introduces the machine-learning framework used for INP prediction based on aerosol chemical and physical metrics. Section 6.5 presents the key results, including instrument intercomparison, the relationships between INPs, biological particles, and ambient aerosol, and the development and evaluation of new INP parameterizations under mixed-source conditions. Finally, Section 6.6 summarizes the main conclusions and discusses their implications for understanding INP sources and variability in North China during wintertime pollution control periods.

6.2 Observation site

The observation period extended from 13 January to 24 March 2022, spanning the pre-Olympic, Olympic (4–20 February), and post-Olympic phases. All measurements were carried out at the Haituo Mountain (HT) site (40.52°N, 115.78°E; 1344 m a.s.l.) in Beijing’ s Yanqing District. HT sits on a wind-exposed ridge roughly 90 km northwest of the city center and about 10 km east of the Xiaohaituo Alpine Skiing Centre, the core venue cluster of the Winter Games. Surrounded by sparsely populated, forested terrain and positioned near the daytime planetary-boundary-layer top—but frequently above it at night—the site samples well-mixed regional air with minimal local emission influence, making it ideal for background aerosol and INP studies in North China.

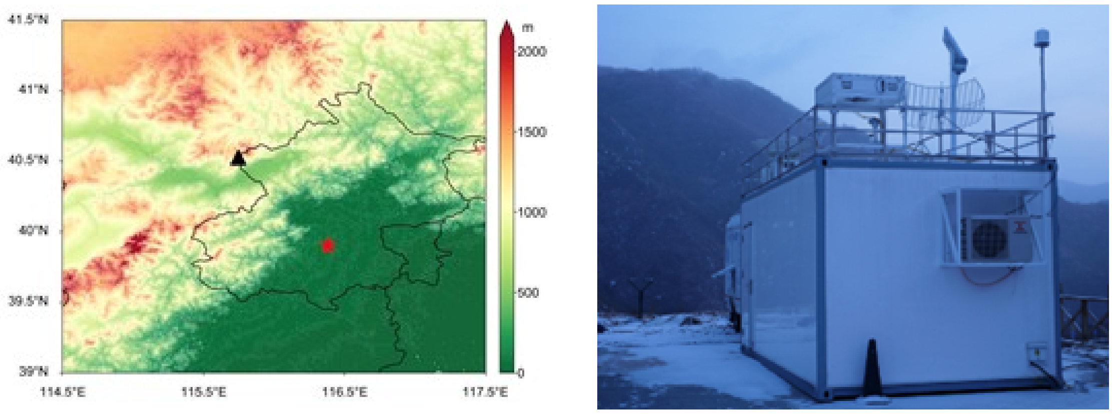

(a) Topography of the Haituo mountain site.

(b) The observation cabin

Figure 6.1: Topography of the Haituo mountain site(a)(The black triangle denotes the Haituo mountain site, whereas the red five-pointed star marks downtown Beijing.) and the observation cabin (b) at the Haituo mountain site.

6.3 Instrument setup

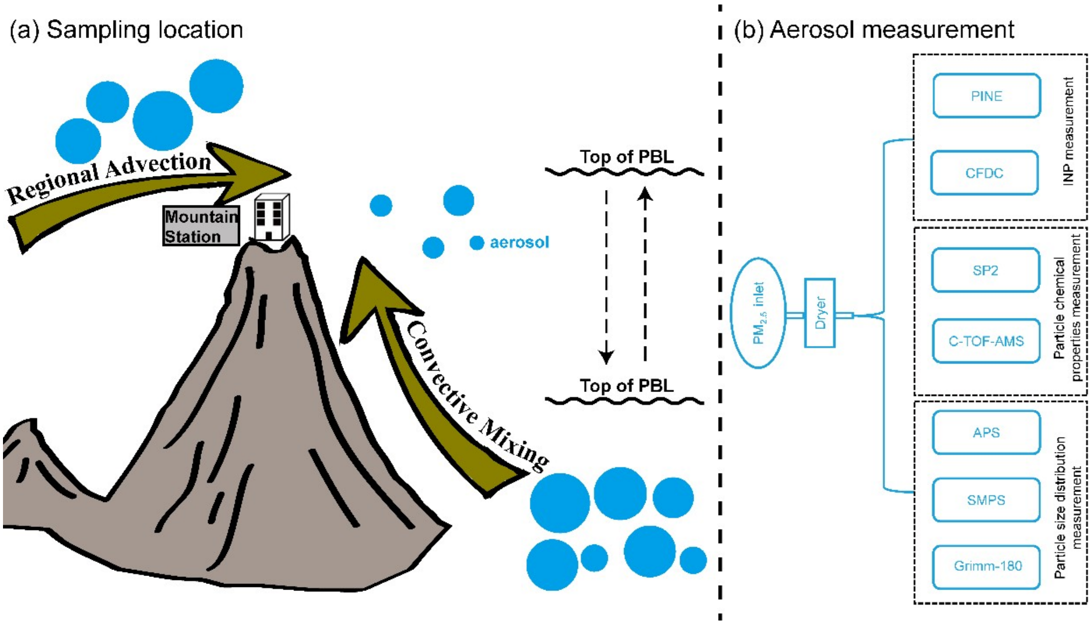

Figure 6.2: (a) Sampling location at the summit of Haituo Mountain, Beijing. The site is influenced by regional advection and convective mixing, and is intermittently located inside or outside the planetary boundary layer (PBL). (b) Aerosol measurement setup during the campaign, showing the instruments deployed for physical and chemical characterization as well as INP measurements.

A comprehensive instrumentation array—spanning aerosol physical and chemical properties and incorporating both online and offline INP measurements—was deployed to yield rigorous, multi-dimensional observations (Figure 6.2). The principal instruments and their specifications are listed in Table 6.1.

Table 6.1: Summary of instrumentation used during the intensive campaign

Instrument	Measured Parameters	Notes / Resolution
Aerosol Instruments		
AMS	NR-PM1 chemical composition	1–5 min resolution
Grimm180	PM_1/2.5/10, total count	6 s resolution
AE33	Black carbon (eBC)	1 s resolution; dual-spot Aethalometer
APS3321	Aerodynamic particle size (0.5–20 µm)	1 s resolution; coarse particles
SMPS3938	Size distribution (14 nm–700 nm)	3 min resolution
WIBS	concentration of fluorescent particles	5 min resolution; 0.5–30 µm particles
PromeOPC	Optical particle size/count	Real-time; light-scattering based
INP Instruments		
CFDC	Online INP under controlled T/RH	Scan mode; flow 1.5 L/min; LOD 0.12 INP/L
PINE	Continuous immersion and deposition INPs	6 min resolution; LOD 0.5 INP/L
INSEKT	Offline immersion freezing INPs	Filters or precip.; −25.5 °C; 0.33 °C/min cooling rate
FINDA	Offline immersion-freezing INPs	Filters or precip. −25 °C; 1 °C/min cooling rate
Meteorological Observations and Diagnostics		
AWS (Automatic Weather Station)	Temperature, RH, wind, pressure	Near-surface observations; 1-min resolution

6.3.1 INP measurement

Online measurements of ambient INP concentrations at −20 °C, −25 °C, and −30 °C were carried out using the BJ-CFDC, which follows the established chamber configuration and operational principles of earlier CFDC models (Rogers et al., 2001). This instrument had previously been deployed in field campaigns in Beijing (Bi et al., 2019). The chamber design comprises a vertical cylindrical flow passage, flanked by two ice-coated walls maintained at controlled temperatures to produce a water-supersaturated environment suitable for ice nucleation.

A key feature distinguishing the BJ-CFDC from other CFDC systems is its integrated automation platform, enabling fully continuous operation. Standard procedures including system evacuation, leak testing, temperature stabilization, ice wall formation, and initiation of sample airflow were programmed into automated sequences. Background corrections were made using filtered-air reference periods. At the end of each measurement cycle, the chamber was reheated to melt the ice layers and evacuated before commencing a new cycle.

During the mountain-site deployment, the BJ-CFDC drew aerosol samples from a shared inlet, located downstream of a 2.5 µm cyclone followed by dual impactors. This configuration was designed to eliminate larger particles and reduce the risk of misclassifying coarse material as ice crystals. Instrumental background INP concentrations remained below $1\,\mathrm{L}^{-1}$ (STP) under clean conditions, but could gradually increase to around $25\,\mathrm{L}^{-1}$ after extended operation (Bi et al., 2019; Y. Z. Ren et al., 2023). To minimize background interference, measurements were performed first at the warmest temperatures, where natural INP concentrations tend to be lowest.

The BJ-CFDC operated sequentially at −20 °C, −25 °C, and −30 °C, with each temperature step maintained for approximately 1.25 h at a relative humidity with respect to water of 106.5(10) %. These settings are optimized for observing immersion freezing processes (DeMott et al., 2017), although other ice nucleation pathways cannot be completely ruled out. Data collected during transition periods with unstable temperature or humidity conditions were excluded from analysis to ensure data reliability.

The Portable Ice Nucleation Experiment (PINE-05-03) was used to quantify ambient number concentrations of INPs in situ via a simulated adiabatic expansion cooling technique (Möhler et al., 2021). As a commercially available system, it provides standardized and reproducible operation across multiple studies (Lacher et al., 2024; Möhler et al., 2021). In addition to its relatively high temporal resolution (less than 12 min), the PINE has the ability for remote and autonomous operation with minimal need for onsite maintenance. The instrument provides INP concentrations approximately every 5–12 minutes. It is capable of simulating atmospheric immersion freezing and deposition ice nucleation, depending on the gas temperature and water saturation within the chamber, both of which are digitally controlled by the user. PINE was operated in a repeating sequence of three modes: “flush”, “expansion”, and “refill”. During the flush mode, ambient air is actively dried using two Perma Pure dryers and introduced into the 10 L chamber at a flow rate of $2\,\mathrm{L\,min}^{-1}$ for 10 min. In the expansion phase, the sample gas is cooled and depressurized via a $3\,\mathrm{L\,min}^{-1}$ pump, reducing pressure to 800 hPa to achieve supersaturation with respect to both ice and water. This adiabatic expansion, typically lasting around one minute, induces freezing in the presence of INPs. An optical particle counter (OPC; fidas-pine, Palas GmbH) positioned downstream detects particles from the chamber. Ice crystals are identified by their optical diameter (typically $> 10\,\mu\mathrm{m}$), distinguishing them from interstitial aerosols and water droplets, and are counted as immersion-mode INPs. During the refill mode, filtered ambient air is introduced for about one minute to reset the chamber for the next cycle. The system’s temperature accuracy is ±2 °C. This study was the first time for the PINE instrument to be operated in China. It was run in an automated cyclic mode to yield continuous ice-activation spectra from −17 °C to −30 °C. Each complete temperature scan lasted approximately 2 h: ambient aerosol was flushed into the chamber at a constant $1.5\,\mathrm{L\,min}^{-1}$ for 240 s, and a $3\,\mathrm{L\,min}^{-1}$ expansion rate was used to activate all the particles and measure the immersion mode INPs. To maintain data integrity, a manual zero-calibration with HEPA-filtered air was performed each day, occupying about one hour and verifying that background counts remained below the detection threshold.

For offline INP measurements, filters were also collected for subsequent INP analysis with INSEKT and FINDA (Y. Ren et al., 2024), which can provide immersion freezing at a temperature range of 0 to approximately −25 °C. In this study, total aerosol particles were collected on a 47 mm-diameter in-line stainless steel filter holder fitted with a 0.2 µm-pore-diameter Nuclepore Track-Etch Membrane (Whatman, Germany) filters on a filter holder at $8\,\mathrm{L\,min^{-1}}$ for 24 hours, controlled by a mass flow controller (Folosi, China) and a vacuum pump (Thomas 2688, USA). After the sampling, the filter with the holder were sealed in a clean plastic bag and stored at −20 °C in a refrigerator and transferred to the laboratory for frozen experiment.

To re-suspend collected particles, the filters were placed into sterile 50 mL polypropylene tubes (Eppendorf), and 10 mL of Milli-Q ultrapure water—filtered through a 0.1 µm pore-diameter membrane—was added. Particle re-suspension was achieved by rotating the tubes at 3200 revolutions per minute for one minute. Working within a laminar flow desk, 32 aliquots of 50 µL from each suspension were dispensed into sterile 96-well PCR trays, which were subsequently placed into immersion freezing (INSEKT and FINDA) blocks. Realtime pixel values of each well were extracted with customized software and cumulative INP concentrations per milliliter of suspension were calculated using the method described by Vali (1971). To determine background INP concentrations, filter blanks (which were loaded into inline filter units and handled in the same way as actual samples) were processed. Finally, the measured INP concentrations in the total suspension volume were scaled to atmospheric INP concentrations (INPs per liter of sampled air) based on the air volume collected. A binomial sampling correction was applied as described in Schiebel (2017).

6.3.2 Aerosol chemical and physical properties

The aerosol chemical compositions which can vaporize at 600 °C, including ammonium sulphate, nitrate, and organic aerosol, were measured by a compact time-of-flight aerosol mass spectrometer (C-TOF-AMS, Aerodyne Inc, USA) (Canagaratna et al., 2007). The ionization efficiency (IE) calibration was conducted by the size-selected (300 nm) ammonium nitrite before and after the observation. The IE of the sulfate, nitrate, chloride, and ammonium was estimated to be 1.0, 1.1, 1.3, and 3.63, respectively, and a default value of 1.4 was assumed for Organic Aerosol (OA). A constant collection efficiency factor (0.5) for all components was used to compensate the particle loss through the lens and bounce at the vaporizer (S. Huang et al., 2017). The atomic oxygen-to-carbon ratio (O:C) was calculated from high-resolution mass spectra data based on the improved ambient method (Canagaratna et al., 2015).

Particle number and aerodynamic size distributions (0.5 µm to 20 µm) were monitored by an Aerodynamic Particle Sizer (APS 3321; 5 min resolution) and a Scanning Mobility Particle Sizer (SMPS 3938; 14 nm to 700 nm; 3 min resolution). Complementary real-time optical counts and mass concentrations ($\mathrm{PM_1}$, $\mathrm{PM_{2.5}}$, $\mathrm{PM_{10}}$) were provided by a Grimm 180 Environmental Dust Monitor (6 s resolution).

6.3.3 WIBS-4A measurements and data analysis

The Wideband Integrated Bioaerosol Sensor (WIBS-4A; Droplet Measurement Technologies, Inc.) provides high-resolution, real-time detection of both fluorescent aerosol particles (FAPs) and non-fluorescent aerosol particles (non-FAPs) (O'Connor et al., 2014). Operating on the principle of ultraviolet light-induced fluorescence, the instrument records the autofluorescence of individual particles across three spectrally unresolved channels—FL1 (280 nm excitation, 310–400 nm emission), FL2 (280 nm excitation, 420–650 nm emission), and FL3 (370 nm excitation, 420–650 nm emission)—while simultaneously measuring forward- and side-scatter diameters (Healy et al., 2012; Yue et al., 2017).

All particles were initially classified as FAPs or non-FAPs based on a fluorescence threshold determined from the instrument's forced-trigger mode. Fluorescent particles were subsequently categorized into seven types according to the combination of emission signals detected across the three channels, following the classification scheme proposed by Perring et al. (2015).

Table 6.2 summarises the excitation and emission wavelength ranges associated with each fluorescence type.

Table 6.2: Excitation and emission wavelength ranges for each WIBS-4A fluorescence channel.

Channel	**Type**	**Excitation (nm)**	**Emission (nm)**
FL1	FL-A	280	310–400
FL2	FL-B	280	420–650
FL3	FL-C	370	420–650
FL1+FL2	FL-AB	280	310–400, 420–650
FL1+FL3	FL-AC	280, 370	310–400, 420–650
FL2+FL3	FL-BC	280, 370	420–650
FL1+FL2+FL3	FL-ABC	280, 370	310–400, 420–650

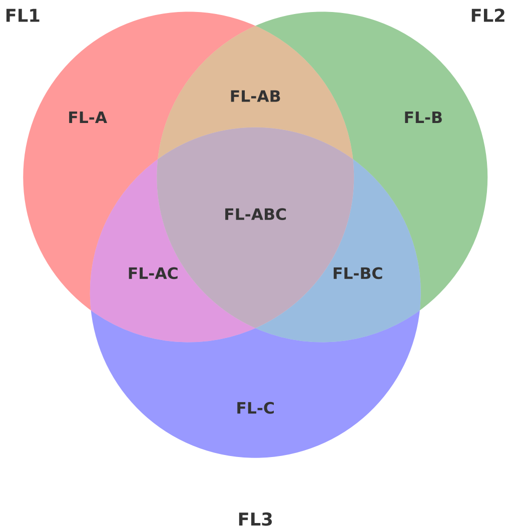

Figure 6.3: Schematic diagram illustrating the classification of FAP-FL1 based on fluorescence detection across WIBS channels FL1, FL2, and FL3.

Figure 6.3 illustrates the classification scheme of FAP-FL1 based on fluorescence detection across WIBS channels. FAP-FL1 is defined as the subset of fluorescent aerosol particles exhibiting detectable fluorescence in the FL1 channel, regardless of signals in FL2 or FL3. Specifically, FAP-FL1 encompasses particles categorized as **FL-A**, **FL-AB**, **FL-AC**, and **FL-ABC**, corresponding to the following combination:

$$\text{FAP-FL1} = \text{FL-A} + \text{FL-AB} + \text{FL-AC} + \text{FL-ABC}$$

This classification enables a focused representation of protein-like biological aerosol particles while minimizing interference from non-biological fluorescent sources.

6.4 Machine learning of ice-nucleating particle data

A random forest (RF) model was employed to predict INP concentrations. The input features included the concentrations of OA, BC, SO_4^{2-}, NO_3^-, NH_4^+, and Cl^-, as well as the OA/BC ratio, the fraction of m/z 44, and the particle number concentration and surface area derived from APS and SMPS measurements. The INP concentration was used as the target output.

The RF model is widely used due to its advantages in handling high-dimensional data and preventing overfitting. During model training, the following hyperparameters were tuned to achieve optimal performance: the number of decision trees (`n_estimators`), maximum tree depth (`max_depth`), minimum number of samples required to split an internal node (`min_samples_split`), and the maximum number of features considered for splitting a node (`max_features`). A detailed introduction to the model is available in Hu et al. (2024).

After optimization, the main hyperparameters were set as follows: `n_estimators` = 100, `max_depth` = 11, `min_samples_leaf` = 8, `min_samples_split` = 8, `random_state` = 34, `max_features` = ‘sqrt’, and `bootstrap` = True. The dataset was randomly split into a training set (80 %) and a test set (20 %). Model training and hyperparameter tuning were conducted using 10-fold cross-validation on the training set. The model performance and uncertainty were evaluated using the correlation coefficient (r) between predicted and observed INP concentrations in the test set.

6.5 Results and discussion

6.5.1 Comparison of different INP instruments

Figure 6.4 presents the INP temperature spectra measured with INSEKT (blue circles), PINE (orange triangles) and BJ-CFDC (green squares) over the entire campaign from 13th January to 22nd March 2022. All instruments were co-located and operated under identical ambient conditions, ensuring direct comparability of the observed INP variability. The INSEKT filters were intended to be sampled daily through the campaign period; however, due to the remote mountaintop location and exceptional circumstances —including multiple unanticipated power outages and unexpected access impediments —we were able to collect only 19 daily filter samples. Despite this, these data provide unique measurements of INP concentrations at the warmer end of the temperature spectrum, complementing the limited temperature coverage of the two online instruments. The PINE instrument performed continuous temperature-ramped scans from –19 °C to –31 °C, yielding a high-resolution INP concentration spectrum (averaged to 1 h means). The BJ-CFDC alternated continuous observations at fixed setpoints of –20 °C, –25 °C, and −30 °C, also reported as 1 h means, delivering highly precise INP concentrations at representative temperatures.

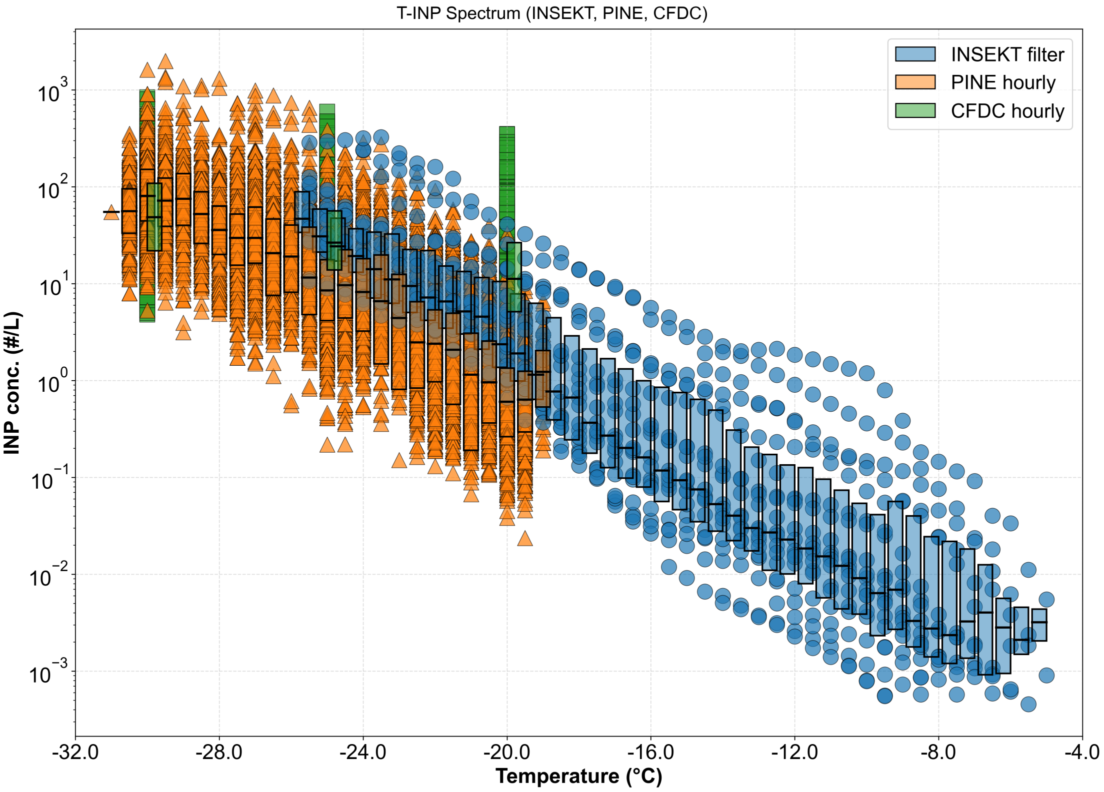

Figure 6.4: INP temperature spectra measured with INSEKT (blue circles), PINE (orange triangles), and BJ-CFDC (green squares) over the entire campaign period. INSEKT data are obtained from the analysis of daily filters, while PINE and BJ-CFDC points represent hourly mean concentrations. The black edge boxes indicate the interquartile range (25th–75th percentiles), and the horizontal line within each box denotes the median (50th percentile).

Figure 6.4 combines the scatter of observed concentrations with overlaid boxplots, whose edges mark the 25th and 75th percentiles and whose central line denotes the median. All three instruments exhibit consistent INP distributions across their overlapping temperature ranges, with concentrations rising steeply as temperature decreases but showing considerable scatter at any fixed temperature. INSEKT covered −5 °C to −25.5 °C, measuring INP concentrations from approximately 5×10^{-4} to $3 \times 10^2\,\mathrm{L}^{-1}$. PINE spanned −19 °C to −31 °C, with concentrations from 2.5×10^{-2} to $2 \times 10^3\,\mathrm{L}^{-1}$. BJ-CFDC at −30 °C observed concentrations between 0.7 and $2 \times 10^3\,\mathrm{L}^{-1}$.

In the temperature range where INSEKT and PINE overlap (−19 to −25.5 °C), the PINE concentration range encompasses nearly the full extent of INSEKT, although INSEKT detections occur predominantly at the upper-concentration end. Comparing medians across the overlapping range (−19 °C to −25.5 °C), INSEKT concentrations are 0.89–3.82 times those of PINE (mean ratio = 2.46). Within the overlapping measurements of PINE and BJ-CFDC at −20 °C, −25 °C, and −30 °C, BJ-CFDC spans the full PINE concentration range and extends to lower values; at −30 °C, the median PINE concentration is 1.66 times that of BJ-CFDC.

Intercomparisons across INP measurement techniques (PINE, CFDC, INSEKT, FINDA) were performed to evaluate consistency in concentration levels, freezing temperatures, and temporal resolution. While good agreement was observed in general trends, each method exhibited instrument-specific detection thresholds, temperature sensitivities, and variability under specific air masses—especially during dust events.

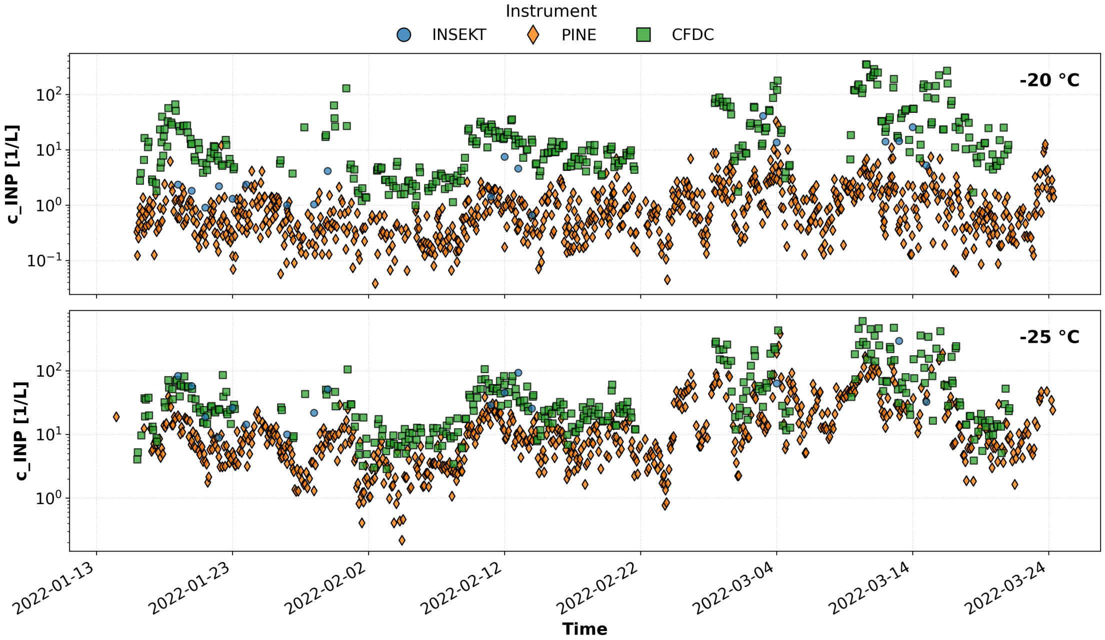

Figure 6.5: Time series of INP concentrations at representative temperatures of −20 °C (top) and −25 °C (bottom), measured by three different instruments: INSEKT (blue circles, daily filters), PINE (orange diamonds, hourly means), and BJ-CFDC (green squares, hourly means) throughout the campaign (13 January–24 March 2022). The *y*-axis is logarithmic to highlight the wide dynamic range of INP concentrations.

Figure 6.5 presents the time series of INP concentrations at −20 °C and −25 °C, as measured by INSEKT, PINE, and BJ-CFDC at the Haituo mountain site during the intensive observation period. INP concentrations at both temperatures exhibited pronounced temporal variability, spanning more than two orders of magnitude, from less than $0.1\,\mathrm{L}^{-1}$ to over $100\,\mathrm{L}^{-1}$. The BJ-CFDC consistently recorded the highest concentrations, particularly during distinct episodic peaks, while PINE generally reported lower values yet accurately captured the major features and temporal fluctuations. INSEKT, based on 24-hour integrated filter samples, provided independent constraints that broadly reflected the trends observed by the online instruments, although short-lived peaks were frequently smoothed as a result of the longer sampling integration. Discrepancies in absolute concentrations among the instruments primarily reflect differences in measurement principles, detection limits, and temporal resolution, as detailed in Table 6.1. Both CFDC and PINE operate in online mode with minute-level resolution, enabling the detection of rapid and transient changes in INP abundance, whereas INSEKT yields daily mean concentrations that may underestimate peak values due to temporal averaging. Additional differences in ice nucleation activation mechanisms and instrument sensitivities to specific INP types and particle sizes further contribute to the observed variability. The co-deployment of three complementary INP instruments at a single site provides robust cross-validation and enhances confidence in the reliability and representativeness of the observed INP temporal dynamics at this high-elevation location.

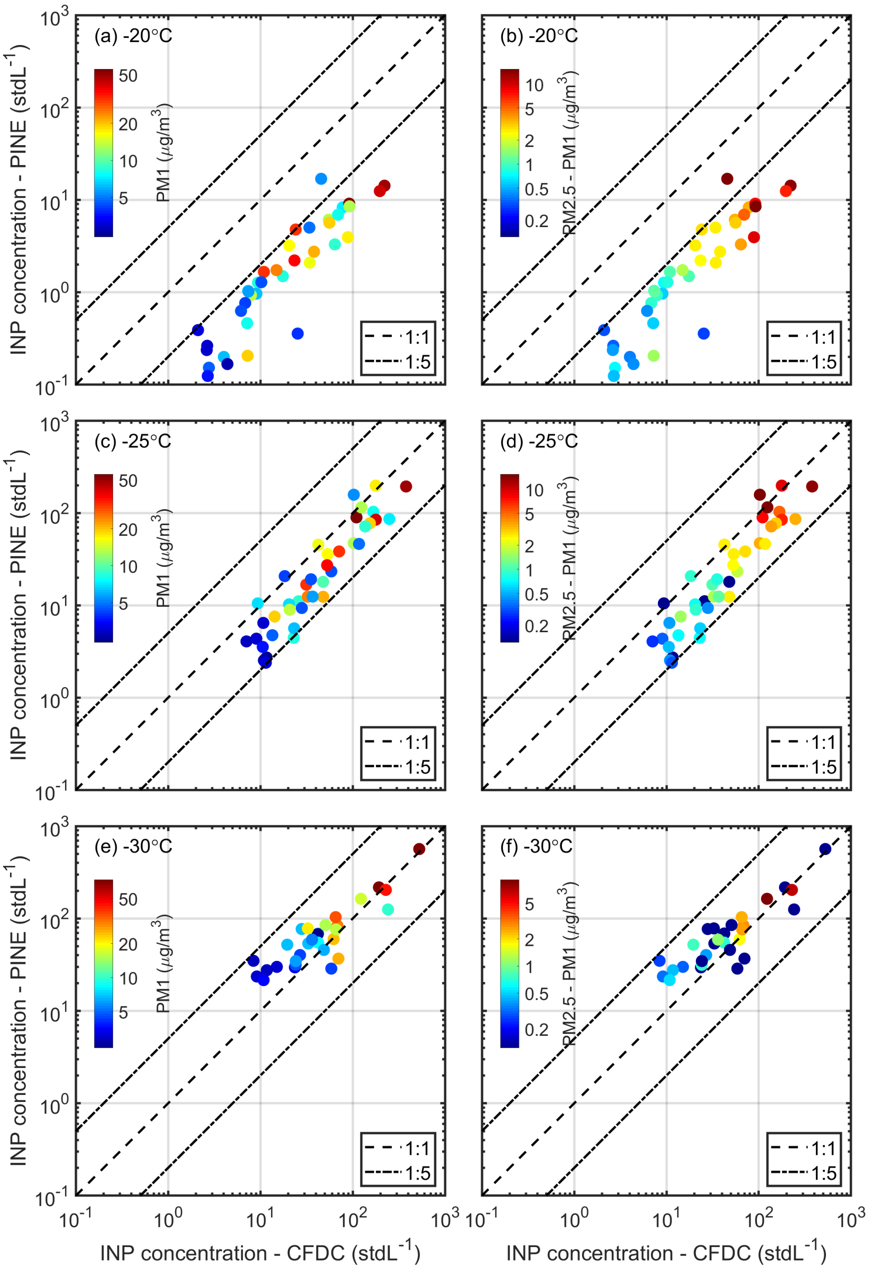

Figure 6.6: Six-panel comparison of INP concentrations measured by BJ-CFDC (x-axis) and PINE (y-axis). Rows correspond to $-20\,^{\circ}$C, $-25\,^{\circ}$C, and $-30\,^{\circ}$C (top to bottom), based on BJ-CFDC setpoints with time-matched PINE data. BJ-CFDC and PINE sampled through identical PM$_{2.5}$ inlets. For each temperature, the same BJ-CFDC–PINE INP pairs are shown in both columns; only the marker color differs. Marker color denotes APS-derived aerosol mass concentration—PM$_1$ in the left column and PM$_{2.5}$–PM$_1$ in the right column (μg m^{-3}). Dashed lines indicate the 1:1 and 1:5 relationships.

Figure 6.6 compares BJ-CFDC and PINE INP concentrations at three BJ-CFDC setpoints (−20 °C, −25 °C, −30 °C) using time-matched PINE data (six panels). BJ-CFDC and PINE sampled through identical $PM_{2.5}$ inlets. For each temperature, the same CFDC–PINE pairs appear in both columns; only the marker color changes to encode APS-derived aerosol mass (left: PM_1; right: $PM_{2.5}$–PM_1). Across −25 °C and −30 °C, the two instruments agree well: most points fall between the 1:1 and 1:5 dashed lines. At −25 °C, BJ-CFDC generally reports higher INP than PINE, as indicated by points lying below the 1:1 line and approaching 1:5. In contrast, at −20 °C agreement degrades, many points fall outside the 1:5 line, with BJ-CFDC exceeding PINE by more than a factor of five. The color gradients further show that INP abundance is more strongly associated with the coarse fraction ($PM_{2.5}$–PM_1) than with the fine mode (PM_1), especially at −20 °C and −25 °C, where higher coarse-mode mass coincides with higher INP concentrations. The fine-mode mass shows a weaker and less consistent relationship. Overall, the figure highlights temperature-dependent instrument differences and points to a dominant role of coarse-mode aerosols in driving ambient INP variability during the study period.

6.5.2 The relationship between INP and biological particles

Observations were conducted during the winter season, when biological aerosol activity is typically suppressed and non-biological sources dominate. Given this context, we aimed to investigate the relationship between WIBS-derived FAP signals and INP concentrations measured using the PINE chamber in the temperature range −31 °C to −19 °C.

To comprehensively evaluate the relationship between WIBS fluorescence signals and INP concentrations, Figure 6.7 presents a heatmap of the R^2 values from log–log regression fits, stratified by channel and freezing temperature. The PINE instrument provided INP concentrations at discrete subzero bins from −30 °C to −19 °C, while WIBS-4A channels encompassed both total and fluorescent particle counts.

For statistical rigor, each regression was subjected to hypothesis testing, and the resulting p-values were adjusted for multiple comparisons using the Benjamini–Hochberg procedure. Only channel–temperature combinations with adjusted p-values ($p_{\mathrm{adj}} < 0.05$) were considered statistically significant and scientifically meaningful. Non-significant results are indicated in the heatmap by red crosses.

The strongest associations were observed at colder temperatures, particularly below −25 °C, with channels such as `wibs_non`, `wibs_ntot`, and `wibs_any` consistently showing the highest R^2 values and statistical significance. In contrast, at temperatures warmer than −20 °C, correlations were generally weaker and often not statistically significant, suggesting reduced sensitivity of WIBS metrics to INP variability under those conditions.

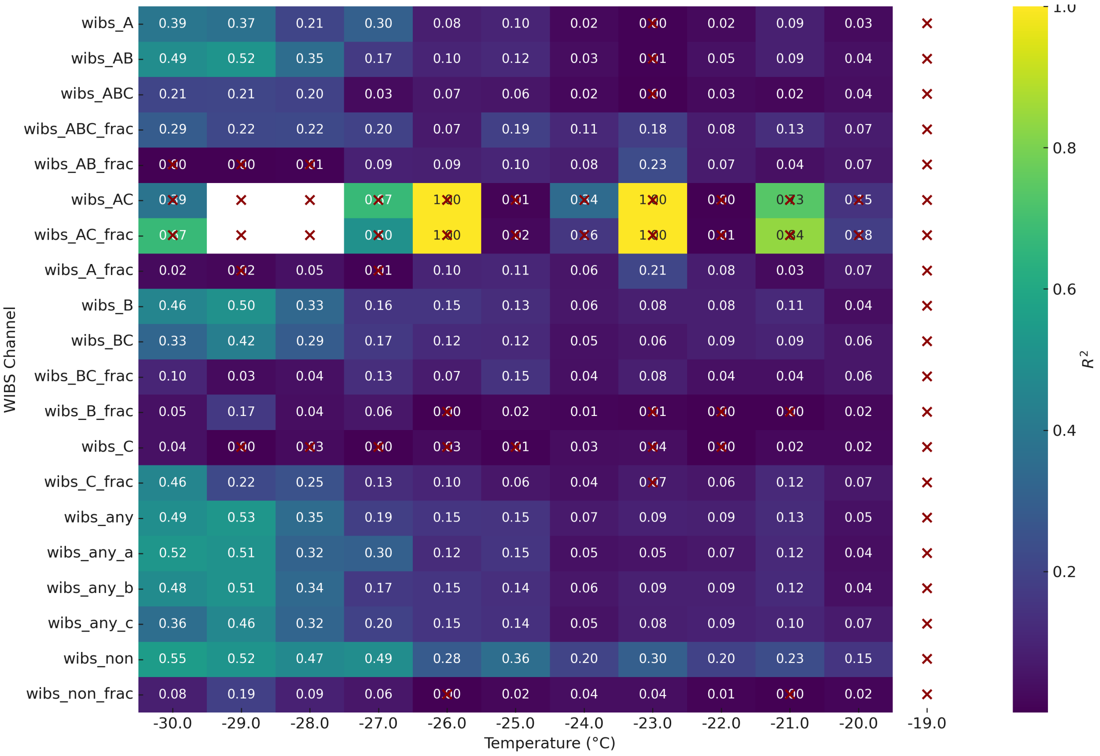

Figure 6.7: Heatmap of coefficient of determination (R^2) values from log–log regressions between WIBS-4A fluorescence channel counts and INP concentrations measured by the PINE instrument across a range of subzero temperatures. Each cell represents a unique channel–temperature pair. Deep color intensity indicates stronger regression fits. Red crosses denote channel–temperature combinations where the correlation was not statistically significant after false discovery rate correction ($p_{\text{adj}} \geq 0.05$). Only statistically significant associations are considered interpretable.

6.5.3 The relationship between INP and ambient aerosol

Despite the stringent Olympic emission-control measures—which sharply curtailed local primary sources—three pronounced haze episodes still developed. Their occurrence highlights that winter pollution over the North China Plain is fundamentally regional rather than strictly local: secondary inorganic aerosol is produced over a broad source area and can be efficiently transported into the mountain boundary layer even when Beijing’ s urban emissions are suppressed. These pollution events seen in Figure 6.8 during the Games are not evidence of control-measure failure at the venue itself, but rather of basin-scale circulation combining with intense regional precursor chemistry to maintain high particle loadings.

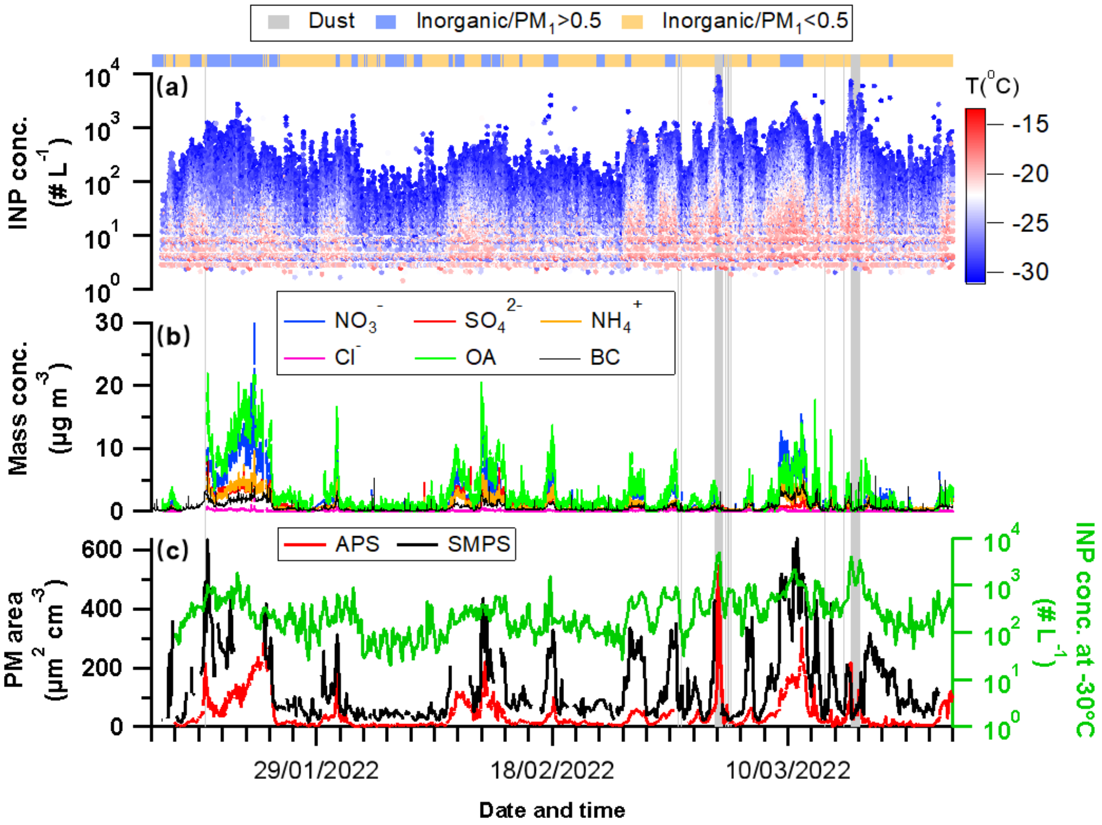

Figure 6.8: Continuous measurements of ice-nucleating particles (INPs) and aerosol physicochemical properties at Haituo mountain, Beijing, partitioned into dust-dominated (grey), inorganic-rich (blue; Inorganic/PM$_1 > 0.5$) and organic-rich (orange; Inorganic/PM$_1 < 0.5$) periods. Time series of (a) INP number concentration at temperatures from $-17\,^{\circ}\mathrm{C}$ to $-30\,^{\circ}\mathrm{C}$ in $0.5\,^{\circ}\mathrm{C}$ increments; (b) mass concentrations of key aerosol species ($\mathrm{SO_4}^{2-}$, $\mathrm{NO_3}^{-}$, OA, BC, etc.); (c) particle surface area in the coarse mode ($> 0.5\,\mu\mathrm{m}$) measured by an APS and in the 14 nm–700 nm range measured by a SMPS, with the green line denoting the INP number concentration at $-30\,^{\circ}\mathrm{C}$.

Figure 6.8 reveals that pollution episodes exhibit markedly higher INP number concentrations than clean periods across the entire immersion-freezing spectrum; this is inconsistent with a previous study (Tian et al., 2022), which also suggested that anthropogenic pollution could contribute to the INPs. During three multi-day haze events, the INP concentration at $-30\,^{\circ}\mathrm{C}$ rises to as high as $900\,\mathrm{L}^{-1}$—eight-fold above the clean-air baseline ($\approx 100\,\mathrm{L}^{-1}$).

Figure 6.8 shows that INP number concentrations peak during the three haze episodes, yet this rise is driven by the sheer increase in particle abundance rather than by enhanced ice-nucleating efficiency. Pollution pulses elevate coarse-mode surface area (APS, $>0.5\,\mu\mathrm{m}$) by roughly a factor of 2 and fine-mode surface area (SMPS, 14 nm to 700 nm) by 50–80 %. Because these particles are heavily coated with highly soluble secondary nitrates and sulfates, their intrinsic ability to catalyze freezing remains low; indeed, the campaign-mean ice-nucleating active site density, n_s, decreases during haze events. In other words, INP concentration rises simply because "more particles beget more nuclei," not because each particle becomes a better nucleus. Hence, while polluted air masses do supply additional INPs, the per-surface-area efficiency and thus the climatic relevance of secondary inorganic aerosol remains far inferior to that of mineral dust.

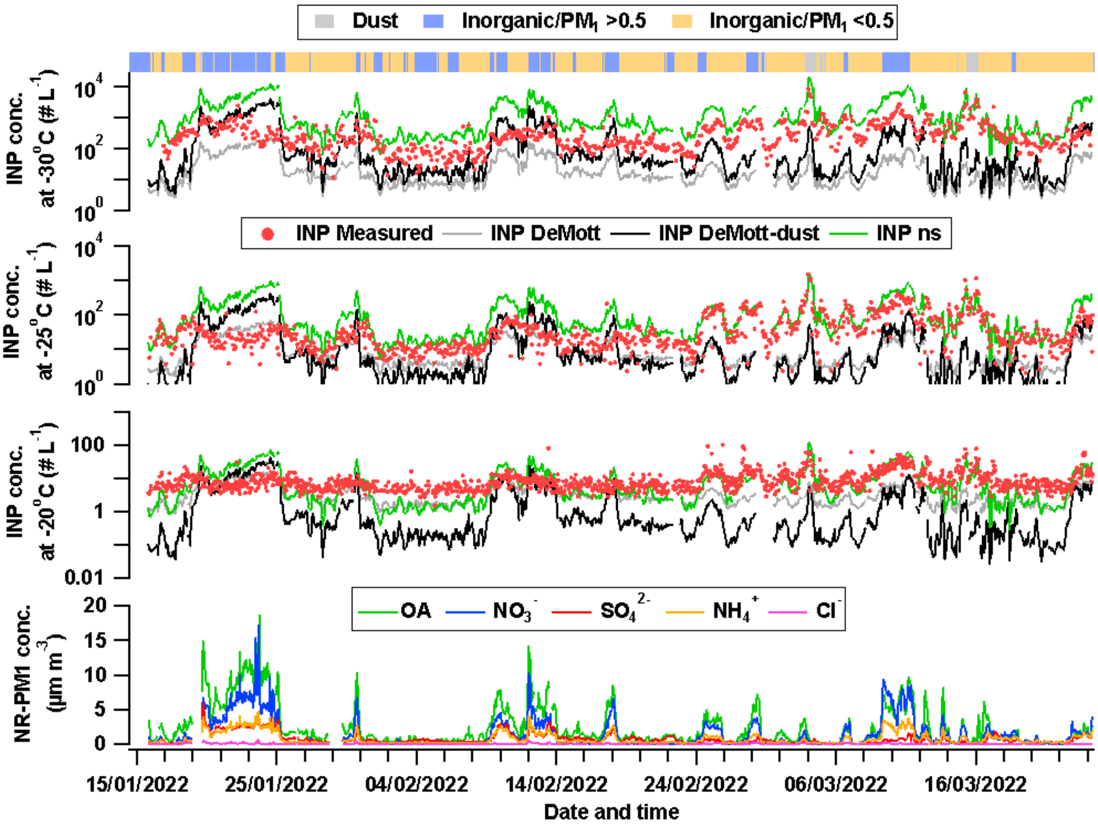

Figure 6.9: Comparison of previous INP parameterizations at −20 °C, −25 °C, and −30 °C; DeMott, Prenni, et al. (2010) and DeMott et al. (2015) were chosen for global average and mineral dust, and Niemand et al. (2012) for mineral dust.

Figure 6.9 presents the performance of three widely used INP parameterizations against the Haituo mountain observations. Panels (a)–(c) show time series of immersion-mode INP number concentrations at −20 °C, −25 °C and −30 °C, respectively. The red dots denote the measurements; colored lines denote predictions from (i) the global-average formulation of DeMott, Prenni, et al. (2010) (N500, grey), (ii) the dust-specific scheme of DeMott et al. (2015) (N500, red), and (iii) the particle-surface-area-based approach of Niemand et al. (2012) (green). The bar above the panels identifies aerosol regimes: dust (dark grey), inorganic-rich /pollution (blue) and organic-rich/clean periods (orange).

The dust-specific parameterizations of DeMott et al. (2015) and Niemand et al. (2012) capture the two brief dust incursions within a factor of five of the observations, confirming their calibration to mineral particles. However, outside these events, both dust schemes overestimate INP concentrations by 0.5–1.5 log units at −25 °C and −30 °C, while the global-average formulation underestimates by 1–2 log units across the campaign. None of the schemes reproduces the gradual INP increase during pollution periods dominated by secondary inorganic aerosol.

The temperature dependence reveals an anthropogenic contribution: at −20 °C the observed INP variability is substantially smaller than predicted by any scheme, and pollution-driven peaks (blue segments) exceed dust peaks, contrary to model forecasts. This indicates that internally mixed, chemically aged anthropogenic particles nucleate ice efficiently at warmer mixed-phase temperatures but lose activity sharply below −25 °C. Consequently, reliance on coarse mineral-dust predictors alone misrepresents both the amplitude and temperature scaling of INPs in a wintertime, high-emission North China environment.

In summary, Figure 6.9 demonstrates that parameterizations relying solely on dust particle number or surface area cannot reproduce INP concentrations during periods when both mineral dust and anthropogenic aerosols contribute, underscoring the need for a newly revised scheme that combines coarse-mode mineral predictors with composition-dependent terms.

6.5.4 The parameterization of INP

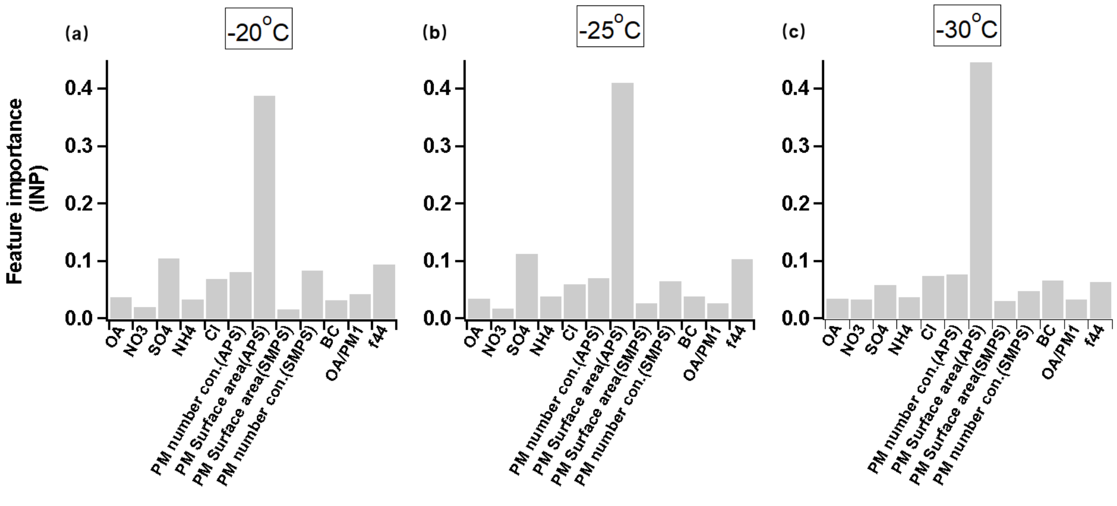

Figure 6.10: Relative importance of twelve predictor variables for explaining immersion-mode INP number concentrations at −20 °C, −25 °C and −30 °C. Predictors include bulk mass concentrations of $SO_4{}^{2-}$, $NO_3{}^{-}$, $NH_4{}^{+}$, Cl^{-}, OA and refractory black carbon; total particle number concentration N_{T} (14 nm–10 µm); coarse-mode number concentration N_{500}; total surface area SA (merged SMPS + APS spectra); and coarse-mode surface area $\mathrm{SA}_{>500\,\mathrm{nm}}$.

Figure 6.10 presents the relative importance of twelve predictor variables for immersion-mode INP number concentrations at −20 °C, −25 °C and −30 °C, as determined by a random-forest regression model. The training set comprised the full five-minute data record ($\approx$ 15 000 observations), stratified into 70 % training and 30 % test subsets, with 300 trees grown using out-of-bag sampling.

To capture both microphysical and compositional controls, the model was supplied with (i) bulk mass concentrations of $SO_4{}^{2-}$, $NO_3{}^{-}$, $NH_4{}^{+}$, Cl^{-}, OA and refractory black carbon (rBC); (ii) the total particle number concentration N_{T} integrated from 14 nm to 10 µm; (iii) the coarse-mode number concentration N_{500}; (iv) the total particle surface area SA derived from merged SMPS+APS spectra; and (v) the coarse-mode surface area $\mathrm{SA}_{>500\mathrm{nm}}$. All predictors were averaged onto the five-minute INP time grid and centred/log-transformed to reduce skewness.

Across all three temperatures, $\mathrm{SA}_{>500\mathrm{nm}}$ emerged as the single most influential predictor, accounting for 27–31 % of the explained variance at −20 °C, 34–38 % at −25 °C and 42–45 % at −30 °C. This ranking is physically plausible: immersion-freezing probability scales with available surface area, and coarse mineral or internally mixed particles provide orders-of-magnitude more surface than sub-micron aerosol at equivalent number loading. The increasing share of $\mathrm{SA}_{>500\mathrm{nm}}$ toward colder temperatures reflects the steep rise in mineral-dust active-site density below −20 °C.

Figure 6.11 illustrates how particle size and composition jointly modulate immersion-mode INP abundance and active-site density (n) in wintertime North China. Panels (a–c) relate INP concentration to coarse-mode number concentration N_{500} (aerodynamic diameter >500 nm) at −20 °C, −25 °C and −30 °C respectively; points are color-coded by inorganic/PM_1 mass ratio to distinguish inorganic-rich pollution, organic-dominated periods and dust periods, with dust points shown as filled symbols. The low coefficients of determination ($R^2 = 0.08, 0.02, 0.12$) indicate that coarse particle counts alone provide minimal predictive power, particularly during high-pollution segments where internally mixed inorganic particles dominate but offer few active sites.

Panels (d–f) replace coarse number with coarse-mode surface area $\mathrm{SA}_{>500\,\mathrm{nm}}$. Here the correlation strengthens ($R^2 = 0.40, 0.50, 0.56$) and the slope converges on the laboratory dust parameterization of (Niemand et al. (2012)). This improvement reflects the physical principle that immersion-freezing probability scales with accessible surface area, and that excluding submicron soluble haze particles suppresses “false-positive” predictors.

Panels (g–i) present the active-site density $n_s(T)$ calculated for each measurement as the ratio of INP number concentration to $\mathrm{SA}_{>500\,\mathrm{nm}}$. Histograms are divided into three composition classes: inorganic-rich (blue, Inorg/PM_1>0.5), organic-rich (green, Inorg/PM_1<0.5) and the full campaign population (grey). Dashed brown lines denote the median n_s for dust periods; solid yellow circles mark individual dust observations.

At cold temperatures (−25 °C and −30 °C), dust observations cluster at the high-efficiency tail and their median n_s exceeds that of polluted haze by approximately one order of magnitude, confirming that freshly transported mineral dust remains the dominant INP source under these conditions. Inorganic-rich haze exhibits the lowest n_s. At the warm end (−20 °C), the efficiency gap narrows as organic-rich pollution attains n_s comparable to dust while inorganic-rich samples remain inefficient, indicating that aged organics—either oxygenated secondary OA or biomass-derived high-molecular-weight fragments—can provide effective ice-nucleating sites near −20 °C.

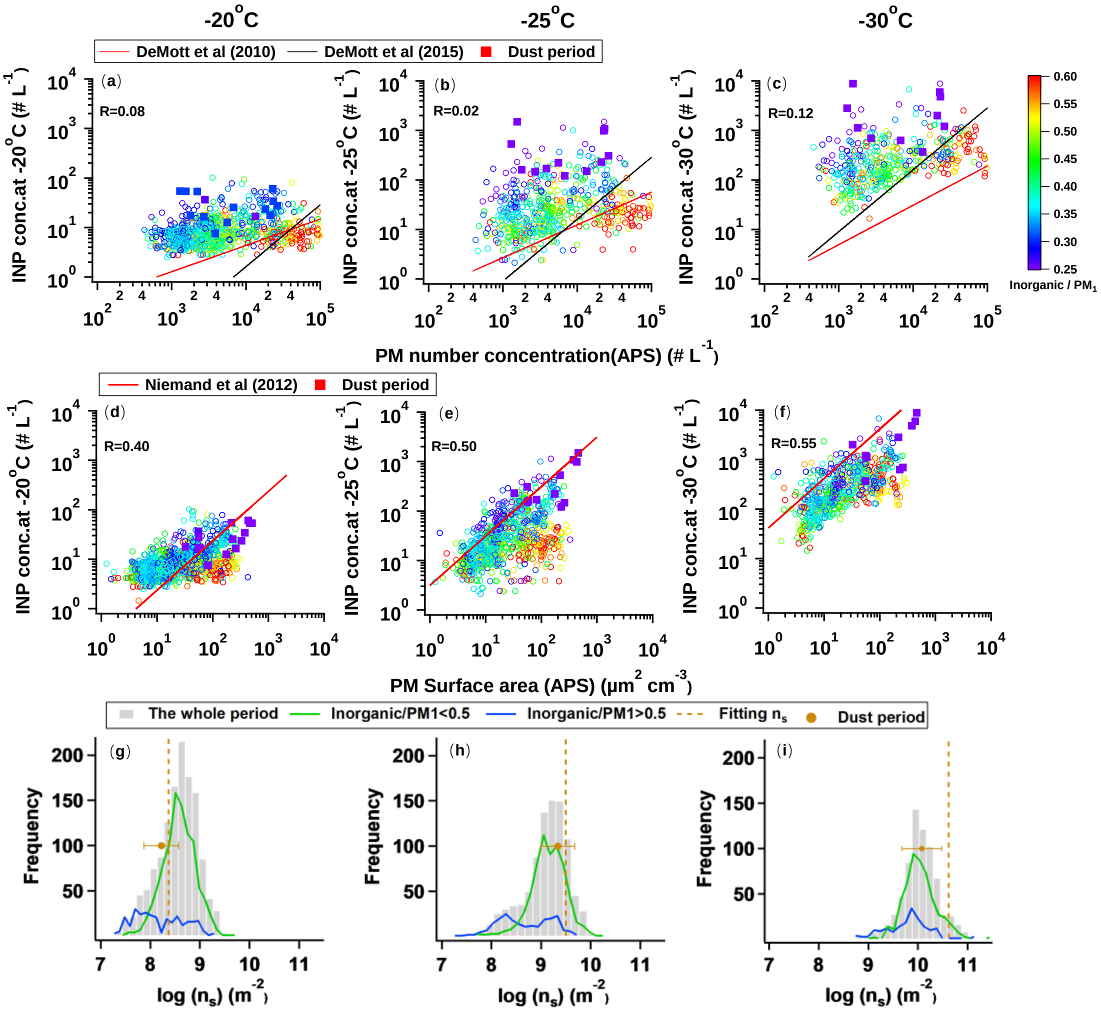

Figure 6.11: Correlations of INP concentrations with coarse-mode particle metrics and derived active-site densities at −20 °C, −25 °C and −30 °C. Panels (a–c) plot immersion-mode INP number concentration against coarse-mode number concentration N_{500} (aerodynamic diameter >500 nm); points are coloured by the inorganic-to-PM_1 mass ratio, with dust periods highlighted by filled symbols. Panels (d–f) replace number concentration with coarse-mode surface area $\mathrm{SA}_{>500\,\mathrm{nm}}$, and the red line shows the laboratory dust parameterization of (Niemand et al. (2012)). Panels (g–i) present histograms of active-site density $n_s(T)$ computed as INP number divided by $\mathrm{SA}_{>500\,\mathrm{nm}}$; composition classes are inorganic-rich (Inorg/PM_1>0.5, blue), organic-rich (Inorg/PM_1<0.5, green) and the full campaign (grey). Dashed brown lines mark median n_s for dust periods and yellow circles individual dust observations.

Collectively, Figure 6.11 demonstrates that parameterizations based solely on coarse-mode particle counts or submicron surface area fail to capture the full INP spectrum in mixed dust–pollution conditions. Using coarse-mode surface area $\mathrm{SA}_{>500\,\mathrm{nm}}$ as a first-order predictor greatly improves predictive skill by excluding the abundant but inactive submicron inorganic aerosol; composition—specifically mineral content at low temperatures and organic contributions near −20 °C—then refines the estimate. These findings support a dual-predictor framework combining coarse surface area scaling with a composition-dependent active-site density to better represent the INP characteristics under mixed dust–pollution conditions in wintertime North China.

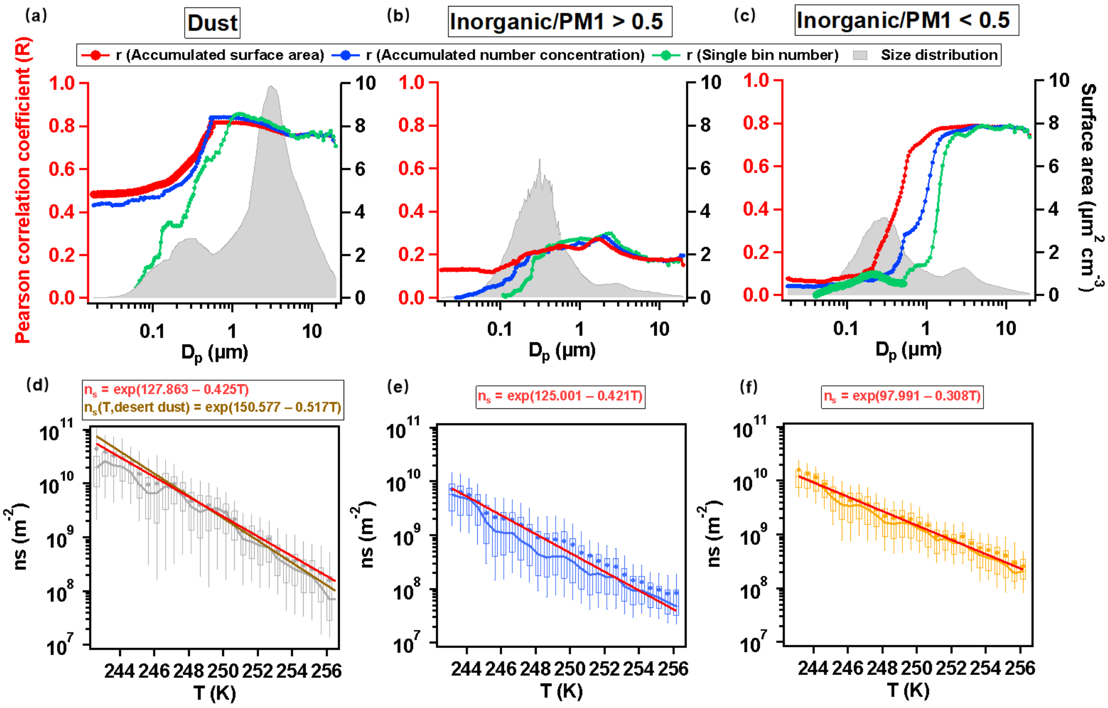

Figure 6.12: Linkage between INP abundance and aerosol size metrics under three compositional regimes. Panels (a)–(c) show Pearson correlation coefficients between immersion-mode INP number concentration and three aerosol predictors as a function of particle diameter D_p: cumulative surface area ($\sum$SA, red), cumulative number concentration ($\sum N$, blue), and single-size-bin number concentration (N_{bin}, green). Panels correspond to dust-dominated periods (a), inorganic-rich/pollution periods (Inorganic/PM$_1$ > 0.5; b), and organic-rich/clean periods (Inorganic/PM$_1$ < 0.5; c); grey histograms show the underlying size distributions. Panels (d)–(f) present empirical active-site-density parameterizations, $n_s(T) = \exp(a+bT)$, derived for the same regimes: dust (d, brown), inorganic-rich (e, blue), and organic-rich (f, orange).

Figure 6.12 quantifies why a coarse-mode surface-area predictor ($\geq 0.5\,\mu$m) provides the most robust link to immersion-mode INPs in the mixed dust–pollution environment of North China. Panels (a)–(c) display Pearson correlation coefficients between INP number concentration at $-25\,°$C and three size-resolved aerosol metrics as functions of particle aerodynamic diameter D_p: cumulative surface area (red), cumulative number concentration (blue) and single-bin number concentration (green). Each curve is plotted against the underlying size distribution (grey histogram) for dust (a), inorganic-dominated haze (Inorganic/PM$_1$ > 0.5; b) and organic-dominated/clean air (Inorganic/PM$_1$ < 0.5; c).

During dust periods the particle-size distribution shifts to radii >1 µm and the surface-area spectrum peaks near 2 µm, so all three predictors correlate strongly with INPs above ~0.7 µm and exceed $R \approx 0.8$ beyond 1 µm. Because both cumulative number and cumulative area capture the same narrow coarse mode, either metric yields similar n_s fits, explaining why both the DeMott-dust ($N_{>0.5\,\mu\text{m}}$)(DeMott et al., 2015) and Niemand-dust (SA$_{>0.5\,\mu\text{m}}$)(Niemand et al., 2012) schemes reproduce dust peaks (Figure 6.9).

In pollution (inorganic-dominated) episodes, the number and surface spectra are centered near 0.2 µm—a regime populated by internally mixed inorganic particles. Panel b shows that below 0.3 µm the correlations of INPs with both cumulative number and cumulative area hover near zero, reflecting the negligible immersion-freezing efficiency of soluble sub-micron aerosols. As diameter increases, the red curve (surface area) begins to climb, reaching $R \approx 0.31$ at 0.8 µm; the blue curve (number) rises more slowly and never exceeds this value.

The right-hand panel (c) represents cleaner or biomass-influenced days (organic-dominated periods, Inorg/PM < 0.5). Here, the surface-area correlations surge above 0.7 once D_p exceeds 0.5 µm, while the cumulative-number curve saturates near 0.4; this reflects that aged organics (oxygenated secondary OA or high-molecular-weight fragments) can provide active sites effective at -20 °C to -25 °C only when host particles exceed ∼0.3 µm and retain insoluble cores, so the surface-area metric naturally highlights these larger particles.

Panels (d)–(f) translate these empirical relationships into regime-specific active-site-density parameterizations $n_s(T) = \exp(a + bT)$ fitted to coarse-mode surface-area data (error bars denote $\pm 1\sigma$). Dust yields the highest intercept $a = 127.9$, inorganic haze the lowest $a = 125.0$, and organic periods an intermediate $a = 97.0$, while all slopes $b \approx -0.42\,\mathrm{K}^{-1}$ align with classical active-site theory. Compared with one-size-fits-all schemes, these regime-resolved curves reduce root-mean-square error by 40–60 %, underscoring the value of a size-filtered surface-area predictor.

These results clarify that INP increases during haze stem not from per-particle efficiency gains but from co-transport of a small number of coarse mineral or soot-bearing particles whose surface area dominates nucleation statistics. Selecting $\mathrm{SA}_{>0.5\,\mu\mathrm{m}}$as the primary predictor therefore (i) targets the size range most likely to host genuine active sites and (ii) suppresses the dilutive effect of abundant but ineffective fine-mode particles. In dust-rich air masses either number or area metrics perform adequately, but in polluted or organic-rich regimes surface area is demonstrably superior, justifying a dual-predictor framework—coarse surface area for first-order scaling augmented by composition-dependent active-site densities—that better represents the INP characteristics under mixed dust–pollution conditions during wintertime in North China.

6.6 Summary

A nine-week, high-time-resolution INP and aerosol dataset collected on Haituo Mountain during the 2022 Beijing Winter-Olympic emission-control period was analyzed to quantify the relative roles of mineral dust, anthropogenic pollution, and organic aerosol in governing the wintertime INP reservoir over North China. Five overarching conclusions emerge:

1. **Mineral dust dominates at cold mixed-phase temperature regime.** Two brief dust outbreaks increased coarse-mode surface area by an order of magnitude and pushed $-30\,^{\circ}\mathrm{C}$ INP concentrations above $1 \times 10^3\,\mathrm{L}^{-1}$, matching active-site densities reported for Asian dust; dust-tuned parameterizations (DeMott et al., 2015; Niemand et al., 2012) reproduced these peaks within a factor of five, confirming their applicability when mineral particles dominate the aerosol spectrum.

2. **Pollution raises INP counts but lowers per-particle efficiency.** During three multi-day haze events $\mathrm{PM}_{2.5}$ reached $50\,\mu\mathrm{g\,m}^{-3}$ and $-25\,^{\circ}\mathrm{C}$ INP concentrations increased to 5 to $300\,\mathrm{L}^{-1}$, yet active-site density n_s fell by roughly one order

of magnitude relative to dust periods, because haze injects vast numbers of submicron inorganic particles that add surface area but exhibit little intrinsic activity.

3. **Biological INPs are negligible in midwinter at high elevation.** WIBS fluorescence remained near instrumental background throughout the campaign and showed no correlation with INP abundance; consistently sub-freezing surface temperatures and scarce vegetation above 1344 m exclude a significant contribution from primary biological particles.

4. **A size-filtered surface-area predictor outperforms number-based metrics under mixed sources.** Random-forest analysis and correlation mapping demonstrate that coarse-mode surface area ($\mathrm{SA}_{>0.5\,\mu\mathrm{m}}$) explains 35 % to 55 % of INP variance up to twice that of cumulative number ($N_{>0.5\,\mu\mathrm{m}}$), particularly during pollution episodes when sub-micron counts soar because $\mathrm{SA}_{>0.5\,\mu\mathrm{m}}$ excludes "false positives" from the soluble fine mode while retaining sensitivity to larger particles that actually nucleate ice.

5. **Organic aerosol enhances INP activity at the warm end (−20 °C).** At −20 °C, the active-site density of organic-rich samples matches that of dust whereas inorganic-rich samples remain inefficient; literature indicates aged oxygenated organics can catalyze immersion freezing above −25 °C, suggesting a non-negligible organic contribution to the warm tail of the INP spectrum that warrants targeted laboratory confirmation.

A hybrid parameterization is therefore recommended in which (i) $\mathrm{SA}_{>0.5\,\mu\mathrm{m}}$ provides first-order scaling and (ii) regime-dependent active-site densities distinguish mineral, inorganic-pollution, and organic-rich aerosol. Incorporation of this mixed-source scheme into cloud and climate models is expected to improve simulations of winter cloud glaciation and precipitation over East-Asian megacity regions, where dust intrusions and severe haze frequently coexist.

Chapter 7

Summary and Outlook

7.1 General discussion

This dissertation integrates laboratory research (Chapter 4), long-term field observations (Chapter 5), and findings from intensive field campaign (Chapter 6), providing a comprehensive perspective on the abundance, variability, and sources of ice-nucleating particles (INPs) in the Beijing region.

Laboratory quantification of the intrinsic ice nucleation properties of Asian desert dust supports the observed seasonal and episodic variability of INP concentrations in the Beijing atmosphere. Chapter 4 demonstrates that Asian dust exhibits a steeper negative dependence of the INAS density on temperature compared to the benchmark derived from a mixture of desert dusts from multiple source regions, indicating distinct nucleation characteristics. This enhanced temperature sensitivity provides a mechanistic explanation for the persistently high and highly variable INP concentrations observed in spring (the season with the highest dust activity) and at the mountain site, which is more exposed to regional dust transport, as reported in Chapter 5. The parameterizations derived from laboratory results form a critical foundation for accurately simulating cloud formation and radiative properties over East Asia, especially in regions strongly influenced by Asian dust, and may contribute to improving consistency between model predciction and observation.

Beijing’ s distinctive aerosol environment, shaped by a mixture of natural mineral dust and intense anthropogenic pollution, results in highly variable aerosol–cloud interactions. The results presented in this study indicate that mineral dust remains the primary driver for the INP variability, even under heavy pollution conditions. Long-term observations presented in Chapter 5 reveal that based on the offline method, INP concentrations at all sites and temperatures reach their lowest levels even during the severe anthropogenic pollution in winter. The Winter Olympic Games presented and discussed in Chapter 6, which provided a unique natural experiment due to controlled emission reductions, and based on the online measurement using CFDC and PINE, clearly higher INP concentrations were found during the polluted period. About the controversy of the two methods, we highly doubt the filter sampling method under polluted conditions, and suggest design comparison of different sampling time and aerosol loading for future study.

This work also highlights the importance and challenges of multi-instrument application in INP research. The laboratory studies in Chapter 4, employing multiple instruments including AIDA, INKA, and INSEKT, reveal systematic offsets of up to two orders of magnitude in INP measurements, potentially attributable to different sensitivity to nucleation modes or different detection thresholds. During the intensive campaign (Chapter 6), comparison of INSEKT, PINE, BJ-CFDC, and FINDA demonstrated overall consistency in overlapping temperature ranges, yet also revealed instrument-specific detection thresholds, temperature sensitivity, and variability. For example, the BJ-CFDC recorded higher values at around −20 °C, reflecting enhanced sensitivity to certain nucleation modes, particularly during dust events. These findings highlight the complexity of obtaining accurate INP data and underscore the necessity of continued inter-instrument comparison, standardization of measurement protocols, and transparent reporting of instrument-specific sensitivities and operational conditions. For atmospheric models, this necessitates careful evaluation of potential systematic biases across different INP datasets, making comprehensive, multi-instrument studies such as this one indispensable for robust conclusions. Cross-validation and complementary datasets effectively reduce uncertainties inherent to single-instrument measurements.

In summary, the INP population in Beijing cannot be attributed to a single source, but rather represents a dynamic mixture that varies strongly with season, location, and meteorological conditions. Natural mineral dust is the primary driver of INP abundance and variability, particularly in spring and at mountain sites. While anthropogenic pollution is severe, its direct contribution to INPs is less significant than that of natural dust, acting more through indirect aging processes. Observations during the Winter Olympics reinforce this conclusion, as large-scale emission controls produced no significant direct impact on INP concentrations.

7.2 Outlook

The findings of this study contribute to improve regional and global climate models. The newly developed region-specific parameterization for the ice-nucleating properties of Asian desert dust, together with comprehensive long- and short-term field observations, provide observational constraints for developing new or improving existing INP parameterisations in models. Accurate representation of aerosol cloud interactions in polluted environments is critical for reliable climate prediction and impact assessment.

Based on the results and limitations of this study, future research directions are recommended as follows:

- **Advanced physico-chemical characterization:** It is recommended to conduct detailed post-analysis of archived dust and mixed aerosol samples (e.g., X-ray diffraction, electron microscopy, single-particle mass spectrometry). This will enable linking observed INP activity and variability to specific mineralogical compositions, surface features (e.g., fissures, pores), and morphological changes due to aging, thus addressing the limitations identified in Section 4.6 and providing deeper insight into the standards for aerosols acting as INPs.

- **Expansion of monitoring networks:** Long-term, high-resolution INP monitoring should be extended to more diverse sites across China and other regions of Asia to capture broader spatial trends, inter-annual variability, and the impacts of different source regions and transport pathways, building upon the framework established in Chapter 5. This will support a better understanding and model representation of the INP abundance in the atmosphere.

- **Dedicated studies on atmospheric aging:** Laboratory and field investigations should focus on the aging effects of various anthropogenic pollutants (e.g., sulfate, nitrate, organics, black carbon) on the ice-nucleating activity of natural INPs (e.g., mineral dust, biological particles). These studies should examine whether coatings inhibit or enhance activity under different atmospheric conditions, directly addressing the “aging paradox” and the poorly constrained properties of INPs in situations with mixed pollution and dust influence.

- **Model integration and validation:** The newly developed INP parameterization should be implemented in regional atmospheric models to evaluate its impacts on cloud microphysics, precipitation prediction, and regional radiative forcing. Direct testing and validation using independent observational datasets will be essential for refining the representation of INPs in models.
- **Vertical distribution studies:** Further research should address the vertical distribution of INPs in the Beijing region, potentially using tethered balloons, UAVs, or aircraft. This will address the current lack of free tropospheric INP data and provide critical insight into INP transport and their influence on high-altitude cloud formation.

7.3 Final summary

This dissertation significantly advances the understanding of the abundance, variability, and sources of INPs in the Beijing region, providing key data and region-specific parameterizations for atmospheric models, and underscoring the irreplaceable value of multi-instrument joint detection for improving the accuracy and reliability of INP measurements. The findings, particularly those concerning the complex interactions between natural dust and anthropogenic aerosols, have broad applicability to other polluted megacities worldwide. Beijing, as a critical case study, offers insights into how human activities alter natural cloud formation processes, which is essential for understanding and predicting climate change impacts in similar environments. The observed seasonal, spatial, and short-term variability of INPs documented in this work is highly relevant for advancing knowledge of cloud formation, precipitation efficiency, and the radiative balance over East Asia.

Appendix

.1 Appendix for Chapter 4

.1.1 INP concentration spectra of the $< 20\,\mu m$ size fractions of desert dust bulk samples

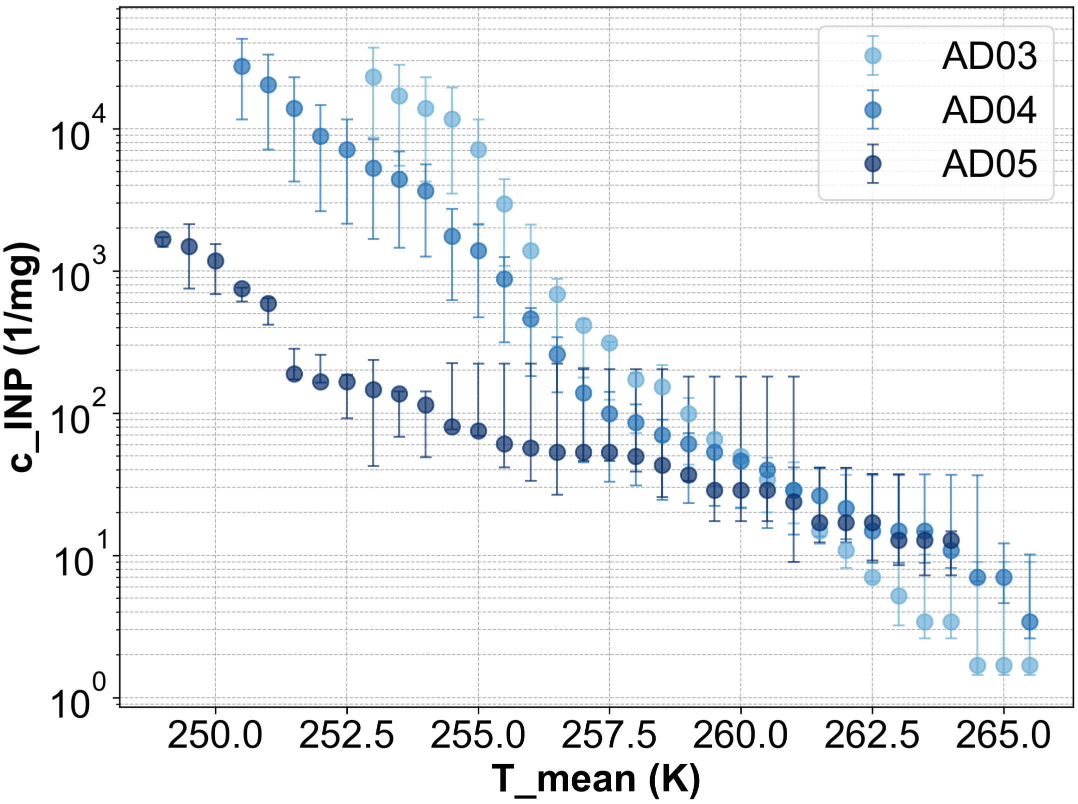

Figure 1: Ice-nucleating particle concentration spectra measured by the INSEKT instrument for the $< 20\,\mu m$ size fractions of desert dust bulk samples. AD03, AD04, and AD05 are each represented by blue circles, with the color gradient increasing in intensity from light blue for AD03, to medium blue for AD04, and dark blue for AD05.

Figure 1 compares the temperature-dependent INP concentration spectra measured by INSEKT for the $< 20\,\mu m$ fractions of four desert dust samples: AD03, AD04, and AD05 are all depicted as blue circles, with the color shade ranging from light blue (AD03) to dark blue (AD05). Each $3\,\mu g$ fraction was suspended in $< 10\,\mu L$ of nanopure water and subjected to the droplet-freezing assay, yielding the temperature-dependent INP concentration profiles.

All three samples display the characteristic steep decline in c_{INP} with increasing temperature, spanning approximately from $\sim 10^5\,\mathrm{L^{-1}\,mg^{-1}}$ around 250 K to below $10^1\,\mathrm{L^{-1}\,mg^{-1}}$ by 265 K. AD03 and AD04 follow nearly identical spectra at all temperatures. In the "high-temperature" regime ($T \gtrsim 257\,\mathrm{K}$), AD03–AD05 each display INP concentrations of order 10^0–$10^2\,\mathrm{L^{-1}\,mg^{-1}}$.As temperature decreases into the "low-temperature" regime ($T \lesssim 255\,\mathrm{K}$), AD03 gives INP concentrations approximately five times greater than AD04 at the same temperatures, whereas AD05 remains about one order of magnitude lower than AD04.These observations reveal that, while all three Asian dusts share broadly similar ice-nucleating behavior at warmer subzero conditions, their relative activities diverge at colder temperatures, with AD03 maintaining a higher efficacy.

.1.2 Reproducibility of APS Number Size Distributions for Sample AD03 in INAD02

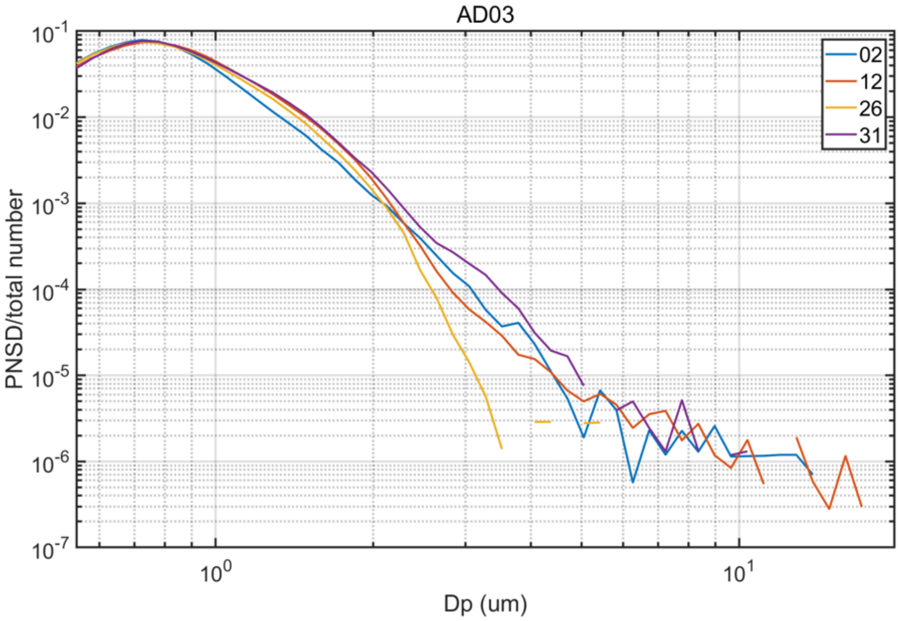

Figure 2: Particle number size distributions (PNSD) for the AD03 sample, measured by the Aerodynamic Particle Sizer (APS) during four separate experiments in the INAD02 campaign. Each curve represents one experiment (labels 02, 12, 26, and 31). The distributions are normalized to the total particle number concentration in each case.

Figure 2 presents the normalized particle number size distributions (PNSD) of the AD03 sample, as measured by the Aerodynamic Particle Sizer (APS) in four independent experiments during the INAD02 campaign. Across all trials, the AD03 sample exhibits highly consistent and reproducible particle size distributions, as each run' s distribution normalized by total particle number concentration retains the same characteristic features regardless of experimental conditions. This repeatability underscores the robustness of the aerosolization and measurement protocol, providing a reliable basis for subsequent comparative analyses of ice-nucleating properties using these aerosol preparations.

.2 Appendix for Chapter 5

.2.1 Comparison of weekly-averaged INP concentrations across sites and periods

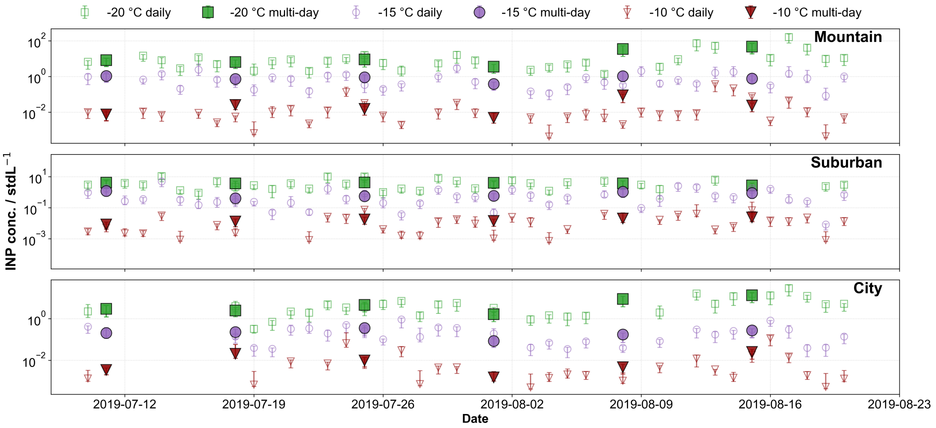

(a) 2019-07-10–2019-08-21

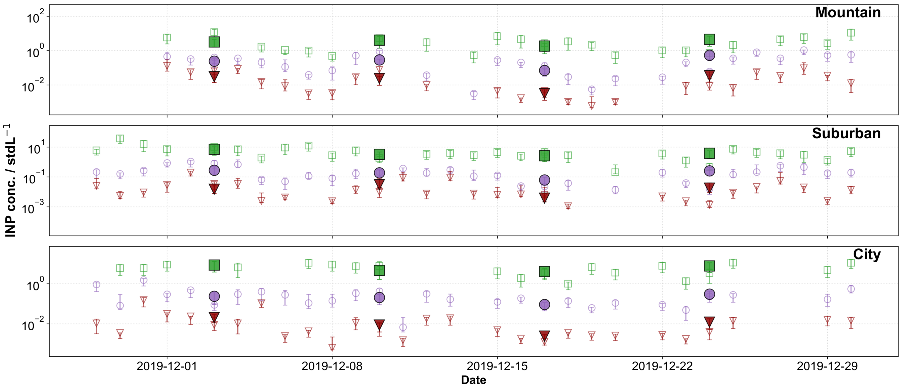

(b) 2019-11-28–2019-12-30

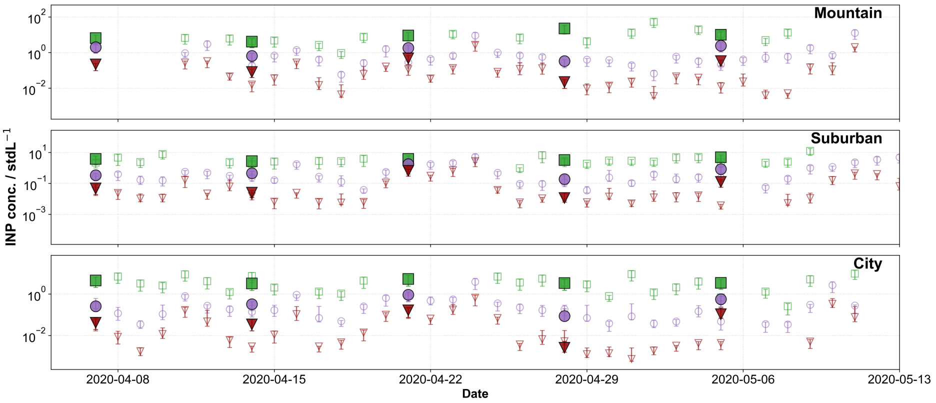

(c) 2020-04-07–2020-05-11

Figure 3: Weekly-averaged time series of INP concentrations at the mountain, suburban, and city sites, shown for three representative periods: (a) 2019-07-10 to 2019-08-21, (b) 2019-11-28 to 2019-12-30, and (c) 2020-04-07 to 2020-05-11.

Figure 3 shows the Weekly-averaged time series of INP concentrations at the mountain, suburban, and city sites, shown for three representative periods:(a) 2019-07-10 to 2019-08-21, (b) 2019-11-28 to 2019-12-30, and (c) 2020-04-07 to 2020-05-11. Daily data have been aggregated to weekly means to reduce short-term variability and facilitate direct seasonal and site-to-site comparisons. Comparing the original daily data (faded points) and the weekly means (bold markers), it is apparent that weekly averaging smooths out some extreme values while retaining the general variability and trends present in the daily data. This approach enables a robust comparison across sites and seasons with weekly data, while daily-resolution data are retained for case studies and event-based analyses in subsequent sections.

.2.2 Site- and season-specific comparison of mean and median INP temperature spectra

Figure 4 presents the mean and median INP temperature spectra for the mountain, suburban, and city sites across four seasons, enabling a direct comparison of these two statistical metrics at each location.

At all three sites, the mean INP concentrations exceed the median across the full temperature range, with the most pronounced differences observed at the mountain site, especially at lower temperatures. This systematic disparity between mean and median is indicative of positively skewed INP distributions, where episodic high-INP events elevate the mean but have a smaller effect on the median. Such behavior is particularly evident in spring and autumn at the mountain site.

During winter, the difference between mean and median narrows further across all sites, pointing to decreased variability in INP sources and atmospheric conditions during this season.

Comparing the three locations, the mountain site consistently exhibits the highest INP concentrations in most seasons and over the entire temperature range, underscoring the dominant contribution of natural sources and the effect of site elevation and exposure. While all sites show a seasonal pattern with higher INP concentrations in spring and autumn than in summer and winter, the city site displays more closely aligned summer and winter curves, and the winter INP concentrations at this site remain low for both mean and median, indicating a limited influence of episodic.

Overall, these results highlight significant temporal and spatial variability in INP abundance and emphasize the importance of employing both mean and median statistics to characterize the frequency and intensity of INP-relevant events. The divergence between these metrics, especially at the mountain site, underscores the critical role of sporadic high-INP episodes in shaping the overall distribution.

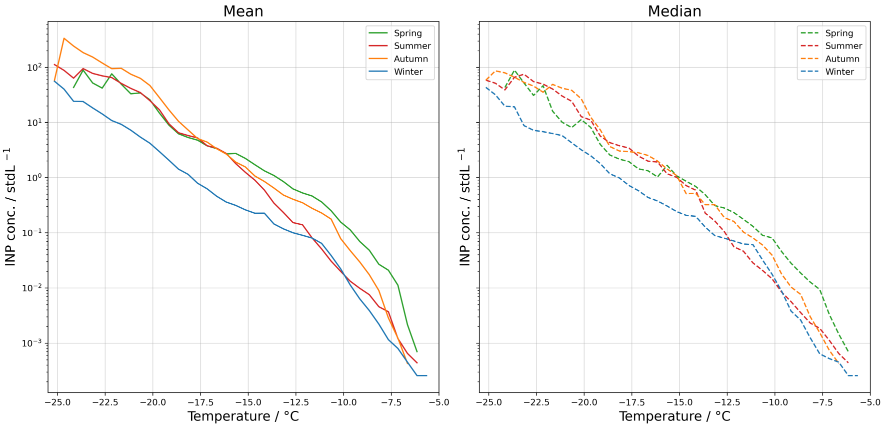

(a) mountain site

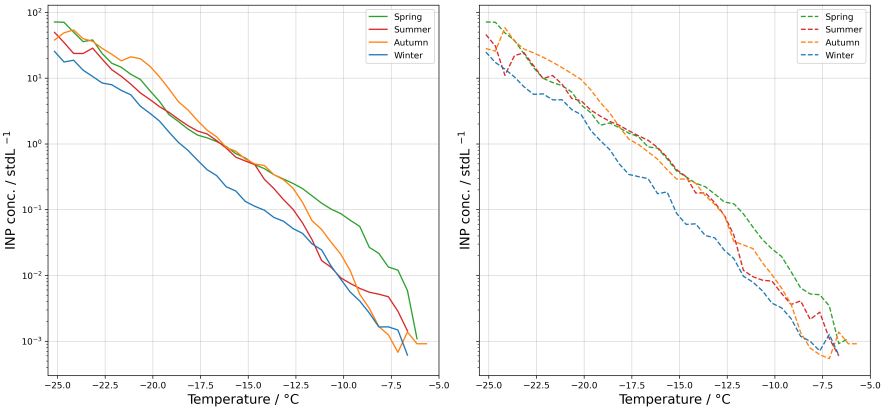

(b) suburban site

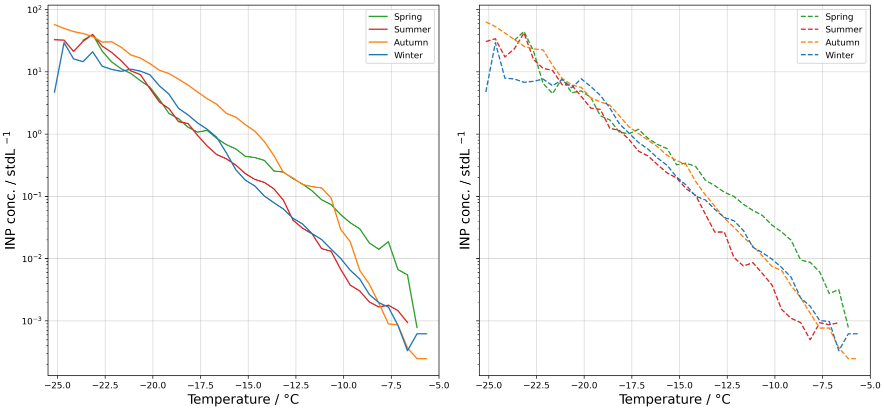

(c) city site

Figure 4: Comparison of mean and median INP temperature spectra measured with INSEKT at mountain site (upper left), suburban site (upper right) and city site (bottom) for the different seasons from July 2019 to July 2020.

.3 Appendix for Chapter 6

Table 1: Definitions of fluorescence-resolved (FL-resolved) particles used in this study.

Short name	Description
PBAPs	Primary biological aerosol particles
FAPs	Fluorescent aerosol particles
non-FAPs	Non-fluorescent biological aerosol particles
FAP-FL1	Fluorescent particles detected in channel FL1 (280 nm excitation, 310–400 nm detection)
FAP-FL2	Fluorescent particles detected in channel FL2 (280 nm excitation, 420–650 nm detection)
FAP-FL3	Fluorescent particles detected in channel FL3 (370 nm excitation, 420–650 nm detection)
FL A	Fluorescent particles detected in channel FL1 only
FL B	Fluorescent particles detected in channel FL2 only
FL C	Fluorescent particles detected in channel FL3 only
FL AB	Fluorescent particles detected in channels FL1 and FL2
FL AC	Fluorescent particles detected in channels FL1 and FL3
FL BC	Fluorescent particles detected in channels FL2 and FL3
FL ABC	Fluorescent particles detected in channels FL1, FL2, and FL3

Bibliography

Abbatt, J. P. D., Benz, S., Cziczo, D. J., Kanji, Z., Lohmann, U., & Möhler, O. (2006). Solid ammonium sulfate aerosols as ice nuclei: A pathway for cirrus cloud formation. *Science*, *313*(5794), 1770–1773. https://doi.org/10.1126/science.1129726

Adams, M. P., Tarn, M. D., Sanchez-Marroquin, A., Porter, G. C. E., O'Sullivan, D., Harrison, A. D., Cui, Z., Vergara-Temprado, J., Carotenuto, F., Holden, M. A., Daily, M. I., Whale, T. F., Sikora, S. N. F., Burke, I. T., Shim, J.-U., McQuaid, J. B., & Murray, B. J. (2020). A major combustion aerosol event had a negligible impact on the atmospheric ice-nucleating particle population. *Journal of Geophysical Research: Atmospheres*, *125*(22), e2020JD032938. https://doi.org/10.1029/2020JD032938

An, Z., Huang, R.-J., Zhang, R., Tie, X., Li, G., Cao, J., Zhou, W., Shi, Z., Han, Y., Gu, Z., & Ji, Y. (2019). Severe haze in northern China: A synergy of anthropogenic emissions and atmospheric processes. *Proceedings of the National Academy of Sciences*, *116*(18), 8657–8666. https://doi.org/10.1073/pnas.1900125116

Asher, E. C., Christensen, J. N., Post, A., Perry, K., Cliff, S. S., Zhao, Y., Trousdell, J., & Faloona, I. (2018). The transport of Asian dust and combustion aerosols and associated ozone to north America as observed from a mountaintop monitoring site in the California coast range. *Journal of Geophysical Research: Atmospheres*, *123*(10), 5667–5680. https://doi.org/10.1029/2017JD028075

Atkinson, J. D., Murray, B. J., Woodhouse, M. T., Whale, T. F., Baustian, K. J., Carslaw, K. S., Dobbie, S., O'Sullivan, D., & Malkin, T. L. (2013). The importance of feldspar for ice nucleation by mineral dust in mixed-phase clouds. *Nature*, *498*(7454), 355–358. https://doi.org/10.1038/nature12278

Barahona, D. (2018). On the thermodynamic and kinetic aspects of immersion ice nucleation. *Atmospheric Chemistry and Physics*, *18*(23), 17119–17141. https://doi.org/10.5194/acp-18-17119-2018

Belosi, F., Santachiara, G., & Prodi, F. (2011). Eyjafjallajökull volcanic eruption: Ice nuclei and particle characterization. *Atmospheric and Climate Sciences*, *1*(2), 48–54. https://doi.org/10.4236/acs.2011.12005

Benz, S., Megahed, K., Möhler, O., Saathoff, H., Wagner, R., & Schurath, U. (2005). T-dependent rate measurements of homogeneous ice nucleation in cloud droplets using a large atmospheric simulation chamber. *Journal of Photochemistry and Photobiology, A: Chemistry*, *176*(1), 208–217. https://doi.org/10.1016/j.jphotochem.2005.08.026

Bergeron, T. (1935). On the physics of clouds and precipitation. *Proc. 5th Assembly UGGI, Lisbon, Portugal, 1935*, 156–180.

Bi, K., McMeeking, G. R., Ding, D. P., Levin, E. J. T., DeMott, P. J., Zhao, D. L., Wang, F., Liu, Q., Tian, P., Ma, X. C., Chen, Y. B., Huang, M. Y., Zhang, H. L., Gordon, T. D., & Chen, P. (2019). Measurements of ice nucleating particles in

Beijing, China. *Journal of Geophysical Research: Atmospheres*, *124*(14), 8065–8075. https://doi.org/10.1029/2019JD030609

Bi, K., Huang, M., Ma, X., Tian, P., Chen, Y., & Ding, D. (2020). Observation and analysis on atmospheric ice nucleating particles with online continuous flow diffusion chamber in winter in north china. *Chinese Journal of Atmospheric Sciences (in Chinese)*, *6*(3), 315–323. （原文：毕凯, 黄梦宇, 马新成, 等. 2020. 在线连续流量扩散云室对华北冬季大气冰核的观测分析 [J]. 大气科学, 44(6): 1243−1257. DOI: 10.3878/j.issn.1006-9895.1911.19194）.

Bogert, P. (2024). *Ice-nucleating particles in the free troposphere: Long-term observation and first measurements at cirrus formation temperatures using the novel portable ice nucleation experiment PINEair* [Doctoral dissertation, Karlsruher Instituts für Technologie (KIT)].

Boose, Y., Baloh, P., Plötze, M., Ofner, J., Grothe, H., Sierau, B., Lohmann, U., & Kanji, Z. A. (2019). Heterogeneous ice nucleation on dust particles sourced from nine deserts worldwide – part 2: Deposition nucleation and condensation freezing. *Atmospheric Chemistry and Physics*, *19*(2), 1059–1076. https://doi.org/10.5194/acp-19-1059-2019

Boose, Y., Welti, A., Atkinson, J., Ramelli, F., Danielczok, A., Bingemer, H. G., Plötze, M., Sierau, B., Kanji, Z. A., & Lohmann, U. (2016). Heterogeneous ice nucleation on dust particles sourced from nine deserts worldwide – part 1: Immersion freezing. *Atmospheric Chemistry and Physics*, *16*(23), 15075–15095. https://doi.org/10.5194/acp-16-15075-2016

Bras, Y., Freney, E., Canzi, A., Amato, P., Bouvier, L., Pichon, J.-M., Picard, D., Minguillón, M. C., Pérez, N., & Sellegri, K. (2024). Seasonal variations, origin, and parameterization of ice-nucleating particles at a mountain station in central France. *Earth and Space Science*, *11*(6), e2022EA002467. https://doi.org/10.1029/2022EA002467

Brunner, C., Brem, B. T., Collaud Coen, M., Conen, F., Steinbacher, M., Gysel-Beer, M., & Kanji, Z. A. (2022). The diurnal and seasonal variability of ice-nucleating particles at the high altitude station Jungfraujoch (3580 m a.s.l.), switzerland. *Atmospheric Chemistry and Physics*, *22*(11), 7557–7573. https://doi.org/10.5194/acp-22-7557-2022

Brunner, C., & Kanji, Z. A. (2021). Continuous online monitoring of ice-nucleating particles: Development of the automated horizontal ice nucleation chamber (HINC-Auto). *Atmospheric Measurement Techniques*, *14*, 269–293. https://doi.org/10.5194/AMT-14-269-2021

Bundke, U., Nillius, B., Jaenicke, R., Wetter, T., Klein, H., & Bingemer, H. (2008). The fast ice nucleus chamber FINCH. *Atmospheric Research*, *90*(2), 180–186. https://doi.org/10.1016/j.atmosres.2008.02.008

Burrows, S. M., McCluskey, C. S., Cornwell, G., Steinke, I., Zhang, K., Zhao, B., Zawadowicz, M., Raman, A., Kulkarni, G., China, S., Zelenyuk, A., & DeMott, P. J. (2022). Ice-nucleating particles that impact clouds and climate: Observational and modeling research needs. *Reviews of Geophysics*, *60*(2), e2021RG000745. https://doi.org/10.1029/2021RG000745

Calvo, A. I., Baumgardner, D., Castro, A., Fernández-González, D., Vega-Maray, A. M., Valencia-Barrera, R. M., Oduber, F., Blanco-Alegre, C., & Fraile, R. (2018). Daily behavior of urban fluorescing aerosol particles in northwest Spain. *Atmospheric Environment*, *184*, 262–277. https://doi.org/10.1016/j.atmosenv.2018.04.027

Canagaratna, M. R., Jayne, J. T., Jimenez, J. L., Allan, J. D., Alfarra, M. R., Zhang, Q., Onasch, T. B., Drewnick, F., Coe, H., Middlebrook, A., Delia, A., Williams, L. R., Trimborn, A. M., Northway, M. J., DeCarlo, P. F., Kolb, C. E., Davidovits, P., & Worsnop, D. R. (2007). Chemical and microphysical characterization of ambient aerosols with the aerodyne aerosol mass spectrometer. *Mass Spectrometry Reviews*, *26*(2), 185–222. https://doi.org/10.1002/mas.20115

Canagaratna, M. R., Jimenez, J. L., Kroll, J. H., Chen, Q., Kessler, S. H., Massoli, P., Hildebrandt Ruiz, L., Fortner, E., Williams, L. R., Wilson, K. R., Surratt, J. D., Donahue, N. M., Jayne, J. T., & Worsnop, D. R. (2015). Elemental ratio measurements of organic compounds using aerosol mass spectrometry: Characterization, improved calibration, and implications. *Atmospheric Chemistry and Physics*, *15*(1), 253–272. https://doi.org/10.5194/acp-15-253-2015

Cantrell, W., & Heymsfield, A. (2005). Production of ice in tropospheric clouds - a review. *BULLETIN OF THE AMERICAN METEOROLOGICAL SOCIETY*, *86*(6), 795–807. https://doi.org/10.1175/BAMS-86-6-795

Che, Y., Dang, J., Fang, W., Shen, X., Sun, J., Chen, Y., & Qian, Y. (2019). Measurements of natural ice nucleating particles in Beijing in the spring of 2017. *Atmospheric Environment*, *200*, 170–177. https://doi.org/10.1016/j.atmosenv.2018.12.020

Che, Y., Zhang, J., Zhao, C., Fang, W., Xue, W., Yang, W., Ji, D., Dang, J., Duan, J., Sun, J., Shen, X., & Zhou, X. (2021). A study on the characteristics of ice nucleating particles concentration and aerosols and their relationship in Spring in Beijing. *Atmospheric Research*, *247*, 105196. https://doi.org/10.1016/j.atmosres.2020.105196

Chen, J., Wu, Z., Augustin-Bauditz, S., Grawe, S., Hartmann, M., Pei, X., Liu, Z., Ji, D., & Wex, H. (2018). Ice-nucleating particle concentrations unaffected by urban air pollution in Beijing, China. *Atmospheric Chemistry and Physics*, *18*(5), 3523–3539. https://doi.org/10.5194/acp-18-3523-2018

Chen, J., Wu, Z., Gong, X., Qiu, Y., Chen, S., Zeng, L., & Hu, M. (2024). Anthropogenic dust as a significant source of ice-nucleating particles in the urban environment. *Earth's Future*, *12*(1), e2023EF003738. https://doi.org/10.1029/2023EF003738

Chen, J., Wu, Z., Chen, J., Reicher, N., Fang, X., Rudich, Y., & Hu, M. (2021). Size-resolved atmospheric ice-nucleating particles during east Asian dust events. *Atmospheric Chemistry and Physics*, *21*(5), 3491–3506. https://doi.org/10.5194/acp-21-3491-2021

Chen, J., Wu, Z., Meng, X., Zhang, C., Chen, J., Qiu, Y., Chen, L., Fang, X., Wang, Y., Zhang, Y., Chen, S., Gao, J., Li, W., & Hu, M. (2023). Observational evidence for the non-suppression effect of atmospheric chemical modification on the ice nucleation activity of east Asian dust. *Science of the Total Environment*, *861*, 160708. https://doi.org/10.1016/j.scitotenv.2022.160708

Chen, Q., Yin, Y., Jiang, H., Chu, Z., Xue, L., Shi, R., Zhang, X., & Chen, J. (2019). The roles of mineral dust as cloud condensation nuclei and ice nuclei during the evolution of a hail storm. *Journal of Geophysical Research: Atmospheres*, *124*(24), 14262–14284. https://doi.org/10.1029/2019JD031403

Cheng, B., Yue, S., Hu, W., Ren, L., Deng, J., Wu, L., & Fu, P. (2020). Summertime fluorescent bioaerosol particles in the coastal megacity Tianjin, north China. *Science of the Total Environment*, *723*, 137966. https://doi.org/10.1016/j.scitotenv.2020.137966

Clancy, J. H., Markey, E., Martínez-Bracero, M., Maya-Manzano, J. M., McGillicuddy, E. J., Sewell, G., Sarda-Estève, R., Baisnée, D., Vélez-Pereira, A. M., Davis, G., & O'Connor, D. J. (2025). Comparative analysis of real-time fluorescence-based spectroscopic instruments: Bioaerosol detection in the urban environment of Dublin city, Ireland. *Atmosphere*, *16*(3), 275. https://doi.org/10.3390/atmos16030275

Conen, F., Morris, C. E., Leifeld, J., Yakutin, M. V., & Alewell, C. (2011). Biological residues define the ice nucleation properties of soil dust. *Atmospheric Chemistry and Physics*, *11*(18), 9643–9648. https://doi.org/10.5194/acp-11-9643-2011

Connolly, P. J., Möhler, O., Field, P. R., Saathoff, H., Burgess, R., Choularton, T., & Gallagher, M. (2009). Studies of heterogeneous freezing by three different desert dust samples. *Atmospheric Chemistry and Physics*, *9*(8), 2805–2824. https://doi.org/10.5194/acp-9-2805-2009

Corbin, J., Rehbein, P., Evans, G., & Abbatt, J. (2012). Combustion particles as ice nuclei in an urban environment: Evidence from single-particle mass spectrometry. *Atmospheric Environment*, *51*, 286–292. https://doi.org/10.1016/j.atmosenv.2012.01.007

Crawford, I., Robinson, N. H., Flynn, M. J., Foot, V. E., Gallagher, M. W., Huffman, J. A., Stanley, W. R., & Kaye, P. H. (2014). Characterisation of bioaerosol emissions from a Colorado pine forest: Results from the BEACHON-RoMBAS experiment. *Atmospheric Chemistry and Physics*, *14*(16), 8559–8578. https://doi.org/10.5194/acp-14-8559-2014

Creamean, J. M., Suski, K. J., Rosenfeld, D., Cazorla, A., DeMott, P. J., Sullivan, R. C., White, A. B., Ralph, F. M., Minnis, P., Comstock, J. M., Tomlinson, J. M., & Prather, K. A. (2013). Dust and biological aerosols from the Sahara and Asia influence precipitation in the western U.S. *Science*, *339*(6127), 1572–1578. https://doi.org/10.1126/science.1227279

Creamean, J. M., Barry, K., Hill, T. C. J., Hume, C., DeMott, P. J., Shupe, M. D., Dahlke, S., Willmes, S., Schmale, J., Beck, I., Hoppe, C. J. M., Fong, A., Chamberlain, E., Bowman, J., Scharien, R., & Persson, O. (2022). Annual cycle observations of aerosols capable of ice formation in central Arctic clouds. *Nature Communications*, *13*(1), 3537. https://doi.org/10.1038/s41467-022-31182-x

Curry, J. A., & Khvorostyanov, V. I. (2012). Assessment of some parameterizations of heterogeneous ice nucleation in cloud and climate models. *Atmospheric Chemistry and Physics*, *12*(2), 1151–1172. https://doi.org/10.5194/acp-12-1151-2012

Cziczo, D. J., Froyd, K. D., Gallavardin, S. J., Moehler, O., Benz, S., Saathoff, H., & Murphy, D. M. (2009). Deactivation of ice nuclei due to atmospherically relevant surface coatings. *Environmental Research Letters*, *4*(4), 44013. https://doi.org/10.1088/1748-9326/4/4/044013

Cziczo, D. J., Froyd, K. D., Hoose, C., Jensen, E. J., Diao, M., Zondlo, M. A., Smith, J. B., Twohy, C. H., & Murphy, D. M. (2013). Clarifying the dominant sources and mechanisms of cirrus cloud formation. *Science*, *340*(6138), 1320–1324. https://doi.org/10.1126/science.1234145

Daellenbach, K. R., Cai, J., Hakala, S., Dada, L., Yan, C., Du, W., Yao, L., Zheng, F., Ma, J., Ungeheuer, F., Vogel, A. L., Stolzenburg, D., Hao, Y., Liu, Y., Bianchi, F., Uzu, G., Jaffrezo, J.-L., Worsnop, D. R., Donahue, N. M., & Kulmala, M. (2024). Substantial contribution of transported emissions to organic aerosol in Beijing. *Nature Geoscience*, *17*(8), 747–754. https://doi.org/10.1038/s41561-024-01493-3

David, R. O., Cascajo-Castresana, M., Brennan, K. P., Rösch, M., Els, N., Werz, J., Weichlinger, V., Boynton, L. S., Bogler, S., Borduas-Dedekind, N., Marcolli, C., & Kanji, Z. A. (2019). Development of the droplet ice nuclei counter zurich (DRINCZ): Validation and application to field-collected snow samples. *Atmospheric Measurement Techniques*, *12*(12), 6865–6888. https://doi.org/10.5194/amt-12-6865-2019

DeMott, P. J., Cziczo, D. J., Prenni, A. J., Murphy, D. M., Kreidenweis, S. M., Thomson, D. S., Borys, R., & Rogers, D. C. (2003). Measurements of the concentration and composition of nuclei for cirrus formation. *Proceedings of the National Academy of Sciences*, *100*(25), 14655–14660. https://doi.org/10.1073/pnas.2532677100

DeMott, P. J., Prenni, A. J., Liu, X., Kreidenweis, S. M., Petters, M. D., Twohy, C. H., Richardson, M. S., Eidhammer, T., & Rogers, D. C. (2010). Predicting global atmospheric ice nuclei distributions and their impacts on climate. *Proceedings of the National Academy of Sciences*, *107*(25), 11217–11222. https://doi.org/10.1073/pnas.0910818107

DeMott, P. J., Prenni, A. J., McMeeking, G. R., Sullivan, R. C., Petters, M. D., Tobo, Y., Niemand, M., Möhler, O., Snider, J. R., Wang, Z., & Kreidenweis, S. M. (2015). Integrating laboratory and field data to quantify the immersion freezing ice nucleation activity of mineral dust particles. *Atmospheric Chemistry and Physics*, *15*(1), 393–409. https://doi.org/10.5194/acp-15-393-2015

DeMott, P. J., Hill, T. C. J., Petters, M. D., Bertram, A. K., Tobo, Y., Mason, R. H., Suski, K. J., McCluskey, C. S., Levin, E. J. T., Schill, G. P., Boose, Y., Rauker, A. M., Miller, A. J., Zaragoza, J., Rocci, K., Rothfuss, N. E., Taylor, H. P., Hader, J. D., Chou, C., … Kreidenweis, S. M. (2017). Comparative measurements of ambient atmospheric concentrations of ice nucleating particles using multiple immersion freezing methods and a continuous flow diffusion chamber. *Atmospheric Chemistry and Physics*, *17*(18), 11227–11245. https://doi.org/10.5194/acp-17-11227-2017

DeMott, P. J., Mirrielees, J. A., Petters, S. S., Cziczo, D. J., Petters, M. D., Bingemer, H. G., Hill, T. C. J., Froyd, K., Garimella, S., Hallar, A. G., Levin, E. J. T., McCubbin, I. B., Perring, A. E., Rapp, C. N., Schiebel, T., Schrod, J., Suski, K. J., Weber, D., Wolf, M. J., … Brooks, S. D. (2025). Field intercomparison of ice nucleation measurements: The fifth international workshop on ice nucleation phase 3 (FIN-03). *Atmospheric Measurement Techniques*, *18*(3), 639–672. https://doi.org/10.5194/amt-18-639-2025

DeMott, P. J., Möhler, O., Cziczo, D. J., Hiranuma, N., Petters, M. D., Petters, S. S., Belosi, F., Bingemer, H. G., Brooks, S. D., Budke, C., Burkert-Kohn, M., Collier, K. N., Danielczok, A., Eppers, O., Felgitsch, L., Garimella, S., Grothe, H., Herenz, P., Hill, T. C. J., … Zenker, J. (2018). The fifth international workshop on ice nucleation phase 2 (FIN-02): Laboratory intercomparison of ice nucleation measurements. *Atmospheric Measurement Techniques*, *11*(11), 6231–6257. https://doi.org/10.5194/amt-11-6231-2018

DeMott, P. J., & Prenni, A. J. (2010). New directions: Need for defining the numbers and sources of biological aerosols acting as ice nuclei. *Atmospheric Environment*, *44*(15), 1944–1945. https://doi.org/10.1016/j.atmosenv.2010.02.032

Després, VivianeR., Huffman, J., Burrows, S. M., Hoose, C., Safatov, AleksandrS., Buryak, G., Fröhlich-Nowoisky, J., Elbert, W., Andreae, MeinratO., Pöschl, U., & Jaenicke, R. (2012). Primary biological aerosol particles in the atmosphere:

A review. *Tellus B: Chemical and Physical Meteorology*, *64*(1), 15598. https://doi.org/10.3402/tellusb.v64i0.15598

Ding, S., Zhao, D., He, C., Huang, M., He, H., Tian, P., Liu, Q., Bi, K., Yu, C., Pitt, J., Chen, Y., Ma, X., Chen, Y., Jia, X., Kong, S., Wu, J., Hu, D., Hu, K., Ding, D., & Liu, D. (2019). Observed interactions between black carbon and hydrometeor during wet scavenging in mixed-phase clouds. *Geophysical Research Letters*, *46*(14), 8453–8463. https://doi.org/10.1029/2019GL083171

Du, A., Sun, J., Liu, H., Xu, W., Zhou, W., Zhang, Y., Li, L., Du, X., Li, Y., Pan, X., Wang, Z., & Sun, Y. (2023). Mixing state and effective density of aerosol particles during the Beijing 2022 Olympic Winter Games. *Atmospheric Chemistry and Physics*, *23*(21), 13597–13611. https://doi.org/10.5194/acp-23-13597-2023

Fahey, D. W., Gao, R.-S., Möhler, O., Saathoff, H., Schiller, C., Ebert, V., Krämer, M., Peter, T., Amarouche, N., Avallone, L. M., Bauer, R., Bozóki, Z., Christensen, L. E., Davis, S. M., Durry, G., Dyroff, C., Herman, R. L., Hunsmann, S., Khaykin, S. M., … Wienhold, F. G. (2014). The AquaVIT-1 intercomparison of atmospheric water vapor measurement techniques. *Atmospheric Measurement Techniques*, *7*(9), 3177–3213. https://doi.org/10.5194/amt-7-3177-2014

Fan, J., Leung, L. R., Rosenfeld, D., & DeMott, P. J. (2017). Effects of cloud condensation nuclei and ice nucleating particles on precipitation processes and supercooled liquid in mixed-phase orographic clouds. *Atmospheric Chemistry and Physics*, *17*(2), 1017–1035. https://doi.org/10.5194/acp-17-1017-2017

Field, P. R., Möhler, O., Connolly, P., Krämer, M., Cotton, R., Heymsfield, A. J., Saathoff, H., & Schnaiter, M. (2006). Some ice nucleation characteristics of Asian and Saharan desert dust. *Atmospheric Chemistry and Physics*, *6*(10), 2991–3006. https://doi.org/10.5194/acp-6-2991-2006

Flagan, R. C. (1999). On differential mobility analyzer resolution. *Aerosol Science & Technology*. https://doi.org/10.1080/027868299304417

Fletcher, N. H. (1958). Size effect in heterogeneous nucleation. *Journal of Chemical Physics*, *29*(3), 572–576. https://doi.org/10.1063/1.1744540

Fletcher, N. H. (1962). *The physics of rainclouds*. University Press.

Fletcher, N. H. (2011). *The physics of rainclouds*. Cambridge University Press.

Forde, E., Gallagher, M., Foot, V., Sarda-Esteve, R., Crawford, I., Kaye, P., Stanley, W., & Topping, D. (2019). Characterisation and source identification of biofluorescent aerosol emissions over winter and summer periods in the United Kingdom. *Atmospheric Chemistry and Physics*, *19*(3), 1665–1684. https://doi.org/10.5194/acp-19-1665-2019

Froyd, K. D., Yu, P., Schill, G. P., Brock, C. A., Kupc, A., Williamson, C. J., Jensen, E. J., Ray, E., Rosenlof, K. H., Bian, H., Darmenov, A. S., Colarco, P. R., Diskin, G. S., Bui, T., & Murphy, D. M. (2022). Dominant role of mineral dust in cirrus cloud formation revealed by global-scale measurements. *Nature Geoscience*, *15*(3), 177–183. https://doi.org/10.1038/s41561-022-00901-w

Gabey, A. M., Gallagher, M. W., Whitehead, J., Dorsey, J. R., Kaye, P. H., & Stanley, W. R. (2010). Measurements and comparison of primary biological aerosol above and below a tropical forest canopy using a dual channel fluorescence spectrometer. *Atmospheric Chemistry and Physics*, *10*(10), 4453–4466. https://doi.org/10.5194/acp-10-4453-2010

Gabey, A. M., Stanley, W. R., Gallagher, M. W., & Kaye, P. H. (2011). The fluorescence properties of aerosol larger than 0.8 mm in urban and tropical rainforest locations.

Atmospheric Chemistry and Physics, *11*(11), 5491–5504. https://doi.org/10.5194/acp-11-5491-2011

Gao, K., Vogel, F., Foskinis, R., Vratolis, S., Gini, M. I., Granakis, K., Billault-Roux, A.-C., Georgakaki, P., Zografou, O., Fetfatzis, P., Berne, A., Papayannis, A., Eleftheridadis, K., Möhler, O., & Nenes, A. (2024). Biological and dust aerosols as sources of ice-nucleating particles in the eastern Mediterranean: Source apportionment, atmospheric processing and parameterization. *Atmospheric Chemistry and Physics*, *24*(17), 9939–9974. https://doi.org/10.5194/acp-24-9939-2024

Gao, R. S., J. P., S., K. K., K., D. W., F., L. A., W., T. L., T., J. R., S., J. G., S., E. S., C., J.-H., H., P., D., T. B., O., & and Worsnop, D. R. (2007). A novel method for estimating light-scattering properties of soot aerosols using a modified single-particle soot photometer. *Aerosol Science and Technology*, *41*(2), 125–135. https://doi.org/10.1080/02786820601118398

Garimella, S., Kristensen, T. B., Ignatius, K., Welti, A., Voigtländer, J., Kulkarni, G. R., Sagan, F., Kok, G. L., Dorsey, J., Nichman, L., Rothenberg, D. A., Rösch, M., Kirchgäßner, A. C. R., Ladkin, R., Wex, H., Wilson, T. W., Ladino, L. A., Abbatt, J. P. D., Stetzer, O., … Cziczo, D. J. (2016). The spectrometer for ice nuclei (SPIN): An instrument to investigate ice nucleation. *Atmospheric Measurement Techniques*, *9*(7), 2781–2795. https://doi.org/10.5194/amt-9-2781-2016

Garimella, S., Rothenberg, D. A., Wolf, M. J., David, R. O., Kanji, Z. A., Wang, C., Rösch, M., & Cziczo, D. J. (2017). Uncertainty in counting ice nucleating particles with continuous flow diffusion chambers. *Atmospheric Chemistry and Physics*, *17*(17), 10855–10864. https://doi.org/10.5194/acp-17-10855-2017

Govindarajan, A. G., & Lindow, S. E. (1988). Size of bacterial ice-nucleation sites measured *in situ* by radiation inactivation analysis. *Proceedings of the National Academy of Sciences*, *85*(5), 1334–1338. https://doi.org/10.1073/pnas.85.5.1334

Grawe, S., Augustin-Bauditz, S., Hartmann, S., Hellner, L., Pettersson, J. B. C., Prager, A., Stratmann, F., & Wex, H. (2016). The immersion freezing behavior of ash particles from wood and brown coal burning. *Atmospheric Chemistry and Physics*, *16*(21), 13911–13928. https://doi.org/10.5194/acp-16-13911-2016

Hader, J. D., Wright, T. P., & Petters, M. D. (2014). Contribution of pollen to atmospheric ice nuclei concentrations. *Atmospheric Chemistry and Physics*, *14*(11), 5433–5449. https://doi.org/10.5194/acp-14-5433-2014

Harrison, A. D., Whale, T. F., Carpenter, M. A., Holden, M. A., Neve, L., O'Sullivan, D., Vergara Temprado, J., & Murray, B. J. (2016). Not all feldspars are equal: A survey of ice nucleating properties across the feldspar group of minerals. *Atmospheric Chemistry and Physics*, *16*(17), 10927–10940. https://doi.org/10.5194/acp-16-10927-2016

Harrison, A. D., Lever, K., Sanchez-Marroquin, A., Holden, M. A., Whale, T. F., Tarn, M. D., McQuaid, J. B., & Murray, B. J. (2019). The ice-nucleating ability of quartz immersed in water and its atmospheric importance compared to k-feldspar. *Atmospheric Chemistry and Physics*, *19*(17), 11343–11361. https://doi.org/10.5194/acp-19-11343-2019

Harrison, A. D., Whale, T. F., Rutledge, R., Lamb, S., Tarn, M. D., Porter, G. C. E., Adams, M. P., McQuaid, J. B., Morris, G. J., & Murray, B. J. (2018). An instrument for quantifying heterogeneous ice nucleation in multiwell plates using infrared emissions to detect freezing. *Atmospheric Measurement Techniques*, *11*(10), 5629–5641. https://doi.org/10.5194/amt-11-5629-2018

Hartmann, S., Augustin, S., Clauss, T., Wex, H., Šantl-Temkiv, T., Voigtländer, J., Niedermeier, D., & Stratmann, F. (2013). Immersion freezing of ice nucleation active protein complexes. *Atmospheric Chemistry and Physics*, *13*(11), 5751–5766. https://doi.org/10.5194/acp-13-5751-2013

Hazra, A., Mallick, C., Mohan, G. M., Vani, K. G., Kumar, V. A., Chowdhury, R., Chaudhari, H. S., Das, S. K., Konwar, M., Pokhrel, S., Deshpande, S., Ghude, S. D., Pandithurai, G., & Pawar, S. D. (2022). Understanding the impact of ice nucleation on lightning and rainfall: A case study. *Atmospheric Research*, *278*, 106350. https://doi.org/10.1016/j.atmosres.2022.106350

He, C., Yin, Y., Huang, Y., Kuang, X., Cui, Y., Chen, K., Jiang, H., Kiselev, A., Möhler, O., & Schrod, J. (2023). The vertical distribution of ice-nucleating particles over the north China Plain: A case of cold front passage. *Remote Sensing*, *15*(20), 4989. https://doi.org/10.3390/rs15204989

Healy, D. A., O'Connor, D. J., Burke, A. M., & Sodeau, J. R. (2012). A laboratory assessment of the waveband integrated bioaerosol sensor (WIBS-4) using individual samples of pollen and fungal spore material. *Atmospheric Environment*, *60*, 534–543. https://doi.org/10.1016/j.atmosenv.2012.06.052

Herbert, R. J., Sanchez-Marroquin, A., Grosvenor, D. P., Pringle, K. J., Arnold, S. R., Murray, B. J., & Carslaw, K. S. (2025). Gaps in our understanding of ice-nucleating particle sources exposed by global simulation of the UK earth system model. *Atmospheric Chemistry and Physics*, *25*(1), 291–325. https://doi.org/10.5194/acp-25-291-2025

Hernandez, M., Perring, A. E., McCabe, K., Kok, G., Granger, G., & Baumgardner, D. (2016). Chamber catalogues of optical and fluorescent signatures distinguish bioaerosol classes. *Atmospheric Measurement Techniques*, *9*(7), 3283–3292. https://doi.org/10.5194/amt-9-3283-2016

Hill, T. C. J., DeMott, P. J., Tobo, Y., Fröhlich-Nowoisky, J., Moffett, B. F., Franc, G. D., & Kreidenweis, S. M. (2016). Sources of organic ice nucleating particles in soils. https://doi.org/10.5194/acp-2016-1

Hill, T. C. J., Malfatti, F., McCluskey, C. S., Schill, G. P., Santander, M. V., Moore, K. A., Rauker, A. M., Perkins, R. J., Celussi, M., Levin, E. J. T., Suski, K. J., Cornwell, G. C., Lee, C., Negro, P. D., Kreidenweis, S. M., Prather, K. A., & DeMott, P. J. (2023). Resolving the controls over the production and emission of ice-nucleating particles in sea spray. *Environmental Science: Atmospheres*, *3*(6), 970–990. https://doi.org/10.1039/D2EA00154C

Hill, T. C. J., Moffett, B. F., DeMott, P. J., Georgakopoulos, D. G., Stump, W. L., & Franc, G. D. (2014). Measurement of ice nucleation-active bacteria on plants and in precipitation by quantitative PCR. *Applied and Environmental Microbiology*, *80*(4), 1256–1267. https://doi.org/10.1128/AEM.02967-13

Hiranuma, N., Augustin-Bauditz, S., Bingemer, H., Budke, C., Curtius, J., Danielczok, A., Diehl, K., Dreischmeier, K., Ebert, M., Frank, F., Hoffmann, N., Kandler, K., Kiselev, A., Koop, T., Leisner, T., Möhler, O., Nillius, B., Peckhaus, A., Rose, D., … Yamashita, K. (2015). A comprehensive laboratory study on the immersion freezing behavior of illite NX particles: A comparison of 17 ice nucleation measurement techniques. *Atmospheric Chemistry and Physics*, *15*(5), 2489–2518. https://doi.org/10.5194/acp-15-2489-2015

Hiranuma, N., Möhler, O., Yamashita, K., Tajiri, T., Saito, A., Kiselev, A., Hoffmann, N., Hoose, C., Jantsch, E., Koop, T., & Murakami, M. (2015). Ice nucleation by cellulose and its potential contribution to ice formation in clouds. *Nature Geoscience*, *8*(4), 273–277. https://doi.org/10.1038/ngeo2374

Holden, M. A., Campbell, J. M., Meldrum, F. C., Murray, B. J., & Christenson, H. K. (2021). Active sites for ice nucleation differ depending on nucleation mode. *Proceedings of the National Academy of Sciences*, *118*(18), e2022859118. https://doi.org/10.1073/pnas.2022859118

Hoose, C., & Möhler, O. (2012). Heterogeneous ice nucleation on atmospheric aerosols: A review of results from laboratory experiments. *Atmospheric Chemistry and Physics*, *12*(20), 9817–9854. https://doi.org/10.5194/acp-12-9817-2012

Hoose, C., Kristjánsson, J. E., Chen, J.-P., & Hazra, A. (2010). A classical-theory-based parameterization of heterogeneous ice nucleation by mineral dust, soot, and biological particles in a global climate model. *Journal of the Atmospheric Sciences*, *67*(8), 2483–2503. https://doi.org/10.1175/2010JAS3425.1

Hu, W., Wang, Z., Huang, S., Ren, L., Yue, S., Li, P., Xie, Q., Zhao, W., Wei, L., Ren, H., Wu, L., Deng, J., & Fu, P. (2020). Biological aerosol particles in polluted regions. *Current Pollution Reports*, *6*(2), 65–89. https://doi.org/10.1007/s40726-020-00138-4

Hu, Y., Tian, P., Huang, M., Bi, K., Schneider, J., Umo, N. S., Ullmerich, N., Höhler, K., Jing, X., Xue, H., Ding, D., Liu, Y., Leisner, T., & Möhler, O. (2023). Characteristics of ice-nucleating particles in Beijing during spring: A comparison study of measurements between the suburban and a nearby mountain area. *Atmospheric Environment*, *293*, 119451. https://doi.org/10.1016/j.atmosenv.2022.119451

Huang, K., Zhuang, G., Li, J., Wang, Q., Sun, Y., Lin, Y., & Fu, J. S. (2010). Mixing of Asian dust with pollution aerosol and the transformation of aerosol components during the dust storm over China in spring 2007. *Journal of Geophysical Research: Atmospheres*, *115*. https://doi.org/10.1029/2009JD013145

Huang, R.-J., Zhang, Y., Bozzetti, C., Ho, K.-F., Cao, J.-J., Han, Y., Daellenbach, K. R., Slowik, J. G., Platt, S. M., Canonaco, F., Zotter, P., Wolf, R., Pieber, S. M., Bruns, E. A., Crippa, M., Ciarelli, G., Piazzalunga, A., Schwikowski, M., Abbaszade, G., … Prévôt, A. S. H. (2014). High secondary aerosol contribution to particulate pollution during haze events in China. *Nature*, *514*(7521), 218–222. https://doi.org/10.1038/nature13774

Huang, S., Poulain, L., van Pinxteren, D., van Pinxteren, M., Wu, Z., Herrmann, H., & Wiedensohler, A. (2017). Latitudinal and seasonal distribution of particulate MSA over the Atlantic using a validated quantification method with HR-ToF-AMS. *Environmental Science & Technology*, *51*(1), 418–426. https://doi.org/10.1021/acs.est.6b03186

Huang, S., Hu, W., Chen, J., Wu, Z., Zhang, D., & Fu, P. (2021). Overview of biological ice nucleating particles in the atmosphere. *Environment International*, *146*, 106197. https://doi.org/10.1016/j.envint.2020.106197

Huffman, J. A., Prenni, A. J., DeMott, P. J., Pöhlker, C., Mason, R. H., Robinson, N. H., Fröhlich-Nowoisky, J., Tobo, Y., Després, V. R., Garcia, E., Gochis, D. J., Harris, E., Müller-Germann, I., Ruzene, C., Schmer, B., Sinha, B., Day, D. A., Andreae, M. O., Jimenez, J. L., … Pöschl, U. (2013). High concentrations of biological aerosol particles and ice nuclei during and after rain. *Atmospheric Chemistry and Physics*, *13*(13), 6151–6164. https://doi.org/10.5194/acp-13-6151-2013

Huffman, J. A., Treutlein, B., & Pöschl, U. (2010). Fluorescent biological aerosol particle concentrations and size distributions measured with an ultraviolet aerodynamic particle sizer (UV-APS) in central Europe. *Atmospheric Chemistry and Physics*, *10*(7), 3215–3233. https://doi.org/10.5194/acp-10-3215-2010

Hummel, M., Hoose, C., Pummer, B., Schaupp, C., Fröhlich-Nowoisky, J., & Möhler, O. (2018). Simulating the influence of primary biological aerosol particles on clouds by heterogeneous ice nucleation. *Atmospheric Chemistry and Physics*, *18*(20), 15437–15450. https://doi.org/10.5194/acp-18-15437-2018

IPCC. (2021). Summary for policymakers. In *Climate change 2021: The physical science basis. contribution of working group to the sixth assessment report of the intergovernmental panel on climate change*. Cambridge University Press.

Iwata, A., & Matsuki, A. (2018). Characterization of individual ice residual particles by the single droplet freezing method: A case study in the Asian dust outflow region. *Atmospheric Chemistry and Physics*, *18*(3), 1785–1804. https://doi.org/10.5194/acp-18-1785-2018

Järvinen, E., Vochezer, P., Möhler, O., & Schnaiter, M. (2014). Laboratory study of microphysical and scattering properties of corona-producing cirrus clouds. *Applied Optics*, *53*(31), 7566–7575. https://doi.org/10.1364/AO.53.007566

Jiang, H., Yin, Y., Chen, K., Chen, Q., He, C., & Sun, L. (2020). The measurement of ice nucleating particles at Tai'an city in east China. *Atmospheric Research*, *232*, 104684. https://doi.org/10.1016/j.atmosres.2019.104684

Jiang, H., Yin, Y., Su, H., Shan, Y., & Gao, R. (2015). The characteristics of atmospheric ice nuclei measured at the top of Huangshan (the yellow mountains) in southeast China using a newly built static vacuum water vapor diffusion chamber. *Atmospheric Research*, *153*, 200–208. https://doi.org/10.1016/j.atmosres.2014.08.015

Jiang, H., Yin, Y., Wang, X., Gao, R., Yuan, L., Chen, K., & Shan, Y. (2016). The measurement and parameterization of ice nucleating particles in different backgrounds of China. *Atmospheric Research*, *181*, 72–80. https://doi.org/10.1016/j.atmosres.2016.06.013

Kaaden, N., Massling, A., Schladitz, A., Müller, T., Kandler, K., Schütz, L., Weinzierl, B., Petzold, A., Tesche, M., Leinert, S., Deutscher, C., Ebert, M., Weinbruch, S., & Wiedensohler, A. (2009). State of mixing, shape factor, number size distribution, and hygroscopic growth of the Saharan anthropogenic and mineral dust aerosol at Tinfou, Morocco. *Tellus B*, *61*(1), 51–63. https://doi.org/10.1111/j.1600-0889.2008.00388.x

Kanji, Z. A., DeMott, P. J., Möhler, O., & Abbatt, J. P. D. (2011). Results from the university of Toronto continuous flow diffusion chamber at ICIS 2007: Instrument intercomparison and ice onsets for different aerosol types. *Atmospheric Chemistry and Physics*, *11*(1), 31–41. https://doi.org/10.5194/acp-11-31-2011

Kanji, Z. A., & Abbatt, J. P. D. (2006). Laboratory studies of ice formation via deposition mode nucleation onto mineral dust and N-Hexane soot samples. *Journal of Geophysical Research: Atmospheres*, *111*(D16). https://doi.org/10.1029/2005JD006766

Kanji, Z. A., & Abbatt, J. P. D. (2009). The university of Toronto continuous flow diffusion chamber (UT-CFDC): A simple design for ice nucleation studies. *Aerosol Science and Technology*, *43*(7), 730–738. https://doi.org/10.1080/02786820902889861

Kanji, Z. A., Ladino, L. A., Wex, H., Boose, Y., Burkert-Kohn, M., Cziczo, D. J., & Krämer, M. (2017). Overview of ice nucleating particles. *Meteorological Monographs*, *58*, 1.1–1.33. https://doi.org/10.1175/AMSMONOGRAPHS-D-16-0006.1

Kashchiev, D. (2000). *Nucleation: Basic theory with applications*. Elsevier.

Kawai, K., Matsui, H., & Tobo, Y. (2021). High potential of Asian dust to act as ice nucleating particles in mixed-phase clouds simulated with a global aerosol-climate model. *Journal of Geophysical Research: Atmospheres*, *126*(12), e2020JD034263. https://doi.org/10.1029/2020JD034263

Khvorostyanov, V. I., & Curry, J. A. (2005). The theory of ice nucleation by heterogeneous freezing of deliquescent mixed CCN. part ii: Parcel model simulation. *Journal of the Atmospheric Sciences*, *62*(2), 261–285. https://doi.org/10.1175/jas-3367.1

Kim, J.-S., & Park, K. (2012). Atmospheric aging of Asian dust particles during long range transport. *Aerosol Science and Technology*, *46*(8), 913–924. https://doi.org/10.1080/02786826.2012.680984

Kirkby, J., Curtius, J., Almeida, J., Dunne, E., Duplissy, J., Ehrhart, S., Franchin, A., Gagné, S., Ickes, L., Kürten, A., Kupc, A., Metzger, A., Riccobono, F., Rondo, L., Schobesberger, S., Tsagkogeorgas, G., Wimmer, D., Amorim, A., Bianchi, F., … Kulmala, M. (2011). Role of sulphuric acid, ammonia and galactic cosmic rays in atmospheric aerosol nucleation. *Nature*, *476*(7361), 429–433. https://doi.org/10.1038/nature10343

Knopf, D. A., Wang, B., Laskin, A., Moffet, R. C., & Gilles, M. K. (2010). Heterogeneous nucleation of ice on anthropogenic organic particles collected in Mexico city: Ice nucleation on anthropogenic aerosol. *Geophysical Research Letters*, *37*(11), n/a–n/a. https://doi.org/10.1029/2010GL043362

Knopf, D. A., & Alpert, P. A. (2023). Atmospheric ice nucleation. *Nature Reviews Physics*, *5*(4), 203–217. https://doi.org/10.1038/s42254-023-00570-7

Kong, X., Wolf, M. J., Roesch, M., Thomson, E. S., Bartels-Rausch, T., Alpert, P. A., Ammann, M., Prisle, N. L., & Cziczo, D. J. (2018). A continuous flow diffusion chamber study of sea salt particles acting as cloud nuclei: Deliquescence and ice nucleation. *Tellus B: Chemical and Physical Meteorology*, *70*(1). https://b.tellusjournals.se/articles/10.1080/16000889.2018.1463806

Koop, T., Luo, B., Tsias, A., & Peter, T. (2000). Water activity as the determinant for homogeneous ice nucleation in aqueous solutions. *Nature*, *406*(6796), 611–614. https://doi.org/10.1038/35020537

Korolev, A., McFarquhar, G., Field, P. R., Franklin, C., Lawson, P., Wang, Z., Williams, E., Abel, S. J., Axisa, D., Borrmann, S., Crosier, J., Fugal, J., Krämer, M., Lohmann, U., Schlenczek, O., Schnaiter, M., & Wendisch, M. (2017). Mixed-phase clouds: Progress and challenges. *Meteorological Monographs*, *58*, 5.1–5.50. https://doi.org/10.1175/amsmonographs-d-17-0001.1

Korolev, A., Heckman, I., Wolde, M., Ackerman, A. S., Fridlind, A. M., Ladino, L. A., Lawson, R. P., Milbrandt, J., & Williams, E. (2020). A new look at the environmental conditions favorable to secondary ice production. *Atmospheric Chemistry and Physics*, *20*(3), 1391–1429. https://doi.org/10.5194/acp-20-1391-2020

Kulkarni, G., & Dobbie, S. (2010). Ice nucleation properties of mineral dust particles: Determination of onset rh_i, in active fraction, nucleation time-lag, and the effect of active sites on contact angles. *Atmospheric Chemistry and Physics*, *10*(1), 95–105. https://doi.org/10.5194/acp-10-95-2010

Kulkarni, G., Sanders, C., Zhang, K., Liu, X., & Zhao, C. (2014). Ice nucleation of bare and sulfuric acid-coated mineral dust particles and implication for cloud properties: Ice formation on dust particles. *Journal of Geophysical Research: Atmospheres*, *119*(16), 9993–10011. https://doi.org/10.1002/2014JD021567

Kulkarni, P., Baron, P. A., & Willeke, K. (Eds.). (2011). *Aerosol measurement: Principles, techniques, and applications* (3rd ed). Wiley. https://onlinelibrary.wiley.com/doi/book/10.1002/9781118001684?msockid=29e31800ce4961161dfe091bcfa3600d

Kulmala, M., Vehkamäki, H., Petäjä, T., Dal Maso, M., Lauri, A., Kerminen, V. M., Birmili, W., & McMurry, P. H. (2004). Formation and growth rates of ultrafine atmospheric particles: A review of observations. *Journal of Aerosol Science*, *35*(2), 143–176. https://doi.org/10.1016/j.jaerosci.2003.10.003

Lacher, L., Adams, M. P., Barry, K., Bertozzi, B., Bingemer, H., Boffo, C., Bras, Y., Büttner, N., Castarede, D., Cziczo, D. J., DeMott, P. J., Fösig, R., Goodell, M., Höhler, K., Hill, T. C. J., Jentzsch, C., Ladino, L. A., Levin, E. J. T., Mertes, S., … Freney, E. (2024). The puy de dôme ice nucleation intercomparison campaign (PICNIC): Comparison between online and offline methods in ambient air. *Atmospheric Chemistry and Physics*, *24*(4), 2651–2678. https://doi.org/10.5194/acp-24-2651-2024

Li, W., Li, J., Ma, T., Chang, Z., Casuccio, G. S., Gao, J., & Li, H. (2024). Physiochemistry and sources of individual particles in response to intensified controls during the 2022 Winter Olympics in Beijing. *Journal of Environmental Management*, *352*, 119946. https://doi.org/10.1016/j.jenvman.2023.119946

Li, Y., & Du, B. (2003). Measurement and analysis of atmospheric ice nucleating particle concentration in the tianshan mountain area of xinjiang. *Journal of Nanjing Institute of Meteorology*, *26*, 364–370. https://lib.cqvip.com/Qikan/Article/Detail?id=8044713&from=Qikan_Article_Detail（原文：李艳伟, 杜秉玉. 新疆天山山区大气冰核浓度的测量及分析 [J]. 南京气象学院学报,2003,26(3):364-370）.

Lian, C., Wang, W., Chen, Y., Zhang, Y., Zhang, J., Liu, Y., Fan, X., Li, C., Zhan, J., Lin, Z., Hua, C., Zhang, W., Liu, M., Li, J., Wang, X., An, J., & Ge, M. (2022). Long-term winter observation of nitrous acid in the urban area of Beijing. *Journal of Environmental Sciences*, *114*, 334–342. https://doi.org/10.1016/j.jes.2021.09.010

Liu, D., Allan, J. D., Young, D. E., Coe, H., Beddows, D., Fleming, Z. L., Flynn, M. J., Gallagher, M. W., Harrison, R. M., Lee, J., Prevot, A. S. H., Taylor, J. W., Yin, J., Williams, P. I., & Zotter, P. (2014). Size distribution, mixing state and source apportionment of black carbon aerosol in london during wintertime. *Atmospheric Chemistry and Physics*, *14*(18), 10061–10084. https://doi.org/10.5194/acp-14-10061-2014

Liu, D., Ding, S., Zhao, D., Hu, K., Yu, C., Hu, D., Wu, Y., Zhou, C., Tian, P., Liu, Q., Wu, Y., Zhang, J., Kong, S., Huang, M., & Ding, D. (2020). Black carbon emission and wet scavenging from surface to the top of boundary layer over Beijing region. *Journal of Geophysical Research: Atmospheres*, *125*(17), e2020JD033096. https://doi.org/10.1029/2020JD033096

Liu, X., & Penner, J. E. (2005). Ice nucleation parameterization for global models. *Meteorologische Zeitschrift*, 499–514. https://doi.org/10.1127/0941-2948/2005/0059

Liu, Y., Yan, C., Feng, Z., Zheng, F., Fan, X., Zhang, Y., Li, C., Zhou, Y., Lin, Z., Guo, Y., Zhang, Y., Ma, L., Zhou, W., Liu, Z., Dada, L., Dällenbach, K., Kontkanen, J., Cai, R., Chan, T., … Kulmala, M. (2020). Continuous and comprehensive atmospheric observations in Beijing: A station to understand the complex urban atmospheric environment. *Big Earth Data*, *4*(3), 295–321. https://doi.org/10.1080/20964471.2020.1798707

Liu, Y., Xu, X., Yang, X., He, J., Ji, D., & Wang, Y. (2022). Significant reduction in fine particulate matter in Beijing during 2022 Beijing Winter Olympics. *Environ-*

mental Science & Technology Letters, *9*(10), 822–828. https://doi.org/10.1021/acs.estlett.2c00532

Lohmann, U., & Feichter, J. (2005). Global indirect aerosol effects: A review. *Atmospheric Chemistry and Physics*, *5*(3), 715–737. https://doi.org/10.5194/acp-5-715-2005

Ludlam, F. H. (1948). The forms of ice-clouds. *Quarterly Journal of the Royal Meteorological Society*, *74*(319), 39–56. https://doi.org/10.1002/qj.49707431905

Mahant, S., Yadav, S., Gilbert, C., Kjærgaard, E. R., Jensen, M. M., Kessler, T., Bilde, M., & Petters, M. D. (2023). An open-hardware community ice nucleation cold stage for research and teaching. *Hardwarex*, *16*, e00491. https://doi.org/10.1016/j.ohx.2023.e00491

Maki, L. R., Galyan, E. L., Chang-Chien, M.-M., & Caldwell, D. R. (1974). Ice nucleation induced by *pseudomonas syringae*. *Applied Microbiology*, *28*(3), 456–459. https://doi.org/10.1128/am.28.3.456-459.1974

Mamouri, R. E., & Ansmann, A. (2016). Potential of polarization Lidar to provide profiles of CCN- and INP-relevant aerosol parameters. *Atmospheric Chemistry and Physics*, *16*(9), 5905–5931. https://doi.org/10.5194/acp-16-5905-2016

Marcolli, C. (2014). Deposition nucleation viewed as homogeneous or immersion freezing in pores and cavities. *Atmospheric Chemistry and Physics*, *14*(4), 2071–2104. https://doi.org/10.5194/acp-14-2071-2014

Marcolli, C., Gedamke, S., Peter, T., & Zobrist, B. (2007). Efficiency of immersion mode ice nucleation on surrogates of mineral dust. *Atmospheric Chemistry and Physics*, *7*(19), 5081–5091. https://doi.org/10.5194/acp-7-5081-2007

Markey, E., Hourihane Clancy, J., Martínez-Bracero, M., Sarda-Estève, R., Baisnée, D., McGillicuddy, E. J., Sewell, G., Skjøth, C. A., & O'Connor, D. J. (2024). Spectroscopic detection of bioaerosols with the wibs-4+: Anthropogenic and meteorological impacts. *Science of the Total Environment*, *943*, 173649. https://doi.org/10.1016/j.scitotenv.2024.173649

Masson-Delmotte, V., Zhai, P., Pirani, A., Connors, S. L., Péan, C., Berger, S., Caud, N., Chen, Y., Goldfarb, L., Gomis, M. I., Huang, M., Leitzell, K., Lonnoy, E., Matthews, J. B. R., Maycock, T. K., Waterfield, T., Yelekçi, Ö., Yu, R., & Zhou, B. (Eds.). (2021). *Climate change 2021: The physical science basis. contribution of working group I to the sixth assessment report of the intergovernmental panel on climate change*. Cambridge University Press. https://doi.org/10.1017/9781009157896

McCluskey, C. S., Hill, T. C. J., Humphries, R. S., Rauker, A. M., Moreau, S., Strutton, P. G., Chambers, S. D., Williams, A. G., McRobert, I., Ward, J., Keywood, M. D., Harnwell, J., Ponsonby, W., Loh, Z. M., Krummel, P. B., Protat, A., Kreidenweis, S. M., & DeMott, P. J. (2018). Observations of ice nucleating particles over southern ocean waters. *Geophysical Research Letters*, *45*(21). https://doi.org/10.1029/2018GL079981

McCluskey, C. S., Hill, T. C. J., Malfatti, F., Sultana, C. M., Lee, C., Santander, M. V., Beall, C. M., Moore, K. A., Cornwell, G. C., Collins, D. B., Prather, K. A., Jayarathne, T., Stone, E. A., Azam, F., Kreidenweis, S. M., & DeMott, P. J. (2017). A dynamic link between ice nucleating particles released in nascent sea spray aerosol and oceanic biological activity during two mesocosm experiments. *Journal of the Atmospheric Sciences*, *74*(1), 151–166. https://doi.org/10.1175/JAS-D-16-0087.1

Megahed, K. (2007). *The impact of mineral dust aerosol particles on cloud formation* [Thesis]. Universitäts- und Landesbibliothek Bonn. https://bonndoc.ulb.uni-bonn.de/xmlui/handle/20.500.11811/3083

Meyers, M. P., DeMott, P. J., & Cotton, W. R. (1992). New primary ice-nucleation parameterizations in an explicit cloud model. *Journal of Applied Meteorology and Climatology*, *31*(7), 708–721. https://doi.org/10.1175/1520-0450(1992)031<0708:NPINPI>2.0.CO;2

Miller, A. J., Brennan, K. P., Mignani, C., Wieder, J., David, R. O., & Borduas-Dedekind, N. (2021). Development of the drop freezing ice nuclei counter (FINC), intercomparison of droplet freezing techniques, and use of soluble lignin as an atmospheric ice nucleation standard. *Atmospheric Measurement Techniques*, *14*(4), 3131–3151. https://doi.org/10.5194/amt-14-3131-2021

Möhler, O., DeMott, P. J., Vali, G., & Levin, Z. (2007). Microbiology and atmospheric processes: The role of biological particles in cloud physics. *Biogeosciences (online)*, *4*(6), 1059–1071. https://doi.org/10.5194/bg-4-1059-2007

Möhler, O., Field, P. R., Connolly, P., Benz, S., Saathoff, H., Schnaiter, M., Wagner, R., Cotton, R., Krämer, M., Mangold, A., & Heymsfield, A. J. (2006). Efficiency of the deposition mode ice nucleation on mineral dust particles. *Atmospheric Chemistry and Physics*, *6*(10), 3007–3021. https://doi.org/10.5194/acp-6-3007-2006

Möhler, O., Georgakopoulos, D. G., Morris, C. E., Benz, S., Ebert, V., Hunsmann, S., Saathoff, H., Schnaiter, M., & Wagner, R. (2008). Heterogeneous ice nucleation activity of bacteria: New laboratory experiments at simulated cloud conditions. *Biogeosciences*, *5*(5), 1425–1435. https://doi.org/10.5194/bg-5-1425-2008

Möhler, O., Stetzer, O., Schaefers, S., Linke, C., Schnaiter, M., Tiede, R., Saathoff, H., Kramer, M., Mangold, A., Budz, P., Zink, P., Schreiner, J., Mauersberger, K., Haag, W., Karcher, B., & Schurath, U. (2003). Experimental investigation of homogeneous freezing of sulphuric acid particles in the aerosol chamber AIDA. *Atmospheric Chemistry and Physics*, 13.

Möhler, O., Adams, M., Lacher, L., Vogel, F., Nadolny, J., Ullrich, R., Boffo, C., Pfeuffer, T., Hobl, A., Weiß, M., Vepuri, H. S. K., Hiranuma, N., & Murray, B. J. (2021). The portable ice nucleation experiment (PINE): A new online instrument for laboratory studies and automated long-term field observations of ice-nucleating particles. *Atmospheric Measurement Techniques*, *14*(2), 1143–1166. https://doi.org/10.5194/amt-14-1143-2021

Mossop, S. C. (1970). Concentrations of ice crystals in clouds. *Bulletin of the American Meteorological Society*, *51*(6), 474–480. https://doi.org/10.1175/1520-0477(1970)051<0474:COICIC>2.0.CO;2

Muhlbauer, A., & Lohmann, U. (2009). Sensitivity studies of aerosol–cloud interactions in mixed-phase orographic precipitation. *Journal of the Atmospheric Sciences*, *66*(9), 2517–2538. https://doi.org/10.1175/2009JAS3001.1

Mülmenstädt, J., Sourdeval, O., Delanoë, J., & Quaas, J. (2015). Frequency of occurrence of rain from liquid-, mixed-, and ice-phase clouds derived from a-train satellite retrievals. *Geophysical Research Letters*, *42*(15), 6502–6509. https://doi.org/10.1002/2015GL064604

Murphy, D. M., & Koop, T. (2005). Review of the vapour pressures of ice and supercooled water for atmospheric applications. *Quarterly Journal of the Royal Meteorological Society*, *131*(608), 1539–1565. https://doi.org/10.1256/qj.04.94

Murray, B. J., Broadley, S. L., Wilson, T. W., Atkinson, J. D., & Wills, R. H. (2011). Heterogeneous freezing of water droplets containing kaolinite particles. *Atmos. Chem. Phys.*, *11*(9), 4191–4207. https://doi.org/10.5194/acp-11-4191-2011

Murray, B. J., O'Sullivan, D., Atkinson, J. D., & Webb, M. E. (2012). Ice nucleation by particles immersed in supercooled cloud droplets. *Chemical Society Reviews*, *41*(19), 6519. https://doi.org/10.1039/c2cs35200a

Murray, B. J., Carslaw, K. S., & Field, P. R. (2021). Opinion: Cloud-phase climate feedback and the importance of ice-nucleating particles. *Atmospheric Chemistry and Physics*, *21*(2), 665–679. https://doi.org/10.5194/acp-21-665-2021

Niedermeier, D., Shaw, R. A., Hartmann, S., Wex, H., Clauss, T., Voigtländer, J., & Stratmann, F. (2011). Heterogeneous ice nucleation: Exploring the transition from stochastic to singular freezing behavior. *Atmospheric Chemistry and Physics*, *11*(16), 8767–8775. https://doi.org/10.5194/acp-11-8767-2011

Niemand, M., Möhler, O., Vogel, B., Vogel, H., Hoose, C., Connolly, P., Klein, H., Bingemer, H., DeMott, P., Skrotzki, J., & Leisner, T. (2012). A particle-surface-area-based parameterization of immersion freezing on desert dust particles. *Journal of the Atmospheric Sciences*, *69*(10), 3077–3092. https://doi.org/10.1175/JAS-D-11-0249.1

O'Connor, D. J., Healy, D. A., Hellebust, S., Buters, J. T. M., & Sodeau, J. R. (2014). Using the WIBS-4 (waveband integrated bioaerosol sensor) technique for the on-line detection of pollen grains. *Aerosol Science and Technology*, *48*(4), 341–349. https://doi.org/10.1080/02786826.2013.872768

O'Sullivan, D., Adams, M., Tarn, M., Harrison, A., Vergara-Temprado, J., Porter, G., Holden, M., Sanchez-Marroquin, A., Carotenuto, F., Whale, T., McQuaid, J., Walshaw, R., Hedges, D. H. P., Burke, I., Cui, Z., & Murray, B. (2018). Contributions of biogenic material to the atmospheric ice-nucleating particle population in north western Europe. *Scientific Reports*, *8*, null. https://doi.org/10.1038/s41598-018-31981-7

O'Sullivan, D., Murray, B. J., Malkin, T. L., Whale, T. F., Umo, N. S., Atkinson, J. D., Price, H. C., Baustian, K. J., Browse, J., & Webb, M. E. (2014). Ice nucleation by fertile soil dusts: Relative importance of mineral and biogenic components. *Atmospheric Chemistry and Physics*, *14*(4), 1853–1867. https://doi.org/10.5194/acp-14-1853-2014

O'Sullivan, D., Murray, B. J., Ross, J. F., Whale, T. F., Price, H. C., Atkinson, J. D., Umo, N. S., & Webb, M. E. (2015). The relevance of nanoscale biological fragments for ice nucleation in clouds. *Scientific Reports*, *5*(1), 8082. https://doi.org/10.1038/srep08082

O'Sullivan, D., Murray, B. J., Ross, J. F., & Webb, M. E. (2016). The adsorption of fungal ice-nucleating proteins on mineral dusts: A terrestrial reservoir of atmospheric ice-nucleating particles. *Atmospheric Chemistry and Physics*, *16*(12), 7879–7887. https://doi.org/10.5194/acp-16-7879-2016

Peckhaus, A., Kiselev, A., Hiron, T., Ebert, M., & Leisner, T. (2016). A comparative study of K-rich and Na/Ca-rich feldspar ice-nucleating particles in a nanoliter droplet freezing assay. *Atmospheric Chemistry and Physics*, *16*(18), 11477–11496. https://doi.org/10.5194/acp-16-11477-2016

Perring, A., Schwarz, J., Baumgardner, D., Hernandez, M., Spracklen, D., Heald, C., Gao, R., Kok, G., McMeeking, G., McQuaid, J., & Fahey, D. (2015). Airborne observations of regional variation in fluorescent aerosol across the United States.

Journal of Geophysical Research, *120*(3), 1153–1170. https://doi.org/10.1002/2014JD022495

Petters, M. D., & Kreidenweis, S. M. (2007). A single parameter representation of hygroscopic growth and cloud condensation nucleus activity. *Atmospheric Chemistry and Physics*, *7*(8), 1961–1971. https://doi.org/10.5194/acp-7-1961-2007

Phillips, V. T. J., DeMott, P. J., & Andronache, C. (2008). An empirical parameterization of heterogeneous ice nucleation for multiple chemical species of aerosol. *Journal of the Atmospheric Sciences*, *65*(9), 2757–2783. https://doi.org/10.1175/2007JAS2546.1

Pöhlker, C., Huffman, J. A., & Pöschl, U. (2012). Autofluorescence of atmospheric bioaerosols – fluorescent biomolecules and potential interferences. *Atmospheric Measurement Techniques*, *5*(1), 37–71. https://doi.org/10.5194/amt-5-37-2012

Pöschl, U. (2005). Atmospheric aerosols: Composition, transformation, climate and health effects. *Angewandte Chemie International Edition*, *44*(46), 7520–7540. https://doi.org/10.1002/anie.200501122

Pruppacher, H. R., & Klett, J. D. (1997). *Microphysics of clouds and precipitation* (2nd ed.). Kluwer Academic Publishers.

Pruppacher, H., & Klett, J. (2010). *Microphysics of clouds and precipitation* (L. A. Mysak & K. Hamilton, Eds.; Vol. 18). Springer Netherlands. https://doi.org/10.1007/978-0-306-48100-0

Pummer, B. G., Bauer, H., Bernardi, J., Bleicher, S., & Grothe, H. (2012). Suspendable macromolecules are responsible for ice nucleation activity of birch and conifer pollen. *Atmospheric Chemistry and Physics*, *12*(5), 2541–2550. https://doi.org/10.5194/acp-12-2541-2012

Reicher, N., Budke, C., Eickhoff, L., Raveh-Rubin, S., Kaplan-Ashiri, I., Koop, T., & Rudich, Y. (2019). Size-dependent ice nucleation by airborne particles during dust events in the eastern Mediterranean. *Atmospheric Chemistry and Physics*, *19*(17), 11143–11158. https://doi.org/10.5194/acp-19-11143-2019

Reid, J. S., Koppmann, R., Eck, T. F., & Eleuterio, D. P. (2005). A review of biomass burning emissions part ii: Intensive physical properties of biomass burning particles. *Atmospheric Chemistry and Physics*, *5*(3), 799–825. https://doi.org/10.5194/acp-5-799-2005

Ren, Y. Z., Bi, K., Fu, S. Z., Tian, P., Huang, M. Y., Zhu, R. H., & Xue, H. W. (2023). The relationship of aerosol properties and ice-nucleating particle concentrations in Beijing. *Journal of Geophysical Research: Atmospheres*, *128*(10), e2022JD037383. https://doi.org/10.1029/2022JD037383

Ren, Y., Fu, S., Bi, K., Zhang, H., Lin, X., Cao, K., Zhang, Q., & Xue, H. (2024). Freezing nucleus spectra for hailstone samples in China from droplet freezing experiments. *Journal of Geophysical Research: Atmospheres*, *129*(10), e2023JD040505. https://doi.org/10.1029/2023JD040505

Riemer, N., Ault, A. P., West, M., Craig, R. L., & Curtis, J. H. (2019). Aerosol mixing state: Measurements, modeling, and impacts. *Reviews of Geophysics*, *57*(2), 187–249. https://doi.org/10.1029/2018RG000615

Rogers, D. C. (1988). Development of a continuous flow thermal gradient diffusion chamber for ice nucleation studies. *Atmospheric Research*, *22*(2), 149–181. https://doi.org/10.1016/0169-8095(88)90005-1

Rogers, D. C., DeMott, P. J., Kreidenweis, S. M., & Chen, Y. (2001). A continuous-flow diffusion chamber for airborne measurements of ice nuclei. *Journal of Atmo-*

spheric and Oceanic Technology, *18*(5), 725–741. https://doi.org/10.1175/1520-0426(2001)018<0725:ACFDCF>2.0.CO;2

Roshchina, V. (2003). Autofluorescence of plant secreting cells as a biosensor and bioindicator reaction. *Journal of Fluorescence*, *13*(5), 403–420. https://doi.org/10.1023/A:1026164922760

Sanchez-Marroquin, A., West, J. S., Burke, I. T., McQuaid, J. B., & Murray, B. J. (2021). Mineral and biological ice-nucleating particles above the south east of the British Isles. *Environ. Sci.: Atmos.*, *1*(4), 176–191. https://doi.org/10.1039/D1EA00003A

Savage, N. J., Krentz, C. E., Könemann, T., Han, T. T., Mainelis, G., Pöhlker, C., & Huffman, J. A. (2017). Systematic characterization and fluorescence threshold strategies for the wideband integrated bioaerosol sensor (WIBS) using size-resolved biological and interfering particles. *Atmospheric Measurement Techniques*, *10*(11), 4279–4302. https://doi.org/10.5194/amt-10-4279-2017

Schiebel, T. (2017). *Ice nucleation activity of soil dust aerosols*. https://doi.org/10.5445/IR/1000076327

Schneider, J., Höhler, K., Heikkilä, P., Keskinen, J., Bertozzi, B., Bogert, P., Schorr, T., Umo, N. S., Vogel, F., Brasseur, Z., Wu, Y., Hakala, S., Duplissy, J., Moisseev, D., Kulmala, M., Adams, M. P., Murray, B. J., Korhonen, K., Hao, L., ... Möhler, O. (2021). The seasonal cycle of ice-nucleating particles linked to the abundance of biogenic aerosol in boreal forests. *Atmos. Chem. Phys.*, *21*(5), 3899–3918. https://doi.org/10.5194/acp-21-3899-2021

Schneider, J., Höhler, K., Wagner, R., Saathoff, H., Schnaiter, M., Schorr, T., Steinke, I., Benz, S., Baumgartner, M., Rolf, C., Krämer, M., Leisner, T., & Möhler, O. (2021). High homogeneous freezing onsets of sulfuric acid aerosol at cirrus temperatures. *Atmospheric Chemistry and Physics*, *21*(18), 14403–14425. https://doi.org/10.5194/acp-21-14403-2021

Schnell, R. C. (1977). Ice nuclei in seawater, fog water and marine air off the coast of Nova Scotia: Summer 1975. *Journal of the Atmospheric Sciences*, *34*(8), 1299–1305. https://doi.org/10.1175/1520-0469(1977)034<1299:INISFW>2.0.CO;2

Schrod, J., Thomson, E. S., Weber, D., Kossmann, J., Pöhlker, C., Saturno, J., Ditas, F., Artaxo, P., Clouard, V., Saurel, J.-M., Ebert, M., Curtius, J., & Bingemer, H. G. (2020). Long-term deposition and condensation ice-nucleating particle measurements from four stations across the globe. *Atmospheric Chemistry and Physics*, *20*(24), 15983–16006. https://doi.org/10.5194/acp-20-15983-2020

Seinfeld, J. H., & Pandis, S. N. (2006). *Atmospheric chemistry and physics: From air pollution to climate change* (2nd ed). J. Wiley.

Shaw, R. A., Cantrell, W., Chen, S., Chuang, P., Donahue, N., Feingold, G., Kollias, P., Korolev, A., Kreidenweis, S., Krueger, S., Mellado, J. P., Niedermeier, D., & Xue, L. (2020). Cloud–aerosol–turbulence interactions: Science priorities and concepts for a large-scale laboratory facility. *Bulletin of the American Meteorological Society*. https://repository.library.noaa.gov/view/noaa/29399

Shi, A., Zhen, G., & You, L. (2006). Observational analysis of surface atmospheric ice nuclei in henan county, qinghai province, autumn 2003. *Journal of Applied Meteorology*, *17*, 245–249. http://qikan.camscma.cn/jamsweb/article/id/20060241?viewType=HTML （原文：石爱丽, 郑国光, 游来光. 2003 年秋季青海省河南县地面大气冰核观测分析. 应用气象学报, 2006, 17(2): 245-249.）

Singh, A., & Kuang, C. (2024). Scanning mobility particle sizer (SMPS) instrument handbook, DOE/SC-ARM-TR–147, 1245993. https://doi.org/10.2172/1245993

Steinke, I., Möhler, O., Kiselev, A., Niemand, M., Saathoff, H., Schnaiter, M., Skrotzki, J., Hoose, C., & Leisner, T. (2011). Ice nucleation properties of fine ash particles from the eyjafjallajökull eruption in April 2010. *Atmospheric Chemistry and Physics*, *11*(24), 12945–12958. https://doi.org/10.5194/acp-11-12945-2011

Steinke, I., Hiranuma, N., Funk, R., Höhler, K., Tüllmann, N., Umo, N. S., Weidler, P. G., Möhler, O., & Leisner, T. (2020). Complex plant-derived organic aerosol as ice-nucleating particles – more than the sums of their parts? *Atmospheric Chemistry and Physics*, *20*(19), 11387–11397. https://doi.org/10.5194/acp-20-11387-2020

Stetzer, O., Baschek, B., Lüönd, F., & Lohmann, U. (2008). The zurich ice nucleation chamber (ZINC)-a new instrument to investigate atmospheric ice formation. *Aerosol Science and Technology*, *42*(1), 64–74. https://doi.org/10.1080/02786820701787944

Su, H., Yin, Y., Zhou, D., Wang, J., & Liu, Y. (2023). Comparative analysis of atmospheric ice nucleation concentration and nuclei mechanism in huangshan and shenyang. *Chinese Journal of Atmospheric Sciences (in Chinese)*, *47*(3), 667–682. https://doi.org/10.3878/j.issn.1006-9895.2210.21148 （原文：苏航, 银燕, 周德平, 等. 2023. 黄山和沈阳大气冰核数浓度及核化机制对比分析 [J]. 大气科学, 47(3): 667—682. DOI: 10.3878/j.issn.1006-9895.2210.21148.）

Sullivan, R. C., Guazzotti, S. A., Sodeman, D. A., & Prather, K. A. (2007). Direct observations of the atmospheric processing of Asian mineral dust. *Atmospheric Chemistry and Physics*, *7*(5), 1213–1236. https://doi.org/10.5194/acp-7-1213-2007

Sullivan, R. C., Petters, M. D., DeMott, P. J., Kreidenweis, S. M., Wex, H., Niedermeier, D., Hartmann, S., Clauss, T., Stratmann, F., Reitz, P., Schneider, J., & Sierau, B. (2010). Irreversible loss of ice nucleation active sites in mineral dust particles caused by sulphuric acid condensation. *Atmospheric Chemistry and Physics*, *10*(23), 11471–11487. https://doi.org/10.5194/acp-10-11471-2010

Sullivan, S. C., Hoose, C., & Nenes, A. (2017). Investigating the contribution of secondary ice production to in-cloud ice crystal numbers. *Journal of Geophysical Research: Atmospheres*, *122*(17), 9391–9412. https://doi.org/10.1002/2017JD026546

Taketani, F., Tobo, Y., Miyakawa, T., Takigawa, M., Zhu, C., & Kanaya, Y. (2025). Impact of siberian wildfires on ice-nucleating particle concentrations over the northwestern pacific. *Environmental Science & Technology*, *59*(5), 2565–2574. https://doi.org/10.1021/acs.est.4c04889

Taqieddin, A., Allshouse, M. R., & Alshawabkeh, A. N. (2018). Editors' choice—critical review—mathematical formulations of electrochemically gas-evolving systems. *Journal of the Electrochemical Society*, *165*(13), E694. https://doi.org/10.1149/2.0791813jes

Tarn, M. D., Sikora, S. N. F., Porter, G. C. E., O'Sullivan, D., Adams, M., Whale, T. F., Harrison, A. D., Vergara-Temprado, J., Wilson, T. W., Shim, J.-u., & Murray, B. J. (2018). The study of atmospheric ice-nucleating particles via microfluidically generated droplets. *Microfluidics and Nanofluidics*, *22*(5), 52. https://doi.org/10.1007/s10404-018-2069-x

Tian, P., Liu, D., Bi, K., Huang, M., Wu, Y., Hu, K., Li, R., He, H., Ding, D., Hu, Y., Liu, Q., Zhao, D., Qiu, Y., Kong, S., & Xue, H. (2022). Evidence for anthropogenic organic aerosols contributing to ice nucleation. *Geophysical Research Letters*, *49*(17), e2022GL099990. https://doi.org/10.1029/2022GL099990

Tobo, Y. (2016). An improved approach for measuring immersion freezing in large droplets over a wide temperature range. *Scientific Reports*, *6*(1), 32930. https://doi.org/10.1038/srep32930

Tobo, Y., Prenni, A. J., DeMott, P. J., Huffman, J. A., McCluskey, C. S., Tian, G., Pöhlker, C., Pöschl, U., & Kreidenweis, S. M. (2013). Biological aerosol particles as a key determinant of ice nuclei populations in a forest ecosystem. *Journal of Geophysical Research: Atmospheres*, *118*(17), 10, 100–10, 110. https://doi.org/10.1002/jgrd.50801

Tobo, Y., Uetake, J., Matsui, H., Moteki, N., Uji, Y., Iwamoto, Y., Miura, K., & Misumi, R. (2020). Seasonal trends of atmospheric ice nucleating particles over Tokyo. *Journal of Geophysical Research: Atmospheres*, *125*(23), e2020JD033658. https://doi.org/10.1029/2020JD033658

Toprak, E., & Schnaiter, M. (2013). Fluorescent biological aerosol particles measured with the waveband integrated bioaerosol sensor WIBS-4: Laboratory tests combined with a one year field study. *Atmospheric Chemistry and Physics*, *13*(1), 225–243. https://doi.org/10.5194/acp-13-225-2013

TSI. (2002). Model 3010 condensation particle counter instruction manual.

TSI. (2013). Aerodynamic particle sizer manual model 3321 user's manual. https://www.kenelec.com.au/wp-content/uploads/2016/06/TSI_3321_Aerodynamic_Particle_Sizer_Manual.pdf

Twohy, C. H., DeMott, P. J., Russell, L. M., Toohey, D. W., Rainwater, B., Geiss, R., Sanchez, K. J., Lewis, S., Roberts, G. C., Humphries, R. S., McCluskey, C. S., Moore, K. A., Selleck, P. W., Keywood, M. D., Ward, J. P., & McRobert, I. M. (2021). Cloud-nucleating particles over the southern ocean in a changing climate. *Earth's Future*, *9*(3), e2020EF001673. https://doi.org/10.1029/2020EF001673

Ullrich, R., Hoose, C., Möhler, O., Niemand, M., Wagner, R., Höhler, K., Hiranuma, N., Saathoff, H., & Leisner, T. (2017). A new ice nucleation active site parameterization for desert dust and soot. https://doi.org/10.1175/JAS-D-16-0074.1

Umo, N. S., Murray, B. J., Baeza-Romero, M. T., Jones, J. M., Lea-Langton, A. R., Malkin, T. L., O'Sullivan, D., Neve, L., Plane, J. M. C., & Williams, A. (2015). Ice nucleation by combustion ash particles at conditions relevant to mixed-phase clouds. *Atmospheric Chemistry and Physics*, *15*(9), 5195–5210. https://doi.org/10.5194/acp-15-5195-2015

Uno, I., Eguchi, K., Yumimoto, K., Takemura, T., Shimizu, A., Uematsu, M., Liu, Z., Wang, Z., Hara, Y., & Sugimoto, N. (2009). Asian dust transported one full circuit around the globe. *Nature Geoscience*, *2*(8), 557–560. https://doi.org/10.1038/ngeo583

Urban, R. C., Lima-Souza, M., Caetano-Silva, L., Queiroz, M. E. C., Nogueira, R. F., Allen, A. G., Cardoso, A. A., Held, G., & Campos, M. L. A. (2012). Use of levoglucosan, potassium, and water-soluble organic carbon to characterize the origins of biomass-burning aerosols. *Atmospheric Environment*, *61*, 562–569. https://doi.org/10.1016/j.atmosenv.2012.07.082

Vali, G., DeMott, P. J., Möhler, O., & Whale, T. F. (2015). Technical note: A proposal for ice nucleation terminology. *Atmospheric Chemistry and Physics*, *15*(18), 10263–10270. https://doi.org/10.5194/acp-15-10263-2015

Vali, G. (1971). Quantitative evaluation of experimental results an the heterogeneous freezing nucleation of supercooled liquids. *J. Atmos. Sci.*, *28*, 402–409. https://doi.org/10.1175/1520-0469(1971)028<0402:QEOERA>2.0.CO;2

Vignon, É., Alexander, S. P., DeMott, P. J., Sotiropoulou, G., Gerber, F., Hill, T. C. J., Marchand, R., Nenes, A., & Berne, A. (2021). Challenging and improving the simulation of mid-level mixed-phase clouds over the high-latitude southern ocean. *Journal of Geophysical Research: Atmospheres*, *126*(7), e2020JD033490. https://doi.org/10.1029/2020JD033490

Vogel, F. (2022). *Short-term variation in measurements of atmospheric ice-nucleating particle concentrations.*

Wagh, S., Singh, P., Ghude, S. D., Safai, P., Prabhakaran, T., & Kumar, P. P. (2021). Study of ice nucleating particles in fog-haze weather at New Delhi, India: A case of polluted environment. *Atmospheric Research*, *259*, 105693. https://doi.org/10.1016/j.atmosres.2021.105693

Wagner, R., Benz, S., Möhler, O., Saathoff, H., & Schurath, U. (2006). Probing ice clouds by broadband mid-infrared extinction spectroscopy: Case studies from ice nucleation experiments in the AIDA aerosol and cloud chamber. *Atmospheric Chemistry and Physics*, *6*(12), 4775–4800. https://doi.org/10.5194/acp-6-4775-2006

Wagner, R., Kaufmann, J., Möhler, O., Saathoff, H., Schnaiter, M., Ullrich, R., & Leisner, T. (2018). Heterogeneous ice nucleation ability of NaCl and sea salt aerosol particles at cirrus temperatures. *Journal of Geophysical Research: Atmospheres*, *123*(5), 2841–2860. https://doi.org/10.1002/2017JD027864

Wagner, R., Kiselev, A., Möhler, O., Saathoff, H., & Steinke, I. (2016). Pre-activation of ice-nucleating particles by the pore condensation and freezing mechanism. *Atmospheric Chemistry and Physics*, *16*(4), 2025–2042. https://doi.org/10.5194/acp-16-2025-2016

Wagner, R., & Möhler, O. (2013). Heterogeneous ice nucleation ability of crystalline sodium chloride dihydrate particles. *Journal of Geophysical Research: Atmospheres*, *118*(10), 4610–4622. https://doi.org/10.1002/jgrd.50325

Wang, P. K. (2013). *Physics and dynamics of clouds and precipitation*. Cambridge University Press. https://doi.org/10.1017/CBO9780511794285

Wegener, A. (1912). Thermodynamik der atmosphäre. *Nature*, *90*, 31. https://doi.org/10.1038/090031a0

Welker, R. W. (2012). Chapter 4 - size analysis and identification of particles. In R. Kohli & K. L. Mittal (Eds.), *Developments in surface contamination and cleaning* (pp. 179–213). William Andrew Publishing. https://doi.org/10.1016/B978-1-4377-7883-0.00004-3

Wex, H., Huang, L., Zhang, W., Hung, H., Traversi, R., Becagli, S., Sheesley, R. J., Moffett, C. E., Barrett, T. E., Bossi, R., Skov, H., Hünerbein, A., Lubitz, J., Löffler, M., Linke, O., Hartmann, M., Herenz, P., & Stratmann, F. (2019). Annual variability of ice-nucleating particle concentrations at different Arctic locations. *Atmospheric Chemistry and Physics*, *19*(7), 5293–5311. https://doi.org/10.5194/acp-19-5293-2019

Whale, T. F., Murray, B. J., O'Sullivan, D., Wilson, T. W., Umo, N. S., Baustian, K. J., Atkinson, J. D., Workneh, D. A., & Morris, G. J. (2015). A technique for quantifying heterogeneous ice nucleation in microlitre supercooled water droplets. *Atmospheric Measurement Techniques*, *8*(6), 2437–2447. https://doi.org/10.5194/amt-8-2437-2015

Whitby, K. T. (1978). The physical characteristics of sulfur aerosols. *Atmospheric Environment (1967)*, *12*(1–3), 135–159. https://doi.org/10.1016/0004-6981(78)90196-8

Wilbourn, E. K., Lacher, L., Guerrero, C., Vepuri, H. S. K., Höhler, K., Nadolny, J., Pantoya, A. D., Möhler, O., & Hiranuma, N. (2024). Measurement report: A comparison of ground-level ice-nucleating-particle abundance and aerosol properties during autumn at contrasting marine and terrestrial locations. *Atmospheric Chemistry and Physics*, *24*(9), 5433–5456. https://doi.org/10.5194/acp-24-5433-2024

Wilson, J. C., & Liu, B. Y. H. (1980). Aerodynamic particle size measurement by laser-doppler velocimetry. *Journal of Aerosol Science*, *11*(2), 139–150. https://doi.org/10.1016/0021-8502(80)90030-0

Wilson, T. W., Ladino, L. A., Alpert, P. A., Breckels, M. N., Brooks, I. M., Browse, J., Burrows, S. M., Carslaw, K. S., Huffman, J. A., Judd, C., Kilthau, W. P., Mason, R. H., McFiggans, G., Miller, L. A., Nájera, J. J., Polishchuk, E., Rae, S., Schiller, C. L., Si, M., … Murray, B. J. (2015). A marine biogenic source of atmospheric ice-nucleating particles. *Nature*, *525*(7568), 234–238. https://doi.org/10.1038/nature14986

Yadav, S., Venezia, R. E., Paerl, R. W., & Petters, M. D. (2019). Characterization of ice-nucleating particles over northern India. *Journal of Geophysical Research: Atmospheres*, *124*(19), 10467–10482. https://doi.org/10.1029/2019JD030702

Yang, L., Yin, Y., Yang, S., Jiang, H., Xiao, H., Chen, Q., Su, H., & Chen, C. (2013). Measurement and analysis of atmospheric ice nuclei in Nanjing. *Chinese Journal of Atmospheric Sciences (in Chinese)*, *37*(3), 579–594. https://doi.org/10.3878/j.issn.1006-9895.2012.11242

Yang, Y., & Liu, R. (2022). Anthropogenic aerosols effects on ice clouds: A review. *Atmosphere*, *13*(6), 910. https://doi.org/10.3390/atmos13060910

Yau, M., & Rogers, R. R. (1989). *A short course in cloud physics*. https://shop.elsevier.com/books/a-short-course-in-cloud-physics/yau/978-0-08-057094-5

You, L., Yang, S., Wang, X., & Pi, J. (2002). Study of ice nuclei concentration at Beijing in spring of 1995 and 1996. *Acta Meteorologica Sinica*, *60*(1), 101–109.

Yue, S., Li, L., Xu, W., Zhao, J., Ren, H., Ji, D., Li, P., Zhang, Q., Wei, L., Xie, Q., Pan, X., Wang, Z., Sun, Y., & Fu, P. (2022). Biological and nonbiological sources of fluorescent aerosol particles in the urban atmosphere. *Environmental Science & Technology*, *56*(12), 7588–7597. https://doi.org/10.1021/acs.est.1c07966

Yue, S., Ren, H., Fan, S., Sun, Y., Wang, Z., & Fu, P. (2016). Springtime precipitation effects on the abundance of fluorescent biological aerosol particles and HULIS in Beijing. *Scientific Reports*, *6*(1), 29618. https://doi.org/10.1038/srep29618

Yue, S., Ren, H., Fan, S., Wei, L., Zhao, J., Bao, M., Hou, S., Zhan, J., Zhao, W., Ren, L., Kang, M., Li, L., Zhang, Y., Sun, Y., Wang, Z., & Fu, P. (2017). High abundance of fluorescent biological aerosol particles in winter in Beijing, China. *ACS Earth and Space Chemistry*, *1*(8), 493–502. https://doi.org/10.1021/acsearthspacechem.7b00062

Zelinka, M. D., Randall, D. A., Webb, M. J., & Klein, S. A. (2017). Clearing clouds of uncertainty. *Nature Climate Change*, *7*, 674–678. https://doi.org/10.1038/nclimate3402

Zhang, C., Wu, Z., Chen, J., Chen, J., Tang, L., Zhu, W., Pei, X., Chen, S., Tian, P., Guo, S., Zeng, L., Hu, M., & Kanji, Z. A. (2022). Ice-nucleating particles from multiple aerosol sources in the urban environment of Beijing under mixed-phase cloud conditions. *Atmospheric Chemistry and Physics*, *22*(11), 7539–7556. https://doi.org/10.5194/acp-22-7539-2022

Zhang, J., Lian, C., Wang, W., Ge, M., Guo, Y., Ran, H., Zhang, Y., Zheng, F., Fan, X., Yan, C., Daellenbach, K. R., Liu, Y., Kulmala, M., & An, J. (2022). Amplified role of potential hono sources in o3 formation in north china plain during autumn haze aggravating processes. *Atmospheric Chemistry and Physics*, *22*(5), 3275–3302. https://doi.org/10.5194/acp-22-3275-2022

Zhang, Q., Jimenez, J. L., Canagaratna, M. R., Allan, J. D., Coe, H., Ulbrich, I., Alfarra, M. R., Takami, A., Middlebrook, A. M., Sun, Y. L., Dzepina, K., Dunlea, E., Docherty, K., DeCarlo, P. F., Salcedo, D., Onasch, T., Jayne, J. T., Miyoshi, T., Shimono, A., … Worsnop, D. R. (2007). Ubiquity and dominance of oxygenated species in organic aerosols in anthropogenically-influenced northern hemisphere midlatitudes. *Geophysical Research Letters*, *34*(13). https://doi.org/10.1029/2007GL029979

Zhang, W., Zhuang, G., Huang, K., Li, J., Zhang, R., Wang, Q., Sun, Y., Fu, J. S., Chen, Y., Xu, D., & Wang, W. (2010). Mixing and transformation of asian dust with pollution in the two dust storms over the northern china in 2006. *Atmospheric Environment*, *44*(28), 3394–3403. https://doi.org/10.1016/j.atmosenv.2010.06.011

Zhao, B., Wang, Y., Gu, Y., Liou, K.-N., Jiang, J. H., Fan, J., Liu, X., Huang, L., & Yung, Y. L. (2019). Ice nucleation by aerosols from anthropogenic pollution. *Nature Geoscience*, *12*(8), 602–607. https://doi.org/10.1038/s41561-019-0389-4

Zhou, D., Hong, Y., Wang, Y., Liu, N., Zhang, Y., & Li, L. (2016). Observation on distributions of atmospheric ice nuclei concentration and size under the influence of dust weather. *JOURNAL OF DESERT RESEARCH*, *36*(6), 1672–1678. https://doi.org/10.7522/j.issn.1000-694X.2016.00052 （原文：周德平, 洪也, 王扬锋, 刘宁微, 张云海, 李丽光. 沙尘天气过程对沈阳大气冰核浓度与尺度分布的影响 [J]. 中国沙漠, 2016, 36(6): 1672-1678.）

Ziemba, L. D., Beyersdorf, A. J., Chen, G., Corr, C. A., Crumeyrolle, S. N., Diskin, G., Hudgins, C., Martin, R., Mikoviny, T., Moore, R., Shook, M., Thornhill, K. L., Winstead, E. L., Wisthaler, A., & Anderson, B. E. (2016). Airborne observations of bioaerosol over the southeast united states using a wideband integrated bioaerosol sensor. *Journal of Geophysical Research: Atmospheres*, *121*(14), 8506–8524. https://doi.org/10.1002/2015JD024669